Dynamics of ligands on gold surfaces to obtain Janus nanoclusters : a theoretical and experimental investigation

Jesus Gustavo Lugo Preciado

▶ **To cite this version:**

Jesus Gustavo Lugo Preciado. Dynamics of ligands on gold surfaces to obtain Janus nanoclusters : a theoretical and experimental investigation. Material chemistry. Université Pierre et Marie Curie - Paris VI; Université de Liège, 2016. English. NNT : 2016PA066570 . tel-01539565

HAL Id: tel-01539565

https://theses.hal.science/tel-01539565

Submitted on 15 Jun 2017

HAL is a multi-disciplinary open access archive for the deposit and dissemination of scientific research documents, whether they are published or not. The documents may come from teaching and research institutions in France or abroad, or from public or private research centers.

L'archive ouverte pluridisciplinaire **HAL**, est destinée au dépôt et à la diffusion de documents scientifiques de niveau recherche, publiés ou non, émanant des établissements d'enseignement et de recherche français ou étrangers, des laboratoires publics ou privés.

FACULTY OF SCIENCE
Université de Liège
Theoretical physical chemistry
Supervisor: Professor Françoise Remacle

Université Pierre et Marie Curie
Condensed matter chemistry laboratory
Co – Supervisor: Professor Corinne Chanéac

Dynamics of ligands on gold surface to obtain Janus nanoclusters: A theoretical and experimental investigation

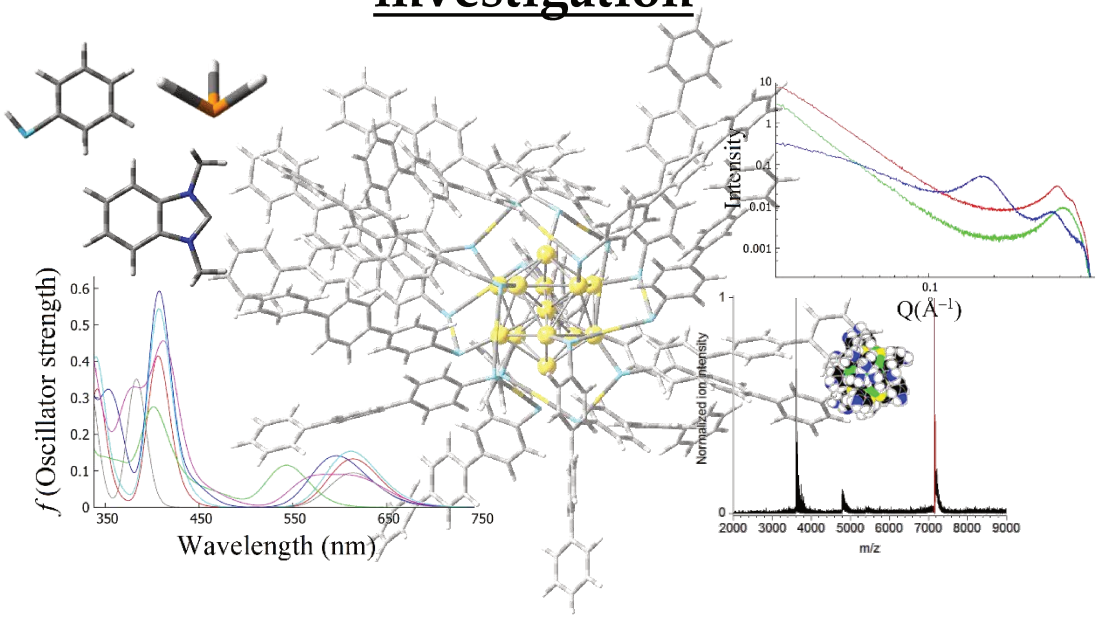

Academic year 2015-2016

Dissertation presented by
Gustavo Lugo
To obtain the degree of
Doctor in Science

Acknowledgments

First I would like to express my gratitude to my PhD supervisor, Prof. Françoise Remacle. I would like to thank her patience and support during these 3 years. Her guidance, knowledge, experience and very fruitful discussions were essential for this research and for the writing of this thesis. I thank her as well for sharing her passion for science, especially in quantum chemistry and for teaching me two very important lessons: critical thinking and skepticism. It has been an honor to have worked with her.

I would like to thank also my co – supervisor, Prof. Corinne Chanéac for having me in LCMCP at UPMC and give me the opportunity to work with her. I thank Prof. Corinne Chanéac for her support during my stay in Paris and for all the facilities I had access to. I would like to express my special appreciation for her advices and the time she spent mentoring me on the synthesis and characterization of gold nanoclusters. I thank as well Dr. David Portehault, Dr. Olivier Durupthy, Dr. Patrick Legriel and Dr. Mohamed Selmane at UPMC for their help and availability.

Besides my supervisor, I am very thankful to Prof. Bernarld Leyh at ULg for his guidance, sharing his knowledge and collaboration on the mass spectrometry of gold nanoclusters and for those interesting discussions.

A very special thanks to Dr. Barbara Fresch for all the insightful discussions we had, her encouragement and motivation. Also for all the material she provided for my work.

A very special thanks to Dr. Jean – François Greisch at the KIT, Germany for the ESI – MS and IMS – MS measurements. I thank him as well for the time he spent on the interpretations on the mass spectrometry results and the knowledge he shared with me. His contributions and collaboration were indispensable on the characterization of our synthesized nanoclusters.

I would like to thank as well Dr. Danielle Laurencin and Dr. Sebastien Richeter at the Institut Charles Gerhardt in the Université de Montpellier, France and Dr. Frederic Tielens at UPMC with whom a very interesting collaboration involving theory and experiments on the reactivity of gold nanoparticles and nanoclusters towards *n* – heterocyclic carbenes has been performed.

I am very grateful to Dr. Benoît Mignolet with whom I spent very good time for his help and advices. Also, I thank my office mates and friends Dr. Ana Ballester, Valérie Schwanen and Dr. Astrid Nikodem for their advice and support.

Last but not the least, I am very thankful to my family and friends.

Abstract

We performed a joint computational – experimental investigation of the dynamics of ligand exchange on gold nanoclusters (GNC) surface with the aim to understand how to control the structural and optical properties of GNC through the design of their ligand shell. Our computational studies were carried out in the framework of the Kohn – Sham implementation of density functional theory in quantum chemistry. We analyzed the main features of UV – Vis spectra computed at the TD – DFT / CAM – B3LYP level for the Au_{13}, Au_{25}, and Au_{28} metallic cores protected by thiolate, chloride, and phosphine ligands. Our results show that it is possible to tune the energy of the lowest absorption band of gold clusters by ligand shell engineering in order to control the charge redistribution between ligand shell and metallic core.

In parallel we synthesized a set of $Au_{25}(ATP)_x(TP)_{18-x}$ clusters with different ATP/TP ratios using an *adapted* Demessence protocol by combining 4ATP (4 – aminothiophenol) and TP (thiophenol) ligands. ESI – MS measurements evidence that for these mixed ligand shells the Au_{25} nuclearity is preserved. However, the addition of the DDT (1 – dodecanethiol) ligand in the mixture leads to nanoparticle formation. FT – IR spectroscopy confirms the absorption of two different ligands on the gold surface and SAXS shows that we have a good correlation between the distance between two clusters and the length of the ligand protecting them.

Furthermore, we collaborated with the Institut Charles Gerhardt in the Université de Montpellier, France whose experimental results show that several *n* – heterocyclic carbenes (NHC) bearing different groups on the N atoms exhibit similar reactivity when protecting a gold nanosurface. The formation of the bis(NHC) Au^I gold complexes is evidenced by ^{13}C NMR. In order to complement and interpret the experimental results, we carried out a computational study of the adsorption of a single NHC on Au_{38} which acts as a model for the gold surface, as well as of the fully NHC ligated Au_{38} cluster. The joint experimental – theoretical study, in particular the comparison between computed and ^{13}C NMR spectra allows proposing a possible mechanism explaining the formation of $[NHC – Au – NHC]^+$ complexes and the erosion experienced by the nanoparticle.

Finally, we carried out a comparison of the mode of binding and the structural and optical properties of the fully ligated PH_3 and NHC GNC with metallic cores of different nuclearities. Our computations show that the Au – P bond is weaker than the Au – NHC one. Additionally, our study confirms that the ligand – to – metal charge transfer is an important parameter for understanding the electronic transitions and the UV – Vis spectra in these clusters. Our computations on the PH_3 – Au_{38} set of complexes show that there is a site selectivity for the reactivity for the PH_3 interacting on the Au_{38} surface which allows predicting where the PH_3 is likely to be adsorbed. This selectivity is not observed in the case of the binding of a single NHC ligand on the surface of the Au_{38} cluster.

Content

Chapter I. Introduction 0

References 8

Chapter II. Electronic structure methodology 15

Introduction 15

2.1 Density Functional Theory 17

2.2 Equilibrium geometry determination and the Berny optimization algorithm 22

2.3 Thermochemistry and vibrational analysis 24

2.3.1 Computation of thermochemical quantities 24

2.3.2 Computation of normal mode frequencies 26

2.4 Charge distribution computation 27

2.5 Time dependent DFT 29

2.6 Solvation. The Polarizable – continuum model (PCM) 31

2.7 Hybrid QM – MM methodology 33

2.7.1 Principles of the QM – MM method 34

2.7.2 The QM – MM junction 37

2.8 References 38

Chapter III. Charge redistribution effects on the UV – Vis spectra of small ligated gold clusters 43

Introduction 43

3.1 Publication 1 46

3.2 References 59

Chapter IV. Geometry , electronic structure and optical properties of the $[Au_{25}(SR)_{18}]^-$ (R = CH_3, TP, SPhPh, SPhPhPh, 4ATP) and the Janus $[Au_{25}(SR')_x(SR'')_{18-x}]^-$ (R' = Ph and R'' = 4ATP, $CH_3(CH_2)_4COOH$) clusters 61

Introduction 61

4.1 The monoligand protected $[Au_{25}(SR)_{18}]^-$ cluster 63

4.1.1 Structure and partial charge distribution of the monoligand protected $[Au_{25}(SR)_{18}]^-$ 63

4.1.2 Optical properties 70

4.2 The Janus $[Au_{25}(SR')_x(SR'')_{18-x}]^-$ cluster (R' = Ph (TP) and R'' = 4ATP, $CH_3(CH_2)_4COOH$) 74

4.2.1 Structure and partial charge distribution of the Janus $[Au_{25}(TP)x(S(CH_2)_5COOH)_{18-x}]^-$ 74
4.2.2 Structure and partial charge distribution effects of thiolate ligands on the Janus $[Au_{25}(TP)x(4ATP)_{18-x}]^-$ cluster 79
4.2.3 Optical properties 83
4.3 Conclusion 92
4.4 References 93
Chapter V. Experimental approach to gold nanocluster synthesis and characterization 97
Introduction 97
5.1 Synthesis and characterisation of the $Au_{25}(TP)_{18}$ and $Au_{25}(4ATP)_{18}$ nanoclusters 99
5.1.1 Synthesis protocol of the $Au_{25}(TP)_{18}$ and $Au_{25}(4ATP)_{18}$ nanoclusters 99
5.1.2 Characterization of the $Au_{25}(TP)_{18}$ and $Au_{25}(4ATP)_{18}$ nanoclusters 101
5.2 The $Au_{25}(SR)_{18}(SR')_{18-x}$ cluster synthesis protocol by simultaneous ligand addition 116
5.2.1 Synthesis protocol of the $Au_{25}(SR)_{18}(SR')_{18-x}$ nanoclusters 116
5.2.2 Characterization of the $Au_{25}(SR)_{18}(SR')_{18-x}$ clusters 117
5.3 Conclusions 128
5.4 References 129
Chapter VI. Experimental and theoretical study of the reactivity of gold nanoparticles towards benzimidazole – 2 – ylidene ligand 133
Introduction 133
6.1 Publication 2 135
6.2 References 149
Chapter VII. Dynamics of phosphine and 1, 3 – dimethyl – 1H – benzimidazolium ligand on gold nanocluster surface 151
7.1 Introduction 151
7.2 Structure and natural charge distribution 152
7.3 Optical properties 157
7.4 Site reactivity of the PH_3 on the Au_{38} cluster surface. Comparison with NHC 165
7.5 Conclusions 173
7.6 References 174
Conclusions and Perspectives 179
References 182
Appendices 183

1. Supporting information: Charge Redistribution Effects on the UV-Vis Spectra of Small Ligated Gold Clusters: a Computational Study. (Chapter III)..... 183

2. Supporting information: Experimental and Theoretical Study of the Reactivity of Gold Nanoparticles towards Benzimidazole-2 – ylidene Ligands. (Chapter VI)..... 188

List of figures

Chapter I

Figure 1. *Computed optical absorption spectra of the ligated anions $[Au_{25}(SCH_3)]^-$, $[Au_{25}(SPh)]^-$ and the cation $[Au_{25}(SCH_3)]^+$ GNC at the TD – DFT level. 4*
Figure 2*. Structure of the NHC ligands, benzimidazolium salts, NHC – Au^I complexes, and NHC – functionalized AuNPs discussed in [21]. 6*

Chapter II

Figure 1*. Partitioning of a system into different regions studied by a hybrid potential. There are 2 regions in this representation. The QM (in the center) which corresponds to high – level quantum – mechanical calculations while the dark green area, MM, is modeled with molecular mechanics force fields. 34*

Chapter III

Chapter IV

Figure 1*. Computed equilibrium geometries of the bare Au_{25} core (a) and the $[Au_{25}(SR)_{18}]^-$ set of clusters: (b) $[Au_{25}(SCH_3)_{18}]^-$, (c) $[Au_{25}(4ATP)_{18}]^-$, (d) $[Au_{25}(TP)_{18}]^-$, (e) $[Au_{25}(SPhPh)_{18}]^-$ and (f) $[Au_{25}(SPhPhPh)_{18}]^-$. The Au atoms are shown in yellow, the C atoms in grey, the dark blue junctions stand for N, S is represented in navy blue and H is in white. 64*
Figure 2*. Computed equilibrium geometries of the bare Au_{25} core (a) and the $[Au_{25}(SPhPhPh)_{18}]^-$ highlighting three of the ligand interactions; panel a) the upside view, panel b) the side view and panel c) the staple. 65*
Figure 3*. Histogram of the Au – Au distances of the bare Au_{25} core (a) and the $[Au_{25}(SR)_{18}]^-$ clusters: (b) $[Au_{25}(SCH_3)_{18}]^-$, (c) $[Au_{25}(4ATP)_{18}]^-$, (d) $[Au_{25}(TP)_{18}]^-$, (e) $[Au_{25}(SPhPh)_{18}]^-$ and (f) $[Au_{25}(SPhPhPh)_{18}]$. 66*
Figure 4*. Histogram of the radial distances in the bare Au_{25}^- core in panel (a) and the $[Au_{25}(SR)_{18}]^-$ clusters: panel (b) $[Au_{25}(SCH_3)_{18}]^-$, panel (c) $[Au_{25}(4ATP)_{18}]^-$, panel (d) $[Au_{25}(TP)_{18}]^-$, panel (e) $[Au_{25}(SPhPh)_{18}]^-$ and panel (f) $[Au_{25}(SPhPhPh)_{18}]^-$. 68*
Figure 5*. Computed UV−vis absorption spectra of the $[Au_{25}(SR)_{18}]^-$ clusters at the DFT/CAM – B3LYP level. 70*
Figure 6*. Computed UV−vis absorption spectra of the $[Au_{25}(SR)_{18}]^-$ clusters at the DFT/CAM – B3LYP level. The height of the vertical bars give the oscillator strength of each transition and the spectra are obtained by convolution with Gaussian line shapes (σ = 0.085 eV). 72*
Figure 7*. Schematic representation of the energy levels (with a degeneracy threshold of 0.13 eV) together with the isocontour of the corresponding orbitals (isovalue 0.02 $Å^{-3}$) of the $[Au_{25}(SPhPh)_{18}]^-$ cluster at the DFT/CAM – B3LYP level. 73*

***Figure 8**. Molecular orbital diagram of the $[Au_{25}(SR)_{18}]^-$ clusters at the DFT/CAM – B3LYP level. The red bars are the p – SAMO 3 – fold quasi – degenerate HOMO (HOMO – 1, HOMO – 1 and HOMO – 2) and the blue bars stand for the five d – SAMO; the two degenerate LUMO and the 3 – fold quasi – degenerate LUMO + 1.* 73
***Figure 9**. Computed equilibrium geometries of the $[Au_{25}(TP)_{18}]^-$ cluster in panel (a) and of the Janus $[Au_{25}(TP)_x(S(CH_2)_5COOH)_{18-x}]^-$ clusters: panel (b) $[Au_{25}(TP)_{16}(S(CH_2)_5COOH)_2]^-$ cluster, panel (c) $[Au_{25}(TP)_{14}(S(CH_2)_5COOH)_4]^-$, panel (d) $[Au_{25}(TP)_{12}(S(CH_2)_5COOH)_6]^-$ and (e) $[Au_{25}(TP)_{10}(S(CH_2)_5COOH)_8]^-$. The Au atoms are shown in yellow, the C atoms in grey, the dark blue junctions stand for N, S is represented in navy blue and H is in white.* 75
***Figure 10**. Histogram of the Au – Au distances of the $[Au_{25}(TP)_{18}]^-$ (in panel a) and the Janus $[Au_{25}(TP)_x(S(CH_2)_5COOH)_{18-x}]^-$ clusters: panel (b) $[Au_{25}(TP)_{16}(S(CH_2)_5COOH)_2]^-$, panel (c) $[Au_{25}(TP)_{14}(S(CH_2)_5COOH)_4]^-$, panel (d) $[Au_{25}(TP)_{12}(S(CH_2)_5COOH)_6]^-$ and panel (e) $[Au_{25}(TP)_{10}(S(CH_2)_5COOH)_8]^-$* 77
***Figure 11**. Histogram of the radial distances of the $[Au_{25}(TP)_{18}]^-$ (in panel a) and the Janus $[Au_{25}(TP)_x(S(CH_2)_5COOH)_{18-x}]^-$ clusters: panel (b) $[Au_{25}(TP)_{16}(S(CH_2)_5COOH)_2]^-$, panel (c) $[Au_{25}(TP)_{14}(S(CH_2)_5COOH)_4]^-$, panel (d) $[Au_{25}(TP)_{12}(S(CH_2)_5COOH)_6]^-$ and panel (e) $[Au_{25}(TP)_{10}(S(CH_2)_5COOH)_8]^-$* 78
***Figure 12**. Computed equilibrium geometries of the monoligand protected $[Au_{25}(TP)_{18}]^-$ in panel (a) the Janus $[Au_{25}(4ATP)_x(TP)_{18-x}]^-$ clusters: panel (b) $[Au_{25}(4ATP)_4(TP)_{14}]^-$, panel (c) the $[Au_{25}(4ATP)_9(TP)_9]^-$ and panel (d) the $[Au_{25}(4ATP)_{13}(TP)_5]^-$ and the monoligand protected $[Au_{25}(4ATP)_{18}]^-$ cluster in panel (e). In panels (f), (g) and (h) the 4ATP ligands of (b), (c) and (d) are highlighted. The Au atoms are shown in yellow, the C atoms in grey, the dark blue junctions stand for N, S is represented in navy blue and H is in white.* 80
***Figure 13**. Histogram of the Au – Au distances of the monoligand protected $[Au_{25}(TP)_{18}]^-$ in panel (a), the Janus $[Au_{25}(4ATP)_x(TP)_{18-x}]^-$ clusters: panel (b) $[Au_{25}(4ATP)_4(TP)_{14}]^-$, (c) $[Au_{25}(4ATP)_9(TP)_9]^-$ and (d) the $[Au_{25}(4ATP)_{13}(TP)_5]^-$ cluster and the $[Au_{25}(TP)_{18}]^-$ in panel (e).* 81
***Figure 14**. Histogram of the radial distances of the monoligand protected $[Au_{25}(TP)_{18}]^-$ in panel (a), the Janus $[Au_{25}(4ATP)_x(TP)_{18-x}]^-$ clusters: panel (b) $[Au_{25}(4ATP)_4(TP)_{14}]^-$, (c) $[Au_{25}(4ATP)_9(TP)_9]^-$ and (d) the $[Au_{25}(4ATP)_{13}(TP)_5]^-$ cluster and the $[Au_{25}(TP)_{18}]^-$ in panel (e).* 82
***Figure 15**. Computed UV−vis absorption spectra of the monoligand protected $[Au_{25}(TP)_{18}]^-$ and the Janus $[Au_{25}(TP)_x(S(CH_2)_5COOH)_{18-x}]^-$ clusters at the DFT/CAM – B3LYP level.* 84
***Figure 16**. Computed UV−vis absorption spectra of the monoligand protected $[Au_{25}(TP)_x]^-$ and the Janus $[Au_{25}(TP)_x(S(CH_2)_5COOH)_{18-x}]^-$ clusters at the DFT/CAM – B3LYP level. The height of the vertical bars give the oscillator strength of each transition and the spectra are obtained by convolution with Gaussian line shapes (σ = 0.085 eV).* 86
***Figure 17**. Molecular orbital diagram of the Janus $[Au_{25}(TP)_x(S(CH_2)_5COOH)_{18-x}]^-$ clusters at the DFT/CAM – B3LYP level. The red bars are the p – SAMO three – fold quasi – degenerate HOMO (HOMO – 1, HOMO – 1 and HOMO – 2) and the blue bars stand for the 5 d – SAMO; the two degenerate LUMO and the 3 – fold quasi – degenerate LUMO + 1. The AcM6 label was used for $S(CH_2)_5COOH$ ligand.* 87
***Figure 18**. Computed UV−vis absorption spectra of the Janus $[Au_{25}(4ATP)_x(TP)_{18-x}]^-$ clusters together with the monoligand protected $[Au_{25}(4ATP)_{18}]^-$ and the $[Au_{25}(TP)_{18}]^-$ at the DFT/CAM – B3LYP level.* 88
***Figure 19**. Computed UV−vis absorption spectra of the Janus $[Au_{25}(4ATP)_x(TP)_{18-x}]^-$ clusters together with the monoligand protected $[Au_{25}(4ATP)_{18}]^-$ and the $[Au_{25}(TP)_{18}]^-$ at the DFT/CAM – B3LYP level. The height of the vertical bars give the oscillator strength*

of each transition and the spectra are obtained by convolution with Gaussian line shapes (σ = 0.085 eV). 89
***Figure 20**. Molecular orbital diagram of the Janus $[Au_{25}(4ATP)_x(TP)_{18-x}]^-$ clusters at the DFT/CAM – B3LYP level. The red bars are the p – SAMO three – fold quasi – degenerate HOMO (HOMO – 1, HOMO – 1 and HOMO – 2) and the blue bars stand for the 5 d – SAMO; the two degenerate LUMO and the 3 – fold quasi – degenerate LUMO + 1.* 90
***Figure 21**. Schematic representation of the energy levels (with a degeneracy threshold of 0.13 eV) together with the isocontour of the corresponding orbitals (isovalue 0.02 $Å^{-3}$) of the Janus $[Au_{25}(4ATP)_9(TP)_9]^-$ cluster at the DFT/CAM – B3LYP level.* 91

Chapter V

***Figure 1.** Scheme of the synthesis of ligated Au_{25} cluster. Rate of addition of solution A and C was 60 ml/ h except for TP for which a rate of 45 ml / h was used. Stirring rate was 500 rpm. Quantities of ligand, reductant agent and the $HAuCl_4$– $3H_2O$ are specified in table 1.* 100
***Figure 2.** FT – IR spectra of the single ligand protected gold clusters by 4ATP (a), TP (b) and DDT (c). The ligand used for cluster protection is indicated at the top right of every spectrum. 4ATP stands for 4 – aminothiophenol, TP for thiophenol and DDT for 1 – dodecanethiol.* 102
***Figure 3.** TEM images of TP gold clusters synthesized by the Demessence method. The cluster size distribution is shown at the right. The average diameter is 1.10 ± 0.51 nm. 480 clusters were taken into account to obtain the size distribution in THF.* 103
***Figure 4.** TEM image of 4ATP gold clusters synthesized by the Demessence method. The cluster size distribution is shown at the right. The average diameter is 1.23 ± 0.20 nm. Only 74 clusters were taken into account to obtain the size distribution due to the aggregates formed.* 103
***Figure 5.** TEM image of DDT gold clusters synthesized by the Demessence method. The cluster size distribution is shown at the right. The average diameter is 1.05 ± 0.68 nm. 1443 clusters were taken into account to obtain the size distribution.* 104
***Figure 6.** Schematic representation of the distance measure by the SAXS technique.* 105
***Figure 7**. SAXS profiles of the $Au_{25}(TP)_{18}$ (in red), $Au_{25}(4ATP)_{18}$ (green) and the $Au_n(4ATP)_m$ synthesized. SAXS measurements were performed in powder using a potential difference of 0.45 kV and an electrical current of 0.5 mA. Figure provided by Dr. Mohamed Selmane.* 106
***Figure 8.** Negative – mode ESI – MS spectrum of the $[Au_{25}(TP)_{18}]^-$ cluster. The arrival time distribution is shown on the right as an inset. Clusters were analyzed in DCM. Figure provided by Dr. J.-F Greisch (KIT).* 107
***Figure 9.** Survival yield fragmentation pattern for the $[Au_{25}(TP)_{18}]^-$ cluster as a function of the collision energy in arbitrary units (a.u.). Clusters were analyzed in DCM. The inset at the left shows the masses of the different fragments. The purple curve stands for the $[Au_{25}(TP)_{18}]^-$ cluster (6890 Da) while the green curve (5665 Da) represents the $Au_{21}(TP)_{14}$ (i.e. $Au_{25}(TP)_{18}$ – $Au_{21}(TP)_{14}$). The maximum relative yield of the for the $Au_{21}(TP)_{14}$ clusters is found at a collision energy of 64 a.u. Figure provided by Dr. J.-F Greisch (KIT)* 108
***Figure 10.** Negative – mode ESI – MS spectrum of the $[Au_{25}(4ATP)_{18}]^-$ cluster. The inset shows the isotopomer splitting highlighting the presence of other charge states (other than one) in very low intensities. Clusters were analyzed in DMSO. Figure provided by Dr. J.-F Greisch (KIT).* 109

***Figure 11**. Survival yield fragmentation pattern of the $[Au_{25}(4ATP)_{18}]^-$ cluster. Clusters were analyzed in DMSO. The legend reports the masses of the different fragments. The purple curve stands for the $Au_{25}(4ATP)_{18}$ cluster (7160 Da) while the green curve (5875 Da) represents the $Au_{21}(TP)_{14}$ (i.e. $Au_{25}(4ATP)_{18} – Au_4(TP)_4$). The maximum relative yield of the for the $Au_{21}(TP)_{14}$ clusters is found at 64 a.u. Figure provided by Dr. J.-F Greisch (KIT).* 110*

***Figure 12.** Separation according to cross section (and charge) of selected clusters for the $[Au_{25}(4ATP)_{18}]^-$ cluster. Arrival time profile for the $[Au_{25}(4ATP)_{18}]_x^{x-}$ cluster aggregates. Clusters were analyzed in DCM. Figure provided by Dr. J.-F Greisch (KIT).* 110*

***Figure 13**. Computed IMB He cross – sections for the $[Au_{25}(4ATP)_{18}]_x^{x-}$ aggregates by Mobcal as a function of the number of units. Figure provided by Dr. J.-F Greisch (KIT).* 111*

***Figure 14**. Converted TWI – MS cross – section of the for the $[Au_{25}(4ATP)_{18}]_x^{x-}$ aggregates. Figure provided by Dr. J.-F Greisch (KIT).* 112*

***Figure 15**. TWIMS converted cross – section of the $[Au_{25}(4ATP)_{18}]_x^{x-}$ aggregates as a function of the drift time (tD). The black circles stand for the model and the lines represent the experimental results. Figure provided by Dr. J.-F Greisch (KIT).* 113*

***Figure 16**. TGA of the single thiolate - capped clusters in air: at the top, the $Au_{25}(4ATP)_{18}$ indicated with the NH_2 group and at the bottom the $Au_{25}(TP)_{18}$ cluster (SPh).* 114*

***Figure 17**. UV – vis spectra of the $Au_{25}(4ATP)_{18}$ (in green) and the $Au_{25}(TP)_{18}$ (in red) clusters measured in DMF and DCM, respectively.* 115*

***Figure 18**. FT – IR spectra of the single ligand protected gold clusters by 4ATP (a) and DDT (c) and also the two different ligand capped clusters by 4ATP and DDT (b). The ligand used is indicated at the top right of every spectrum. 4ATP stands for 4 – aminothiophenol and DDT for 1 – dodecanethiol.* 119*

***Figure 19.** FT – IR spectra of the single ligand protected gold clusters by DDT(a) and TP (c) and also the two different ligand capped clusters (in b). The ligand used is indicated at the top right of every spectrum. The dotted circle in (b) highlights the **double C – C bond stretching** at 1577.49 cm^{-1} and the **(sp^2) C – H stretching at** 3051.53 cm^{-1} the of the benzene ring in TP.* 120*

***Figure 20**. FT – IR spectra of the single ligand protected gold clusters by 4ATP (a) and TP (c) and also the two different ligand capped clusters in (c). The ligand used is indicated at the top right of every spectrum. 4ATP stands for 4 –aminothiophenol and TP for thiophenol.* 121*

***Figure 21.** TEM image of $Au_z(4ATP)_x(DDT)_y$ clusters synthesized by the Demessence method. The cluster size distribution is shown at the right. The average diameter is 0.92 ± 0.10 nm. 6852 clusters were taken into account to obtain the size distribution.* 122*

***Figure 22.** TEM image of $Au_{z'}(TP)_{x'}(4ATP)_{y'}$ clusters synthesized by the Demessence method. The cluster size distribution is shown at the right. The average diameter is 1.33 ± 0.37 nm. 6852 clusters were taken into account to obtain the size distribution.* 122*

***Figure 23.** TEM image of $Au_{z''}(TP)_{x''}(DDT)_{y''}$ clusters synthesized by the Demessence method. The cluster size distribution is shown at the right. The average diameter is 1.33 ± 0.36 nm. 5432 clusters were taken into account to obtain the size distribution.* 122*

***Figure 24**. Positive – mode ESI – MS spectrum of the $[Au_{25}(4ATP)_x(TP)_{18-x}]^-$ set of clusters. The arrival time distribution is shown at the right as an inset. Clusters were analyzed in DCM. Figure provided by Dr. J.-F Greisch (KIT).* 123*

***Figure 25**. Positive – mode ESI – MS spectrum of the $[Au_{25}(4ATP)_x(TP)_{18-x}]^-$ set of clusters. Upside the dicharged and the monocharged mass spectra are shown while below the comparison between the experimental and the theoretical (in different colors) are presented. Figure provided by Dr. J.-F Greisch (KIT)* 124*

***Figure 26**. Positive – mode ESI – MS spectrum of the monocharged $[Au_{25}(4ATP)_x(TP)_{18-x}]^-$ set of clusters. The composition of the ligand layer is shown for the different*

protected clusters obtained. A detailed description of the ligand interaction proposed by Dr. J.-F Greisch is shown in figure 28. Figure provided by Dr. J.-F Greisch (KIT). 125
***Figure 27**. Positive – mode ESI – MS spectrum of the dicharged $[Au_{25}(4ATP)_x(TP)_{18-x}]^-$ set of clusters. The composition of the ligand layer is shown for the different protected clusters obtained. A detailed description of the ligand interaction proposed by Dr. J.-F Greisch is shown in figure 28. Figure provided by Dr. J.-F Greisch (KIT).* 126
***Figure 28**. The TP and the 4ATP ligands and the two different hypothetical conformations of the N = N interligand bridges can take. In the case of a bridging conformation of the dimer without gold at one end the sulfur is likely deprotonated. In purple we show the stoichiometry of the ligand/dimer as used in figure 26 and 27.* 126
***Figure 29**. UV – vis spectra of the $Au_{25}(4ATP)_x(TP)_{18-x}$ measured in DMF.* 127

Chapter VI

Chapter VII

***Figure 1**. Equilibrium geometry of the bare Au_{13}^{5+} cluster (panel a)), of $[Au_{13}NHC_{10}Cl_2]^{3+}$ (panel b))and an upper view in panel c). Panel d) shows the carbene ligand used in this study. Panel e) the $[Au_{13}NHC_8Cl_4]^+$ cluster and its upper view in panel f). Equilibrium geometries were calculated in the gas phase using DFT at the CAM-B3LYP level. The LANL2MB pseudopotential and basis set were used for Au atoms and the 6 – 31G(d) basis set for the atoms of the ligand layer. Yellow atoms stand for Au, green spheres Cl, blue junctions represent N, gray C and H is shown in white.* 153
***Figure 2.** Equilibrium geometry of (a) the $Au_{20}(PH_3)_8$, b) the $Au_{20}NHC_8$ clusters and c) schematic comparison of the Au_{20} edges lengths in Å. Calculations have been performed in the gas phase using DFT at the CAM-B3LYP level. The LANL2MB pseudopotential and basis set were used for Au atoms and the 6 – 31G(d) basis set for the atoms of the ligand layer. Yellow atoms stand for Au, blue represents N, gray C and H atoms are shown in white.* 154
***Figure 3.** Equilibrium geometry of the phosphine – coated Au_{38} cluster studied. Au atoms are in yellow, S is represented by blue junctions, C in grey, P in purple, N in blue spheres and H in white. Calculations have been performed in the gas phase at the DFT CAM – B3LYP LANL2MB / 6 – 31G (d) level. The $Au_{38}NHC_9$ can be seen in reference [34].* 155
***Figure 4**. MO diagram of the $[Au_{13}NHC_{10}Cl_2]^{3+}$ cluster. Isocontours of the frontier molecular orbitals are shown as well as the orbital energy in eV. The degeneracy threshold is 0.13 eV and the isovalue is 0.02 $Å^{-3}$. The CAM – B3LYP functional was used together with the LANL2MB pseudopotential and basis set for Au and the 6 – 31G(d) basis set for the ligand layer.* 158
***Figure 5.** Computed UV − Vis absorption spectra of the $[Au_{13}dppe_5Cl_2]^{3+}$ (taken from ref. [11]) and $[Au_{13}NHC_{10}Cl_2]^{3+}$ clusters. The spectra are computed at the TD – DFT level at the equilibrium geometry of the ground state. The CAM – B3LYP functional was used together with the LANL2MB pseudopotential and basis set for Au and the 6 – 31G(d) basis set for the ligand layer.* 158
***Figure 6.** MO diagram of the $[Au_{13}NHC_8Cl_4]^+$ cluster. Isocontours of the frontier molecular orbitals are shown as well as the orbital energy in eV. The degeneracy threshold is 0.13 eV and the isovalue 0.02 $Å^{-3}$. The CAM – B3LYP functional was used together with the LANL2MB pseudopotential and basis set for Au and the 6 – 31G(d) basis set for the ligand layer.* 161
***Figure 7.** Computed UV − Vis absorption spectra of the $[Au_{13}(P(Ph_2)CH_3)_8Cl_4]^{3+}$ (taken from ref. [11]) and $[Au_{13}NHC_{10}Cl_2]^{3+}$ clusters. The electronic excited states are computed*

at the TD-DFT level. The CAM – B3LYP functional was used together with the LANL2MB pseudopotential and basis set for Au and the 6 – 31G(d) basis set for the ligand layer. 162
Figure 8. *Computed UV − Vis absorption spectra of the* $[Au_{13}NHC_8Cl_4]^{3+}$ *(and* $[Au_{13}NHC_{10}Cl_2]^{3+}$ *clusters. The electronic excited states are computed at the TD-DFT level. The CAM – B3LYP functional was used together with the LANL2MB pseudopotential and basis set for Au and the 6 – 31G(d) basis set for the ligand layer.* 163
Figure 9*. Computed UV − Vis absorption spectra of the* $Au_{20}NHC_8$ *and* $Au_{20}(PH_3)_8$ *clusters. The excited electronic states are computed at the TD – DFT level. The CAM – B3LYP functional was used together with the LANL2MB pseudopotential and basis set for Au and the 6 – 31G(d) basis set for the ligand layer.* 164
Figure 10*. Comparison of the computed optical spectra between the phosphine and the NHC protected* Au_{38} *clusters. The excited electronic states are computed at the TD – DFT level. The CAM – B3LYP functional was used together with the LANL2MB pseudopotential and basis set for Au and the 6 – 31G(d) basis set for the ligand layer.* 165
Figure 11. *Equilibrium geometries of the different* $Au_{38} – PH_3$ *complex configurations studied. Au atoms are in yellow, P in purple and H in white. Calculations have been performed in the gas phase at the DFT CAM – B3LYP LANL2MB / 6 – 31G (d) level. Unfortunately, no equilibrium structure was found for configurations 6, 10 and 11.* 166
Figure 12*. Histogram of the Au – Au distances of the bare and the different* $PH_3 – Au_{38}$ *complexes structures. The equilibrium structures have been computed at the DFT LANL2MB / 6 – 31G(d) level.* 169
Figure 13*. Histogram of the radial distances of gold atoms in the bare* Au_{38} *and the different* $PH_3 – Au_{38}$ *complexes structures. The equilibrium structures have been computed at the DFT LANL2MB / 6 – 31G(d) level.* 170
Figure 14*. Natural charges of the gold atoms in the bare* Au_{38} *in its equilibrium geometry computed at the DFT level. The relativistic pseudopotential and basis set LANL2MB was used for gold and the 6 – 31G(d) for the ligands. Circles of the same colour highlight the gold atoms of the same charge. The double circle represents an atom on the back of another.* 171

List of tables

Chapter I

Chapter II

Chapter III

Chapter IV

***Table 1**. Label, cluster stoichiometry and S – C, $Au_{(C)}$ – Au_{12} and $Au_{(C)}$ – Au_{staple} bond lengths in (Å) of the $[Au_{25}(SR)_{18}]^-$ clusters. $Au_{(C)}$ stands for the central atom in the icosahedral Au_{13} while Au_{12} represents the rest of the Au atoms. $Au_{staples}$ represent the Au atoms left which form the staple motif.* 69*

***Table 2**. Label, cluster stoichiometry, partial charges of the different fragments in the clusters and HOMO – LUMO gap values (H – L gap) of the $[Au_{25}(SR)_{18}]^-$ clusters.* 69*

***Table 3**. Label, cluster stoichiometry, partial charge on the Au_{13} core (NBO) and characteristics of the first and second band of the $[Au_{25}(SR)_{18}]^-$ set of clusters.* 74*

***Table 4**. Label, cluster stoichiometry and S – C, $Au_{(C)}$ – Au_{12} and $Au_{(C)}$ – Au_{staple} distances in (Å) of the Janus $[Au_{25}(TP)_x(S(CH_2)_5COOH)_{18-x}]^-$ set of clusters together with the monoligand protected $[Au_{25}(TP)_{18}]^-$. $Au_{(C)}$ stands for the central atom in the icosahedral Au_{13} while Au_{12} represents the rest of the Au atoms. $Au_{staples}$ represent the Au atoms left which form the staple motif.* 79*

***Table 5**. Label, cluster stoichiometry, partial charge of the different fragments in the clusters and HOMO – LUMO gap (H – L gap) of the Janus $[Au_{25}(TP)_x(S(CH_2)_5COOH)_{18-x}]^-$ set of clusters together with the monoligand protected $[Au_{25}(TP)_{18}]^-$. The partial charges for TP and $S(CH_2)_5COOH$ represent the charge per ligand.* 79*

***Table 6**. Label, cluster stoichiometry, S – C, $Au_{(C)}$ – Au_{12} and $Au_{(C)}$ – Au_{staple} distances in (Å) of the Janus $[Au_{25}(4ATP)_x(TP)_{18-x}]^-$ clusters: (a) shows the $[Au_{25}(4ATP)_4(TP)_{14}]^-$, (c) the $[Au_{25}(4ATP)_9(TP)_9]^-$ and (e) the $[Au_{25}(4ATP)_{13}(TP)_5]^-$ cluster for the two different ligands. $Au_{(C)}$ stands for the central atom in the icosahedral Au_{13} while Au_{12} represents the rest of the Au atoms. $Au_{staples}$ represent the Au atoms left which form the staple motif.* 83*

***Table 7**. Label, cluster stoichiometry, partial charges of the different fragments in the clusters and HOMO – LUMO gap (H – L gap) of the Janus $[Au_{25}(4ATP)_x(TP)_{18-x}]^-$ clusters: (a) shows the $[Au_{25}(4ATP)_4(TP)_{14}]^-$, (c) the $[Au_{25}(4ATP)_9(TP)_9]^-$ and (e) the $[Au_{25}(4ATP)_{13}(TP)_5]^-$ cluster. The partial charge for TP and $S(CH_2)_5COOH$ represent the charge per ligand.* 83*

***Table 8**. Label, cluster stoichiometry and characteristics of the first and second band of the Janus $[Au_{25}(TP)_x(S(CH_2)_5COOH)_{18-x}]^-$ clusters* 87*

***Table 9**. Label, cluster stoichiometry and characteristics of the first and second band of the Janus $[Au_{25}(4ATP)_x(TP)_{18-x}]^-$ clusters.* 90*

Chapter V

Table 1. *Substance used in the synthesis of the single ligated Au_{25}, quantities in mmol and mg, structural formula of every ligand and the mass of solvent (THF) is shown. 100*
Table 2. *q Vector and calculated distance (d) between to gold clusters collected from SAXS analysis of the clusters synthesized. 104*
Table 3. *Sample table, total mass of the sample, residual mass, mast loss and the metal – to – ligand ratio for the 4ATP and the TP single ligand protected clusters synthesized. 115*
Table 4. *Quantities of different substances used in the two ligand synthesis of protected gold clusters. The THF used was anhydrous. 117*

Chapter VI

Chapter VII

Table 1. *Cluster stoichiometry, the length of the Au – L bond of phosphine and carbene passivated clusters and total partial charge on the ligand shell (phosphine or NHC; labeled NBO ligand shell) and on the metal core (NBO Au_n, n = 13, 20 or 38). Calculations have been performed in the gas phase at the DFT CAM – B3LYP LANL2MB / 6 – 31G (d) level of theory. The number in brackets is the natural charge per ligand. 156*
Table 2. *Complex label, relative free energy (ΔG), binding energy (B.E.), HOMO – LUMO (H – L) gap, the natural charge of the Au atom bound to the phosphine ligand in the bare cluster (NBO Au – PH_3), the natural charge of the metallic core in the complex (NBO Au_{38}), P – Au bond length (P – Au length) and coordination number (C.N). Results for configurations 6, 10 and 11 are not shown since unfortunately we did not find any equilibrium geometry in these cases. Calculations have been performed in the gas phase at the DFT CAM – B3LYP LANL2MB / 6 – 31G (d) level of theory. 167*
Table 3*. Deformation energy (E_d) of the system Au_{38} – L. L being PH_3 or NHC ligand. Equilibrium structures of configuration 6, 10 and 11 have not been found in the phosphine case. 172*

Chapter I. Introduction

Ultra – small gold nanoclusters (GNC) exhibit interesting optical properties relevant for applications in catalysis, [1-6] material science [7-9] and medicine. [10-13] Contrary to their nanoparticle counterpart, GNCs show a well – defined structure and stoichiometry instead of a distribution of size and ligand coverage. Since at the nanoscale, size and ligand coverage control the optical and electronic properties, stoichiometric GNC are materials of choice for synthetizing new materials with engineered reproducible properties and for controlling them through a better understanding of the relation between their structure and properties.

Several ligands can be used to passivate GNCs and nanoparticles, for example; amines,[14] thioethers,[15] thiolates [16-20], n – heterocyclic carbenes [21, 22] and phosphines [23-29] leading to a large range of clusters with different core stoichiometry and properties. Ligand protection is not only a way to prevent the formation of larger clusters or nanoparticles, it can also be used to functionalize the cluster. It is well documented that the character of the ligand (electron – donor or attractor) and the presence of different ligands and their organization on the shell have a significant effect on the GNC structure, charge distribution between the metal core and ligand shell and properties. [30-32] Moreover, the structure of the ligand and the mode of grafting on the metal surface can limit the size of the cluster. [1] For instance, phosphine ligands are weakly bound to gold followed by a charge transfer from the ligand shell to the core. Phosphine does not distort the metal core significantly, however the opposite effect takes place in the case of thiolate. [30, 33] They notably distort the bare cluster compared to phosphine and their structure is composed of an inner gold core surrounded by {– SR – Au – SR – Au – SR −} or {– SR – Au – SR −} "*staple*" motifs. Additionally, theoretical work show a shorter binding energy for phosphine GNCs which can explain why in some cases theses nanoclusters are used as a precursors to obtain thiolate coated particles. [28]

The properties of GNCs can be tuned also by protecting the metal core by a mixture of different ligands instead of one hence, taking advantage of the versatility of the metal surface. Exploring different ligand combinations and core morphologies and stoichiometry we open the door to the large field of GNCs functionalization. As mentioned above, the nature of the ligands and their spatial organization turns to be extremely important on the understanding of their optical properties. Two different ligand shell can show different separation domains; Janus configuration; that is to say, ligand spatially segregated, in stripes and randomly organized. Among these, Janus nanoparticles have attracted a lot of attention due to their interesting and characteristic ligand shell asymmetry. As a consequence, they can be used for display applications [34] or – due to their surface properties – as stabilizing agents for emulsions and foams. [35]

Scanning transmission microscope (STM) shows that for gold nanoparticles with 3 – 8 nm diameter a stripe configuration is reported, [36-38] while nuclear Overhauser enhancement spectroscopy (NOESY)

indicates a ligand shell in a Janus – like domain at of 1.5 nm diameters. [39] Patchy or randomly organized ligands in the protecting shell is found in the range 1.5 – 3 nm of diameter. These studies show that the separation ligand domain can be modified by varying the ligand composition and the metal core size. It is suggested that the segregation of ligands depends on the curvature (cluster diameter) and the ligand length difference.

There was in recent years significant progress in the synthesis of thiolate and phosphine ligated gold clusters [24, 28, 40-45] as well in their experimental [22, 27, 29, 41, 42, 46-48] and theoretical [21, 31, 32, 49-54] characterization. However, the identification of the relation between their physicochemical properties and their structure remains a major challenge. Moreover, to achieve synthetic methodologies where one can control the size of the nanocluster and overcome polydispersity remains a challenge. Fortunately, development of GNC synthesis methodologies together with mass spectrometry, X – ray diffraction and scattering and UV – Vis spectroscopy have allowed to characterize several *magic number* clusters. Understanding their stability have led to the establishment of the superatomic model [55] and the electron shell closing concept [56] (based on the Jellium model [57]).

Brust *et al.* reported the first gold nanoparticle capped by thiolate ligands in 1994 [58] and in 2005 the first mass spectrometry study determining a GNC structure. [18] Suggestion that the gold core is highly deformed by the thiolate ligand shell by Garzón [59] and the *divide and protect* concept proposed by Häkkinen [60] together with the structural determination work opened the way to synthesis control of the well – defined size GNCs. Also, the use of single X – Ray diffraction on the $Au_{102}(SR)_{144}$ represented a breakthrough on the study of GNCs since it was the first successful crystallization allowing the cluster structure determination. [61] It is worth mentioning that, in 2008, Zhu and Aikens assign HOMO – to – LUMO character to the lowest energy band in the UV – Vis spectrum of $Au_{25}(SCH_2CH_2Ph)_{18}$ by performing linear response TD – DFT calculation on the anion $[Au_{25}(SH)_{18}]^-$ model, successfully correlating the cluster structure and the optical absorption profile. [48, 62]

The stoichiometry of GNCs is, nowadays, relatively easy to obtain thanks to electrospray ionization (ESI – MS) and ion – mobility separation (IMS – MS) mass spectrometry as well as UV – Vis spectroscopy. However, the atomic structure, that is to say, the organization of the gold atoms in space (its equilibrium geometry) and also that of ligands in the protecting shell is hard to determine. It is actually this difficulty on the structural determination what motivates the use of computational chemistry. DFT is a powerful tool which has strongly contributed on the structural prediction and comprehension of chemical, electronic and optical properties of thiolate, [17, 53, 62-64] phosphine [27, 30-32] and also recently *n* – heterocyclic [21, 22] carbene capped GNC.

Regarding the challenges GNCs represent, the main objective of this thesis is to obtain an insight about how parameters such as; the metal core nuclearity and morphology, the nature of the ligand absorbed on the gold surface and the interligand interactions modify the optical and electronic properties of GNC. For this purpose, a theoretical and an experimental investigations have been carried out.

In the computational part, the structural determination of different phosphine, chloride, thiolate and *n* – heterocyclic carbene coated GNC with Au_{13}, Au_{20}, Au_{28}, Au_{25} and Au_{38} metal cores has been performed at the DFT / CAM – B3LYP level of theory using Gaussian 09 [65], taking as starting point the available crystallographic data [16, 25, 66, 67] (except for Au_{20} where no crystallographic data is yet available). In all of the cases, the ligand protected GNCs show a very close structure to those found experimentally by X – Ray diffraction. For the thiolated capped GNC, the classical *divide and protect* scheme is shown: the structures are composed of an inner gold core surrounded by {– SR – Au – SR – Au – SR −} or {– SR – Au – SR −} "*staple*" motifs.

On the other hand, UV – Vis spectroscopy is normally used to follow the synthesis of GNCs since these nanosystems show a typical optical profile depending on their specific stoichiometry. [16, 24, 45, 48, 63] No surface plasmon resonance is present in this size regime,.[68, 69] The UV – Vis spectra of GNCs is usually characterized by a *tail – and – humps* profile, with relatively weak absorption bands in the visible region which involve the HOMO – LUMO transition [30, 53, 62, 63, 70] while the main band falls in the UV. The optical profile is strongly dependent on the metal core nuclearity and geometry. However, no obvious correlation between these two cluster parameters and the position in energy of the lower energy transitions is found. Here, we compute the UV – Vis spectra at the equilibrium geometry of the ground electronic state using TD – DFT method for the different structures we mentioned above.

Particular attention has been devoted to the $[Au_{25}(SR)_{18}]^-$ (SR being a thiolate ligand) cluster because of its chemical stability, [28, 71] luminescence [72] and catalytic applications. [71, 73-77] The X – Ray characterization made by Murray *et al* [66] in 2008 showed that the crystal structure of the $[Au_{25}(SR)_{18}]^-$ cluster consists of an icosahedral Au_{13} gold core protected by six RS – $(Au – SR)_2$ staple motifs. Also in 2008, Jin *et al.* [48] confirmed the structure also by X – Ray crystallography and NMR analyses and measured its experimental UV – Vis spectroscopy showing three well – defined molecule – like transitions at 1.8, 2.75 and 3.1 eV. The first one at 1.8 corresponds to an HOMO – LUMO transition (as mentioned above). Computational studies have found the same core – staple structure and very good agreement with the optical profiles confirming the experimental results. [64, 78] This motivated us to focus on the synthesis of this particular and stable GNC. Hence, in the experimental part, first, we aim to synthesize the monoligand protected Au_{25} cluster using different ligands: 4 – aminothiophenol (4ATP), thiophenol (TP) and 1 – dodecanethiol (DDT) by using the approach developed by Demessence *et al*. [79] as well as to perform the characterization of their structural and optical properties. Also, successful synthesis and characterization of the two ligand protected $Au_{25}(4ATP)_x(TP)_{18-x}$ by adding simultaneously both ligands in the synthesis process was achieved. Even though the synthesis of GNCs is significantly sensitive to experimental conditions (temperature, concentration of reactants, ligand addition time, etc.), addition TP and 4ATP leads to the Au_{25} core nuclearity protected by different 4ATP/TP ratios.

Additionally, ligand exchange reaction was also explored as synthetic method to obtain two different ligand protected GNCs at different ligand (ligand A / ligand B) ratio. For this purpose, the well – characterized

$Au_{25}(4ATP)_{18/17}$ [79] was used as a precursor in solution and, addition of a second ligand was performed to start the exchange reaction. Different (ligand A / ligand B) ratios (75, 50 and 22%) were explored.

Finally, ESI – MS, IMS – MS , UV – Vis and FT – IR spectroscopy, TEM (transmission electron microscopy) and SAXS (small angle X – Ray scattering) characterization techniques were used to characterize the clusters synthesized.

The thesis is organized in seven chapters. Chapter 1 is devoted to the introduction. In chapter 2 we describe the electronic structure methodology used in this work. In chapter 3 we study and compare the UV – Vis spectra, computed at the TD – DFT / CAMB3LYP level, of the Au_{13}, Au_{25}, and Au_{28} metallic cores protected by thiolate, chloride, and phosphine ligands. We show, by investigating several model clusters and experimentally reported ones that the charge redistribution between the gold core and the ligand shell can be controlled by the electron character (acceptor or donor) of the ligands absorbed on the gold cluster and their spatial organization on the metal surface. We find that *the more negative the partial charge of the metal core is, the more the spectrum is red shifted* (see figure 1).[30] The identified trend between the natural partial charge on the gold core and the position of the lowest energy band is robust and remains valid even for small clusters with little structural or electronic similarity. Our computations show that it is possible to tune the position of the lowest absorption band by tailoring the amount of electron density on the metallic core with an appropriate design of the ligand shell. Also, our calculations confirm that, the organization of the ligand protecting the core and the charge state of the GNC have a significant impact on the optical properties.

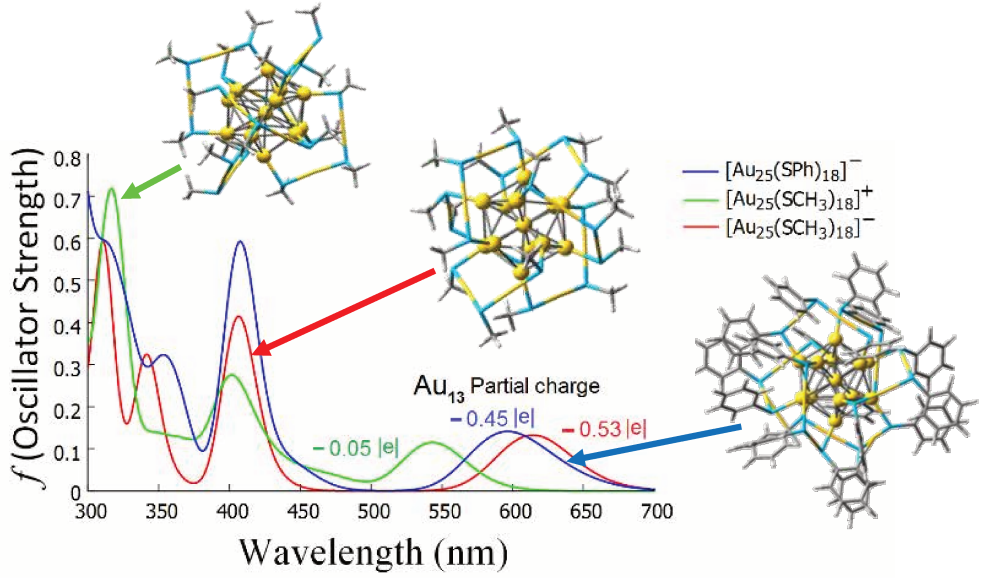

Figure 1. *Computed optical absorption spectra of the ligated anions $[Au_{25}(SCH_3)]^-$, $[Au_{25}(SPh)]^-$ and the cation $[Au_{25}(SCH_3)]^+$ GNC at the TD – DFT level.*

In chapter 4, we study of the structural and optical properties of two different ligand protected gold clusters at the DFT level. Again, the Au_{25} core was used as a model. Gold core protection by different ligands; the TP, 4ATP and also the 6 – mercaptohexanoic acid (S – $(CH_2)_5COOH$, called here 6MHA) was investigated in three different ligand configurations: ligands spatially segregated (also known as Janus), [39, 80-82] forming stripes [36, 83] and randomly organized. Our computations confirm the stability of the Au_{25} metal framework since in most of the cases no significant deformation was experienced by the mixing of thiolate ligands. Also, different 4ATP/TP ligand on the $Au_{25}(4ATP)_x(TP)_{18-x}$ was studied theoretically. Our computations show a blue shift for the Janus $Au_{25}(4ATP)_9(TP)_9$ cluster which corresponds to the 1:1 ligand ratio compared to the other two Janus configurations.

In chapter 5, we show that we successfully reproduced the $Au_{25}(TP)_{18}$ and $Au_{25}(4ATP)_{18}$ cluster synthesis developed by Demessence. [79] Also, the synthesis of the two different ligand protected $Au_{25}(SR)_{18}$ clusters was carried out by adapting the same synthetic approach by adding two different ligands in the synthesis solution at the same time. Three different ligands have been used: 4 – aminothiophenol (4ATP), thiophenol (TP) and 1 – dodecanethiol (DDT). ESI – MS confirms that we successfully obtained a set of $Au_{25}(ATP)_x(TP)_{18-x}$ clusters with different ATP/TP ratios while aggregation is experienced for DDT capped metal cores leading to the formation of nanoparticles. FT – IR spectroscopy confirms the absorption of two different ligands on the gold surface. Additionally, SAXS shows that we have a very good correlation between the distance between clusters and the length of the ligand protecting them. Synthesis and characterization of the thiolate gold nanoclusters have been performed at the Laboratoire de la chimie de la matière condensée de Paris (LCMCP) at the UPMC except for the ESI – MS and the IMS – MS measurements which have been done at the Karlsruhe Institute of Technology, Germany under the supervision of Prof. B. Leyh (ULg) and Dr. J.-F Greisch (KIT). The analysis on the mass spectrometry results have been carried out by Prof. B. Leyh (ULg) and Dr. J.-F Greisch (KIT). The computation of the TWIMS converted cross – section have been done by Dr. J.-F Greisch (KIT) by using the Mobcal software. [84, 85]

On the other hand, *n* – heterocyclic carbenes (NHC) have received a lot of attention since they – as the phosphine ligands – are σ donor [86] but show a stronger metal – ligand bond, even stronger than thiolates. [87, 88] Moreover – also as in the phosphine case – it is possible to replace the organic group bearing the N atoms (P atom for phosphines) or modify the head backbone leading to the possibility of tuning the size, reactivity and properties of GNCs and gold nanocrystals. [21, 22, 89] Again, the structural determination and ligand organization analysis of such materials turns out to be very complicated because of their small size and also, in the carbene case, the formation of $[NHC – Au – NHC]^+$ and NHC – Au – Cl complexes [21, 22, 87] makes the study of the grafting of NHCs on gold nanocluster surfaces challenging. At this stage, computational chemistry can shed some light to have an insight and to understand how the structure and optical properties are affected by the NHC ligand layer. Chapter 6 and 7 are devoted to a joint experimental study and to a pure computational study of the NHC protected GNCs respectively.

In chapter 6, we study the reactivity of gold nanoparticles (AuNPs) and GNCs towards benzimidazole – 2 – ylidene ligands (*n* – heterocyclic carbenes; NHC). This study involves an experimental part, performed by Dr. M. Rodriguez Castillo, Dr. D. Laurencin, Dr. S. Clement, Dr. Y. Guari and Dr. S. Richeter at the Institut Charles Gerhardt in the Université de Montpellier, France and a computational part on the NHC – Au_{38} set of complexes followed by a NMR spectra computation on $Au_{38}(NHC)_n$ cluster performed by us and by Dr. Frederic Tielens from UPMC. Experimental results show that – by comparing different NHCs with different groups bearing the N atoms (see figure 2) – all NHCs exhibit similar reactivity. Erosion of the AuNPs under the effect of the NHC and the formation of bis(NHC) gold complexes ([NHC – Au – NHC]$^+$) was also demonstrated confirming the strong C – Au bond. [90]

Our computational study of the NHCa – Au_{38} (NHC bearing CH_3 on the N atoms: 1, 3 – dimethyl – 1H – benzimidazolium, called here NHCa) complex in 12 different configurations (NHCa attached to 12 different Au atoms on the Au_{38} surface) shows that the binding of a single NHCa ligand on a 38 gold cluster surface produces a significant modification on the cluster geometry, on the natural charge distribution of the gold atoms and also on the electronic structure of the complex. In most of the cases, the presence of the NHCa ligand triggers a distortion of the 38 gold core by pulling the gold atoms together. Also, we find that, the bonding of the NHCa on the Au_{38} is even stronger than thiolates and characterized by a charge transfer from the ligand shell to the metal core. The $Au_{38}NHCa_9$ is also proposed as a model of a fully ligated GNC to performed NMR calculations in order to interpret NMR – experimental data. Finally, a possible mechanism to explain the formation of [NHC – Au – NHC]+ complexes is proposed. The computed binding energies and configuration are in agreement with DFT solid state computations where the carbene binds on a gold surface.

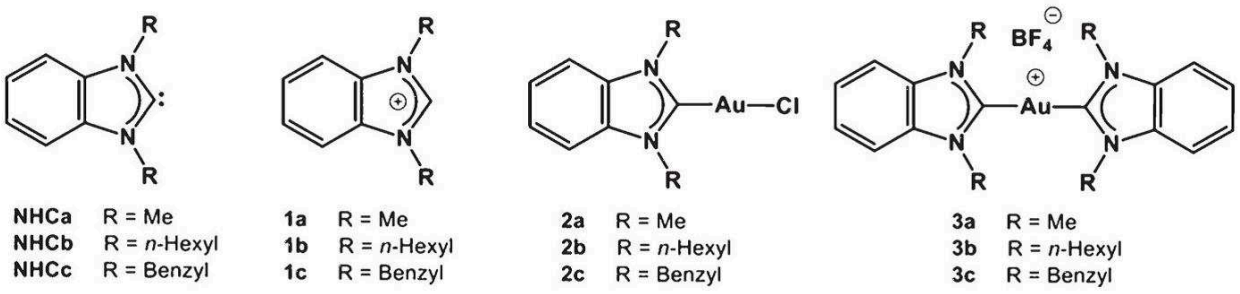

***Figure 2**. Structure of the NHC ligands, benzimidazolium salts, NHC – Au^I complexes, and NHC – functionalized AuNPs discussed in [21].*

The last chapter, 7, reports on the computational results for the grafting of PH_3 and NHCa ligands on different gold nanocluster surfaces: the Au_{13}, the tetrahedral Au_{20} and the Au_{38} cores. A comparison between carbene and phosphine for gold nanocluster passivation is showed. The structural and optical

properties are analyzed at the DFT / CAMB3LYP level of theory. Our calculations confirm that, PH_3 weakly binds a gold nanocluster surface adapting an “on top” position. NHCa, on the other hand, forms strong covalent bonds with gold. No significant structural reorganization of the metal core was observed for PH_3 capped clusters unlike for NHCa. [21] In both cases; phosphine and NHCa binding is characterized by a charge transfer from the ligand shell to the metal core. When interacting on the Au_{20} and Au_{38} nanocluster surfaces, NHCa shows a stronger electro – donor character. Also, our computations show, in all of the 3 different clusters studied, a larger Au – P bond compared to the Au – C in carbene ligated clusters found in [21]. This suggest a weaker Au – P bond.

Additionally, our study on the PH_3 – Au_{38} set of complexes provides understanding of the site selectivity of the adsorption of PH_3 on a gold nanocluster surface; PH_3 will only interact with the most positively charged and less coordinated Au atoms. The study of PH_3 – Au_{38} complex and the proposed structure of the fully ligated $Au_{38}(PH_3)_9$ model are in good agreement, since in the fully ligated nanocluster the nine PH_3 are attached on those gold atoms showing the more positive natural partial charge and the shortest coordination number.

Our computational investigations confirm that DFT is a powerful tool for the understanding of ligand – metal interactions and that the natural charge distribution can be used to predict the preferred sites on the gold nanocluster surface for the PH_3 to interact.

Further studies on the effect of the organic group bearing the N atoms, the phenyl backbone on the NHC or on the P atoms should be performed in order to understand the role of interligand interactions on the stability, reactivity and optical properties of nanoclusters. The comprehension of the effect of the ligand shell on the structure and properties of metal nanoclusters is essential for a control functionalization of these small particles and obtain materials with desired properties.

Conclusions and perspectives of this work are presented after chapter 7.

References

1. de Silva, N., J.-M. Ha, A. Solovyov, M.M. Nigra, I. Ogino, S.W. Yeh, K.A. Durkin, and A. Katz, *A bioinspired approach for controlling accessibility in calix[4]arene-bound metal cluster catalysts.* Nat Chem, 2010. **2**(12): p. 1062-1068.
2. Wang, Y., X.-K. Wan, L. Ren, H. Su, G. Li, S. Malola, S. Lin, Z. Tang, H. Häkkinen, B.K. Teo, Q.-M. Wang, and N. Zheng, *Atomically Precise Alkynyl-Protected Metal Nanoclusters as a Model Catalyst: Observation of Promoting Effect of Surface Ligands on Catalysis by Metal Nanoparticles.* Journal of the American Chemical Society, 2016. **138**(10): p. 3278-3281.
3. Corma, A., P. Concepción, M. Boronat, M.J. Sabater, J. Navas, M.J. Yacaman, E. Larios, A. Posadas, M.A. López-Quintela, D. Buceta, E. Mendoza, G. Guilera, and A. Mayoral, *Exceptional oxidation activity with size-controlled supported gold clusters of low atomicity.* Nat Chem, 2013. **5**(9): p. 775-781.
4. Yamazoe, S., K. Koyasu, and T. Tsukuda, *Nonscalable Oxidation Catalysis of Gold Clusters.* Accounts of Chemical Research, 2014. **47**(3): p. 816-824.
5. Liu, Y., H. Tsunoyama, T. Akita, S. Xie, and T. Tsukuda, *Aerobic Oxidation of Cyclohexane Catalyzed by Size-Controlled Au Clusters on Hydroxyapatite: Size Effect in the Sub-2 nm Regime.* ACS Catalysis, 2011. **1**(1): p. 2-6.
6. Oliver-Meseguer, J., A. Leyva-Perez, S.I. Al-Resayes, and A. Corma, *Formation and stability of 3-5 atom gold clusters from gold complexes during the catalytic reaction: dependence on ligands and counteranions.* Chemical Communications, 2013. **49**(71): p. 7782-7784.
7. Chen, Y.-S., H. Choi, and P.V. Kamat, *Metal-Cluster-Sensitized Solar Cells. A New Class of Thiolated Gold Sensitizers Delivering Efficiency Greater Than 2%.* Journal of the American Chemical Society, 2013. **135**(24): p. 8822-8825.
8. Arkill, K.P., J.M. Mantell, S.R. Plant, P. Verkade, and R.E. Palmer, *Using size-selected gold clusters on graphene oxide films to aid cryo-transmission electron tomography alignment.* Scientific Reports, 2015. **5**: p. 9234.
9. Zedan, A.F., S. Moussa, J. Terner, G. Atkinson, and M.S. El-Shall, *Ultrasmall Gold Nanoparticles Anchored to Graphene and Enhanced Photothermal Effects by Laser Irradiation of Gold Nanostructures in Graphene Oxide Solutions.* ACS Nano, 2013. **7**(1): p. 627-636.
10. Kwak, K., S.S. Kumar, K. Pyo, and D. Lee, *Ionic Liquid of a Gold Nanocluster: A Versatile Matrix for Electrochemical Biosensors.* ACS Nano, 2014. **8**(1): p. 671-679.
11. MacLeod, M.J. and J.A. Johnson, *PEGylated N-Heterocyclic Carbene Anchors Designed To Stabilize Gold Nanoparticles in Biologically Relevant Media.* Journal of the American Chemical Society, 2015. **137**(25): p. 7974-7977.
12. Sun, C., Y. Yuan, Z. Xu, T. Ji, Y. Tian, S. Wu, J. Lei, J. Li, N. Gao, and G. Nie, *Fine-Tuned H-Ferritin Nanocage with Multiple Gold Clusters as Near-Infrared Kidney Specific Targeting Nanoprobe.* Bioconjugate Chemistry, 2015. **26**(2): p. 193-196.
13. Huang, K., H. Ma, J. Liu, S. Huo, A. Kumar, T. Wei, X. Zhang, S. Jin, Y. Gan, P.C. Wang, S. He, X. Zhang, and X.-J. Liang, *Size-Dependent Localization and Penetration of Ultrasmall Gold Nanoparticles in Cancer Cells, Multicellular Spheroids, and Tumors in Vivo.* ACS Nano, 2012. **6**(5): p. 4483-4493.
14. Gomez, S., K. Philippot, V. Colliere, B. Chaudret, F. Senocq, and P. Lecante, *Gold nanoparticles from self-assembled gold() amine precursors.* Chemical Communications, 2000(19): p. 1945-1946.
15. Kanaras, A.G., F.S. Kamounah, K. Schaumburg, C.J. Kiely, and M. Brust, *Thioalkylated tetraethylene glycol: a new ligand for water soluble monolayer protected gold clusters.* Chemical Communications, 2002(20): p. 2294-2295.

16. Zeng, C., T. Li, A. Das, N.L. Rosi, and R. Jin, *Chiral Structure of Thiolate-Protected 28-Gold-Atom Nanocluster Determined by X-ray Crystallography.* Journal of the American Chemical Society, 2013. **135**(27): p. 10011-10013.
17. Lopez-Acevedo, O. and H. Häkkinen, *Derivatives of the thiolate-protected gold cluster Au25(SR)18 -1.* The European Physical Journal D, 2011. **63**(2): p. 311-314.
18. Negishi, Y., K. Nobusada, and T. Tsukuda, *Glutathione-Protected Gold Clusters Revisited: Bridging the Gap between Gold(I)−Thiolate Complexes and Thiolate-Protected Gold Nanocrystals.* Journal of the American Chemical Society, 2005. **127**(14): p. 5261-5270.
19. Beqa, L., D. Deschamps, S. Perrio, A.-C. Gaumont, S. Knoppe, and T. Bürgi, *Ligand Exchange Reaction on Au38(SR)24, Separation of Au38(SR)23(SR')1 Regioisomers, and Migration of Thiolates.* The Journal of Physical Chemistry C, 2013. **117**(41): p. 21619-21625.
20. Peterle, T., A. Leifert, J. Timper, A. Sologubenko, U. Simon, and M. Mayor, *Multidentate thioether ligands coating gold nanoparticles.* Chemical Communications, 2008(29): p. 3438-3440.
21. Rodríguez-Castillo, M., G. Lugo-Preciado, D. Laurencin, F. Tielens, A. van der Lee, S. Clément, Y. Guari, J.M. López-de-Luzuriaga, M. Monge, F. Remacle, and S. Richeter, *Experimental and Theoretical Study of the Reactivity of Gold Nanoparticles Towards Benzimidazole-2-ylidene Ligands.* Chemistry – A European Journal, 2016: p. n/a-n/a.
22. Rodriguez-Castillo, M., D. Laurencin, F. Tielens, A. van der Lee, S. Clement, Y. Guari, and S. Richeter, *Reactivity of gold nanoparticles towards N-heterocyclic carbenes.* Dalton Transactions, 2014. **43**(16): p. 5978-5982.
23. Galan, B.R., E.S. Wiedner, M.L. Helm, J.C. Linehan, and A.M. Appel, *Effects of Phosphine–Carbene Substitutions on the Electrochemical and Thermodynamic Properties of Nickel Complexes.* Organometallics, 2014. **33**(9): p. 2287-2294.
24. Shichibu, Y., K. Suzuki, and K. Konishi, *Facile synthesis and optical properties of magic-number Au13 clusters.* Nanoscale, 2012. **4**(14): p. 4125-4129.
25. Shichibu, Y. and K. Konishi, *HCl-Induced Nuclearity Convergence in Diphosphine-Protected Ultrasmall Gold Clusters: A Novel Synthetic Route to "Magic-Number" Au13 Clusters.* Small, 2010. **6**(11): p. 1216-1220.
26. Guidez, E.B., A. Hadley, and C.M. Aikens, *Initial Growth Mechanisms of Gold-Phosphine Clusters.* The Journal of Physical Chemistry C, 2011. **115**(14): p. 6305-6316.
27. Fresch, B., E. Hanozin, F. Dufour, and F. Remacle, *Interplay of structural and electronic stabilizing factors in neutral and cationic phosphine protected Au13 clusters.* The European Physical Journal D, 2012. **66**(12): p. 1-9.
28. Shichibu, Y., Y. Negishi, T. Tsukuda, and T. Teranishi, *Large-Scale Synthesis of Thiolated Au25 Clusters via Ligand Exchange Reactions of Phosphine-Stabilized Au11 Clusters.* Journal of the American Chemical Society, 2005. **127**(39): p. 13464-13465.
29. Konishi, K., *Phosphine-Coordinated Pure-Gold Clusters: Diverse Geometrical Structures and Unique Optical Properties/Responses*, in *Gold Clusters, Colloids and Nanoparticles I*, P.D.M. Mingos, Editor. 2014, Springer International Publishing: Cham. p. 49-86.
30. Lugo, G., V. Schwanen, B. Fresch, and F. Remacle, *Charge Redistribution Effects on the UV–Vis Spectra of Small Ligated Gold Clusters: a Computational Study.* The Journal of Physical Chemistry C, 2015.
31. Periyasamy, G. and F. Remacle, *Ligand and Solvation Effects on the Electronic Properties of Au55 Clusters: A Density Functional Theory Study.* Nano Letters, 2009. **9**(8): p. 3007-3011.
32. Dufour, F., B. Fresch, O. Durupthy, C. Chaneac, and F. Remacle, *Ligand and Solvation Effects on the Structural and Electronic Properties of Small Gold Clusters.* The Journal of Physical Chemistry C, 2014. **118**(8): p. 4362-4376.

33. Yao, H. and M. Iwatsu, *Water-Soluble Phosphine-Protected Au11 Clusters: Synthesis, Electronic Structure, and Chiral Phase Transfer in a Synergistic Fashion.* Langmuir, 2016. **32**(13): p. 3284-3293.
34. Nisisako, T., T. Torii, T. Takahashi, and Y. Takizawa, *Synthesis of Monodisperse Bicolored Janus Particles with Electrical Anisotropy Using a Microfluidic Co-Flow System.* Advanced Materials, 2006. **18**(9): p. 1152-1156.
35. Glaser, N., D.J. Adams, A. Böker, and G. Krausch, *Janus Particles at Liquid–Liquid Interfaces.* Langmuir, 2006. **22**(12): p. 5227-5229.
36. Cesbron, Y., C.P. Shaw, J.P. Birchall, P. Free, and R. Lévy, *Stripy Nanoparticles Revisited.* Small, 2012. **8**(24): p. 3714-3719.
37. Jackson, A.M., J.W. Myerson, and F. Stellacci, *Spontaneous assembly of subnanometre-ordered domains in the ligand shell of monolayer-protected nanoparticles.* Nat Mater, 2004. **3**(5): p. 330-336.
38. Jackson, A.M., Y. Hu, P.J. Silva, and F. Stellacci, *From Homoligand- to Mixed-Ligand- Monolayer-Protected Metal Nanoparticles: A Scanning Tunneling Microscopy Investigation.* Journal of the American Chemical Society, 2006. **128**(34): p. 11135-11149.
39. Kim, H., R.P. Carney, J. Reguera, Q.K. Ong, X. Liu, and F. Stellacci, *Synthesis and Characterization of Janus Gold Nanoparticles.* Advanced Materials, 2012. **24**(28): p. 3857-3863.
40. Zhang, H.-F., M. Stender, R. Zhang, C. Wang, J. Li, and L.-S. Wang, *Toward the Solution Synthesis of the Tetrahedral Au20 Cluster.* The Journal of Physical Chemistry B, 2004. **108**(33): p. 12259-12263.
41. Copley, R.C.B. and D.M.P. Mingos, *Synthesis and characterization of the centred icosahedral cluster series [Au9MIB4Cl4(PMePh2)8][C2B9H12], where MIB= Au, Ag or Cu.* Journal of the Chemical Society, Dalton Transactions, 1996(4): p. 491-500.
42. Johnson, G.E., T. Priest, and J. Laskin, *Synthesis and Characterization of Gold Clusters Ligated with 1,3-Bis(dicyclohexylphosphino)propane.* ChemPlusChem, 2013. **78**(9): p. 1033-1039.
43. Qian, H., Y. Zhu, and R. Jin, *Size-Focusing Synthesis, Optical and Electrochemical Properties of Monodisperse Au38(SC2H4Ph)24 Nanoclusters.* ACS Nano, 2009. **3**(11): p. 3795-3803.
44. Pichugina, D.A., N.E. Kuz'menko, and A.F. Shestakov, *Ligand-protected gold clusters: the structure, synthesis and applications.* Russian Chemical Reviews, 2015. **84**(11): p. 1114.
45. Qian, H., M. Zhu, U.N. Andersen, and R. Jin, *Facile, Large-Scale Synthesis of Dodecanethiol-Stabilized Au38 Clusters.* The Journal of Physical Chemistry A, 2009. **113**(16): p. 4281-4284.
46. Johnson, G.E., A. Olivares, D. Hill, and J. Laskin, *Cationic gold clusters ligated with differently substituted phosphines: effect of substitution on ligand reactivity and binding.* Physical Chemistry Chemical Physics, 2015. **17**(22): p. 14636-14646.
47. Farrag, M., M. Tschurl, A. Dass, and U. Heiz, *Infra-red spectroscopy of size selected Au25, Au38 and Au144 ligand protected gold clusters.* Physical Chemistry Chemical Physics, 2013. **15**(30): p. 12539-12542.
48. Zhu, M., C.M. Aikens, F.J. Hollander, G.C. Schatz, and R. Jin, *Correlating the Crystal Structure of A Thiol-Protected Au25 Cluster and Optical Properties.* Journal of the American Chemical Society, 2008. **130**(18): p. 5883-5885.
49. Wang, J., G. Wang, and J. Zhao, *Structures and electronic properties of Cu20, Ag20, and Au20 clusters with density functional method.* Chemical Physics Letters, 2003. **380**(5–6): p. 716-720.
50. Wu, K., J. Li, and C. Lin, *Remarkable second-order optical nonlinearity of nano-sized Au20 cluster: a TDDFT study.* Chemical Physics Letters, 2004. **388**(4–6): p. 353-357.
51. Yamijala, S.S., A. Bandyopadhyay, and S.K. Pati, *Nitrogen-Doped Graphene Quantum Dots as Possible Substrates to Stabilize Planar Conformer of Au20 over Its Tetrahedral Conformer: A Systematic DFT Study.* The Journal of Physical Chemistry C, 2014. **118**(31): p. 17890-17894.

52. Goel, S., K.A. Velizhanin, A. Piryatinski, S.A. Ivanov, and S. Tretiak, *Ligand Effects on Optical Properties of Small Gold Clusters: A TDDFT Study.* The Journal of Physical Chemistry C, 2012. **116**(5): p. 3242-3249.
53. Aikens, C.M., *Effects of Core Distances, Solvent, Ligand, and Level of Theory on the TDDFT Optical Absorption Spectrum of the Thiolate-Protected Au25 Nanoparticle.* The Journal of Physical Chemistry A, 2009. **113**(40): p. 10811-10817.
54. Molina, L.M. and B. Hammer, *The activity of the tetrahedral Au20 cluster: charging and impurity effects.* Journal of Catalysis, 2005. **233**(2): p. 399-404.
55. Castleman, A.W. and S.N. Khanna, *Clusters, Superatoms, and Building Blocks of New Materials.* The Journal of Physical Chemistry C, 2009. **113**(7): p. 2664-2675.
56. Walter, M., J. Akola, O. Lopez-Acevedo, P.D. Jadzinsky, G. Calero, C.J. Ackerson, R.L. Whetten, H. Grönbeck, and H. Häkkinen, *A unified view of ligand-protected gold clusters as superatom complexes.* Proceedings of the National Academy of Sciences, 2008. **105**(27): p. 9157-9162.
57. Cohen, M.L., M.Y. Chou, W.D. Knight, and W.A. De Heer, *Physics of metal clusters.* The Journal of Physical Chemistry, 1987. **91**(12): p. 3141-3149.
58. Brust, M., M. Walker, D. Bethell, D.J. Schiffrin, and R. Whyman, *Synthesis of thiol-derivatised gold nanoparticles in a two-phase Liquid-Liquid system.* Journal of the Chemical Society, Chemical Communications, 1994(7): p. 801-802.
59. Garzón, I.L., C. Rovira, K. Michaelian, M.R. Beltrán, P. Ordejón, J. Junquera, D. Sánchez-Portal, E. Artacho, and J.M. Soler, *Do Thiols Merely Passivate Gold Nanoclusters?* Physical Review Letters, 2000. **85**(24): p. 5250-5251.
60. Häkkinen, H., M. Walter, and H. Grönbeck, *Divide and Protect: Capping Gold Nanoclusters with Molecular Gold−Thiolate Rings.* The Journal of Physical Chemistry B, 2006. **110**(20): p. 9927-9931.
61. Jadzinsky, P.D., G. Calero, C.J. Ackerson, D.A. Bushnell, and R.D. Kornberg, *Structure of a Thiol Monolayer-Protected Gold Nanoparticle at 1.1 Å Resolution.* Science, 2007. **318**(5849): p. 430-433.
62. Aikens, C.M., *Origin of Discrete Optical Absorption Spectra of M25(SH)18− Nanoparticles (M = Au, Ag).* The Journal of Physical Chemistry C, 2008. **112**(50): p. 19797-19800.
63. Pei, Y., Y. Gao, and X.C. Zeng, *Structural Prediction of Thiolate-Protected Au38: A Face-Fused Bi-icosahedral Au Core.* Journal of the American Chemical Society, 2008. **130**(25): p. 7830-7832.
64. Tlahuice-Flores, A., R.L. Whetten, and M. Jose-Yacaman, *Ligand Effects on the Structure and the Electronic Optical Properties of Anionic Au25(SR)18 Clusters.* The Journal of Physical Chemistry C, 2013. **117**(40): p. 20867-20875.
65. Frisch, M.J.T., G. W.; Schlegel, H. B.; Scuseria, G. E.;, M.A.C. Robb, J. R.; Scalmani, G.; Barone, V.; Mennucci,, and G.A.e.a. B.; Petersson, *Gaussian 09, Revision D01.* Gaussian, Inc.: Wallingford, CT,, 2009.
66. Heaven, M.W., A. Dass, P.S. White, K.M. Holt, and R.W. Murray, *Crystal Structure of the Gold Nanoparticle [N(C8H17)4][Au25(SCH2CH2Ph)18].* Journal of the American Chemical Society, 2008. **130**(12): p. 3754-3755.
67. Qian, H., W.T. Eckenhoff, Y. Zhu, T. Pintauer, and R. Jin, *Total Structure Determination of Thiolate-Protected Au38 Nanoparticles.* Journal of the American Chemical Society, 2010. **132**(24): p. 8280-8281.
68. Qian, H., M. Zhu, Z. Wu, and R. Jin, *Quantum Sized Gold Nanoclusters with Atomic Precision.* Accounts of Chemical Research, 2012. **45**(9): p. 1470-1479.
69. Jin, R., *Quantum sized, thiolate-protected gold nanoclusters.* Nanoscale, 2010. **2**(3): p. 343-362.
70. Bae, G.-T. and C.M. Aikens, *Time-Dependent Density Functional Theory Studies of Optical Properties of Au Nanoparticles: Octahedra, Truncated Octahedra, and Icosahedra.* The Journal of Physical Chemistry C, 2015. **119**(40): p. 23127-23137.

71. Shivhare, A., S.J. Ambrose, H. Zhang, R.W. Purves, and R.W.J. Scott, *Stable and recyclable Au25 clusters for the reduction of 4-nitrophenol.* Chemical Communications, 2013. **49**(3): p. 276-278.
72. Shibu, E.S., M.A.H. Muhammed, T. Tsukuda, and T. Pradeep, *Ligand Exchange of Au25SG18 Leading to Functionalized Gold Clusters: Spectroscopy, Kinetics, and Luminescence.* The Journal of Physical Chemistry C, 2008. **112**(32): p. 12168-12176.
73. Kwak, K., S.S. Kumar, K. Pyo, and D. Lee, *Ionic Liquid of a Gold Nanocluster: A Versatile Matrix for Electrochemical Biosensors.* ACS Nano, 2013. **8**(1): p. 671-679.
74. Chong, H., P. Li, S. Wang, F. Fu, J. Xiang, M. Zhu, and Y. Li, *Au25 Clusters as Electron-Transfer Catalysts Induced the Intramolecular Cascade Reaction of 2-nitrobenzonitrile.* Sci. Rep., 2013. **3**.
75. Kawasaki, H., S. Kumar, G. Li, C. Zeng, D.R. Kauffman, J. Yoshimoto, Y. Iwasaki, and R. Jin, *Generation of Singlet Oxygen by Photoexcited Au25(SR)18 Clusters.* Chemistry of Materials, 2014. **26**(9): p. 2777-2788.
76. Kauffman, D.R., D. Alfonso, C. Matranga, H. Qian, and R. Jin, *Experimental and Computational Investigation of Au25 Clusters and CO2: A Unique Interaction and Enhanced Electrocatalytic Activity.* Journal of the American Chemical Society, 2012. **134**(24): p. 10237-10243.
77. Shivhare, A., D.M. Chevrier, R.W. Purves, and R.W.J. Scott, *Following the Thermal Activation of Au25(SR)18 Clusters for Catalysis by X-ray Absorption Spectroscopy.* The Journal of Physical Chemistry C, 2013. **117**(39): p. 20007-20016.
78. Akola, J., M. Walter, R.L. Whetten, H. Häkkinen, and H. Grönbeck, *On the Structure of Thiolate-Protected Au25.* Journal of the American Chemical Society, 2008. **130**(12): p. 3756-3757.
79. Lavenn, C., F. Albrieux, G. Bergeret, R. Chiriac, P. Delichere, A. Tuel, and A. Demessence, *Functionalized gold magic clusters: Au25(SPhNH2)17.* Nanoscale, 2012. **4**(23): p. 7334-7337.
80. Lattuada, M. and T.A. Hatton, *Synthesis, properties and applications of Janus nanoparticles.* Nano Today, 2011. **6**(3): p. 286-308.
81. Vilain, C., F. Goettmann, A. Moores, P. Le Floch, and C. Sanchez, *Study of metal nanoparticles stabilised by mixed ligand shell: a striking blue shift of the surface-plasmon band evidencing the formation of Janus nanoparticles.* Journal of Materials Chemistry, 2007. **17**(33): p. 3509-3514.
82. Wang, B., B. Li, B. Zhao, and C.Y. Li, *Amphiphilic Janus Gold Nanoparticles via Combining "Solid-State Grafting-to" and "Grafting-from" Methods.* Journal of the American Chemical Society, 2008. **130**(35): p. 11594-11595.
83. Liu, X., M. Yu, H. Kim, M. Mameli, and F. Stellacci, *Determination of monolayer-protected gold nanoparticle ligand–shell morphology using NMR.* Nat Commun, 2012. **3**: p. 1182.
84. Mesleh, M.F., J.M. Hunter, A.A. Shvartsburg, G.C. Schatz, and M.F. Jarrold, *Structural Information from Ion Mobility Measurements: Effects of the Long-Range Potential.* The Journal of Physical Chemistry, 1996. **100**(40): p. 16082-16086.
85. Shvartsburg, A.A. and M.F. Jarrold, *An exact hard-spheres scattering model for the mobilities of polyatomic ions.* Chemical Physics Letters, 1996. **261**(1): p. 86-91.
86. Nolan, S.P., *N-Heterocyclic Carbenes in Synthesis.* WILEY-VCH Verlag GmbH and Co. KGaA, 2006.
87. Hurst, E.C., K. Wilson, I.J.S. Fairlamb, and V. Chechik, *N-Heterocyclic carbene coated metal nanoparticles.* New Journal of Chemistry, 2009. **33**(9): p. 1837-1840.
88. Ling, X., N. Schaeffer, S. Roland, and M.-P. Pileni, *Superior Oxygen Stability of N-Heterocyclic Carbene-Coated Au Nanocrystals: Comparison with Dodecanethiol.* Langmuir, 2015. **31**(47): p. 12873-12882.
89. Zhukhovitskiy, A.V., M.G. Mavros, T. Van Voorhis, and J.A. Johnson, *Addressable Carbene Anchors for Gold Surfaces.* Journal of the American Chemical Society, 2013. **135**(20): p. 7418-7421.
90. Crespo, J., Y. Guari, A. Ibarra, J. Larionova, T. Lasanta, D. Laurencin, J.M. Lopez-de-Luzuriaga, M. Monge, M.E. Olmos, and S. Richeter, *Ultrasmall NHC-coated gold nanoparticles obtained through*

solvent free thermolysis of organometallic Au(i) complexes. Dalton Transactions, 2014. **43**(42): p. 15713-15718.

Chapter II. Electronic structure methodology

Introduction

The morphology of the gold core, the nature of the ligands, their mode of grafting on the metal surface and the presence of dopants have been analyzed in recent years showing the significant impact these parameters have on the catalytic and optical properties of gold nanoclusters (GNC). [1-5] ESI and IMS mass spectrometry, UV – Vis and FT – IR spectroscopy and X – Ray diffraction characterization techniques provided important information for elucidation of GNC structures and their properties. [6-12] However, because of their ultra – small size, the determination of the structure and the study of the properties of ligand capped GNCs remains a challenge. The ligand organization on the gold surface, for instance, cannot be easily determined experimentally because of the small sizes (of the order of 1 – 2 nm) however, it could be used as advantage to tune the optical properties of GNCs.[13-15] For these reasons, computational chemistry and electronic structure methods play a complementary role to the experimental characterizations in the understanding of the electronic structure of GNCs and its impact on their structural and optical properties.

GNCs have a large number of atoms and electrons. The computation of their electronic structure by wave function based quantum chemistry methods is very demanding. DFT methods based on the electron density require to treat only 3 electronic variables at a given configuration of the nuclei compared to the 3N for wave function methods (where N is the number of electron of the system). Solid state DFT implementations were extensively used to investigate GNCs.[12, 16-27] Recently, thanks to the significant increase in computer resources, mainly memory, it became possible to compute the electronic structure of GNCs (ground and excited electronic states) and to determine their equilibrium geometry using the Kohn – Sham [28, 29] implementation of DFT in quantum chemistry. This is the methodology we adopted in this thesis. The Kohn – Sham implementation implies to use 3N electronic coordinates. Its cost is basically equivalent to that of a Hartree – Fock computation (that is to say, one determinantal wave function) when hybrid functionals are used. The use of pure functionals can considerably speed up the computation since only one electron integrals need to be computed.

A further challenge is that the gold atom has a heavy nucleus. Therefore, the electrons in gold (and in general in post – lanthanide elements) experience a strong nuclear field, and move at velocities comparable to that of light. For this reason, relativistic effects become important and have an impact on the chemical properties,[30] structure,[31] catalytic activity and electronic structure [32]. Relativistic effects are also responsible for weak "'aurophilic'" interactions. [32-35] Due to the relativistic effects the 6s outer shell of Au undergoes a contraction which leads to a decrease in the 5d – 6s gap. As a consequence, there is a larger s – d hybridization in gold. [34]

Including relativistic effects in quantum chemistry computation is a very challenging task, even for atoms. Moreover, the computation of the electronic structure and properties of heavy elements compounds represents a considerable computational cost due to their large number of electrons. The use of effective core potentials represents a good approximation for transition metal compounds. It allows to both reduce the number of active electrons to the valence electrons and to take relativistic effects into account. When using effective core potentials, the chemically inert core electrons are replaced by an effective potential and the relativistic effects on the outer valence electrons are included, leading to a more feasible calculation. [36-38]

Another problem to face is the description of the ligand shell and the ligand – Au interface. Noncovalent interactions and dispersion forces play an important role on the stability of gold – organic complexes [39] and also on their structure [40, 41]. Among the different computational approaches, many determinant wave function quantum chemistry methodologies, such as Coupled Cluster (CCSD(T)), provide an accurate description of non – bonding van der Waals interactions. Unfortunately, the use of this method it is not feasible for the nanoclusters studied here because of their size (number of electrons and number of nuclear degrees of freedom). An alternative is to use a perturbative approach, such as MP2 (Møller – Plesset perturbation theory) that has been employed in several investigations as a reference for DFT studies where different functionals are tested [39, 40, 42] since MP2 offers a good description of dispersion forces for the ground state. Theoretical studies on bare and protected small gold clusters have shown that computations using the long – range corrected CAM – B3LYP functional provides a good agreement with MP2. [40, 43]

Therefore, here, the quantum chemistry Kohn – Sham implementation of Density Functional Theory is used to study the effect of the metal core structure, of the chemical nature of the ligand on the gold surface and also of the impact of two different ligands protecting a metal core on the electronic structure and optical properties. All computations on the bare and protected gold clusters were carried out using the Gaussian 09 program.[44] The long – range corrected functional CAM – B3LYP [36] was used together with the LANL2MB relativistic corrected pseudopotentials and basis sets [37, 38] for the gold atoms and the 6 – 31G(d) Gaussian basis set for the ligand shell. Natural population analysis and natural bond orbital methodologies [45, 46] were used to compute the partial charges on the atoms of the clusters. Contributions from different fragments (gold core and the ligands) to the frontier molecular orbitals and the density of states (DOS) were obtained with AOMix program [47] using the default MPA (Mulliken population analysis). The excited states and the UV – Vis spectra were computed at the equilibrium geometry of the ground electronic state with the linear response TD – DFT method as implemented in Gaussian 09.

In this chapter, first, we describe the foundations of ground state Density Functional Theory followed by a brief explanation of the Berny algorithm implemented by H. Bernhard Schlegel [48] used to compute the equilibrium structure of the ground state of the gold clusters. Then, the description of the computation of thermodynamic quantities such as ΔG, ΔH and ΔS for ligand binding is outlined. Also, a brief overview of charge distribution computation [45, 46] is provided. In order to ensure the charge distribution trends and

since no absolute definition of atom charge has been established, we compared the results of Natural population analysis with those of the CHelpG [49] and the M – K [50] charge distribution approaches.

2.1 Density Functional Theory

An isolated non – relativistic *N* – electron, M nuclei – system with no time – dependent interactions can be described by solving the time – independent Schrödinger equation: [51]

$$\widehat{H}\Psi_j(\boldsymbol{r},\boldsymbol{R}) = E_j\Psi_j(\boldsymbol{r},\boldsymbol{R}) \tag{1}$$

Where $\widehat{H}$ represents the full time – independent Hamiltonian operator, $\Psi_j(\boldsymbol{r},\boldsymbol{R})$ the wave function describing the "j" state of the system, E_j stands for the total energy, "***r***" represents the 3N electronic coordinates and "***R***" refers to the 3M coordinates of the nuclei. For a molecular system, the non – relativistic stationary full Hamiltonian $\widehat{H}$ is written as follow:

$$\widehat{H} = -\frac{\hbar^2}{2m_e}\sum_i^N \nabla_i^2 - \frac{\hbar^2}{2}\sum_\alpha^M \frac{1}{M_\alpha}\nabla_\alpha^2 + \sum_\alpha^{M-1}\sum_{\beta>\alpha}^{M} \frac{Z_\alpha Z_\beta e^2}{4\pi\varepsilon_0|\boldsymbol{R_\alpha}-\boldsymbol{R_\beta}|} - \sum_\alpha^M\sum_i^N \frac{Z_\alpha e^2}{4\pi\varepsilon_0|\boldsymbol{R_\alpha}-\boldsymbol{r_i}|} + \sum_i^{N-1}\sum_{j>i}^{N} \frac{e^2}{4\pi\varepsilon_0|\boldsymbol{r_i}-\boldsymbol{r_j}|} \tag{2}$$

The subscript "*i*" and "*j*" in equation 2 run on the electron coordinates while "α" and "β" refer to the nuclei. The Laplacian is represented by ∇_i^2 and the mass of electrons and nuclei are m_e and M_α, respectively. The vectors $\boldsymbol{R_\alpha}$ and $\boldsymbol{R_\beta}$ stand for the nuclei position in space while $\boldsymbol{r_i}$ and $\boldsymbol{r_j}$ stand for the electrons. The nuclear charges are expressed as Z. In Eq. (2), the first and second term stand for the electrons and nuclei kinetic energy. The third and the fourth ones represent the nuclear repulsion and nuclear – electron attraction, respectively. The fourth term ($-\sum_\alpha\sum_i \frac{Z_\alpha e^2}{4\pi\varepsilon_0|\boldsymbol{R_\alpha}-\boldsymbol{r_i}|} = V_{en}(\boldsymbol{r_i})$) is also known as the external potential on the electron "*i*" due to the nuclei. Finally, the last term in Eq. (2) is the electron – electron repulsion.

When two electronic states are relatively far in energy, it is possible to decouple the electron and nuclear motion. This decoupling, known as the Born and Oppenheimer (BO) approximation, is possible because the proton is approximately 1836 times heavier than the electron. Therefore one can consider that the nuclei move much more slowly than the electrons and that the electronic density adjusts instantaneously to a specific nuclear configuration. It is important to clarify that this approximation does not state that the nuclei are not moving but that the electron density relaxation with respect to a specific nuclear configuration is instantaneous (adiabatic). Making the BO approximation allows to write the full wave function of Eq. (1) as a product:

$$\Psi(\boldsymbol{r},\boldsymbol{R}) \approx \Phi_n^{elec}(\boldsymbol{r};\boldsymbol{R})\chi_{nv}^{nucl}(\boldsymbol{R}) \tag{3}$$

Where n and ν stand for the different electronic and vibrational states, respectively. In Eq. (3), the nuclear and electronic motions have been decoupled and the total wave function has been written as a product of two functions: the nuclear wave function, $\chi^{nucl}(\boldsymbol{R})$, which depends on the nuclear coordinates "***R***" and the electronic wave function, $\Phi^{elec}(\boldsymbol{r};\boldsymbol{R})$, which depends on the electron coordinates "**r**" but also depends parametrically on the nuclear coordinates "***R***". The $\Phi^{elec}(\boldsymbol{r};\boldsymbol{R})$ function is an eigenfunction of the electronic Hamiltonian at a given geometry of the nuclei, defined as:

$$\hat{H}^{elec} = -\frac{\hbar^2}{2m_e}\sum_{i}^{N}\nabla_i^2 - \sum_{\alpha}^{M}\sum_{i}^{N}\frac{Z_\alpha e^2}{4\pi\varepsilon_0|\boldsymbol{R_\alpha} - \boldsymbol{r_i}|} + \sum_{i}^{N-1}\sum_{j>i}^{N}\frac{e^2}{4\pi\varepsilon_0|\boldsymbol{r_i} - \boldsymbol{r_j}|} \quad (4)$$

The last term in Eq. (4) is the electron – electron repulsion. Only this term in the electronic Hamiltonian is not one – to – one additive and makes the $\Phi^{elec}(\boldsymbol{r};\boldsymbol{R})$ non – separable, leading to a complicated differential equation with 3N variables (where N is the number of electrons). If implemented directly on the one electron density, DFT offers a better option over *ab – initio* wave function methods since the electronic density depends on the coordinate of a single electron only.

DFT is a widely used and successful quantum – mechanical method in chemistry and physics, particularly suited for large systems. The main idea of DFT is that the energy of a system can be obtained from the electron density. The one electron density, $\rho(\boldsymbol{r})$ is a function on the electron position surrounding the nuclei, and the electronic energy of the ground state can be shown to be a functional of the electron density ($E[\rho(r)]$). For a *N* – electron system, starting from a *N* electron electronic wave function, $\rho(\boldsymbol{r})$ can be written as follows: [52]

$$\rho(\boldsymbol{r}) = N\sum_{all\ m_s}\int\dots\int|\Psi(\boldsymbol{r},\boldsymbol{r}_2,\dots,\boldsymbol{r_N},\boldsymbol{m_{s1}},\boldsymbol{m_{s2}},\dots,\boldsymbol{m_{sN}})|^2 d\boldsymbol{r_2}\dots d\boldsymbol{r}_N \quad (5)$$

DFT is based on the Hohenberg – Kohn theorems. The first theorem states that *the electron density of the ground state (ρ_{GS}) uniquely determines the external potential (up to an arbitrary constant)*.[28] In the DFT, the electronic energy of a system in its ground state is calculated as follows:

$$E_{GS} = E[\rho_{GS}(\boldsymbol{r})] = T[\rho_{GS}(\boldsymbol{r})] + V_{ne}[\rho_{GS}(\boldsymbol{r})] + V_{ee}[\rho_{GS}(\boldsymbol{r})] + E_{XC}[\rho_{GS}(\boldsymbol{r})] \quad (6)$$

Where $T[\rho_{GS}(\boldsymbol{r})]$ is the electron kinetic energy, $V_{ne}[\rho_{GS}(\boldsymbol{r})]$ is the nuclear – electron interaction, $V_{ee}[\rho_{GS}(\boldsymbol{r})]$ is the electron – electron interaction and $E_{XC}[\rho_{GS}(\boldsymbol{r})]$ is the exchange – correlation energy.

DFT takes a fictitious system with non – interacting electrons where the $\rho_{GS}(\boldsymbol{r})$ is the same as in the real system. This implies that in the fictitious system, the nuclei have the same positions and atomic numbers as in the real one. The fact that the electrons do not interact allows us to express our Hamiltonian as the sum of one – electron operators. As a consequence, its eigenfunction can be represented as a single Slater determinant built by one – electron wavefunctions (orbitals) and hence, its eigenvalues are the sum

of the one – electron eigenvalues. Thus, we can express the electron density in terms of these one – electron functions with n_i electrons (0, 1, 2), that is to say, the orbitals $\{\varphi_i(r)\}$:

$$\rho(r) = \sum_{i=1}^{N/2} n_i |\varphi_i(\boldsymbol{r})|^2 \tag{7}$$

In the KS implementation, the kinetic energy ($T[\rho_{GS}(\boldsymbol{r})]$ in Eq. (6) is first calculated for a system with non – interacting electrons and, hence it can be written also in terms of the $\{\varphi_i(r)\}$ orbitals:

$$T_s[\rho_{GS}(\boldsymbol{r})] = \sum_{i=1}^{N} \left\langle \varphi_i \middle| -\frac{1}{2}\nabla_i{}^2 \middle| \varphi_i \right\rangle \tag{8}$$

On the other hand, the potential $V_{ne}[\rho(\boldsymbol{r})]$ in Eq. (6) can be expressed in term of the $\{\varphi_i(r)\}$ as well:

$$V_{ne}[\rho(\boldsymbol{r})] = \sum_{i}^{N} \left\langle \varphi_i \middle| \sum_{\alpha=1}^{M} \frac{Z_\alpha}{|\boldsymbol{r_i} - \boldsymbol{R_\alpha}|} \middle| \varphi_i \right\rangle \tag{9}$$

And the electron – electron interaction $V_{ee}[\rho(\boldsymbol{r})]$ is:

$$V_{ee}[\rho(\boldsymbol{r})] = \sum_{i}^{N} \left\langle \varphi_i \middle| \frac{1}{2} \int \frac{\rho'(\boldsymbol{r})}{|\boldsymbol{r_i} - \boldsymbol{r'}|} dr' \middle| \varphi_i \right\rangle \tag{10}$$

The last term in Eq. (6); $E_{XC}[\rho_{GS}(\boldsymbol{r})]$ contains effects of exchange and correlation as well as the difference between the $T_s[\rho_{GS}(\boldsymbol{r})]$ and the kinetic energy of the real system.

We can rewrite Eq. (6) then, as follows:

$$E[\rho_{GS}(\boldsymbol{r})] = \sum_{i=1}^{N} \left\langle \varphi_i \middle| -\frac{1}{2}\nabla_i{}^2 \middle| \varphi_i \right\rangle - \sum_{i}^{N} \left\langle \varphi_i \middle| \sum_{\alpha=1}^{M} \frac{Z_\alpha}{|\boldsymbol{r_i} - \boldsymbol{R_\alpha}|} \middle| \varphi_i \right\rangle + \sum_{i}^{N} \left\langle \varphi_i \middle| \frac{1}{2} \int \frac{\rho'(\boldsymbol{r})}{|\boldsymbol{r_i} - \boldsymbol{r'}|} d\boldsymbol{r'} \middle| \varphi_i \right\rangle + E_{XC}[\rho_{GS}(\boldsymbol{r})] \tag{11}$$

Hohenberg and Kohn showed in their second theorem that the energy of the ground state can be obtained variationally; *the exact ground state electron density is the one that minimizes the total energy*. Our $\rho_{GS}(\boldsymbol{r})$ can be obtained within the $\{\varphi_i(r)\}$ set of functions (Eq. 7) which can be expanded as a linear combination of atomic orbitals (AO). Therefore, we have to find the AO coefficients which minimize $E[\rho_{GS}(\boldsymbol{r})]$ analogous to what is done in Hartree – Fock theory. Notice that, in Eq. (10) the electron density ($\rho'(\boldsymbol{r})$) and the set of orbitals $\{\varphi_i(r)\}$ are required to obtain $V_{ee}[\rho(\boldsymbol{r})]$. Thus, the KS implementation needs also an iterative method in order to obtain the $\{\varphi_i(r)\}$ orbitals and then the $\rho(\boldsymbol{r})$. The $\{\varphi_i(r)\}$ set of orbitals are called Kohn - Sham (KS) orbitals and they satisfy:

$$h_i^{KS}\varphi_i = \varepsilon_i\varphi_i \tag{12}$$

Where h_i^{KS} has the form:

$$h_i^{KS} = -\frac{1}{2}\nabla_i{}^2 - \sum_{\alpha=1}^{M}\frac{Z_\alpha}{|\boldsymbol{r_i} - \boldsymbol{R_\alpha}|} + \int\frac{\rho'(\boldsymbol{r})}{|\boldsymbol{r_i} - \boldsymbol{r}'|}dr' + V_{XC}(\boldsymbol{r}) \tag{13}$$

Here $V_{XC}(\boldsymbol{r_i})$ is the exchange – correlation potential and it is defined as follows:

$$V_{XC}(\boldsymbol{r}) = V_{XC}[\rho(\boldsymbol{r})] = \frac{\delta E_{XC}[\rho(\boldsymbol{r})]}{\delta\rho} \tag{14}$$

All this leads to the well – known one – electron Kohn – Sham equations. KS equations have as objective to compute the ground state energy and to find the optimal KS orbitals to minimize the electronic energy.

$$\left\{-\frac{1}{2}\nabla_i{}^2 - \sum_{\alpha=1}^{M}\frac{Z_\alpha}{|\boldsymbol{r_i} - \boldsymbol{R_\alpha}|} + \int\frac{\rho'(\boldsymbol{r})}{|\boldsymbol{r_i} - \boldsymbol{r}'|}dr' + V_{XC}(\boldsymbol{r})\right\}\varphi_i = \varepsilon_i\varphi_i \tag{15}$$

Where the ε_i are the KS orbital energies.

As mentioned before, the KS orbitals can be expressed as a liner combination of atomic orbitals $\{\chi_k\}$, that is to say;

$$\varphi_i = \sum_{k=1}^{m} c_{ki}\chi_k \tag{16}$$

If we introduce Eq. (16) in Eq. (12) we obtain:

$$\sum_{k=1}^{m}(h_{ik}^{KS} - \varepsilon_i S_{ik})c_{ki} = 0 \quad for\ i = 1,\ 2 \ldots m \tag{17}$$

Where $S_{ik} = \langle\chi_i|\chi_k\rangle$ is the overlap integral. Initial AO orbitals allow us to compute an initial set of KS orbitals and estimate a first $\rho(r)$ by using Eq. (16) and then Eq. (7). We can then obtain $V_{XC}(\boldsymbol{r})$ (by using a functional, discussed below) and build the h_i^{KS} in Eq. (13). This leads to the KS equations (see Eq. 15 and Eq. 17) which can be solved to obtain an improved c_{ki} set of coefficients which are used to build an improved KS orbitals (Eq. 16) which form a better electron density (Eq. 7). After we calculate a better $\rho(r)$ this can be used in equation 14 and 15 to have an improved $V_{XC}(\boldsymbol{r})$ and h_i^{KS} and again, solve Eq. (17) to obtain a new set of c_{ki} coefficients and start the process again. The process continues self – consistently until the

exchange-correlation potential $V_{XC}(\boldsymbol{r})$ and the KS set of orbitals converge. Having now the converged $\rho(r)$ and $E_{XC}[\rho_{GS}(\boldsymbol{r})]$ we can use Eq. (13) to compute the electronic energy $E[\rho_{GS}(\boldsymbol{r})]$.

DFT is an exact theory however, the analytical form of $E_{XC}[\rho(\boldsymbol{r})]$ is not known thus, approximations have to be introduced. Many functionals have been developed over the years trying to approximate the forms of the exchange – correlation energy functional.

The simplest way to approximate the $E_{XC}[\rho(\boldsymbol{r})]$ functional is by using the so – called local density approximation (LDA). Here, the exchange – correlation energy functional is expressed as:

$$E_{XC}^{LDA}[\rho(\boldsymbol{r})] = \int \rho(\boldsymbol{r})\varepsilon_{XC}(\rho)d\boldsymbol{r} \tag{18}$$

Where $\varepsilon_{XC}(\rho)$ is the exchange – correlation energy per particle of a homogeneous electron gas of charge density $\rho(\boldsymbol{r})$. The $\varepsilon_{XC}(\rho)$ can be divided in an exchange ($\varepsilon_X(\rho)$) and a correlation ($\varepsilon_C(\rho)$) part, as follows:

$$\varepsilon_{XC}(\rho) = \varepsilon_X(\rho) + \varepsilon_C(\rho) \tag{19}$$

Where the exchange part is given by the Dirac exchange – energy functional;

$$\varepsilon_X(\rho) = \frac{3}{4}\left(\frac{3}{\pi}\right)^{1/3}\rho(\boldsymbol{r})^{1/3} \tag{20}$$

And accurate values for $\varepsilon_C(\rho)$ are available thanks to the Quantum Monte Carlo for the uniform electron gas. LDA can be used only when the value of the $\varepsilon_{XC}(\rho)$ at some point $\boldsymbol{r_p}$ can be computed exclusively from the value of the electron density at that point, $\rho(\boldsymbol{r_p})$.

However, what makes our molecular system different from the uniform electron gas is the fact that $\rho(\boldsymbol{r})$ is changing in space. Taking into account that the electron density is not spatially uniform can be used to improve the LDA functionals by making them depend also on the electron density gradient:

$$E_{XC}^{GGA}[\rho(\boldsymbol{r})] = E_{XC}^{LDA}[\rho(\boldsymbol{r})] + \Delta\varepsilon_{XC}\left[\frac{|\nabla\rho(\boldsymbol{r})|}{\rho(\boldsymbol{r})^{3/4}}\right] \tag{21}$$

These type of functionals are called general gradient approximation functionals (GGA). And, most of them are built by adding to the LDA approximation a correction term, as can be seen in Eq. (21). The PW91, [53, 54] PBE [55] and BLYP [56] are examples of GGA functionals (exchange and correlation).

Additionally, we can have hybrid functionals. Unlike the previous discussed pure functionals, these functionals combine the Hartree – Fock method (Hartree - Fock exchange) and DFT (LDA and GGA). Examples of these are PBE0, [57] the HSE [58] and the B3LYP [59, 60] functionals. For instance, the B3LYP functional defines the exchange – correlation energy functional as:

$$E_{XC}^{B3LYP} = (1-a)E_{XC}^{LSDA} + aE_X^{HF} + b\Delta E_X^B + (1-c)E_C^{LSDA} + c(1-a)E_C^{LYP} \quad (22)$$

Where the parameter a, b and c are chosen to give good fits to experimental data ($a = 0.20$, $b = 0.72$ and $c = 0.81$). [61] As already mentioned, in this work, the long – range corrected CAM – B3LYP functional is used since it shows a good agreement with MP2 results. [40, 43] CAM – B3LYP functional is the long – range corrected B3LYP. CAM – B3LYP corrects the long – range deficiencies in B3LYP which leads to a better description of molecules with long bonds and reaction barriers.

2.2 Equilibrium geometry determination and the Berny optimization algorithm

Within the Born – Oppenheimer approximation (see Eq. 3), the nuclear wave equation has the form:

$$\left[\hat{T}_{nucl} + E_n^{elect}(\boldsymbol{R}) + \hat{V}_{nucl-nucl}\right]\chi_{nv}^{nucl}(\boldsymbol{R}) = E_{nv}\chi_{nv}^{nucl}(\boldsymbol{R}) \quad (23)$$

Where $\hat{T}_{nucl}$ stands for the nuclear kinetic energy (see the second term in Eq. 2), E_{nv} is the total energy including; electronic, vibrational, rotational and translational contributions, $\hat{V}_{nucl-nucl}$ is the nuclear repulsion (see the third term in Eq. 2) and $E_n^{elect}(\boldsymbol{R})$ represents a potential energy for the nuclei motion. The total potential energy, $V(R)$ can be expressed then as:

$$V(R) = E_n^{elect}(\boldsymbol{R}) + \hat{V}_{nucl-nucl} \quad (24)$$

The electronic energy $E_n^{elect}(R)$ is obtained by solving Eq. (11) and the self – consistent field method explained in the previous section to obtain KS orbitals in the Kohn – Sham [28, 29] implementation of DFT.

Equation 24 leads to concept of *potential energy surface* (PES). The PES is the potential for the nuclei motion $V(R)$ and the concept of a PES is very important since it dictates the movement of nuclei in a molecular system, hence, governing its reactivity. The characterization of PES allows us to study and predict chemical reaction barriers and mechanisms, molecular equilibrium and transition state structures and to compute vibrational spectra. However, for a big system with a large number of degrees of freedom the determination of the PES (hypersurface, actually) can be a huge work.

A stationary point is a geometry on the PES for which the gradient is zero ($\nabla[V(R)] = 0$). Two kinds of stationary points can be found in a PES; minima where the second derivative of the potential energy for all coordinates is greater than zero and, the opposite case called unstable point. The global minimum represents the equilibrium geometry of the molecule. For polyatomic systems the gradient $\nabla[V(R)]$ is a 3M vector (M being the number of nuclei) and the second derivatives are gathered in a 3M × 3M matrix called Hessian matrix.

To study only the thermodynamics of a system, it is sufficient to find the equilibrium geometry. In the vicinity of a minimum, the potential can be approximated as a quadratic potential and therefore the

harmonic – oscillator model can be applied to compute the vibrational profile and the normal modes frequencies. To get to the harmonic approximation, the PES is expanded in a Taylor series at the equilibrium geometry:

$$V(x_1, x_2 \dots x_n) = V(x_1^{st}, x_2^{st} \dots x_n^{st}) + \sum_{i=1}^{n}(x_i - x_i^{st})\nabla V(x_1^{st}, x_2^{st} \dots x_n^{st}) + \frac{1}{2}\sum_{i=1}^{n}\sum_{j=1}^{n} H_{ij}(V)(x_i - x_i^{st})(x_j - x_j^{st}) \tag{25}$$

The set $\{x_1, x_2 \dots x_n\}$ represents the coordinates of a specific nuclear configuration (in close vicinity of the equilibrium geometry: $\{x_1^{st}, x_2^{st} \dots x_n^{st}\}$) and $H_{ij}(V)$ is the Hessian matrix computed at the equilibrium geometry, expressed as:

$$H_{ij}(V) = \frac{\partial^2 V(\boldsymbol{R})}{\partial x_i \partial x_j} \tag{26}$$

As mentioned above, for a stable point, the gradient is zero and all the eigenvalue of the Hessian matrix are positive (except for those who correspond to the motion of the center of mass, here the Hessian matrix eigenvalues are zero). For an unstable point, the gradient is zero and we can have one or more eigenvalues of the Hessian matrix negative. If one or more of the Hessian matrix eigenvalues are negative, we have a maximum along those internal coordinates. We call that point a transition state. It is important to clarify the fact that having all positive eigenvalues does not ensure we are in the global minimum (which corresponds to the equilibrium geometry), it could also be secondary minimum higher in energy.

Since we take the equilibrium geometry as reference, then $\nabla V(x_1^{st}, x_2^{st} \dots x_n^{st}) = 0$, hence:

$$V(x_1, x_2 \dots x_n) = V(x_1^{st}, x_2^{st} \dots x_n^{st}) + \frac{1}{2}\sum_{i=1}^{n}\sum_{j=1}^{n} H_{ij}(V)(x_i - x_i^{st})(x_j - x_j^{st}) \tag{27}$$

The algorithm used in this work to find the equilibrium geometry of the GNCs is called Berny [48] algorithm in redundant internal coordinates [62-64] using GEDIIS (geometry optimization method using an energy – represented direct inversion in the iterative subspace algorithm)[65] and it is implemented in Gaussian 09. Here is a brief explanation about how the algorithm finds the equilibrium geometry:

1) Having our guess of the equilibrium structure and considering that the KS orbitals are obtained already from the self – consistent procedure and having in mind that, analytic first derivatives are available for almost all density functionals,[66] the electronic energy, nuclear repulsion and the potential $V(R)$ can be calculated together with a first estimation of the Hessian matrix by using connectivity derived from atomic radii and a simple valence force field. [67]

2) The first Hessian matrix guess is improved at each point by calculating the gradient. Notice that we are looking for $\nabla[V(R)] = 0$ and $\nabla[V(R)] = -F$, where *F* stands for the force the nuclei feel due to the potential.
3) The trust radius is updated, that is to say, the maximum size for the optimization step. [68]
4) If a minimum is detected a 5th or 4th order polynomial is used to fit the line between the initial point and that which could be the new configuration (or already the minimum). To ensure that the polynomial has an only one minimum the fit is subjected to the constraint that the second derivative of the polynomial just reach zero at its minimum. [52]
5) Maximum force component and maximum step component are used as convergence criteria to evaluate the new nuclear configuration. The step is the change between the most recent point and the next to be computed.
6) If the new configuration does not reach the convergence criteria, the midpoint of the line connecting the new and the best previous point is taken as a new configuration.
7) All the optimization steps apply themselves until a minimum is localized within the convergence criteria.

2.3 Thermochemistry and vibrational analysis

2.3.1 Computation of thermochemical quantities

The computation of thermodynamic quantities such as ΔG, ΔS and ΔH allows us to calculate the binding energy of a molecule, compare the stability of different system configurations and to determine the free energy and enthalpies of formation of a specific reaction product.

The contributions to the canonical partition function (*q*), total internal thermal energy (E_{Tot}), entropy (Δ*S*) and heat capacity (C_v) from the vibrational, rotational, electronic and translational motion are calculated for the ground electronic state assuming an isolated molecule and assuming that the first electronic excitation energy is much larger than k_BT (where k_B is the Boltzmann constant and T is the temperature in K).

By considering all the motion contributions, and the fact that we consider an isolated molecule we can write the total internal thermal energy as:

$$E_{Tot} = E_{Vib} + E_{Rot} + E_{Elec} + E_{Trans} \tag{28}$$

$$E_{Tot} = R\sum_{g} \Theta_{v,g}\left(\frac{1}{2} + \frac{1}{e^{\Theta_{v,g}/T} - 1}\right) + \frac{3}{2}RT + 0 + \frac{3}{2}RT \tag{29}$$

Where E_{Vib}, E_{Rot}, E_{Elec} and E_{Trans} are the vibrational, rotational, electronic and translational motion contribution to the total the total internal thermal energy (E_{Tot}), respectively. $\Theta_{v,g} = {h\nu_K}/{k_B}$ is known as the characteristic vibrational temperature, *g* stands for the vibrational mode label and R is the gas constant. In equation 29 we have substituted the expression for each contribution to the total internal energy in Eq. (28) in the same order of appearance. As mentioned above, the algorithm used here assumes that the first electronic excitation energy is much larger than k_BT.Therefore, excited states are not accessible at any temperature. Further, the energy of the ground state is set to zero. These assumptions simplify the electronic motion contribution expression to the partition function making it independent of the temperature. As a consequence, the electronic motion contribution to the total internal thermal energy E_{Elec} is zero (compare Eq. 28 and Eq. 29).

Next, we calculate the enthalpy ΔH as:

$$\Delta H = E_{Tot} + k_BT \tag{30}$$

And, the Gibbs free energy is calculated then, as follows:

$$\Delta G = \Delta H - T\Delta S_{Tot} \tag{31}$$

With ΔS_{Tot} being the total entropy which comes from the summation of all the entropic contributions from vibrational, rotational, electronic and translational motion, analogously as for the total internal thermal energy:

$$\Delta S_{Tot} = \Delta S_{Vib} + \Delta S_{Rot} + \Delta S_{Elec} + \Delta S_{Trans} \tag{32}$$

$$\Delta S_{Tot} = R\sum_g \left[\frac{\Theta_{v,g}/T}{e^{\Theta_{v,g}/T}-1} - \ln(1-e^{\Theta_{v,g}/T})\right] + Rln(q_{Rot}+\frac{3}{2}) + Rln(q_{Elec}) + R\left[ln(q_{Trans}) + \frac{5}{2}\right] \tag{33}$$

In equation 33 we have substituted the expression for each entropic contribution in Eq. (32) in the same order. q_{Rot}, q_{Elec} and q_{Trans} are the rotational, electronic and translational contribution to the canonical partition function.

All the thermochemical quantities calculated include the zero point energy (ZPE) which within the harmonic – oscillator approximation can be calculated as $ZPE = \frac{1}{2}\sum_{k=1}^{3N-6} h\nu_k$, where ν_k is the harmonic vibrational frequency.

Finally, the total Gibbs free energy and the total enthalpy of the molecule are calculated by adding the electronic energy (see eq. 11) of the ground state to ΔH and ΔG in Eq. 30 and Eq. 31, respectively.

The binding energy (*BE*) of a complex can be calculated using the information provided by the thermochemical analysis. The binding energy of a GNC protected by ***n*** ligand units, for instance, is defined as:

$$BE = \Delta G_{Complex} - \Delta G_{Bare} - n\Delta G_{Ligand} \quad (34)$$

$\Delta G_{Complex}$, ΔG_{Bare} and ΔG_{Ligand} in Eq. (34) are the free energies of the full system (the protected GNC), the bare cluster and the ligand itself, all in their equilibrium structure. BE is an important parameter to take into account when we are interested on the analysis of bond strength in a complex, site reactivity studies and also ligand exchange reactions. [69]

2.3.2 Computation of normal mode frequencies

The Hessian H_{ij} matrix (see Eq. 26) allows us to compute the normal mode frequencies and force constants. This gives us information about the strength of a bond. The next steps summarize how the normal mode frequencies are calculated:

1) First we have to be sure that the first derivative of the energy respect the atom displacement is zero, that is to say, the geometry of the molecule corresponds to point where the forces on the nuclei are zero.
2) Conversion of the force constants calculated by the Hessian matrix to a mass weighted coordinates is performed. The new Hessian matrix, $H_{ij}{}'(V)$ can be expressed as:

$$H_{ij}{}' = \frac{1}{\sqrt{m_i m_j}}\left(\frac{\partial^2 V(R)}{\partial X_i \partial X_j}\right)_{eq} \quad (35)$$

   Here, m_i and m_j are the mass of the atoms corresponding to the set of coordinates X_i and X_j, respectively, at the equilibrium geometry.
3) Determination of principal axes of inertia, separation of rotation and translation to only analyze the 3M – 6 or 3M – 5 vibrations is performed (M being the number of nuclei). Finally, transformation of the Hessian matrix to internal coordinates is done. More details about these three calculations can be found by consulting reference [70].
4) Diagonalization of H_{ij} yields the 3M eigenvectors and 3M eigenvalues. The Hessian eigenvectors are called normal modes and the squared root of the eigenvalues ($\lambda_k^{1/2}$) provide the frequencies of the normal modes (υ_k), as can be seen in the next equation:

$$\upsilon_k = \frac{\sqrt{\lambda_k}}{2\pi} \quad (36)$$

As mentioned in the geometry optimization section, if all the calculated frequencies are real, we are at the global minimum or at a saddle point (secondary minimum on the PES). If some of the frequencies are imaginary, we are at a transition state.

2.4 Charge distribution computation

Calculation of atomic charges could be very helpful for the understanding of the grafting on ligand – metal systems. Depending on the nature of the ligand (whether if it is electron donor or acceptor) and by knowing the atomic charges on the metal surface, one is able to predict the preferred sites for a ligand to interact. Moreover, it has been shown that the charge distribution on hybrid metal – organic systems have a significant impact on their optical [13] and surface properties.

Unfortunately, there is no absolute definition of partial charges. Therefore, several approaches have been developed in order to obtain these values. [45, 46, 50, 71] By default, Mulliken population analysis [72] is performed by Gaussian 09. As already told, the $\{\varphi_i\}$ set can be expanded on an AO basis set:

$$\varphi_i = \sum_{k=1}^{m} c_{ki}\chi_k \tag{37}$$

The probability associated with one electron in φ_i is then;

$$|\varphi_i|^2 = 1 = \sum_{k=1}^{m} {c_{ki}}^2 + 2c_{1i}c_{2i}S_{12} + 2c_{1i}c_{3i}S_{13} + \cdots \tag{38}$$

Where $S_{ij} = \langle\chi_i|\chi_j\rangle$ represents the overlap integral between AO. Mulliken proposed that the ${c_{ki}}^2$ represent the net population of one electron in the MO φ_i to the χ_k AO orbital. And that one electron in the MO φ_i contributes $2c_{1i}c_{2i}S_{12}$ to the overlap population between χ_1 and χ_2, for instance.

Having n_i electrons in the φ_i orbital ($n_i = 0, 1, 2$), the Mulliken net population n_r in χ_r and the overlap population n_{r-s} between χ_r and χ_s are defined as follows:

$$n_r = \sum_i n_i {c_{ri}}^2 \quad \text{and} \quad n_{r-s} = \sum_i n_i(2c_{ri}c_{si}S_{sr}) \tag{39}$$

For each basis function, the gross population N_r is expressed as:

$$N_r = n_r + \frac{1}{2}\sum_{s\neq r} n_{r-s} \tag{40}$$

Addition of the gross population of all the basis functions on atom A gives the gross atomic population. The Mulliken net atomic charge in A is defined as:

$$q_A = Z_A - \sum_{r \in A} N_r \tag{41}$$

However, this method does not show any convergence while increasing the size of the basis set. The assignment of half the overlap population to each basis function (see Eq. 40) is arbitrary and it can actually give chemically meaningless results, as occupation numbers larger than 2 or with negative values. Therefore, here we use Natural Population Analysis (NPA) [45, 46] to obtain the natural partial charges based on a orthonormal set of *natural bond orbitals* (NBO).

Natural atomic orbitals (NAO) are a 1 – center localized monoelectronic functions which are eigenfunctions of the first – order reduced density matrix [73] which is a generalization of the density function (see Eq. 5). The first – order reduced density matrix can be expressed in the KS $\{\varphi_i\}$ basis set: [73]

$$\gamma(\boldsymbol{r_1}, \boldsymbol{r'_1}) = \sum_{ij} \varphi_i(\boldsymbol{r_1}) \gamma_{ij} \varphi_j^*(\boldsymbol{r'_1}) \tag{42}$$

Where γ_{ij} is:

$$\gamma_{ij} = \int d\boldsymbol{r_1} d\boldsymbol{r'_1} \varphi_i^*(\boldsymbol{r_1}) \gamma(\boldsymbol{r_1}, \boldsymbol{r'_1}) \varphi_j(\boldsymbol{r'_1}) \tag{43}$$

Since $\gamma(\boldsymbol{r_1}, \boldsymbol{r'_1})$ is Hermitian, when it is not diagonal it is possible to define an orthonormal basis set $\{\eta_i\}$ related to $\{\varphi_i\}$ by a unitary transformation, in which the $\gamma(\boldsymbol{r_1}, \boldsymbol{r'_1})$ matrix is diagonal.

$$\gamma(\boldsymbol{r_1}, \boldsymbol{r'_1}) = \sum_{i} \lambda_i \eta_i(\boldsymbol{r_1}) \eta_i^*(\boldsymbol{r'_1}) \tag{44}$$

$\eta_i(r_1)$ are the natural orbitals and λ_i comes from unitary transformation $\lambda = \mathrm{U}^{\dagger} \gamma \mathrm{U}$ (with U being a unitary matrix). The NAOs are then used to compute the NBOs. NBOs can be classified as core, lone pair or bond orbital resembling the Lewis dot structure. Using the NBOs, one can carry out a population analysis. [52] The advantage is that NBOs converge by improving the basis set used.

As mentioned at the beginning of this section, there is not an absolute definition of partial charges, hence it is important to be sure that we can rely on our results. Some studies on ligand capped GNCs show that by using different approaches to compute the partial charges; NBO, M – K, AIM and CHelpG, for instance, the same trends are found. [43, 69] The main difference between NBO and the other two approaches is the fact that NBO scheme is based on localized natural atomic orbitals while the M – K and the CHelpG methods are computed to be consistent with the molecular electrostatic potential (MEP) which is an observable. A molecule can be seen as a group of charged points (nuclei) smeared out into a continuous distribution. In quantum chemistry the MEP $\phi(\boldsymbol{r_1})$ of a molecule at point 1 is defined as follows: [52]

$$\phi(\boldsymbol{r_1}) = \sum_{\alpha} \frac{Z_\alpha e}{4\pi\varepsilon_0 \boldsymbol{r_{1\alpha}}} - e\int \frac{1}{4\pi\varepsilon_0 \boldsymbol{r_{12}}}\rho(\boldsymbol{r_2})d\boldsymbol{r_2} \quad (45)$$

Where $\rho(r_2)$ is calculated using Eq. (7). $r_{1\alpha}$ is the distance between the nucleus α and the point 1 in space and r_{12} between point 1 and 2. The MEP can be calculated from accurate X – Ray data [74] and it is not strongly dependent on the basis set. The MEP is commonly plotted by a contour map showing curves or surfaces of constant ϕ in a particular region in space.

M – K [50, 71] and CHelpG [49] atomic charges are calculated by using the MEP. As a first step one can calculate the MEP by using the wave function in the region outside the molecule's van der Waals surface. Then, by placing a charge Q_A at each nucleus it is possible to estimate an approximate ϕ profile and to compare with the one calculated previously. The MEP is fitted by varying the Q_A charges.

2.5 Time dependent DFT

DFT is first used to describe the ground electronic state of a system. However, by applying a weak time – dependent oscillating perturbation to the ground state we can obtain information about the excited states. This approach is called time – dependent density functional theory (TD – DFT). Excitation energy and oscillator strengths can be obtained allowing us to compute the UV – Vis spectrum. In TD – DFT, since we are analyzing the response of the ground state of our system to a weak time – dependent oscillating perturbation the time – dependent Schrödinger equation has to be solved.

The theoretical basis of TD – DFT [75] was developed by Runge and Gross. The Runge – Gross theorem states that *there exist a **one – to – one** mapping between time – dependent external potential and the time – dependent densities*. [76] In other words, the expectation value of any operator is a **unique** functional of the time – dependent density. As in the time – independent case, the Runge – Gross theorem for a non – interacting system leads to a Kohn – Sham (KS) (now) time – dependent equations (in atomic units):

$$\left\{-\frac{1}{2}\nabla_i^2 + v(r_i,\boldsymbol{t}) + \int d^3r_i \frac{\rho(r_i,\boldsymbol{t})}{|r-r_i|} + \frac{\delta A[\rho(r_i,\boldsymbol{t})]}{\delta\rho(r_i,\boldsymbol{t})}\right\}\varphi_i(r_i,\boldsymbol{t}) = i\frac{\partial}{\partial t}\varphi_i(r_i,\boldsymbol{t}) \quad (46)$$

With

$$\rho(r_i,\boldsymbol{t}) = \sum_{i=1}^{occ}|\varphi_i(r_i,\boldsymbol{t})|^2 \quad (47)$$

$v(r_i,\boldsymbol{t})$ is the effective potential felt by the electrons. It includes the time – dependent external potential due to the perturbation (electromagnetic field) and the classical Coulomb potential. Analogously to the static case, TD – KS theory is exact, however, $A[\rho(r_i,\boldsymbol{t})]$ (see Eq. 46) which is a functional of the time –

dependent electron density is unknown and approximations have to be done. One of these approximations is that $\rho(r_i, \boldsymbol{t})$ varies slowly with the time and functionals used to compute the ground state can be used.

Linear – response TD – DFT is the formalism used to obtain excitations energies. First, as usually done in perturbation theory, we obtain the energy and the electron density for the unperturbed time – dependent case, then, the perturbation is applied.

The time – dependent KS orbitals can be described on a basis of time – independent single particle wavefunction:

$$\varphi_p(\boldsymbol{r}, t) = \sum_{i=1}^{M} c_i(t)\, \chi_i(\boldsymbol{r}) \tag{48}$$

Substitution of Eq. (48) in Eq. (47) allows us to have the time – dependent electron density in term of the $\chi_i(\boldsymbol{r})$ basis set:

$$\rho(\boldsymbol{r}, t) = \sum_{p} \sum_{q} c_p(t) c_q^*(t) \chi_p(\boldsymbol{r}) \chi_q^*(\boldsymbol{r}) = \sum_{p} \sum_{q} P_{pq} \chi_p(\boldsymbol{r}) \chi_q^*(\boldsymbol{r}) \tag{49}$$

Notice that in Eq. (49) the P_{pq} matrix element contains the time – dependent factors.

Within the TD – DFT, the KS equations (see Eq.46) can be written in matrix form as:

$$i \frac{\delta}{\delta t} \mathbf{C} = \mathbf{F}\mathbf{C} \tag{50}$$

Where the M×M matrix **C** contains the expansion coefficients of each time – dependent $\varphi_p(\boldsymbol{r}, t)$ and the **F** matrix is the KS operator in the one – electron basis $\{\chi_i(\boldsymbol{r})\}$.

As in perturbation theory, the total Hamiltonian and wave function can be written as the sum of the unperturbed term and the perturbation (time – dependent electric field). For the TD – DFT density matrix P_{pq} (see Eq. 49) we have:

$$P_{pq} = P_{pq}^0 + P_{pq}^1 \tag{51}$$

Where the superscript ‘0’ stand for the unperturbed term and ‘1’ for the perturbation. And, for the **F** matrix, the same reasoning can be applied:

$$F = F^0 + F^1 \tag{52}$$

It is possible to prove that after considering the perturbation and inserting them in Eq. (50), this one become: [77]

$$\sum_{q}\left(F_{pq}^{0}P_{qr}^{1}-P_{pq}^{1}F_{qr}^{0}+F_{pq}^{1}P_{qr}^{0}-P_{pq}^{0}F_{qr}^{1}\right)P_{pq}=i\frac{\delta}{\delta t}P_{qr}^{1} \tag{53}$$

The perturbation g_{pq} (being an electric field) has the form:

$$g_{pq}=\frac{1}{2}\left[f_{pq}e^{-i\omega t}+f_{qp}^{*}e^{i\omega t}\right] \tag{54}$$

f_{pq} is a one – electron operator which describes the applied perturbation. Additionally, the first correction to P_{pq} (P_{pq}^{1} in Eq. 51) has the form:

$$P_{pq}^{1}=\frac{1}{2}\left(d_{pq}e^{-i\omega t}+d_{qp}^{*}e^{i\omega t}\right) \tag{55}$$

Where the d_{pq} are the perturbed densities. The perturbation g_{pq} induces a variation of the electronic density with the same frequency as the time- dependent electric field.

The usual TD – DFT equations for the linear response have the following form:

$$F_{aa}^{0}d_{ai}-d_{ai}F_{ii}^{0}+\left[f_{ai}+\sum_{bj}\left(\frac{\delta F_{ai}^{0}}{\delta P_{bj}}d_{bj}+\frac{\delta F_{ai}^{0}}{\delta P_{jb}}d_{bj}\right)\right]P_{ii}^{0}=\omega d_{ai} \tag{56}$$

$$F_{ii}^{0}d_{ia}-d_{ia}F_{aa}^{0}+P_{ii}^{0}\left[f_{ia}+\sum_{bj}\left(\frac{\delta F_{ia}^{0}}{\delta P_{bj}}d_{bj}+\frac{\delta F_{ia}^{0}}{\delta P_{jb}}d_{bj}\right)\right]=\omega d_{ia} \tag{57}$$

Under the assumption that the electronic transition occurs for an infinitesimal perturbation Eq. 56 and Eq. 57 can be transformed into an eigenvalue problem to obtain the excitation energies.

2.6 Solvation. The Polarizable – continuum model (PCM)

Most of our theoretical work was performed in the gas phase. However, in chapter VI the computation of the ^{13}C NMR spectra of the set of $(NHCa)_n$ – Au_{38} complexes, the fully ligated $Au_{38}(NHCa)_9$ model cluster and of the bis(NHC) Au^{I} complex (NHCa being 1, 3 – dimethyl – 1H – benzimidazolium; an n – heterocyclic carbene ligand) were carried out at the DFT / CAM – B3LYP level. It is well known that the signals in a NMR spectrum are significantly affected by the chemical environment. Therefore, the effect of the solvent (d_6 – DMSO) was taken into account on the equilibrium structure as well as in the NMR spectra computation by using the polarizable – continuum model (PCM). [78, 79]

The PCM was developed more than 30 years ago and it still represents an attractive alternative to explicitly models of the solvent effect in a molecular system.

In section 2.4 in this chapter, a molecule is assumed to be a group of charged points (nuclei) smeared out into a continuous distribution. Here, $\rho(\vec{\boldsymbol{r}})$ is the solute charge distribution and $\varepsilon(\vec{\boldsymbol{r}})$ is the general permittivity. The general permittivity takes the value of 1 when $\vec{\boldsymbol{r}}$ falls in the cavity representing the solute (molecule). $\phi_{int}(\vec{\boldsymbol{r}}_{\boldsymbol{k}})$ is the electric potential produced by the charge distribution of the molecule (solute) and the solvent. The cavity in Gaussian 09D is generated via a set of overlapping spheres: each nucleus in the solute molecule is surrounded by a sphere of radius 1.2 times the van der Waals radius of that atom. [80]

To take into account the electrostatic interaction molecule – solvent in the quantum – mechanical calculation, the Hamiltonian has to be modified to add the effect of the solvent. If we consider $\hat{H}^0$ as the Hamiltonian operator in vacuum, the total effective Hamiltonian, $\hat{H}^{eff}$ can be written as:

$$\hat{H}^{eff} = \hat{H}^0 + \hat{V}_{int} \tag{58}$$

Where $\hat{V}_{int}$ is the solute – solvent interaction potential operator. Since we do not have $\hat{V}_{int}$ we do not have the form of the total effective Hamiltonian. The cavity then, is divided in very small regions (*k*) and a charge Q_k is placed in those k^{th} small area (S). The electric potential produced by the polarized dielectric continuum, ϕ_σ can be expressed as:

$$\phi_\sigma(r) = \sum_k \frac{Q_k}{|\boldsymbol{r} - \boldsymbol{r}_{\boldsymbol{k}}|} \tag{59}$$

It is very complicated to obtain $\phi_\sigma(r)$ analytically since the cavity has a complex shape. Therefore, it is compulsory to use numerical methods. The $\phi_\sigma(r)$ potential produced by the polarized dielectric continuum is equal to the electric potential produced by an apparent surface charge Q_k distributed on the surface of the molecule cavity. On the other hand, classical electrostatics indicates the apparent charges Q_k on the surface S_k of the k^{th} region can be calculated as follows:

$$Q_k = \left[\frac{\varepsilon(\vec{\boldsymbol{r}}) - 1}{4\pi\varepsilon(\vec{\boldsymbol{r}})}\right] S_k \nabla\phi_{int}(\vec{\boldsymbol{r}}_{\boldsymbol{k}}) \cdot \boldsymbol{n}_{\boldsymbol{k}} \tag{60}$$

The gradient of the electric potential within the cavity evaluated at the point $\mathbf{r}_k$ is $\nabla\phi_{int}(\vec{\boldsymbol{r}}_{\boldsymbol{k}})$. Equation 60 shows also the normal $\boldsymbol{n}_{\boldsymbol{k}}$ vector to the cavity surface S_k. This $\phi_{int}(\vec{\boldsymbol{r}}_{\boldsymbol{k}})$ electric potential can be seen as the potential contribution from the charge distribution of the molecule (solute) ϕ_M and the polarized dielectric, ϕ_σ as shown in Eq. (59). However, we do not know the form of the $\phi_{int}(\vec{\boldsymbol{r}}_{\boldsymbol{k}})$ potential neither the apparent charges Q_k on the surface. An iterative method has to be used.

$$\phi_{int}(\vec{r}_k) = \phi_M + \phi_\sigma \tag{61}$$

At the beginning ϕ_σ is set to zero, that is to say, $\phi_{int}(\vec{r}_k)^0 = \phi_M$. ϕ_M is calculated by DFT KS orbitals of a molecule in vacuum. An initial estimate of the Q_k apparent charge distribution is computed by using Eq. (60). Next, the just calculated set of apparent charges are used in Eq. (59) to obtain $\phi_\sigma(r)$. We can now use eq. 60 and 61 again to obtain an improved set of apparent charged Q_k and $\phi_{int}(\vec{r}_k)$, respectively. The procedure has to continue until the Q_k converge.

The converged charges are used to find an initial estimate of $\hat{V}_{int}^0$ using the following expression:

$$\hat{V}_{int}^0 = -\sum_i \phi_\sigma(r_i) + \sum_\alpha Z_\alpha \phi_\alpha(R_\alpha) \tag{62}$$

Here, the summations go over the electrons ($\boldsymbol{r_i}$) and nuclei ($\boldsymbol{R_\alpha}$) coordinates. Now, with $\hat{V}_{int}^0$ calculated, Eq. (58) can be used to obtain a better approximation of the electron density for our molecule. The new electron density can be used as well to improve ϕ_M which, by applying Eq. (61), a better $\phi_{int}(\vec{r}_k)$ is obtained. This improved $\phi_{int}(\vec{r}_k)$ is used again in Eq. (60) to start the iterative process all over again. This continues until everything has converged.

An advanced PCM method has been developed by J. Tomasi *et al.* in 1997 known as the integral equation formulation of the PCM [81] that allows us to deal with anisotropic solvents such as liquid crystals.

2.7 Hybrid QM – MM methodology

The size and the complexity of a molecule together with the process under study play a crucial role on the choice of computation methodology. DFT and *ab – initio* approaches provide valuable information on chemical reactions energetics and charge transfer process, for instance. However, for some large systems, for example, macromolecules, such as enzymes or proteins, the use of (quantum mechanics) QM can be extremely demanding computationally and very long, in other words, prohibitive. We have then to compromise on the accuracy of our calculations by using a lower level method. An alternative is to use molecular mechanics (MM) but MM typically does not describe the formation and rupture of bonds in a chemical reaction.

At this point, hybrid QM – MM approach can be very helpful. The basic idea proposed by Warshel and Levitt [82] in 1976 is to divide the whole system in several portions treated with different levels of theory, QM in the most important region and MM for the rest, as exemplified in figure 1. More than 2 layers can be defined since the QM regions can be treated with different QM levels of theory. [83]

In our case, the ligand layer can represent a large number of atoms therefore, QM – MM has been used in few cases only to obtain an equilibrium structure close to the full QM.

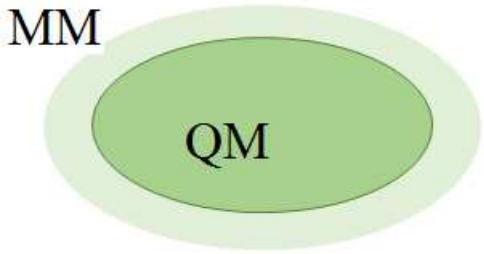

***Figure 1**. Partitioning of a system into different regions studied by a hybrid potential. There are 2 regions in this representation. The QM (in the center) which corresponds to high – level quantum – mechanical calculations while the dark green area, MM, is modeled with molecular mechanics force fields.*

2.7.1 Principles of the QM – MM method

As mention already in section 2.1 (Eq. 1), a non – relativistic molecular system considering time – independent interacting particles can be described by solving the time – independent Schrödinger equation, now taking into account the different regions: QM - MM:

$$\hat{H}_{Eff}\Psi(\boldsymbol{r_i}, \boldsymbol{R_\alpha}, \boldsymbol{R_M}) = E(\boldsymbol{R_\alpha}, \boldsymbol{R_M})\Psi(\boldsymbol{r_i}, \boldsymbol{R_\alpha}, \boldsymbol{R_M}) \tag{63}$$

Where $\boldsymbol{r_i}$ and $\boldsymbol{R_\alpha}$ stand for the coordinates of the electrons and nuclei in the QM region and $\boldsymbol{R_M}$ for the coordinates of the atoms in the MM region, respectively. Here, the *effective hybrid Hamiltonian* [84] can be expressed as:

$$\hat{H}_{Eff} = \hat{H}_{QM} + \hat{H}_{MM} + \hat{H}_{QM/MM} \tag{64}$$

We recall that, the total standard QM Hamiltonian has the form:

$$\hat{H} = -\frac{\hbar^2}{2m_e}\sum_i^N \nabla_i^2 - \frac{\hbar^2}{2}\sum_\alpha^M \frac{1}{M_\alpha}\nabla_\alpha^2 + \sum_\alpha^{M-1}\sum_{\beta>\alpha}^{M} \frac{Z_\alpha Z_\beta e^2}{4\pi\varepsilon_0|\boldsymbol{R_\alpha} - \boldsymbol{R_\beta}|} - \sum_\alpha^M\sum_i^N \frac{Z_\alpha e^2}{4\pi\varepsilon_0|\boldsymbol{R_\alpha} - \boldsymbol{r_i}|} + \sum_i^{N-1}\sum_{j>i}^{N} \frac{e^2}{4\pi\varepsilon_0|\boldsymbol{r_i} - \boldsymbol{r_j}|} \tag{65}$$

The subscript "*i*" and "*j*" in Eq. 65 run on the electron coordinates while "α" and "β" refer to the nuclei. The mass of electrons and nuclei are m_e and M_α, respectively. The vectors $\boldsymbol{R_\alpha}$ and $\boldsymbol{R_\beta}$ stand for the nuclei position in space while $\boldsymbol{r_i}$ and $\boldsymbol{r_j}$ stand for the electrons. The nuclear charges are expressed as Z. The first and second term stand for the electrons and nuclei kinetic energy. The third one and the fourth represent the nuclear repulsion and nuclear – electron attraction, respectively. Finally, the fifth and last term in the molecular Hamiltonian is the electron – electron repulsion.

On the other hand, the MM $\hat{H}_{MM}$ operator only depends on the nuclear coordinates and is written:

$$\widehat{H}_{MM} = E_{Bond} + E_{Angle} + E_{Dihedral} + E_{Coulomb} + E_{LJ} \quad (66)$$

Where E_{Bond}, E_{Angle}, $E_{Dihedral}$, $E_{Coulomb}$ and E_{LJ} represent the bond stretching, angle bending and the dihedral torsion terms and also the (not bonded) electrostatic (Coulomb) and Lennard – Jones interactions, respectively. The interaction functions describing the different part of the MM Hamiltonian form what we call the *force field*.[52, 83] In these functions, electrons are not treated explicitly but only their influence is included in the $\widehat{H}_{MM}$ by using empirical parameters, that is why, MM is not a valid method to model electron rearrangement during a chemical reaction.

The universal force field (UFF) [85] was used in the MM region to optimize the geometry of some of our GNCs. Within UFF the potential energy can be expressed as:

$$E_{MM} = E_{Bond} + E_{Angle} + E_{Dihedral} + E_{LJ} + E_{Coulomb} + E_{Inv} \quad (67)$$

Notice that equations 66 and 67 are practically the same except for the inversion term E_{Inv}. The UFF describes the different interaction terms as follows.

The E_{Bond} is the sum of the potential energies of the stretching of each bond of the molecule. UFF can describe the stretching potential energy, for instance for the atom A and B, $E_{Bond-AB}$ in two forms: it can be modeled by the harmonic oscillator approximation as shown in Eq. (68) or either by a Morse function (see equation 69).[85]

$$E_{Bond-AB} = \frac{1}{2} K_{AB} (\boldsymbol{r_{AB}} - \boldsymbol{r_{eq-AB}})^2 \quad (68)$$

$$E_{Bond-AB} = D_{AB} \left\{ exp \left[- \sqrt{\frac{K_{AB}}{2D_{AB}}} (\boldsymbol{r_{AB}} - \boldsymbol{r_{eq-AB}}) \right] - 1 \right\}^2 \quad (69)$$

Where K_{AB} is the force constant, the bond length $\boldsymbol{r_{AB}}$ at its equilibrium value is $\boldsymbol{r_{eq-AB}}$. D_{AB} in Eq. 69 stands for the bond dissociation energy. The Morse function leads to a better description since it includes anharmonic terms near the equilibrium bond length, $\boldsymbol{r_{eq-AB}}$.

The second term in the UFF, the angle bend formed by atoms A, B and C is described with a small Fourier expansion: [85]

$$E_{Angle-ABC} = K_{ABC} \sum_{n=0}^{m} C_n Cos(n\theta_{ABC}) \quad (70)$$

Where the C_n are chosen to satisfy boundary conditions in the system, for instance, the fact that $E_{Angle-ABC}$ has to have a minimum at the natural bond angle. K_{ABC} is the force constant. Again, $E_{Angle-AB}$ is

taking into account only one set of atoms (A, B and C), in order to obtain the total potential bending energy we have to sum the $E_{Angle-ABC}$ for all possible angles within the system.

Next term in equation 67, $E_{Dihedral}$ represents the torsion of a dihedral angle (A – B – C – D). It is described also:[85]

$$E_{Dihedral-ABCD} = K_{ABCD} \sum_{n=0}^{m} C_n Cos(n\theta_{ABCD}) \tag{71}$$

The meaning of the variables here can be taken analogously as for equation 70. Summation of all the potential energy terms due to different dihedral torsions will give the $E_{Dihedral}$ value to add in equation 67.

Lennard – Jones expressions are used to model van der Waals interactions between atom A and B. E_{LJ-AB} has the form:[85]

$$E_{LJ-AB} = \varepsilon_{AB} \left[-2 \left(\frac{\boldsymbol{r_{eq-AB}}}{\boldsymbol{r_{AB}}} \right)^6 + \left(\frac{\boldsymbol{r_{eq-AB}}}{\boldsymbol{r_{AB}}} \right)^{12} \right] \tag{72}$$

Where ε_{AB} stands for the well depth parameter, $\boldsymbol{r_{eq-AB}}$ gives the value of $\boldsymbol{r_{AB}}$ at the minimum in the E_{LJ-AB} profile. The total E_{LJ} is obtained by summing all the E_{LJ-AB} contributions from different AB pairs.

The electrostatic term in equation 67, $E_{Coulomb}$ is expressed as:[85]

$$E_{Coulomb-AB} = \frac{e^2 Q_A Q_B}{4\pi\epsilon_0 \boldsymbol{R_{AB}}} \tag{73}$$

Where Q_A and Q_B are the assigned atomic charges in A and B, ϵ_0 is the dielectric constant, $\boldsymbol{R_{AB}}$ is the distance A – B and e is the unit charge. The partial charges are calculated by using the *QEq* charge equilibrium scheme.[86] Addition of all the $E_{Coulomb-AB}$ different AB pair contributions will give the total electrostatic potential energy to add in equation 67.

The last term to describe is the *inversion* $E_{Inv-ABCD}$ of an atom A bonded to three other atoms B, C and D. E_{Inv} is written as a small Fourier expansion in ω in UFF:[85]

$$E_{Inv-ABCD} = K_{ABCD}^{Inv} [C_0 + C_1 Cos(\omega_{ABCD}) + C_2 Cos(2\omega_{ABCD})] \tag{74}$$

Here, K_{ABCD}^{Inv} is the force constant and ω_{ABCD} is the angle between the A – D axis ABC plane. As for the other potential energy interaction contributions, summation of all the $E_{Inv-ABCD}$ from different ABCD configurations will give the total inversion potential energy contribution to in equation 67.

2.7.2 The QM – MM junction

QM / MM boundary has to be carefully treated. If, for instance, we have a small molecule in solution, the problem is simple; put the molecule in the QM region and use MM for the solvent. However, in the process of defining the different regions, it is possible that the boundary between the QM and the MM region can go through a bond. This leaves atoms with the dangling bonds that must be saturated. The ONIOM scheme uses a *link atom*. [84] Here, normally an H atom saturates the "broken" bond replacing one of the real atoms (the one which is now in a different region). The link atom is placed on the bond vector between the QM and the MM regions and could also be other atom than H. The approximation used to treat the QM / MM boundary is actually one of the main differences between the QM – MM methods.

Another alternative is to use doubly occupied molecular orbitals to obtain a better description of the electron density in the boundary. Rivali *et al*. [87] proposed to place atomic orbitals localized and hybridized on the dangling bonds in the QM region. The orbital pointing towards the bond between the two regions is kept frozen during the SCF.

The ONIOM approach works by approximating the energy of the real system as:

$$E^{ONIOM} = E^{MM}(RS) + E^{QM}(SM) - E^{MM}(SM) \tag{75}$$

RS in equation 75 refers to real system, that is to say, the whole molecule; the ligand shell and the metal core in our case. SM stands for "small" model that refers to the part which is going to be treated with the more accurate level of theory (QM), the gold core in our GNC.

ONIOM calculation benefit from electrostatic embedding by taking into account the steric and electrostatic properties of the whole system in the modeling process of the QM region. The QM wave function is polarized by adding the partial charges of the MM region in the QM Hamiltonian improving the description of the interaction between the two regions.

2.8 References

1. Gruene, P., et al., *Structures of Neutral Au7, Au19, and Au20 Clusters in the Gas Phase.* Science, 2008. **321**(5889): p. 674-676.
2. Oliver-Meseguer, J., et al., *Formation and stability of 3-5 atom gold clusters from gold complexes during the catalytic reaction: dependence on ligands and counteranions.* Chemical Communications, 2013. **49**(71): p. 7782-7784.
3. Kauffman, D.R., et al., *Experimental and Computational Investigation of Au25 Clusters and CO2: A Unique Interaction and Enhanced Electrocatalytic Activity.* Journal of the American Chemical Society, 2012. **134**(24): p. 10237-10243.
4. Dervishi, E., et al., *Catalytic Conversion of Graphene into Carbon Nanotubes via Gold Nanoclusters at Low Temperatures.* ACS Nano, 2012. **6**(1): p. 501-511.
5. Gao, Y., et al., *Catalytic Activities of Subnanometer Gold Clusters (Au16–Au18, Au20, and Au27–Au35) for CO Oxidation.* ACS Nano, 2011. **5**(10): p. 7818-7829.
6. Harkness, K.M., et al., *Surface Fragmentation of Complexes from Thiolate Protected Gold Nanoparticles by Ion Mobility-Mass Spectrometry.* Analytical Chemistry, 2010. **82**(7): p. 3061-3066.
7. Angel, L.A., et al., *Ion Mobility Mass Spectrometry of Au25(SCH2CH2Ph)18 Nanoclusters.* ACS Nano, 2010. **4**(8): p. 4691-4700.
8. Knoppe, S., et al., *Ligand Exchange Reactions on Au38 and Au40 Clusters: A Combined Circular Dichroism and Mass Spectrometry Study.* Journal of the American Chemical Society, 2010. **132**(47): p. 16783-16789.
9. Farrag, M., et al., *Infra-red spectroscopy of size selected Au25, Au38 and Au144 ligand protected gold clusters.* Physical Chemistry Chemical Physics, 2013. **15**(30): p. 12539-12542.
10. Kurashige, W., et al., *Recent Progress in the Functionalization Methods of Thiolate-Protected Gold Clusters.* The Journal of Physical Chemistry Letters, 2014. **5**(23): p. 4134-4142.
11. Terrill, R.H., et al., *Monolayers in Three Dimensions: NMR, SAXS, Thermal, and Electron Hopping Studies of Alkanethiol Stabilized Gold Clusters.* Journal of the American Chemical Society, 1995. **117**(50): p. 12537-12548.
12. Zhu, M., et al., *Correlating the Crystal Structure of A Thiol-Protected Au25 Cluster and Optical Properties.* Journal of the American Chemical Society, 2008. **130**(18): p. 5883-5885.
13. Lugo, G., et al., *Charge Redistribution Effects on the UV–Vis Spectra of Small Ligated Gold Clusters: a Computational Study.* The Journal of Physical Chemistry C, 2015.
14. Fields-Zinna, C.A., J.F. Parker, and R.W. Murray, *Mass Spectrometry of Ligand Exchange Chelation of the Nanoparticle [Au25(SCH2CH2C6H5)18]1− by CH3C6H3(SH)2.* Journal of the American Chemical Society, 2010. **132**(48): p. 17193-17198.
15. Shibu, E.S., et al., *Ligand Exchange of Au25SG18 Leading to Functionalized Gold Clusters: Spectroscopy, Kinetics, and Luminescence.* The Journal of Physical Chemistry C, 2008. **112**(32): p. 12168-12176.
16. Pyykkö, P., *Theoretical Chemistry of Gold.* Angewandte Chemie International Edition, 2004. **43**(34): p. 4412-4456.
17. Pyykko, P., *Structural properties: Magic nanoclusters of gold.* Nat Nano, 2007. **2**(5): p. 273-274.
18. Xiong, X.-G., et al., *Aspects of bonding in small gold clusters.* International Journal of Mass Spectrometry, 2013. **354–355**: p. 15-18.
19. Hakkinen, H., *Atomic and electronic structure of gold clusters: understanding flakes, cages and superatoms from simple concepts.* Chemical Society Reviews, 2008. **37**(9): p. 1847-1859.
20. Hakkinen, H., *The gold-sulfur interface at the nanoscale.* Nat Chem, 2012. **4**(6): p. 443-455.

21. Häkkinen, H. and U. Landman, *Gold clusters $({\mathrm{Au}}_{N},$ $2<~N<~10)$ and their anions.* Physical Review B, 2000. **62**(4): p. R2287-R2290.
22. Rodriguez-Castillo, M., et al., *Reactivity of gold nanoparticles towards N-heterocyclic carbenes.* Dalton Transactions, 2014. **43**(16): p. 5978-5982.
23. Visart de Bocarmé, T., et al., *Oxygen adsorption on gold nanofacets and model clusters.* The Journal of Chemical Physics, 2006. **125**(5): p. 054703.
24. Aikens, C.M., *Origin of Discrete Optical Absorption Spectra of M25(SH)18− Nanoparticles (M = Au, Ag).* The Journal of Physical Chemistry C, 2008. **112**(50): p. 19797-19800.
25. Barngrover, B.M. and C.M. Aikens, *Oxidation of Gold Clusters by Thiols.* The Journal of Physical Chemistry A, 2013. **117**(25): p. 5377-5384.
26. Walter, M., et al., *A unified view of ligand-protected gold clusters as superatom complexes.* Proceedings of the National Academy of Sciences, 2008. **105**(27): p. 9157-9162.
27. Garzón, I.L., et al., *Lowest Energy Structures of Gold Nanoclusters.* Physical Review Letters, 1998. **81**(8): p. 1600-1603.
28. Hohenberg, P. and W. Kohn, *Inhomogeneous Electron Gas.* Physical Review, 1964. **136**(3B): p. B864-B871.
29. Kohn, W. and L.J. Sham, *Self-Consistent Equations Including Exchange and Correlation Effects.* Physical Review, 1965. **140**(4A): p. A1133-A1138.
30. Thayer, J.S., *Relativistic Effects and the Chemistry of the Heaviest Main-Group Elements.* Journal of Chemical Education, 2005. **82**(11): p. 1721.
31. Gimeno, M.C., *The Chemistry of Gold*, in *Modern Supramolecular Gold Chemistry*. 2009, Wiley-VCH Verlag GmbH & Co. KGaA. p. 1-63.
32. Parish, R.V., *Organogold chemistry: I structure and synthesis.* Gold Bulletin, 1997. **30**(1): p. 3-12.
33. Häkkinen, H., M. Moseler, and U. Landman, *Bonding in Cu, Ag, and Au Clusters: Relativistic Effects, Trends, and Surprises.* Physical Review Letters, 2002. **89**(3): p. 033401.
34. Häkkinen, H. and M. Moseler, *55-Atom clusters of silver and gold: Symmetry breaking by relativistic effects.* Computational Materials Science, 2006. **35**(3): p. 332-336.
35. Rösch, N., et al., *Aurophilicity as Concerted Effect: Relativistic MO Calculations on Carbon-Centered Gold Clusters.* Angewandte Chemie International Edition in English, 1989. **28**(10): p. 1357-1359.
36. Yanai, T., D.P. Tew, and N.C. Handy, *A new hybrid exchange–correlation functional using the Coulomb-attenuating method (CAM-B3LYP).* Chemical Physics Letters, 2004. **393**(1–3): p. 51-57.
37. Hay, P.J. and W.R. Wadt, *Ab initio effective core potentials for molecular calculations. Potentials for the transition metal atoms Sc to Hg.* The Journal of Chemical Physics, 1985. **82**(1): p. 270-283.
38. Hay, P.J. and W.R. Wadt, *Ab initio effective core potentials for molecular calculations. Potentials for K to Au including the outermost core orbitals.* The Journal of Chemical Physics, 1985. **82**(1): p. 299-310.
39. Prakash, M., et al., *Role of size and shape selectivity in interaction between gold nanoclusters and imidazole: a theoretical study.* Journal of Molecular Modeling, 2014. **20**(12): p. 1-14.
40. Dufour, F., et al., *Ligand and Solvation Effects on the Structural and Electronic Properties of Small Gold Clusters.* The Journal of Physical Chemistry C, 2014. **118**(8): p. 4362-4376.
41. Hashmi, A.S.K. and G.J. Hutchings, *Gold Catalysis.* Angewandte Chemie International Edition, 2006. **45**(47): p. 7896-7936.
42. Olson, R.M., et al., *Where Does the Planar-to-Nonplanar Turnover Occur in Small Gold Clusters?* Journal of the American Chemical Society, 2005. **127**(3): p. 1049-1052.
43. Fresch, B., et al., *Interplay of structural and electronic stabilizing factors in neutral and cationic phosphine protected Au13 clusters.* The European Physical Journal D, 2012. **66**(12): p. 1-9.

44. Frisch, M.J.T., G. W.; Schlegel, H. B.; Scuseria, G. E.;, M.A.C. Robb, J. R.; Scalmani, G.; Barone, V.; Mennucci,, and G.A.e.a. B.; Petersson, *Gaussian 09, Revision D01.* Gaussian, Inc.: Wallingford, CT,, 2009.
45. Foster, J.P. and F. Weinhold, *Natural hybrid orbitals.* Journal of the American Chemical Society, 1980. **102**(24): p. 7211-7218.
46. Reed, A.E., L.A. Curtiss, and F. Weinhold, *Intermolecular interactions from a natural bond orbital, donor-acceptor viewpoint.* Chemical Reviews, 1988. **88**(6): p. 899-926.
47. Gorelsky, S.I., *Aomix: Program for Molecular Orbital Analysis; Version 6.X.* University of Ottawa, 2013.
48. Schlegel, H.B., *Optimization of equilibrium geometries and transition structures.* Journal of Computational Chemistry, 1982. **3**(2): p. 214-218.
49. Breneman, C.M. and K.B. Wiberg, *Determining atom-centered monopoles from molecular electrostatic potentials. The need for high sampling density in formamide conformational analysis.* Journal of Computational Chemistry, 1990. **11**(3): p. 361-373.
50. Singh, U.C. and P.A. Kollman, *An approach to computing electrostatic charges for molecules.* Journal of Computational Chemistry, 1984. **5**(2): p. 129-145.
51. Parr, R.G.Y., W., *Density-Functional Theory of Atoms and Molecules.* Oxford Science publications, 1994: p. 325.
52. Levine, I.N., *Quantum Chemistry.* 2004: p. 487.
53. Perdew, J.P., et al., *Atoms, molecules, solids, and surfaces: Applications of the generalized gradient approximation for exchange and correlation.* Physical Review B, 1992. **46**(11): p. 6671-6687.
54. Perdew, J.P., et al., *Erratum: Atoms, molecules, solids, and surfaces: Applications of the generalized gradient approximation for exchange and correlation.* Physical Review B, 1993. **48**(7): p. 4978-4978.
55. Perdew, J.P., K. Burke, and M. Ernzerhof, *Generalized Gradient Approximation Made Simple.* Physical Review Letters, 1996. **77**(18): p. 3865-3868.
56. Becke, A.D., *Density-functional exchange-energy approximation with correct asymptotic behavior.* Physical Review A, 1988. **38**(6): p. 3098-3100.
57. Adamo, C. and V. Barone, *Toward reliable density functional methods without adjustable parameters: The PBE0 model.* The Journal of Chemical Physics, 1999. **110**(13): p. 6158-6170.
58. Paier, J., et al., *Screened hybrid density functionals applied to solids.* The Journal of Chemical Physics, 2006. **124**(15): p. 154709.
59. Stephens, P.J., et al., *Ab Initio Calculation of Vibrational Absorption and Circular Dichroism Spectra Using Density Functional Force Fields.* The Journal of Physical Chemistry, 1994. **98**(45): p. 11623-11627.
60. Kim, K. and K.D. Jordan, *Comparison of Density Functional and MP2 Calculations on the Water Monomer and Dimer.* The Journal of Physical Chemistry, 1994. **98**(40): p. 10089-10094.
61. Becke, A.D., *Density-functional thermochemistry. III. The role of exact exchange.* The Journal of Chemical Physics, 1993. **98**(7): p. 5648-5652.
62. Baker, J., *Techniques for geometry optimization: A comparison of cartesian and natural internal coordinates.* Journal of Computational Chemistry, 1993. **14**(9): p. 1085-1100.
63. Pulay, P. and G. Fogarasi, *Geometry optimization in redundant internal coordinates.* The Journal of Chemical Physics, 1992. **96**(4): p. 2856-2860.
64. Fogarasi, G., et al., *The calculation of ab initio molecular geometries: efficient optimization by natural internal coordinates and empirical correction by offset forces.* Journal of the American Chemical Society, 1992. **114**(21): p. 8191-8201.

65. Li, X. and M.J. Frisch, *Energy-Represented Direct Inversion in the Iterative Subspace within a Hybrid Geometry Optimization Method.* Journal of Chemical Theory and Computation, 2006. **2**(3): p. 835-839.
66. Cramer, C.J., *Essentials of Computational Chemistry. Theories and Models.* 2004. **2nd edition**.
67. Peng, C., et al., *Using redundant internal coordinates to optimize equilibrium geometries and transition states.* Journal of Computational Chemistry, 1996. **17**(1): p. 49-56.
68. Fletcher, R., *Practical Methods of Optimization.* Wiley, New York, 1980.
69. Rodríguez-Castillo, M., et al., *Experimental and Theoretical Study of the Reactivity of Gold Nanoparticles Towards Benzimidazole-2-ylidene Ligands.* Chemistry – A European Journal, 2016: p. n/a-n/a.
70. Cross, E.B.W.J.C.D.P.C., *Molecular vibrations : the theory of infrared and Raman vibrational spectra.* 1955: p. 354.
71. Besler, B.H., K.M. Merz, and P.A. Kollman, *Atomic charges derived from semiempirical methods.* Journal of Computational Chemistry, 1990. **11**(4): p. 431-439.
72. Mulliken, R.S., J. Chem. Phys., 1955. **23**(1833, 1841, 2338, 2343).
73. Attila Szabo, N.S.O., *Modern Quantum Chemistry: Introduction to Advanced Electronic Structure Theory.* Dover publications, 1996: p. 461.
74. Bouhmaida, N., et al., *Gradient vector field and properties of the experimental electrostatic potential: Application to ibuprofen drug molecule.* The Journal of Chemical Physics, 2002. **116**(14): p. 6196-6204.
75. Marques, M.A.L.U., C.A.; Nogueira, F.; Rubio, A.; Burke, K.; Gross, E.K.U., *Time-Dependent Density Functional Theory. Series: Lecture Notes in Physics.* 2006. **Vol. 706**.
76. Runge, E. and E.K.U. Gross, *Density-Functional Theory for Time-Dependent Systems.* Physical Review Letters, 1984. **52**(12): p. 997-1000.
77. Dreuw, A. and M. Head-Gordon, *Single-Reference ab Initio Methods for the Calculation of Excited States of Large Molecules.* Chemical Reviews, 2005. **105**(11): p. 4009-4037.
78. Mennucci, B., *Polarizable continuum model.* Wiley Interdisciplinary Reviews: Computational Molecular Science, 2012. **2**(3): p. 386-404.
79. Mennucci, B., et al., *Polarizable Continuum Model (PCM) Calculations of Solvent Effects on Optical Rotations of Chiral Molecules.* The Journal of Physical Chemistry A, 2002. **106**(25): p. 6102-6113.
80. Barone, V., M. Cossi, and J. Tomasi, *Geometry optimization of molecular structures in solution by the polarizable continuum model.* Journal of Computational Chemistry, 1998. **19**(4): p. 404-417.
81. Cancès, E., B. Mennucci, and J. Tomasi, *A new integral equation formalism for the polarizable continuum model: Theoretical background and applications to isotropic and anisotropic dielectrics.* The Journal of Chemical Physics, 1997. **107**(8): p. 3032-3041.
82. Levitt, A.W.a.M., *Theoretical Studies of Enzymic Reactions: Dielectric, Electrostatic and Steric Stabilization of Reaction of Lysozyme the Carbonium Ion in the Reaction of Lysozyme.* J. Mol. Biol., 1976. **103**: p. 227-249.
83. Salonen, L.M.a.E., *Biomolecular Simulations: Methods and Protocols, Methods in Molecular Biology.* Springer Science+Business Media, 2013. **924**.
84. Field, M.J., P.A. Bash, and M. Karplus, *A combined quantum mechanical and molecular mechanical potential for molecular dynamics simulations.* Journal of Computational Chemistry, 1990. **11**(6): p. 700-733.
85. Rappe, A.K., et al., *UFF, a full periodic table force field for molecular mechanics and molecular dynamics simulations.* Journal of the American Chemical Society, 1992. **114**(25): p. 10024-10035.
86. Rappe, A.K. and W.A. Goddard, *Charge equilibration for molecular dynamics simulations.* The Journal of Physical Chemistry, 1991. **95**(8): p. 3358-3363.

87. Assfeld, X. and J.-L. Rivail, *Quantum chemical computations on parts of large molecules: the ab initio local self consistent field method.* Chemical Physics Letters, 1996. **263**(1): p. 100-106.

Chapter III. Charge redistribution effects on the UV – Vis spectra of small ligated gold clusters

Introduction

While the properties of relatively large gold nanoparticles (with diameter greater than ~2 nm) are characterized by plasmonic excitations with collective nature,[1, 2] the discretized electronic structure of GNCs due to their ultra – small size results in single electron transitions and molecule – like properties. [3, 4]

Jin *et al.* [5] evidenced three well – defined bands in the optical absorption profile of the well – characterized $Au_{25}(SCH_2CH_2Ph)_{18}^-$ cluster around 688, 450 and 400 nm. Additionally, TD – DFT computations on the $Au_{25}(SH)_{18}^-$ model cluster [2] complemented the interpretation of the experimental UV – Vis spectrum of the $Au_{25}(SCH_2CH_2Ph)_{18}^-$ cluster showing that the lowest optical band at 688 nm was due to HOMO – LUMO excitations. The structure of the $Au_{28}(TBBT)_{20}$ cluster (TBBT being 4 – tert – butylbenzenethiolate) analyzed by single crystal X – ray crystallography was also reported by Jin *et al.* together with its experimental UV – Vis spectrum [6]. Only a change of 3 extra gold atoms in the stoichiometry compared to the $Au_{25}(SR)_{18}^-$ is needed to completely modify the metal core structure and hence the optical properties. The $Au_{28}(TBBT)_{20}$ cluster also shows three main bands at 580, 480 and 365 nm. Additionally, Tsunoyama *et al*.[7] reported the experimental UV – Vis spectrum of the thiolate protected $Au_{38}(SR)_{24}$ cluster. In this case, the lowest energy transition (corresponding to HOMO – LUMO excitations [8]) are localized around 1370 nm. These differences and the characteristic optical absorption patterns suggest that the nuclearity of the metal core plays a significant role on the optical properties of GNCs and confirm that their properties present high sensitivity to the number of gold atoms in their stoichiometry.

However, the ligand shell has also an important role not only on the passivation of the core but also on the structure of the metal backbone hence modifying the properties of the bare cluster. Our computations show that thiolates follow the *divide and protect* concept proposed by Häkkinen [9] where a sub – metal core is protected by small staple motifs. For instance, the $Au_{25}(SR)_{18}^-$ cluster is composed of a small Au_{13} core protected by 6 oligomers – SR – Au – SR – Au – SR –. [10] Addionally, Aikens [2, 5] have shown – by carrying out a TD – DFT study on the $Au_{25}(SH)_{18}^-$ model cluster – that most of the contribution to the molecular orbitals involved in the lower energy electronic excitations were coming from the Au_{13} core and that the UV – Vis spectrum was strongly influenced by the Au – Au length in the inner core which can be altered by the staple motif on the cluster surface. All these findings confirm that even though the optical profile appears to be a property of the core in thiolate protected GNCs the ligand shell participates indirectly on the optical absorption profile.

In this chapter, analysis of the optical, electronic and structural properties of several phosphine, chloride and thiolate ligated GNCs, with Au_{13}, Au_{25} and Au_{28} nuclearities at the DFT level is carried out in the gas phase.

Our computations on the icosahedral set of Au_{13} clusters protected by phosphines and chlorides show that their electronic structure is related to that of the bare Au_{13}^{5+} which constitutes a superatomic unit. Our study also confirms that the absorption profiles are highly dependent on the phosphine/chloride ratio as observed experimentally by Konishi *et al.* in ref [11] suggesting that the ligand – to – metal charge transfer is an important parameter to take into account for understanding the role of the ligand shell composition on the optical properties.

Additionally, the family of clusters $[Au_{25}(SR)_{18}]^q$ was studied (R being CH_3 or Ph and q = – 1, +1). Our computed structure for the $Au_{25}(SCH_3)_{18}^-$ cluster is quite close to that experimentally reported for the $Au_{25}(SCH_2CH_2Ph)_{18}^-$ [12] and the computed UV – Vis spectrum shows a good agreement with the experimental one.[5] Since the icosahedral Au_{13} represents a building block for thiolate protected Au_{25} clusters, the comparison of their optical profiles shows that the lowest energy band in $Au_{25}(SCH_3)_{18}^-$ is split due to the lift of the degeneracy of the superatomic D – orbitals, which is a consequence of the presence of the staples. [2, 13]

Furthermore, the possibility of tuning the optical and surface properties of GNCs through the design of the ligand shell suggests that cooperative effects may be important to understand the modulation of the electron density on the metal core.[14] Therefore, the properties of the non – icosahedral Au_{13} cluster capped by two different ligands with opposite electron donor/acceptor character were also investigated in this work. Seven PH_3 and five SCH_3 ligands were used to protect the metal core in four different ligand spatial configurations on the cluster surface. Two of these "ligand configuration" are Janus,[15-18] that is to say, ligands of the same nature spatially segregated, ligands forming stripes [19, 20] and ligands randomly organized (called *mixed*). Our calculations show that ligand shells of donor and acceptor ligands with different spatial organization lead to different equilibrium geometries and hence different UV – Vis spectra are obtained.

The comparison of the computed UV – visible absorption profiles of the icosahedral and amorphous Au_{13} clusters and of the $[Au_{25}(SR)_{18}]^q$ family shows that it is possible to shift the position of the lowest optical absorption band by controlling the electron density in the metallic core through the design of the ligand layer. We found that *the more negative the metallic core is the more the lowest optical absorption band is red shifted.* Interestingly, this trend is also confirmed by the phosphine, thiolate and chloride capped Au_{28} family of clusters studied whose electronic structure does not follow the superatomic model since their metal core does not exhibit spherical symmetry.

Finally, our computations confirm that the electron donor or acceptor character, the spatial organization of the ligands and the charge state play an important role in the regulation of the electron

density in the metallic core in GNCs. We show as well that the position of the lowest energy band can be tuned by the modulation of the electron density in the metal core which can be engineered by the correct design of the ligand layer.

3.1 Publication 1

Charge Redistribution Effects on the UV−Vis Spectra of Small Ligated Gold Clusters: a Computational Study

G. Lugo, V. Schwanen, B. Fresch, and F. Remacle

Department of Chemistry, University of Liège, B4000 Liège, Belgium

J. Phys. Chem. C 2015, 119, 10969 − 10980

Appendix 1: Supporting information. Charge Redistribution Effects on the UV-Vis Spectra of Small Ligated Gold Clusters: a Computational Study

THE JOURNAL OF PHYSICAL CHEMISTRY C

Article

pubs.acs.org/JPCC

Charge Redistribution Effects on the UV−Vis Spectra of Small Ligated Gold Clusters: a Computational Study

G. Lugo, V. Schwanen, B. Fresch, and F. Remacle*

Department of Chemistry, University of Liège, B4000 Liège, Belgium

Supporting Information

ABSTRACT: We analyze and compare the UV−visible absorption profiles, computed at the TD-DFT level, of several thiolate, chloride, and phosphine ligand protected gold clusters with Au_{13}, Au_{25}, and Au_{28} metallic cores. We show by investigating several model clusters and experimentally reported ones that the charge redistribution between the gold core and the ligand shell can be controlled by the electron acceptor or electron donor character of the ligands and their spatial distribution around the metallic core. A correlation between the increase of electronic charge in the gold core and a shift of the optical absorption band toward lower transition energies is highlighted. The identified correlation between the partial charge on the metallic gold core and the position of the lowest electronic transition is robust and remains valid even for small clusters with little structural or electronic similarity.

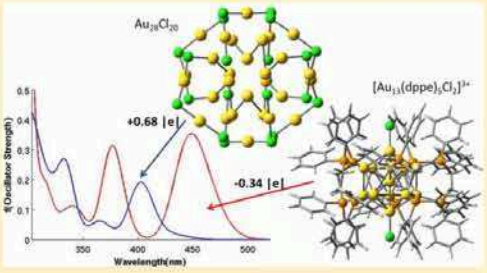

1. INTRODUCTION

Small gold clusters exhibit interesting optical properties relevant for applications in material science and biology. Many thiolate and phosphine ligated gold clusters have been well characterized through intensive experimental and theoretical studies, as reviewed recently in, e.g., refs 1−3. Nonetheless, the identification of general trends in their physicochemical properties remains a major challenge because of their size-specific behavior and the variability typical of the subnanometer scale. Absorption spectra of gold clusters are used to follow the synthesis of size-controlled compounds of specific stoichiometry. Their main features were found to be strongly dependent on the core nuclearity and core geometry[4] but rather insensitive to the number and the nature of the coordinating ligands as well as to the total charge of the cluster.[5] The absorption spectra of compact-core gold clusters is usually characterized by a tail-and-humps spectrum, with relatively weak absorption bands in the visible while the main band falls in the UV. No obvious correlation between the nuclearity of the cluster and the position of the lower energy transitions was reported. The nature of the transitions in the visible has to be established individually for each cluster.

Recent experimental studies pointed out effects of changes in the ligand shell on absorption and fluorescence spectra. Shichibu et al.[6] reported a shift of the position of the absorption bands depending on the number of Cl ligands in a series of Au_{13} clusters stabilized by phosphines and chlorides. In ref 7 Jin et al. focused on the fluorescence quantum yield in a series of $[Au_{25}(SR)_{18}]^q$ (−SR are thiolate alkanes) and correlated enhancement of fluorescence with the charge transfer character of the metal ligand interaction. Moreover, they also observed a damping of the absorption peaks as the positive charge of the cluster was increased. Differences in the absorption profile have been observed for different charge states of the same cluster.[8,9] A theoretical study on the Au_{25} family of clusters pointed out differences in the optical absorption spectra depending on the nature of the SR ligand and explained them in terms of different distortions of the metal core geometry.[10]

Here, on the basis of computational studies carried out at the density functional level of theory, we argue that the charge redistribution between the gold core and the ligand shell plays a major role in determining the energies of the optical transitions. For a given stoichiometry and a global charge, partial charges are computed by partitioning the electronic density of the whole cluster at equilibrium geometry between the metal core and the ligand shell according to the natural bond orbital (NBO) methodology.[11,12] We identify a correlation between the partial charge on the metal core and a shift of the absorption spectrum of the clusters: the more the core is negatively charged, the more the lowest optical transition is shifted to the red. These trends can be expected from general arguments because the charge distribution controls the value of the transition energies and transition dipoles. The low-energy optical transitions are localized within the metallic core and

Special Issue: Current Trends in Clusters and Nanoparticles Conference

Received: November 8, 2014
Revised: February 9, 2015
Published: February 10, 2015

ACS Publications © 2015 American Chemical Society

DOI: 10.1021/jp511120j
J. Phys. Chem. C 2015, 119, 10969−10980

shifted to the red when the core is more negative, which correlates with a decrease of the HOMO−LUMO gap.

The amount of electron density on the metallic core can be tuned by designing the ligand shell. We consider different strategies allowing changing the partial charge on the metallic core, and we show that the correlation between charge redistribution and energy of the optical absorptions holds true in all the cases investigated. In section 3 we will analyze icosahedral-like core Au_{13} clusters with different ratios of chloride and phosphine ligands: our findings are in agreement with experimental results on this family of compounds.[6] We then consider in section 4 nonicosahedral Au_{13} cores passivated by thiolate and phosphine ligands, demonstrating that the spatial organization of donor and acceptor ligands on the cluster surface also induces different charge redistributions and can be exploited to tune the optical properties. In section 5 we consider thiolate protected Au_{25} clusters whose geometry has been resolved.[13,14] Because the electronic structure of both the $Au_{25}(SR)_{18}^-$ anion and the icosahedral Au_{13} clusters can be described in the framework of the superatom paradigm,[15,16] we use this model to describe the optical transitions and show that the same transitions shift in energy due to the different charge accumulated in the metal center of the two families of clusters. We also consider the effect of the global charge state by studying the corresponding cation $Au_{25}(SR)_{18}^+$. In section 6 we consider the Au_{38} cluster with three completely different capping systems, namely, thiolate, chloride or phosphine ligand shells.

On the basis of our computational results we provide evidence that protecting ligands can be used to finely tune the range of optical absorption in gold clusters. The key chemical property allowing such modulation is the electron donor/acceptor character of the ligand shell with respect to the metallic core. We show that both the chemical composition of the ligand shell and the spatial organization of different ligands on the cluster surface can be tailored to control electronic charge redistribution between core and ligands.

2. COMPUTATIONAL METHODOLOGY

All electronic structure computations were carried out at the density functional level of theory as implemented in quantum chemistry with Gaussian 09.[17] The long-range corrected functional CAM-B3LYP[18] was used together with the LANL2DZ (for the Au_{13} clusters) and the LANL2MB (for Au_{25} and Au_{28}) relativistic corrected pseudopotentials and basis sets[19,20] for the metallic core. The 6-31G(d) Gaussian basis set was used for the ligands. This computational level was validated in our previous study of small gold clusters.[21] Frequency calculations on equilibrium geometries showed no imaginary frequencies for all the reported structures with the only exception of the $[Au_{13}(P(Ph_2CH_3))_8Cl_4]^+$ cluster for which complete suppression of imaginary frequencies due to vibrations in the phenyl moieties was not possible. The excited states and the UV−vis spectra were computed at the equilibrium geometry of the ground electronic state with the linear response TD-DFT method as implemented in Gaussian 09. Density of states (DOS) and partial density of states (PDOS) have been generated with the AOMix program[22,23] using the default MPA (Mulliken population analysis) and a Gaussian line shape with width at half-height equal to 0.2 eV. Partial charges on nuclei were computed using the natural population analysis and the natural bond orbital (NBO) methodology.[11,12]

3. ICOSAHEDRAL Au_{13} CLUSTERS WITH DIFFERENT RATIOS OF CHLORIDE/PHOSPHINE LIGANDS

Specific synthetic routes to obtain Au_{13} ligand protected clusters have been developed using phosphines and halides as protecting ligands. Shichibu et al.[24] reported a facile synthesis for icosahedral Au_{13} cluster protected by C_2-bridged diphosphine ligand ($Ph_2P-(CH_2)_2-PPh_2$, dppe) that specifically yields the cluster $[Au_{13}(dppe)_5Cl_2]^{3+}$. In a subsequent study,[6] they repeated the proposed synthesis with different phosphine ligands ($Ph_2P-(CH_2)_m-PPh_2$, m = 3 dppp, m = 4 dppb, and m = 5 dpppe) and identified the main products as belonging to the different class of clusters $[Au_{13}P_8Cl_4]^+$. The optical characterization of the complexes shows that their optical properties depend not only on the core nuclearity but also on the relative number of anionic (chloride) and neutral (phosphine) ligands. Although the spectra of $[Au_{13}(dppe)_5Cl_2]^{3+}$ exhibit distinct absorption bands at 360 and 490 nm, those of the family of clusters $[Au_{13}P_8Cl_4]^+$ appear at 340 nm together with a hump at 430 nm, without significant dependence on the specific phosphine ligand.

To investigate the role of the ligand−metal interaction on the lowest electronic transitions of the Au_{13} clusters, we theoretically characterize the clusters shown in Figure 1. We

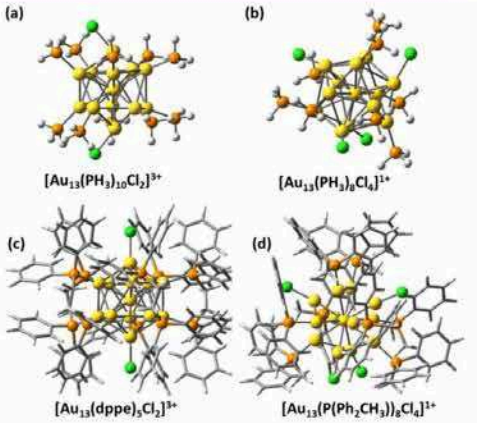

Figure 1. Computed equilibrium geometries of the four icosahedral Au_{13} clusters with mixed phosphine−chloride shells: (a) $[Au_{13}(PH_3)_{10}Cl_2]^{3+}$, (b) $[Au_{13}(PH_3)_8Cl_4]^+$, (c) $[Au_{13}(dppe)_5Cl_2]^{3+}$, and (d) $[Au_{13}(P(Ph_2CH_3))_8Cl_4]^+$. dppe stands for $Ph_2P-(CH_2)_2-PPh_2$. The Cl atoms are shown in green, the P atoms in orange, and the gold atoms in yellow.

first consider the simplified models of the families $[Au_{13}(PH_3)_{10}Cl_2]^{3+}$ and $[Au_{13}(PH_3)_8Cl_4]^+$ where the phosphine ligands are PH_3. We then study the clusters $[Au_{13}(dppe)_5Cl_2]^{3+}$ and $[Au_{13}(P(Ph_2CH_3))_8Cl_4]^+$. The crystallographic structure of $[Au_{13}(dppe)_5Cl_2]^{3+}$ is available[24] and it was used as the starting point for subsequent geometry optimization in the gas phase. The starting geometry of $[Au_{13}(P(Ph_2CH_3))_8Cl_4]^+$ was prepared on the basis of the crystallographic structure of the analogous bimetallic Ag−Au complex.[25] The four clusters are characterized by an icosahedral-like metallic core and their electronic structures are related to the electronic structure of the icosahedral unit

DOI: 10.1021/jp511120j
J. Phys. Chem. C 2015, 119, 10969−10980

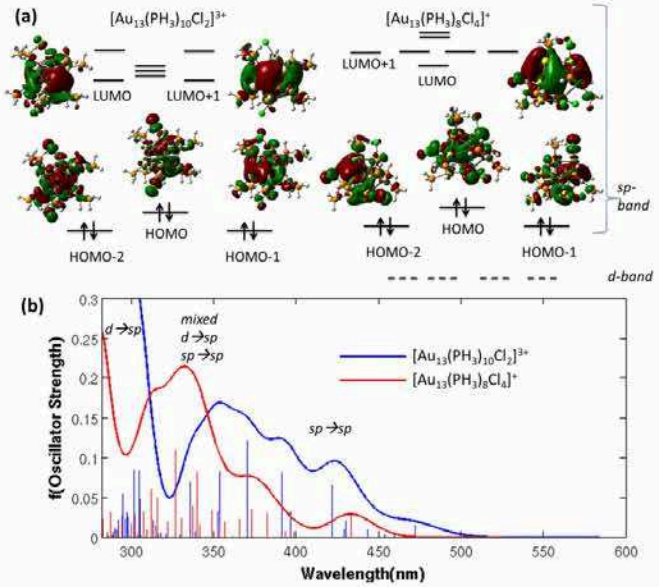

Figure 2. (a) Schematic representation of the energy levels (with a degeneracy threshold of 0.13 eV) involved in the low energy optical transitions of the clusters $[Au_{13}(PH_3)_{10}Cl_2]^{3+}$ and $[Au_{13}(PH_3)_8Cl_4]^{+}$ together with the isocontour of the corresponding orbitals (isovalue 0.03 $Å^{-3}$). (b) Computed UV−vis absorption spectra of the same clusters: the height of the vertical bars give the oscillator strength of each transition, and the spectra are obtained by convolution with Gaussian line shapes (σ = 0.085 eV).

Au_{13}^{5+}. With a formal arrangement of 8 valence electrons, Au_{13}^{5+} constitutes a superatomic unit[15,16] and it is also found as a fundamental building block in gold clusters of higher nuclearity such as Au_{25},[26−29] Au_{38},[30,31] and Au_{40}.[32,33] The HOMO is approximately triply degenerate, and in solid state implementations of DFT, the density of states projected onto spherical harmonics shows that these three orbitals possess mainly p-character, in agreement with the known 8-electron s^2p^6 shell closing in the superatom picture for metals with a single valence s electron.[16] The electronic structures of clusters in Figure 1 maintain significant similarities with the superatom model; the specific properties due to the presence of the ligands will be discussed in details below.

The icosahedral-like metallic core is more distorted in the model systems $[Au_{13}(PH_3)_{10}Cl_2]^{3+}$ and $[Au_{13}(PH_3)_8Cl_4]^{+}$ than in $[Au_{13}(dppe)_5Cl_2]^{3+}$ and $[Au_{13}(P(Ph_2CH_3))_8Cl_4]^{+}$, pointing to the role of phosphine phenyl ligands in preserving the geometry of the metallic core. The gold cores of $[Au_{13}(PH_3)_{10}Cl_2]^{3+}$ and $[Au_{13}(PH_3)_8Cl_4]^{+}$ belong to the point group C_{2h} and C_1, respectively, with a 0.3 Å of tolerance in the atomic positions, whereas the core in $[Au_{13}(dppe)_5Cl_2]^{3+}$ preserves I_h symmetry and belongs to S_{10} in $[Au_{13}(P(Ph_2CH_3))_8Cl_4]^{+}$. The larger observed distortion in the case of the small model ligand PH_3 is due to the chlorine getting closer to the cluster surface and to the absence of the phenyl groups in PH_3 that stabilize the metallic core. The stabilization arises from the steric rigidity of the ligand shell and from the role of the phenyl ring in the charge redistribution, mainly by providing an electron-rich environment for the chlorine that results in less distortion of the metallic core. The shorter Au−Cl bond is found in $[Au_{13}(PH_3)_{10}Cl_2]^{3+}$ and $[Au_{13}(dppe)_5Cl_2]^{3+}$ (on average 2.378 and 2.391 Å, respectively), whereas the addition of chlorines entails a slightly longer Au−Cl bond (on average 2.411 Å in $[Au_{13}(PH_3)_8Cl_4]^{+}$ and 2.427 Å in $[Au_{13}(P(Ph_2CH_3))_8Cl_4]^{+}$).

The densities of electronic states (DOS) of the four clusters present a common structure: the three highest occupied molecular orbitals (HOMO, HOMO−1, and HOMO−2) and the virtual orbitals are mainly composed of s and p atomic orbitals of gold (sp band) while the d band lies lower in energy. In Figure S1 of the Supporting Information, we report the total DOS and the contributions from the gold core, the phosphines and the chlorines in the cases of $[Au_{13}(PH_3)_{10}Cl_2]^{3+}$ and $[Au_{13}P_8Cl_4]^{+}$. Figure 2a shows the level structure of the molecular orbitals (MO's) near the HOMO−LUMO gap as well as their isoamplitude contours for $[Au_{13}(PH_3)_{10}Cl_2]^{3+}$ and $[Au_{13}(PH_3)_8Cl_4]^{+}$. They are characterized by an overall similar structure with the contribution of the chlorines to the frontier orbitals clearly more pronounced for $[Au_{13}(PH_3)_8Cl_4]^{+}$. The orbitals of the sp band are localized mainly in the gold core. The contribution of the gold core to these orbitals is generally >70% while the orbitals just below are well delocalized on the chlorine nuclei and the contribution of the gold core decreases to 50%. The 3-fold quasi-degenerate set (HOMO, HOMO−1, HOMO−2) and the virtual orbitals (LUMO to LUMO+4) maintain a resemblance with the superatomic orbitals (SAO) that characterize the electronic structure of the icosahedral core of the bare Au_{13}^{5+}.[34,35] The HOMO−LUMO gap value increases going from $[Au_{13}(PH_3)_{10}Cl_2]^{3+}$ to $[Au_{13}(PH_3)_8Cl_4]^{+}$; the opening of the gap correlates with a blue-shift of the absorption spectrum.

DOI: 10.1021/jp511120j
J. Phys. Chem. C 2015, 119, 10969−10980

Table 1. Partial Charge Distribution and Characteristics of the Lowest Transition of $[Au_{13}(PH_3)_{10}Cl_2]^{3+}$, $[Au_{13}(PH_3)_8Cl_4]^+$, $[Au_{13}(dppe)_5Cl_2]^{3+}$, and $[Au_{13}(P(Ph_2CH_3))_8Cl_4]^+$ [a]

	natural charge				
	Au_{13}	P	Cl	H−L	lowest transition
$[Au_{13}(PH_3)_{10}Cl_2]^{3+}$	0.53	3.48 (0.35)	−1.01	4.88	2.62 eV, 472.5 nm f = 0.015 228 → 231; 0.188 229 → 230; 0.658
$[Au_{13}(dppe)_5Cl_2]^{3+}$ [b]	−0.34	4.39 (0.44)	−1.05	4.77	2.50 eV, 496.6 nm f = 0.0000 663 → 665; 0.477 663 → 668; −0.125 664 → 666; −0.473 664 → 667; 0.128
$[Au_{13}(PH_3)_8Cl_4]^+$	0.83	2.43 (0.30)	−2.26	5.11	2.86 eV, 433.2 nm f = 0.0290 229 →230; 0.689
$[Au_{13}(P(Ph_2CH_3))_8Cl_4]^+$ [c]	−0.10	3.40 (0.42)	−2.30	4.89	2.65 eV, 467.2 nm f = 0.0114 580 → 582; 0.437 581 → 582; 0.520

[a]Natural charges on the metallic core Au_{13} and on the P and Cl atoms are given in lel. For the P atom, the number in parentheses is the mean charge per P atom. The HOMO−LUMO gaps (H−L) are given in eV. For the lowest excitation, the transition energy (eV and nm) from the GS, its oscillator strength, main excitations, and their amplitudes are reported. [b]Note that this transition is not allowed optically. [c]No frequencies could be obtained for this complex.

The UV−vis absorption spectra were obtained by the calculation of the 40 lowest excited states. The absorption profiles of $[Au_{13}(PH_3)_{10}Cl_2]^{3+}$ and $[Au_{13}(PH_3)_8Cl_4]^+$ are reported in Figure 2b. The transition energies are indicated by the vertical bars whose heights correspond to the oscillator strength of the corresponding transition, and the spectra are obtained by convolution with Gaussian line shapes with σ = 0.085 eV. The two spectra exhibit the tail and humps shape in the low energy region that overlaps with the main UV band. For both model clusters the first excitation (at 472.5 nm for $[Au_{13}(PH_3)_{10}Cl_2]^{3+}$ and 433.2 nm for $[Au_{13}(PH_3)_8Cl_4]^+$) is mainly the HOMO−LUMO transition (86% and 95% for $[Au_{13}(PH_3)_{10}Cl_2]^{3+}$ and $[Au_{13}(PH_3)_8Cl_4]^+$, respectively). Transitions in the region >350 nm are all composed of excitations from the 3-fold quasi-degenerate group of orbitals (HOMO to HOMO−2) to the manifold (LUMO to LUMO+4) (Figure 2a). At higher energy, excitations from the orbitals of the d-band begin to contribute and the transitions around 300 nm are composed exclusively of excitations from the d-band. Even if the absorption profiles of $[Au_{13}(PH_3)_{10}Cl_2]^{3+}$ and of $[Au_{13}(PH_3)_8Cl_4]^+$ present similar patterns, the spectra of the species $[Au_{13}(PH_3)_8Cl_4]^+$ is shifted by about 0.20 eV toward higher energies. The calculated spectral shapes agree fairly well with those measured for the absorption of $[Au_{13}(dppe)_5Cl_2]^{3+}$ and for the family of $[Au_{13}P_8Cl_4]^+$ clusters reported in ref 6. In particular, the blue shift of the four chloride species relative to the two chloride species is consistent with the experimental observation. The shift of the absorption band involves all the transitions, irrespective of the sp → sp or d → sp nature, suggesting that the physical origin of the shift is rather independent from the orbital composition and should be related to a global property. By calculating the natural charges, we find that the blue shift of the absorption spectrum is correlated with a larger positive charge on the metal core. In Table 1, we report the natural charge on the Au_{13} core, on the chlorines, and on the phosphines. The phosphines tend to donate electronic charge but the chlorines are strong electron acceptors, resulting in a partial charge on the gold core of 0.53|el| and 0.83|el| for $[Au_{13}(PH_3)_{10}Cl_2]^{3+}$ and $[Au_{13}(PH_3)_8Cl_4]^+$, respectively. Because the excitations involved in the optical transitions are mainly localized on the gold core, the opening of the optical gap is well explained by the increasing of partial positive charge in the metal core. In the following, we will investigate the generality of this correlation between partial charge in the metallic core and shift of the absorption profile.

To investigate to what extent the simplified model for the phosphine ligands affects the structure, the redistribution of charge and the absorption spectra we now analyze the cluster $[Au_{13}(dppe)_5Cl_2]^{3+}$. As noticed above, the presence of the bidentate ligand has an important effect in constraining the geometry of the metal core to a high symmetry. This is reflected in the higher degeneracy of the frontiers orbitals, whose scheme is reported in the inset of Figure 3. The isocontours of representative orbitals are shown in Figure S2 of the Supporting Information, they conserve the superatomic orbital character already shown in Figure 2a in the case of the model clusters $[Au_{13}(PH_3)_{10}Cl_2]^{3+}$ and $[Au_{13}(PH_3)_8Cl_4]^+$. The high symmetry of the metal core has an important effect on the optical transitions as several of them have negligible oscillator strength, and they are not visible in the spectrum (Figure 3). The calculated spectra agree well with the experimental ones: in particular, the two absorption bands at wavelengths >350 nm correspond to the 360 and 490 nm reported by Schichibu et al.[6] Both these bands are due to a combination of excitations from the 3-fold quasi-degenerate HOMO orbitals to the 5-fold quasi-degenerate LUMO orbital. The first band at 460 nm involves the HOMO and HOMO−1 while the second band at 370 nm involves also the lowest lying HOMO−2 (Figure 3). At wavelengths between 325 and 350 nm we then find some mixed sp → sp/d → sp transitions whereas pure d → sp

DOI: 10.1021/jp511120j
J. Phys. Chem. C 2015, 119, 10969−10980

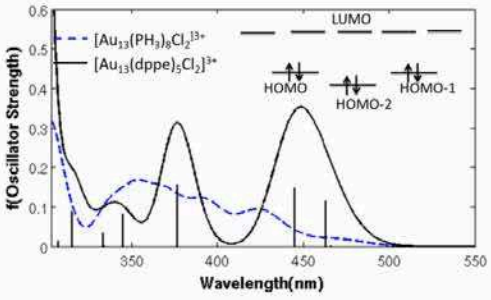

Figure 3. Computed UV–vis absorption spectrum of the cluster $[Au_{13}(dppe)_5Cl_2]^{3+}$ (black line) together with the spectrum of the corresponding model $[Au_{13}(PH_3)_{10}Cl_2]^{3+}$ (blue dashed line). The height of the vertical bars gives the oscillator strength of each transition, and the spectrum is obtained by convolution with Gaussian line shapes (σ = 0.085 eV). The inset reports the schematic energy levels (with a degeneracy threshold of 0.13 eV) involved in the low energy transitions.

transitions dominate at higher energy similarly to the case of model clusters 1 and 2.

The charge redistribution between the metallic core and the two different ligands (chlorides and phosphines) shows an important dependence on the type of the phosphine ligands. The Au_{13} core of $[Au_{13}(dppe)_5Cl_2]^{3+}$ carries a partial negative charge of −0.34|e| whereas a positive partial charge of +0.53|e| is obtained for the core in $[Au_{13}(PH_3)_5Cl_2]^{3+}$ (Table 1). The chlorine nuclei show identical electron acceptor behaviors in both clusters so the different charge on the metallic core is due to the increased electron donor character of the P atom in the dppe (on average +0.44|e| per phosphorus atom) with respect to the simplest phosphine PH_3 (on average +0.35|e| per phosphorus atom). An analogous increase of electronic charge on the metal core is observed for the cluster $[Au_{13}(P(Ph_2CH_3))_8Cl_4]^+$ with respect to the simpler model cluster $[Au_{13}(PH_3)_8Cl_4]^+$. The increment in the gold core electronic charge correlates with a lower value of the HOMO–LUMO gap and a red shift in the optical absorption transitions for both $[Au_{13}(dppe)_5Cl_2]^{3+}$ and $[Au_{13}(P(Ph_2CH_3))_8Cl_4]^+$ with respect to the corresponding model clusters $[Au_{13}(PH_3)_{10}Cl_2]^{3+}$ and $[Au_{13}(PH_3)_8Cl_4]^+$ (Table 1). In the following, to demonstrate the correlation between partial charge in the gold core and shift of the optical absorption range, we will refer to the energy of the first optical transition. In some cases, as for $[Au_{13}(dppe)_5Cl_2]^{3+}$, the lowest energy excited state is almost dark because the corresponding transition is only weakly allowed whereas the intense transition defining the maximum of the absorption band corresponds to the eighth excited state and is located at 2.67 eV (463.4 nm). Nonetheless, the relative energies of the lowest transition in different clusters are indicative of the overall relative shift of the absorption bands, as shown in Figure 3 by plotting the absorption profiles of $[Au_{13}(dppe)_5Cl_2]^{3+}$ and $[Au_{13}(PH_3)_{10}Cl_2]^{3+}$. For completeness, we note that for all the clusters the lowest excited state is a triplet, to which the transition from the ground state is optically forbidden. The singlet and triplet spin states are not contaminated by higher spin states.

4. EFFECT OF THE SPATIAL ORGANIZATION OF A MIXED LIGAND SHELL IN THE $Au_{13}(SCH_3)_5(PH_3)_7$ CLUSTER

In this section, we investigate the effect of the spatial organization of a mixed phosphine–thiolate ligand shell in the model cluster $Au_{13}(SCH_3)_5(PH_3)_7$. The spatial organization of the ligands of the same chemical nature in localized domains leads to "Janus" nanoparticles.[36−39] Previous computational studies on small Au[21] and on Pd[40] clusters showed that, when the mixed shell is made of electron donor and electron acceptor ligands, their spatial organization into domains leads to different charge redistributions between the metal core and the ligand shell. The different organization of ligands on the cluster surface thus represents a possible strategy to tune the partial charge on the gold core in clusters of the same stoichiometry. Here we analyze the effects of different spatial organization of the mixed ligand shell on the absorption spectra of the model $Au_{13}(SCH_3)_5(PH_3)_7$ cluster.

The equilibrium geometries obtained for four different model $Au_{13}(SCH_3)_5(PH_3)_7$ clusters are shown in Figure 4. The four clusters, identify as "mixed", "stripe", "Janus 1", and "Janus 2", differ by the arrangement of the thiolates and phosphines in the ligand shell. In the "Janus" clusters, ligands of the same chemical nature are gathered in different hemispheres whereas they are organized in three stripes in the "stripe" one. Stripe organization of mixed ligand shells have recently been reported.[41−43] Different spatial organizations of the two ligands correspond to different equilibrium geometries of the Au_{13} core. In particular, these clusters do not present a compact icosahedral-like geometry but are characterized by rather amorphous structures. The stripe mixed cluster is the most stable, but quasi degenerate with the Janus 2 arrangement. The values of the global charge on the 13-gold cores are reported in

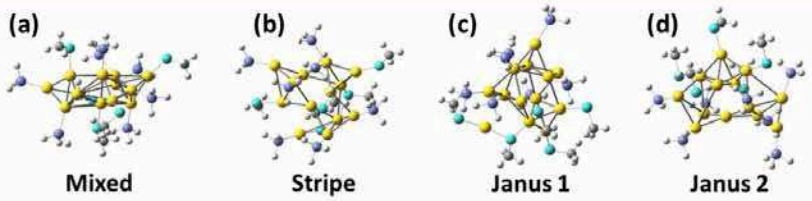

Figure 4. Computed equilibrium geometry of four ligated $Au_{13}(SCH_3)_5(PH_3)_7$ clusters exhibiting different spatial organizations as indicated: (a) "Mixed", (b) "Stripe", (c) "Janus 1", and (d) "Janus 2" ligand organization. Au atoms are in yellow, S in cyan, C in gray, P in violet, and H in white. The "Stripe" organization of the ligands leads to the most stable cluster. The relative free energies (ΔG) of the "Mixed", "Janus 1", and "Janus 2" clusters with respect to the stripe arrangement are respectively 47.07, 74.45, and 5.62 kJ mol^{-1}.

DOI: 10.1021/jp511120j
J. Phys. Chem. C 2015, 119, 10969−10980

Table 2 and show that the spatial organization of the ligands strongly affects the charge distribution in the metallic core. The

Table 2. Natural Charge, HOMO−LUMO (H−L) Gap, and Characteristics of the Lowest Optical Excitation of the Four $Au_{13}(SCH_3)_5(PH_3)_7$ Clusters Exhibiting Different Spatial Organization[a]

	natural charge				
	Au_{13}	SCH_3	PH_3	H−L gap	lowest transition
Mixed	0.096	−1.993	1.897	3.926	1.84 eV, 675.05 nm f = 0.0465 249 → 250; 0.677 249 → 251; 0.101
Stripe	0.12	−1.885	1.767	4.086	1.90 eV, 652.13 nm f = 0.0066 249 → 250; 0.695
Janus 1	0.11	−1.864	1.753	4.094	2.10 eV, 590.07 nm f = 0.0019 247 → 250; 0.140 248 → 250; 0.440 248 → 250; 0.440
Janus 2	0.25	−1.898	1.649	4.363	2.37 eV, 523.53 nm f = 0.0297 249 → 250; 0.641 249 → 251; 0.218

[a]Natural charges are given in lel. The HOMO−LUMO gaps (H−L) are given in eV. For the lowest excitation, the transition energy (eV and nm) from the GS, its oscillator strength, main excitations, and their amplitudes are reported.

Au_{13} core of the "mixed" cluster is the more negative and the "Janus 2" one the most positively charged.

Figure 5 shows the theoretical optical absorption spectra of the four clusters. In the four cases, the lowest transition is mainly due to a HOMO − LUMO excitation (249 → 250) with sp → sp character. The relative position of the main absorption peaks correlates with the partial charge on the Au_{13} metallic core. As in the analysis of the absorption characteristics of the icosahedral Au_{13} clusters passivated with a mixed Cl−phosphine ligand shell discussed above, the shift in the optical spectra is independent of the orbital composition of the transition. The lowest first excitation energy, 1.84 eV, is found for the "Mixed" cluster, that is also characterized by the less positive gold core (0.096lel). The lowest transition of the "Stripe" cluster is slightly higher, 1.90 eV, but with a significantly lower oscillator strength. In the "Stripe" configuration, the partial charge on the Au_{13} core is 0.12lel. We then find the "Janus 1" with a very similar partial charge of 0.11lel in the metallic core and the lowest transition at 2.10 eV whereas the "Janus 2" shows the first transition at 2.37 eV and a partial charge of 0.25lel on the Au_{13} core. As in the previously discussed case of $[Au_{13}(dppe)_5Cl_2]^{3+}$, the lowest transition in "Janus 1" is very weak. However, we show in Figure 5 that the optical spectrum is qualitatively and globally shifted to the blue as the metallic core is becoming more positive. Notice that, unlike in the family of icosahedral-like Au_{13} clusters discussed in the previous section, the geometry of the Au_{13} core in the $Au_{13}(SCH_3)_5(PH_3)_7$ clusters is significantly affected by the arrangement of the ligands. The charge redistribution between the ligands and the metallic core is therefore not only function of the electron donor or acceptor character of the ligands but also of the core geometry. We find, however, that the

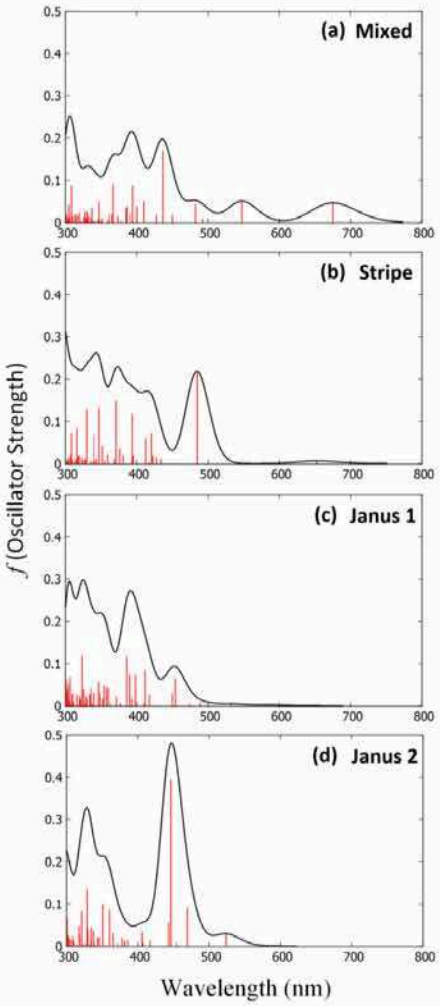

Figure 5. Computed optical spectra of the thiolate−phosphine Au_{13} cluster with different spatial arrangements as shown in Figure 4. The optical spectrum is qualitatively shifting to the blue as the metallic core becomes more positive. In the "Janus 1" case the lowest transition appears at 2.10 eV but with a low intensity (oscillator strength f = 0.0019).

correlation between the partial charge on the metallic core and the position of the absorption band is still valid despite these important geometrical rearrangements.

5. THIOLATE PROTECTED Au_{25} CLUSTERS: EFFECT OF THE GLOBAL CHARGE STATES

The family of clusters $Au_{25}(SR)_{18}^{q}$, with q = −1, 0, +1, has been previously studied both theoretically[10,29,35,44,45] and experimentally.[46] R defines the kind of thiolate ligand used to

DOI: 10.1021/jp511120j
J. Phys. Chem. C 2015, 119, 10969−10980

passivate the cluster, e.g., R = SPh,[47] glutathione,[5,48] 3-mercapto-2-butanol (MB),[5] CH_2CH_2Ph.[14]

We discuss three closed shell models for this family of compounds, namely the clusters $Au_{25}(SCH_3)_{18}^q$ with $q = -1$ and $q = +1$ and the anion $Au_{25}(SPh)_{18}^-$ (Figure 6). In

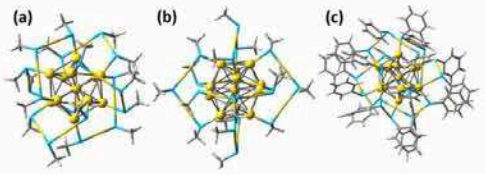

Figure 6. Computed equilibrium geometries of the three ligated Au_{25} clusters: (a) $[Au_{25}(SCH_3)_{18}]^-$, (b) $[Au_{25}(SCH_3)_{18}]^+$, and (c) $[Au_{25}(SPh)_{18}]^-$. Au atoms are shown in yellow, S is represented by the cyan junctions, C in gray, and H in white. The icosahedral Au_{13} core is highlighted by yellow spheres and surrounded by the (−SR−Au−SR−Au−SR−) staple motifs.

agreement with previous studies, we find that in the clusters reported in Figure 6, the metallic Au_{25} core possesses three types of gold atoms: one is at the center, 12 atoms form the vertices of the icosahedron around the central atom, and the remaining 12 gold atoms are stellated on 12 of the 20 faces of the Au_{13} icosahedron. The icosahedral Au_{13} core is protected by six (−SR−Au−SR−Au−SR−) cyclic oligomers.

As shown in previous works[13,35,44,45] and similarly to the Au_{13} clusters discussed in section 3, the frontier orbitals of $Au_{25}(SR)_{18}^-$ are also characterized by a superatomic character (Figure S3, Supporting Information). In view of the particular geometrical arrangement of these clusters, the superatomic character can be intuitively understood as emerging from the Au_{13} icosahedral core surrounded by the six $Au_2(SR)_3$ motifs. The prominent role of the Au_{13} core in determining the structure of the valence electronic shell in this family of clusters is demonstrated by the high contribution of the sp orbitals of the gold atoms of the Au_{13} core (larger than 61%) to the superatomic orbitals. The analogy between the electronic structures of the Au_{13} and Au_{25} families of clusters suggests that we can compare the optical spectra of the icosahedral Au_{13} and Au_{25} species to test further the effect of the core partial charge on the energies of optical transitions.

The experimental optical absorption of $Au_{25}(SCH_2CH_2Ph)_{18}^-$ shows three well-defined bands at 1.8, 2.75, and 3.1 eV that were previously reproduced semi-quantitatively from theoretical calculations at the TD-DFT (SAOP/TZP) level of theory which allowed the assignment of the bands.[13] The splitting between the two lowest bands in the optical absorption spectrum of $Au_{25}(SCH_3)_{18}^-$ shown in Figure 7a is known to arise from the ligand-field splitting of the superatomic D orbitals.[45] The first band centered at 610 nm (due to excitations at energy of 1.9−2.0 eV in good agreement with the experimental value of 1.8 eV) originates from excitations involving transitions from the 3-fold quasi-degenerate HOMO manifold to the LUMO, LUMO+1 quasi-degenerate set. The second band at 405 nm (due to excitation at energy around 3.0 eV, slightly higher in energy than the experimental value of 2.75 eV but still in the range of the typical error of the computational method) originates from excitations from the 3-fold quasi-degenerate HOMO manifold to the LUMO+2 to LUMO+4 3-fold quasi-degenerate set (inset of

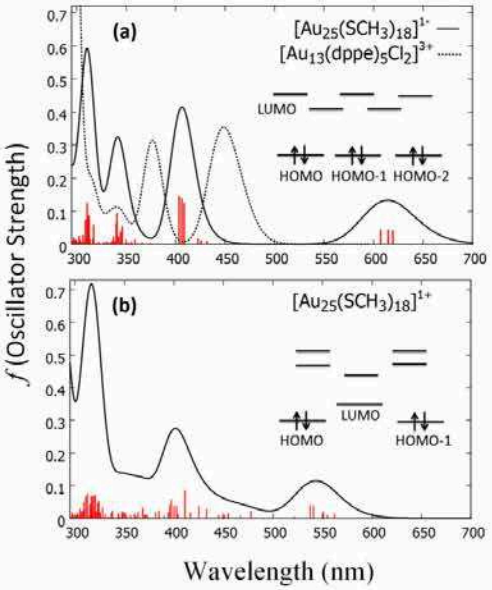

Figure 7. Computed optical absorption spectra of the methanethiolate ligated Au_{25} clusters. Top: the anion $[Au_{25}(SCH_3)_{18}]^-$. Bottom: the cation $[Au_{25}(SCH_3)_{18}]^+$. The dashed line in the spectrum on top shows the computed spectrum of the $[Au_{13}(dppe)_5Cl_2]^{3+}$ cluster (Figure 3). The representative energy orbital diagram is shown as an inset.

Figure 7). Because both the 3-fold quasi-degenerate (HOMO to HOMO+2) set and the (LUMO to LUMO+4) set of orbitals are mainly composed of the sp orbitals of the gold atoms of the Au_{13} core, the first two bands exhibit sp → sp character. At higher energies (in the spectral region at $\lambda < 374$ nm) we find the d → sp transitions. In Figure 7a we compare the calculated optical absorption profiles of $Au_{25}(SCH_3)_{18}^-$ and $[Au_{13}(dppe)_5Cl_2]^{3+}$clusters. As discussed above, in both cases the two bands in the low energy region of the spectrum are due to excitations involving sp → sp transitions between the superatomic orbitals of the Au_{13} core. Despite the similar natures of the excitations in the two clusters, both bands are significantly shifted to the red for $Au_{25}(SCH_3)_{18}^-$. By analyzing the natural charge decomposition in the $Au_{25}(SCH_3)_{18}^-$ cluster (reported in Table 3), we find an overall positive charge by summing up the contribution of all the 25 gold atoms, reflecting the electron withdrawing character of the −SR ligands.[21,49] Nonetheless, the Au_{13} central icosahedral core has a partial negative charge of −0.53|e|, more negative than the Au_{13} core of $[Au_{13}(dppe)_5Cl_2]^{3+}$ (−0.34|e|). For defining the Au_{13} icosahedral core, we consider the (−SR−Au−SR−Au−SR−) moieties as ligands. The correlation highlighted in the families of Au_{13} clusters 1−4 between the partial charge of the core and the shift of the optical absorption is therefore recovered for the $Au_{25}(SCH_3)_{18}$ anion. The more negative (or less positive) is the gold cluster core, the more the absorption spectrum is shifted to the red. This trend is also verified when the partial charges of the Au_{25} and Au_{13} core for $Au_{25}(SCH_3)_{18}^-$ and $Au_{25}(SPh)_{18}^-$ are compared (Table 3). The substitution of

DOI: 10.1021/jp511120j
J. Phys. Chem. C 2015, 119, 10969−10980

Table 3. Natural Charge, HOMO−LUMO (H−L) Gap, and Characteristics of the Lowest Optical Excitation of the Three Au_{25} Clusters Shown in Figure 6[a]

	natural charge					
	Au_{25}	S	CH	Au_{13}	H−L gap	lowest transition
$[Au_{25}(SCH_3)_{18}]^-$	3.10	−3.28	−0.81	−0.53	3.99	1.88 eV, 658.8 nm f = 0.0015 461 → 464; −0.264 461 → 465; −0.115 463 → 464; 0.546 464 → 465; −0.310
$[Au_{25}(SPh)_{18}]^-$	3.06	−2.19	−1.86	−0.45	4.01	1.92 eV, 646.2 nm f = 0.0055 749 → 752; 0.106 750 → 752; −0.101 750 → 753; −0.117 751 → 752; 0.649 751 → 753−0.168
$[Au_{25}(SCH_3)_{18}]^+$	3.89	−2.58	−0.31	−0.05	3.12	2.12 eV, 585.1 nm f = 0.0014 452 → 463; 0.104 461 → 464; 0.431 461 → 465; 0.194 462 → 464; 0.260 462 → 465; −0.389

[a]Natural charges are given in |e|. The HOMO−LUMO gaps (H−L) are given in eV. For the lowest excitation, the transition energy (eV and nm) from the GS, its oscillator strength, main excitations, and their amplitudes are reported.

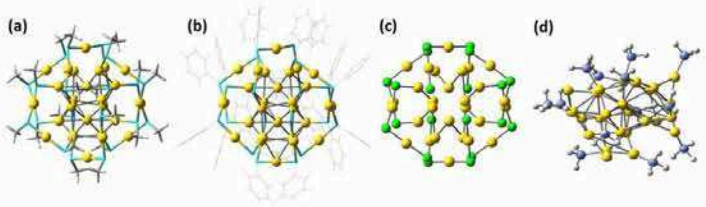

Figure 8. Computed equilibrium geometry of the four ligated Au_{28} clusters: (a) $Au_{28}(SCH_3)_{20}$, (b) $Au_{28}(SPh)_{20}$, (c) $Au_{28}Cl_{20}$, and (d) $Au_{28}(PH_3)_{13}$. Au atoms are represented by the yellow spheres, S by the cyan junctions, C in gray, Cl in green, P in violet spheres, and H in white.

the methanethiolates with the benzenethiolate (cluster c in Figure 6) slightly enhances the electron acceptor character of the ligands, reflected in a less negative partial charge in the Au_{13} core (−0.45 compared to −0.53|e| in $Au_{25}(SCH_3)_{18}^-$) and a slightly less positive charge on the Au_{25} core (3.06 instead of 3.10|e| in $Au_{25}(SCH_3)_{18}^-$). Accordingly, the absorption spectrum of $Au_{25}(SPh)_{18}^-$ (shown in Figure S4, Supporting Information), slightly shifts toward higher energy.

Different oxidation states of the same cluster also affect the core−ligand redistribution of charge. To study the effect of different oxidation states, we consider the positively charged $Au_{25}(SCH_3)_{18}^+$, shown in Figure 6b, that is also a stable charge state of the $Au_{25}(SR)_{18}$ family of clusters.[8,46] Due to the quasi-degeneracy of the 3-fold (HOMO to HOMO−2) set of orbitals in the anion, the positively charged species might be a paramagnetic triplet state. Experimental studies probing the magnetic character of the ground state reached different conclusions. In ref 50 a radical character and paramagnetic properties are reported for $Au_{25}(SR)_{18}^+$, whereas ref 46 reports the formation of diamagnetic singlet state upon oxidation of the neutral $Au_{25}(SR)_{18}^0$. We thus optimized both the singlet and the triplet states, finding that the magnetic ground state is a singlet state with the triplet being 0.32 eV higher in energy in agreement with the experiments of Antonello et al.[8,46] The LUMO orbital of the cation exhibits a p character (Figure S5, Supporting Information) but the HOMO−LUMO gap (3.12 eV) is high enough to disfavor the formation of the triplet. There are, however, two very low energy transitions in the IR (1167−1154 nm) involving excitations from the 2-fold quasi degenerate [HOMO, HOMO−1] set to the LUMO orbital. These transitions are forbidden (f = 0) and in any case outside the range of UV−vis absorption spectrum. The optical spectrum calculated for the cation $Au_{25}(SCH_3)_{18}^+$ reported in Figure 7b shows three distinct absorption bands similar to those of the anion. Due to the overall positive charge, the Au_{13} core is now almost neutral, assuming a partial charge of −0.05|e|, whereas the Au_{25} core carries a positive charge of 3.89|e|, as reported in Table 3. Figure 7b shows that, also in this case, the charge depletion from the gold core correlates with a shift of the optical spectrum toward higher energies. Irrespective of the origin of the change in the charge of the central core, i.e., change in the ligand shell composition or change in the overall

DOI: 10.1021/jp511120j
J. Phys. Chem. C 2015, 119, 10969−10980

Table 4. Natural Charge, HOMO−LUMO (H−L) Gap, and Characteristics of the Lowest Optical Excitation of the Three Ligated Au_{28} Clusters[a]

	natural charge					
	Au_{28}	S	CH	Au_{14}	H−L gap	lowest transition
$Au_{28}(SCH_3)_{20}$	4.03	−3.44	−0.60	−0.15	4.57	2.56 eV, 483.3 nm f = 0.0129 516 → 517; 0.686
$Au_{28}(SPh)_{20}$	3.90	−2.18	−1.71	−0.02	4.44	2.57 eV, 482.8 nm f = 0.0188 836 → 837; 0.662
	natural charge					
	Au_{28}	Cl		Au_{14}	H−L gap	lowest transition
$Au_{28}Cl_{20}$	7.57	−7.57		0.68	4.96	2.85 eV, 434.4 nm f = 0.0139 436 → 437; 0.676
	natural charge					
	Au_{28}	P	H		H−L gap	lowest transition
$Au_{28}(PH_3)_{13}$	−2.90	1.63	1.27		3.45	1.74 eV, 711.3 nm f = 0.0052 383 → 384; 0.634 383 → 385; 0.216

[a]The natural charge on the Au_{14} core is also reported. Natural charges are given in |e|. The HOMO−LUMO gaps (H−L) are given in eV. For the lowest excitation, the transition energy (eV and nm) from the GS, its oscillator strength, main excitations, and their amplitudes are reported.

cluster oxidation state, we find the same correlation between partial charge and shift of the optical absorption.

6. THIOLATE, CHLORINE, AND PHOSPHINE LIGATED Au_{28} CLUSTERS

Electronic properties of thiolate protected gold clusters characterized by a FCC-like ordered core differ considerably from those of their icosahedral counterpart with a similar composition.[3] Among the known nonicosahedral core gold clusters we find $Au_{28}(TBBT)_{20}$ (TBBT: *p-tert*-butylbenzenethiolate) whose crystallographic structure has been reported by Jin et al.[51] The electronic structure and optical properties of this cluster have been recently analyzed computationally in ref 52. Unlike the family of Au_{25} clusters, the 28 gold clusters have no central gold atom and their electronic structure does not follow the superatomic model because of the nonspherical geometry of the metallic core. Here we consider four different ligated Au_{28} clusters, namely $Au_{28}(SCH_3)_{20}$, $Au_{28}(SPh)_{20}$, $Au_{28}Cl_{20}$, and $Au_{28}(PH_3)_{13}$. We devised an initial geometry for the two thiolated model clusters by substituting TBBT by methanethiolate and benzenethiolate ligands in the reported crystallographic structure.[51] On the contrary, there is no crystallographic data regarding chloride and phosphine ligated Au_{28}. We discuss below the equilibrium geometry for $Au_{28}Cl_{20}$ and $Au_{28}(PH_3)_{13}$ that we obtained starting from the same core geometry of the thiolate protected cluster, the computed four equilibrium geometries are shown in Figure 8. In agreement with the results reported by Hakkinen et al.,[52] our calculations show that the optimized structure of $Au_{28}(SCH_3)_{20}$ and $Au_{28}(SPh)_{20}$ clusters can be divided in two gold subunits: a 14 gold atom core and the 14 remaining gold atoms involved in two different types of the staple motifs: two −S−Au−S− and four −S−Au−S−Au−S−. The same structural arrangement is conserved for the chloride protected cluster $Au_{28}Cl_{20}$ whereas the gold core undergoes amorphization upon geometry optimization in the case of $Au_{28}(PH_3)_{13}$.

Jin et al.[51] reported the optical absorption spectrum of $Au_{28}(TBBT)_{20}$. Three bands were found at 365, 480, and 580 nm. Comparison between the calculated spectrum of the $Au_{28}(SCH_3)_{20}$ cluster and the experimental optical spectrum allows us to investigate the nature of the electronic transitions involved. The lowest band at 580 nm (2.14 eV) in the experimental spectrum is theoretically found at 483.3 nm (2.56 eV). It corresponds to the HOMO−LUMO excitation. The second band at 480 nm (2.58 eV) appears in the computed spectrum in the range 2.84−2.94 eV (420.95−435.63 nm). It is due to excitations from the doubly quasi-degenerate HOMO−1, HOMO−2 (Figure S6, Supporting Information) to the LUMO orbital.

Analysis of the orbital composition shows a major contribution of the sp orbitals of the Au_{14} metallic core to the composition of the HOMO (55.84%), the LUMO (72.55%), and the doubly quasi-degenerate HOMO−1 and HOMO−2 orbitals (about 50%) of $Au_{28}(SCH_3)_{20}$. Therefore, the two lowest energy bands of the absorption spectrum have sp → sp character and involve orbitals localized mainly in the gold core. The third experimental band at 365 nm (3.39 eV) is found in the computed spectrum in the range of 3.55−3.74 eV (330.67−349.29 nm). It corresponds to excitations involving a large group of molecular orbitals, mainly from the d-band of the cluster. These orbitals are more delocalized and involve the gold atoms in the staple motifs. A similar analysis holds true for the three bands characterizing the absorption spectrum of the analogous $Au_{28}(SPh)_{20}$ and $Au_{28}Cl_{20}$.

Despite the difference of the geometrical arrangement of the core, the phosphine protected cluster is also characterized by an optical absorption that shows three main bands whose compositions follow a trend similar to ones discussed for the thiolate species. The first one at 711.35 nm (1.74 eV) is mainly due to an excitation from the HOMO to the doubly quasi-degenerate LUMO (Figure S7, Supporting Information, for the scheme of the energy levels). The second band around 572 nm (2.17 eV) corresponds to an ensemble of excitations involving

DOI: 10.1021/jp511120j
J. Phys. Chem. C 2015, 119, 10969−10980

the HOMO, HOMO−1 and the quasi-degenerate LUMO. Orbitals involved in the first two absorption bands have sp character, and they are mainly localized on the metallic core. At higher energy, transitions from the d band are observed.

The analysis of the natural partial charge of the gold atoms (reported in Table 4) in the two thiolated Au_{28} clusters gives a positive value of 4.03|e| in the case of the SCH_3 ligand whereas a 3.89|e| natural charge is found for the 28 gold atoms in the SPh ligand case. The trend is similar to that reported for the anion Au_{25}. It reflects a more pronounced electron acceptor character of the thiolate ligands $-SCH_3$ with respect to the benzenethiolate −SPh. The partial charge of the Au_{14} metallic core is also reported in Table 4. As in the case of Au_{25} where the global natural charge of the Au gold atoms is positive, the partial charge on the Au_{14} metallic core is negative in the thiolate species. Upon substitution of the methanethiolates by benzenethiolates, whereas the Au_{14} core becomes less negative, the overall positive charge on the Au_{28} slightly decreases. The net result is that the positions of the lowest absorption band in $Au_{28}(SCH_3)_{20}$ and $Au_{28}(SPh)_{20}$ are identical within numerical computational accuracy. In our previous studies[21] on smaller Au_{11} clusters we found that chloride ligands are similar to thiolate ligands for many aspects but they tend to accommodate more electronic charge. Here we observe a similar behavior: chlorides stabilize the same geometrical arrangement of the gold core as thiolates, but the gold core accumulates a more positive partial charge (globally 7.57 |e| with a positive charge on the Au_{14} core of 0.68 |e|). The redistribution of charge changes completely in the case of the $Au_{28}(PH_3)_{13}$, where the global natural charge of the gold atoms is negative (−2.90|e|), indicating a charge transfer from the phosphine ligands to the gold atoms as expected.

The UV−vis spectra of chloride, thiolate, and phosphine protected Au_{28} clusters are shown in Figure 9. The spectrum of the chloride capped clusters, characterized by the most positive core in the Au_{28} series, is shifted by about 0.3 eV toward higher energy with respect to the spectrum of the thiolate species. The spectra of the phosphine protected clusters is significantly red-shifted compared with the spectra of the thiolate protected clusters. When comparing the phosphine clusters with the thiolate and chloride species, we should bear in mind that we cannot disentangle the effect of a different gold/ligand charge redistribution from the effects due to the important rearrangement of the core geometry. Nonetheless, the lowest transition of $Au_{28}(SCH_3)_{20}$ cluster falls at 483.3 nm whereas it is at 711.3 nm for the phosphine ligated cluster. In summary, within the family of Au_{28} clusters, a considerable shift of the absorption region toward lower energy correlates with an increase of the electronic density on the gold core induced by changing the chemical nature of the ligand shell.

7. DISCUSSION AND CONCLUSIONS

In small gold ligated clusters, the lowest transition typically involves excitation of orbitals localized on the metallic core. Our model computations show that it is possible to tune the frequency of the lowest absorption band by tailoring the amount of electron density on the metallic core with an appropriate design of the ligand shell. The trend that we identify is that the more negative is the partial charge on the metallic core, the more the lowest absorption band is shifted to the red. We show that this correlation is verified for several small model clusters with Au_{13}, Au_{25}, and Au_{28} metallic cores passivated with different types of electron donor (phosphine ligands) and of electron acceptor ligands (thiolate and chlorine) that lead to different partial charges on the metallic core.

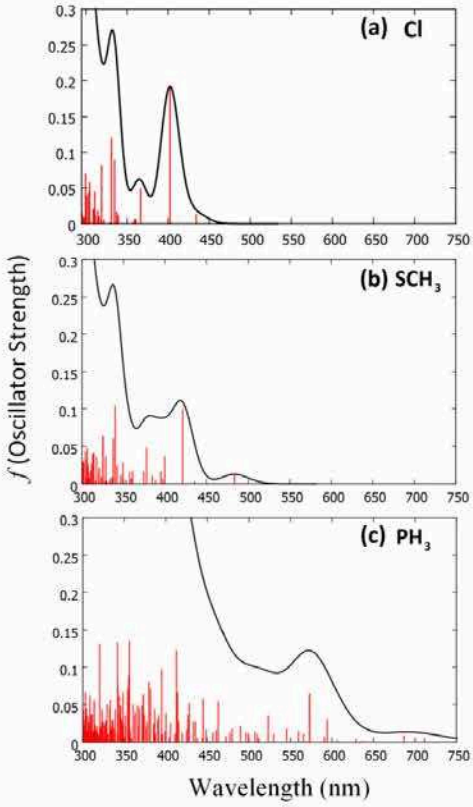

Figure 9. Computed optical absorption spectra of (a)$Au_{28}Cl_{20}$, (b) $Au_{28}(SCH_3)_{20}$, and (c) $Au_{28}(PH_3)_{13}$.

We identified several families of clusters for which one can tune the optical absorption band by controlling the partial charge of the metal core; Figure 10 summarizes our results by reporting the energy of the lowest optical transition as a function of the partial charge in the metallic core for the different families of clusters discussed in this paper. The scatter plot indicates that the correlation is rather *robust*, because it holds within families for which the modulation of the charge is realized by different strategies, but it does not necessarily hold if the comparison is made between clusters belonging to different families. This is understandable because other important characteristics, such as the core nuclearity, the coarse geometrical arrangement and the complexity of the ligand molecules, vary between families and influence the energy range of the optical absorption. A notable exception is represented by the Au_{25} clusters that correlate very well with the Au_{13} model clusters $[Au_{13}(PH_3)_{10}Cl_2]^{3+}$ and $[Au_{13}(PH_3)_8Cl_4]^+$. Within each cluster family, the correlation is found to be independent of the orbital composition of the lowest transition and on the details of the geometry of the metallic core. For the clusters that have been experimentally characterized (the Au_{13}

DOI: 10.1021/jp511120j
J. Phys. Chem. C 2015, 119, 10969−10980

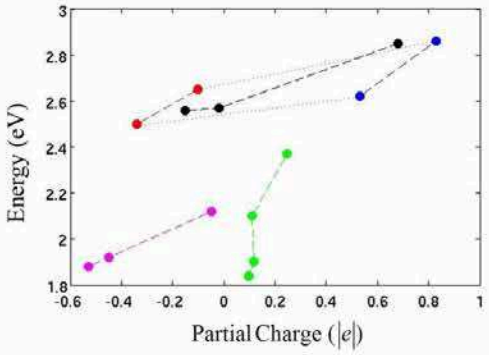

Figure 10. Computed energy of the lowest optical transition as a function of the partial charge on the gold core for different families of clusters. Blue and red points refer to the phosphine−chlorine capped Au_{13} clusters of section 3, green points correspond to the family of neutral Au_{13} clusters discussed in section 4, points in magenta represent the Au_{25} clusters of section 5 (partial charge is for the Au_{13} inner core), and the black points refer to the Au_{28} clusters of section 6 (partial charge is for the Au_{14} inner core; the phosphine protected cluster is not included).

phosphine−Cl ligand shells, thiolate capped Au_{25} and Au_{28}), our computations are in good agreement with the measured absorption spectra.

In summary, we demonstrated that a fine-tuning of the energy of the absorption band of gold clusters can be engineered by considering charge redistribution effects between ligand shell and metallic core. Particularly promising are mixed shells of donor and acceptor ligands, and the possibility offered by the control of the spatial organization of the ligand shell, as was recently reported for Janus nanoparticles[36−39] and stripes.[41−43]

■ ASSOCIATED CONTENT

Supporting Information

Density of states plots for the $[Au_{13}(PH_3)_{10}Cl_2]^{3+}$ and $[Au_{13}(PH_3)_8Cl_4]^{+}$ clusters. Molecular orbital energy diagrams and isocontours of the frontier molecular orbitals of the clusters $[Au_{13}(dppe)_5Cl_2]^{3+}$, $[Au_{25}(SCH_3)_{18}]^{-}$, $[Au_{25}(SCH_3)_{18}]^{+}$, $Au_{28}(SCH_3)_{20}$ and $Au_{28}(PH_3)_{13}$. Comparison of the optical absorption spectra of $[Au_{25}(SCH_3)_{18}]^{-}$ and $[Au_{25}(SPh)_{18}]^{-}$. This material is available free of charge via the Internet at http://pubs.acs.org.

■ AUTHOR INFORMATION

Notes

The authors declare no competing financial interest.

■ ACKNOWLEDGMENTS

F.R., B.F., V.S., and G.L. gratefully acknowledge support of the Actions de Recherches Concertées NANOFORCE (ULg) and of the EC COST action HINT. G.L. acknowledges the support of the EC Ph.D. School IDS-FunMAT. F.R. acknowledges the support of Fonds National de la Recherche Scientifique (Belgium).

■ REFERENCES

(1) Mingos, D. M. Structural and Bonding Issues in Clusters and Nano-Clusters. In *Gold Clusters, Colloids and Nanoparticles II*; Mingos, D. M. P., Ed.; Springer International Publishing: Berlin, 2014; Vol. *162*, pp 1−65.

(2) Konishi, K. Phosphine-Coordinated Pure-Gold Clusters: Diverse Geometrical Structures and Unique Optical Properties/Responses. In *Gold Clusters, Colloids and Nanoparticles I*; Mingos, D. M. P., Ed.; Springer International Publishing: Berlin, 2014; Vol. *161*, pp 49−86.

(3) Chevrier, D. M.; Zeng, C.; Jin, R.; Chatt, A.; Zhang, P. Role of Au_4 Units on the Electronic and Bonding Properties of $Au_{28}(Sr)_{20}$ Nanoclusters from X-ray Spectroscopy. *J. Phys. Chem. C* **2014**, *119*, 1217−1223.

(4) Shichibu, Y.; Kamei, Y.; Konishi, K. Unique [Core+Two] Structure and Optical Property of a Dodeca-Ligated Undecagold Cluster: Critical Contribution of the Exo Gold Atoms to the Electronic Structure. *Chem. Commun.* **2012**, *48*, 7559−7561.

(5) Shibu, E. S.; Muhammed, M. A. H.; Tsukuda, T.; Pradeep, T. Ligand Exchange of $Au_{25}SG_{18}$ Leading to Functionalized Gold Clusters: Spectroscopy, Kinetics, and Luminescence. *J. Phys. Chem. C* **2008**, *112*, 12168−12176.

(6) Shichibu, Y.; Suzuki, K.; Konishi, K. Facile Synthesis and Optical Properties of Magic-Number Au_{13} Clusters. *Nanoscale* **2012**, *4*, 4125−4129.

(7) Wu, Z.; Jin, R. On the Ligand's Role in the Fluorescence of Gold Nanoclusters. *Nano Lett.* **2010**, *10*, 2568−2573.

(8) Venzo, A.; Antonello, S.; Gascón, J. A.; Guryanov, I.; Leapman, R. D.; Perera, N. V.; Sousa, A.; Zamuner, M.; Zanella, A.; Maran, F. Effect of the Charge State (z = −1, 0, +1) on the Nuclear Magnetic Resonance of Monodisperse $Au_{25}[S(CH_2)2Ph]_{18}^{z}$ Clusters. *Anal. Chem.* **2011**, *83*, 6355−6362.

(9) Liu, Z.; Zhu, M.; Meng, X.; Xu, G.; Jin, R. Electron Transfer between $[Au_{25}(SC_2H_4Ph)_{18}]^{-}TOA^{+}$ and Oxoammonium Cations. *J. Phys. Chem. Lett.* **2011**, *2*, 2104−2109.

(10) Tlahuice-Flores, A.; Whetten, R. L.; Jose-Yacaman, M. Ligand Effects on the Structure and the Electronic Optical Properties of Anionic $Au_{25}(Sr)_{18}$ Clusters. *J. Phys. Chem. C* **2013**, *117*, 20867−20875.

(11) Foster, J. P.; Weinhold, F. Natural Hybrid Orbitals. *J. Am. Chem. Soc.* **1980**, *102*, 7211−7218.

(12) Reed, A. E.; Curtiss, L. A.; Weinhold, F. Intermolecular Interactions from a Natural Bond Orbital, Donor-Acceptor Viewpoint. *Chem. Rev.* **1988**, *88*, 899−926.

(13) Zhu, M.; Aikens, C. M.; Hollander, F. J.; Schatz, G. C.; Jin, R. Correlating the Crystal Structure of a Thiol-Protected Au_{25} Cluster and Optical Properties. *J. Am. Chem. Soc.* **2008**, *130*, 5883−5885.

(14) Heaven, M. W.; Dass, A.; White, P. S.; Holt, K. M.; Murray, R. W. Crystal Structure of the Gold Nanoparticle $[N(C_8H_{17})_4]$-$[Au_{25}(SCH_2CH_2Ph)_{18}]$. *J. Am. Chem. Soc.* **2008**, *130*, 3754−3755.

(15) Hakkinen, H. Atomic and Electronic Structure of Gold Clusters: Understanding Flakes, Cages and Superatoms from Simple Concepts. *Chem. Soc. Rev.* **2008**, *37*, 1847−1859.

(16) Walter, M.; Akola, J.; Lopez-Acevedo, O.; Jadzinsky, P. D.; Calero, G.; Ackerson, C. J.; Whetten, R. L.; Grönbeck, H.; Häkkinen, H. A Unified View of Ligand-Protected Gold Clusters as Superatom Complexes. *Proc. Natl. Acad. Sci. U. S. A.* **2008**, *105*, 9157−9162.

(17) Frisch, M. J.; Trucks, G. W.; Schlegel, H. B.; Scuseria, G. E.; Robb, M. A.; Cheeseman, J. R.; Scalmani, G.; Barone, V.; Mennucci, B.; Petersson, G. A.; et al. *Gaussian 09*, Revision D01; Gaussian, Inc.: Wallingford, CT, 2009.

(18) Yanai, T.; Tew, D. P.; Handy, N. C. A New Hybrid Exchange−Correlation Functional Using the Coulomb-Attenuating Method (CAM-B3LYP). *Chem. Phys. Lett.* **2004**, *393*, 51−57.

(19) Hay, P. J.; Wadt, W. R. Ab Initio Effective Core Potentials for Molecular Calculations. Potentials for the Transition Metal Atoms Sc to Hg. *J. Chem. Phys.* **1985**, *82*, 270−283.

(20) Hay, P. J.; Wadt, W. R. Ab Initio Effective Core Potentials for Molecular Calculations. Potentials for K to Au Including the Outermost Core Orbitals. *J. Chem. Phys.* **1985**, *82*, 299−310.

DOI: 10.1021/jp511120j
J. Phys. Chem. C 2015, 119, 10969−10980

(21) Dufour, F.; Fresch, B.; Durupthy, O.; Chaneac, C.; Remacle, F. Ligand and Solvation Effects on the Structural and Electronic Properties of Small Gold Clusters. *J. Phys. Chem. C* **2014**, *118*, 4362−4376.
(22) Gorelsky, S. I. *Aomix: Program for Molecular Orbital Analysis; Version 6.X*, University of Ottawa, 2013.
(23) Gorelsky, S. I.; Lever, A. B. P. Electronic Structure and Spectra of Ruthenium Diimine Complexes by Density Functional Theory and Indo/S. Comparison of the Two Methods. *J. Org. Chem.* **2001**, *635*, 187−196.
(24) Shichibu, Y.; Konishi, K. Hcl-Induced Nuclearity Convergence in Diphosphine-Protected Ultrasmall Gold Clusters: A Novel Synthetic Route to "Magic-Number" Au_{13} Clusters. *Small* **2010**, *6*, 1216−1220.
(25) Copley, R. C. B.; Mingos, D. M. P. Synthesis and Characterization of the Centred Icosahedral Cluster Series $[Au_xMib_4C_{14}(PMePh_2)8][C_2B_9H_{12}]$, Where Mib= Au, Ag or Cu. *J. Chem. Soc., Dalton Trans.* **1996**, 491−500.
(26) Nobusada, K.; Iwasa, T. Oligomeric Gold Clusters with Vertex-Sharing Bi- and Triicosahedral Structures. *J. Phys. Chem. C* **2007**, *111*, 14279−14282.
(27) Shichibu, Y.; Negishi, Y.; Watanabe, T.; Chaki, N. K.; Kawaguchi, H.; Tsukuda, T. Biicosahedral Gold Clusters $[Au_{25}(PPh_3)_{10}(SC_nH_{2n+1})_5C_{12}]^{2+}$ (n = 2−18): A Stepping Stone to Cluster-Assembled Materials. *J. Phys. Chem. C* **2007**, *111*, 7845−7847.
(28) Nishigaki, J.-i.; Yamazoe, S.; Kohara, S.; Fujiwara, A.; Kurashige, W.; Negishi, Y.; Tsukuda, T.; Twisted Bi-Icosahedral, A. Au_{25} Cluster Enclosed by Bulky Arenethiolates. *Chem. Commun.* **2014**, *50*, 839−841.
(29) Akola, J.; Walter, M.; Whetten, R. L.; Häkkinen, H.; Grönbeck, H. On the Structure of Thiolate-Protected Au_{25}. *J. Am. Chem. Soc.* **2008**, *130*, 3756−3757.
(30) Lopez-Acevedo, O.; Tsunoyama, H.; Tsukuda, T.; Häkkinen, H.; Aikens, C. M. Chirality and Electronic Structure of the Thiolate-Protected Au_{38} Nanocluster. *J. Am. Chem. Soc.* **2010**, *132*, 8210−8218.
(31) Qian, H.; Eckenhoff, W. T.; Zhu, Y.; Pintauer, T.; Jin, R. Total Structure Determination of Thiolate-Protected Au_{38} Nanoparticles. *J. Am. Chem. Soc.* **2010**, *132*, 8280−8281.
(32) Malola, S.; Lehtovaara, L.; Knoppe, S.; Hu, K.-J.; Palmer, R. E.; Bürgi, T.; Häkkinen, H. $Au_{40}(Sr)_{24}$ Cluster as a Chiral Dimer of 8-Electron Superatoms: Structure and Optical Properties. *J. Am. Chem. Soc.* **2012**, *134*, 19560−19563.
(33) Qian, H.; Zhu, Y.; Jin, R. Isolation of Ubiquitous $Au_{40}(Sr)_{24}$ Clusters from the 8 kDa Gold Clusters. *J. Am. Chem. Soc.* **2010**, *132*, 4583−4585.
(34) Fresch, B.; Hanozin, E.; Dufour, F.; Remacle, F. Interplay of Structural and Electronic Stabilizing Factors in Neutral and Cationic Phosphine Protected Au_{13} Clusters. *Eur. Phys. J. D* **2012**, *66*, 1−9.
(35) Aikens, C. M. Origin of Discrete Optical Absorption Spectra of $M_{25}(Sh)_{18}^-$ Nanoparticles (M = Au, Ag). *J. Phys. Chem. C* **2008**, *112*, 19797−19800.
(36) Kim, H.; Carney, R. P.; Reguera, J.; Ong, Q. K.; Liu, X.; Stellacci, F. Synthesis and Characterization of Janus Gold Nanoparticles. *Adv. Mater.* **2012**, *24*, 3857−3863.
(37) Lattuada, M.; Hatton, T. A. Synthesis, Properties and Applications of Janus Nanoparticles. *Nano Today* **2011**, *6*, 286−308.
(38) Vilain, C.; Goettmann, F.; Moores, A.; Le Floch, P.; Sanchez, C. Study of Metal Nanoparticles Stabilised by Mixed Ligand Shell: A Striking Blue Shift of the Surface-Plasmon Band Evidencing the Formation of Janus Nanoparticles. *J. Mater. Chem.* **2007**, *17*, 3509−3514.
(39) Wang, B.; Li, B.; Zhao, B.; Li, C. Y. Amphiphilic Janus Gold Nanoparticles Via Combining "Solid-State Grafting-to" and "Grafting-from" Methods. *J. Am. Chem. Soc.* **2008**, *130*, 11594−11595.
(40) Fresch, B.; Remacle, F. Tuning the Properties of Pd Nanoclusters by Ligand Coatings: Electronic Structure Computations on Phosphine, Thiol, and Mixed Phosphine−Thiol Ligand Shells. *J. Phys. Chem. C* **2014**, *118*, 9790−9800.
(41) Cesbron, Y.; Shaw, C. P.; Birchall, J. P.; Free, P.; Lévy, R. Stripy Nanoparticles Revisited. *Small* **2012**, *8*, 3714−3719.
(42) Liu, X.; Yu, M.; Kim, H.; Mameli, M.; Stellacci, F. Determination of Monolayer-Protected Gold Nanoparticle Ligand−Shell Morphology Using NMR. *Nat. Commun.* **2012**, *3*, 1182.
(43) Carney, R. P.; DeVries, G. A.; Dubois, C.; Kim, H.; Kim, J. Y.; Singh, C.; Ghorai, P. K.; Tracy, J. B.; Stiles, R. L.; Murray, R. W.; et al. Size Limitations for the Formation of Ordered Striped Nanoparticles. *J. Am. Chem. Soc.* **2007**, *130*, 798−799.
(44) Aikens, C. M. Geometric and Electronic Structure of $Au_{25}(SPh_x)_{18}^-$ (X = H, F, Cl, Br, CH_3, and OCH_3). *J. Phys. Chem. Lett.* **2010**, *1*, 2594−2599.
(45) Aikens, C. M. Effects of Core Distances, Solvent, Ligand, and Level of Theory on the Tddft Optical Absorption Spectrum of the Thiolate-Protected Au_{25} Nanoparticle. *J. Phys. Chem. A* **2009**, *113*, 10811−10817.
(46) Antonello, S.; Perera, N. V.; Ruzzi, M.; Gascón, J. A.; Maran, F. Interplay of Charge State, Lability, and Magnetism in the Molecule-Like $Au_{25}(Sr)_{18}$ Cluster. *J. Am. Chem. Soc.* **2013**, *135*, 15585−15594.
(47) Negishi, Y.; Chaki, N. K.; Shichibu, Y.; Whetten, R. L.; Tsukuda, T. Origin of Magic Stability of Thiolated Gold Clusters: A Case Study on $Au_{25}(SC_6H_{13})_{18}$. *J. Am. Chem. Soc.* **2007**, *129*, 11322−11323.
(48) Shichibu, Y.; Negishi, Y.; Tsunoyama, H.; Kanehara, M.; Teranishi, T.; Tsukuda, T. Extremely High Stability of Glutathionate-Protected Au_{25} Clusters against Core Etching. *Small* **2007**, *3*, 835−839.
(49) Fresch, B.; Boyen, H. G.; Remacle, F. Magnetostructural Effects in Ligand Stabilized Pd_{13} Clusters: A Density Functional Theory Study. *Nanoscale* **2012**, *4*, 4138−4147.
(50) Akbari-Sharbaf, A.; Hesari, M.; Workentin, M. S.; Fanchini, G. Electron Paramagnetic Resonance in Positively Charged Au_{25} Molecular Nanoclusters. *J. Chem. Phys.* **2013**, *138*, 024305.
(51) Zeng, C.; Li, T.; Das, A.; Rosi, N. L.; Jin, R. Chiral Structure of Thiolate-Protected 28-Gold-Atom Nanocluster Determined by X-ray Crystallography. *J. Am. Chem. Soc.* **2013**, *135*, 10011−10013.
(52) Knoppe, S.; Malola, S.; Lehtovaara, L.; Bürgi, T.; Häkkinen, H. Electronic Structure and Optical Properties of the Thiolate-Protected $Au_{28}(SMe)_{20}$ Cluster. *J. Phys. Chem. A* **2013**, *117*, 10526−10533.

DOI: 10.1021/jp511120j
J. Phys. Chem. C 2015, 119, 10969−10980

3.2 References

1. Kelly, K.L., et al., *The Optical Properties of Metal Nanoparticles: The Influence of Size, Shape, and Dielectric Environment.* The Journal of Physical Chemistry B, 2003. **107**(3): p. 668-677.
2. Aikens, C.M., *Origin of Discrete Optical Absorption Spectra of M25(SH)18− Nanoparticles (M = Au, Ag).* The Journal of Physical Chemistry C, 2008. **112**(50): p. 19797-19800.
3. Qian, H., et al., *Quantum Sized Gold Nanoclusters with Atomic Precision.* Accounts of Chemical Research, 2012. **45**(9): p. 1470-1479.
4. Jin, R., *Quantum sized, thiolate-protected gold nanoclusters.* Nanoscale, 2010. **2**(3): p. 343-362.
5. Zhu, M., et al., *Correlating the Crystal Structure of A Thiol-Protected Au25 Cluster and Optical Properties.* Journal of the American Chemical Society, 2008. **130**(18): p. 5883-5885.
6. Knoppe, S., et al., *Electronic Structure and Optical Properties of the Thiolate-Protected Au28(SMe)20 Cluster.* The Journal of Physical Chemistry A, 2013. **117**(40): p. 10526-10533.
7. Tsunoyama, H., et al., *Formation of Alkanethiolate-Protected Gold Clusters with Unprecedented Core Sizes in the Thiolation of Polymer-Stabilized Gold Clusters.* The Journal of Physical Chemistry C, 2007. **111**(11): p. 4153-4158.
8. Pei, Y., Y. Gao, and X.C. Zeng, *Structural Prediction of Thiolate-Protected Au38: A Face-Fused Bi-icosahedral Au Core.* Journal of the American Chemical Society, 2008. **130**(25): p. 7830-7832.
9. Häkkinen, H., M. Walter, and H. Grönbeck, *Divide and Protect: Capping Gold Nanoclusters with Molecular Gold−Thiolate Rings.* The Journal of Physical Chemistry B, 2006. **110**(20): p. 9927-9931.
10. Pichugina, D.A., N.E. Kuz'menko, and A.F. Shestakov, *Ligand-protected gold clusters: the structure, synthesis and applications.* Russian Chemical Reviews, 2015. **84**(11): p. 1114.
11. Shichibu, Y., K. Suzuki, and K. Konishi, *Facile synthesis and optical properties of magic-number Au13 clusters.* Nanoscale, 2012. **4**(14): p. 4125-4129.
12. Heaven, M.W., et al., *Crystal Structure of the Gold Nanoparticle [N(C8H17)4][Au25(SCH2CH2Ph)18].* Journal of the American Chemical Society, 2008. **130**(12): p. 3754-3755.
13. Aikens, C.M., *Effects of Core Distances, Solvent, Ligand, and Level of Theory on the TDDFT Optical Absorption Spectrum of the Thiolate-Protected Au25 Nanoparticle.* The Journal of Physical Chemistry A, 2009. **113**(40): p. 10811-10817.
14. Dufour, F., et al., *Ligand and Solvation Effects on the Structural and Electronic Properties of Small Gold Clusters.* The Journal of Physical Chemistry C, 2014. **118**(8): p. 4362-4376.
15. Wang, B., et al., *Amphiphilic Janus Gold Nanoparticles via Combining "Solid-State Grafting-to" and "Grafting-from" Methods.* Journal of the American Chemical Society, 2008. **130**(35): p. 11594-11595.
16. Vilain, C., et al., *Study of metal nanoparticles stabilised by mixed ligand shell: a striking blue shift of the surface-plasmon band evidencing the formation of Janus nanoparticles.* Journal of Materials Chemistry, 2007. **17**(33): p. 3509-3514.
17. Kim, H., et al., *Synthesis and Characterization of Janus Gold Nanoparticles.* Advanced Materials, 2012. **24**(28): p. 3857-3863.
18. Lattuada, M. and T.A. Hatton, *Synthesis, properties and applications of Janus nanoparticles.* Nano Today, 2011. **6**(3): p. 286-308.
19. Carney, R.P., et al., *Size Limitations for the Formation of Ordered Striped Nanoparticles.* Journal of the American Chemical Society, 2008. **130**(3): p. 798-799.
20. Cesbron, Y., et al., *Stripy Nanoparticles Revisited.* Small, 2012. **8**(24): p. 3714-3719.

Chapter IV. Geometry , electronic structure and optical properties of the $[Au_{25}(SR)_{18}]^-$ (R = CH_3, TP, SPhPh, SPhPhPh, 4ATP) and the Janus $[Au_{25}(SR')_x(SR'')_{18-x}]^-$ (R' = Ph and R'' = 4ATP, $CH_3(CH_2)_4COOH$) clusters

Introduction

Tuning the optical properties of gold nanocluster is a major challenge due to the complexity of the relation between their structure and physicochemical properties. One of the most important questions to answer is how the nuclearity and the structure of the ligand shell affect the optical absorption profile since different core nuclearities show absorption peaks at different positions.[1-6]. We reported in chapter III and in ref [7] on the effect of the ligand layer on the optical properties of GNC with different sizes and nuclearity of metallic cores.. This chapter is specifically devoted to the effect of the ligand shell on the properties of anionic thiolate protected GNC's with the very stable icosahedral metallic core Au_{25}. We also explore here the effects of a mixed ligand shell on the GNC's properties. The effect of the polarity of the ligand on the optical absorption profile and the distortion suffered by the Au_{25} metallic core have previously been investigated in ref. [8]. Additionally, several studies show that the fluorescence of some protected GNCs can be improved by modifying the ligand shell. [9, 10]

Because the lowest absorption band of the UV – Vis spectrum of GNC's is in most cases due to excitations of MO's localized in the metallic core, one might a priori expect that the structure of the ligands absorbed on the gold surface will not have a significant effect on the optical absorption profile.[11, 12] However, GNC synthesis studies have reported that the gold core nuclearity does not always stay unchanged upon substitution of the ligand shell. [13-16] For instance, Jin *et al.* have shown that the size of GNCs are highly sensitive to the methyl substituent position (*p*, *m* or *o* - isomer) in a methylbenzene thiolates coated GNCs. They found the Au_{130}, Au_{104} and Au_{40} core nuclearities for the *o*, *m* and *p* – methylbenzene thiol isomer protected GNC, respectively. Size decreases in line with the increasing hindrance of the $–CH_3$ group to the gold interface which can be used to obtain GNCs with desired size. [17] Moreover, Pradeep and co – workers showed that it is possible to enhance the solid – state emission in the $Au_{25}(SR)_{18}$ (SR being a thiolate ligand) cluster by substituting glutathione thiolate by 3 – mercapto – 2 – butanol while keeping the core size.[18]

Mixing two kinds of ligands in the protecting ligand shell could represent a good alternative to tune the cluster surface and optical properties. Additionally, recent studies have shown that ligand exchange reactions could lead to two different ligand protected GNCs with optical properties different from their monoligand capped analogues. [7, 8, 18-21] Therefore, it is important to investigate the way molecules assembled when absorbed on the metal core.

Three different subnanometer – ordered ligand domains have been observed in two different – ligand coated GNCs: 'Janus', where the ligands are spatially segregated on the gold surface,[22-26] 'stripe' GNCs,[27, 28] where ordered rings layers of alternating thiolates are formed and those GNCs where the ligands are randomly organized. The size of the cluster and the length of the ligand have been found to be very important parameters on the formation of these ligand ordered domains.[27, 28] For instance, Stellacci and co – workers reported the formation of ordered – ligand domains in two different thiolate protected gold particles by scanning tunneling and transmission electron microscopy.[29] Moreover, they showed that the ligands form separated phases with 5 Å size and that the dimension of this phase can be controlled by ligand composition and the metal core size.[30]

Here, on the basis of computational studies carried out at the DFT level, we compare five different mono – thiolate (SR) protected anionic Au_{25} clusters. The thiolate ligands differ by the nature of the R group. The effect of the ligand shell on the equilibrium geometry, electronic structure and UV – Vis spectrum is analyzed as well as the effect of two different thiolate ligands protecting the metal core at different ligand ratios. Comparison between the mono– and bi – ligand protected anion Au_{25} has been performed.

Our computational study shows that the exchange of different thiolate does not induce a significant distortion on the metal core. This is expected since the Au_{25} core in its icosahedral geometry is very stable and exhibits a superatomic electronic structure character.[7, 31, 32] The representative molecular orbital diagram of $[Au_{25}(SCH_3)_{18}]^-$ are shown in figure 7 in reference [7] of chapter III. Also, the molecular orbital isocontour of the $[Au_{25}(SPhPh)_{18}]^-$ cluster exhibiting the *p* – SAMO of the 3 – fold quasidegenerate HOMO and the *d* – SAMO of the 2 – and 3 – fold quasidegenerate LUMO and LUMO + 1 character, respectively is shown in figure 7 of this chapter. Several studies show that the Au_{13}^{+5} cluster represents a building block for larger GNCs [1, 5, 13, 33-36] including all the clusters studied in this chapter. The Au_{13}^{+5} cluster represents a super atomic unit;[31] its characteristic icosahedral structure and its 8 valence electrons has been used to understand the stability of the Au_{25} core.[37]

On the other hand, the partial charge distribution is also affected by the exchange of ligands and, since the electronic interactions between the icosahedral Au_{13} and the staples influences the orbital energies [8, 12, 38] we confirm here that the charge redistribution between the gold core and the ligand shell plays an important role on the features of the UV – Vis spectrum.

We corroborate that the correlation discussed in chapter III [7] between the partial charge on the metal core and the shift of the absorption spectrum of the clusters is followed by the monoligand capped GNCs studied: the more the core is negatively charged, the more the lowest optical transition is shifted to the red.

Additionally, we report in this chapter on two different thiolate protected anion Au_{25} clusters: the $[Au_{25}(TP)_x(S(CH_2)_5COOH)_{18-x}]^-$ and the $[Au_{25}(4ATP)_x(TP)_{18-x}]^-$ clusters, both in Janus configuration, (where TP means thiophenol and 4ATP means 4 – aminothiophenol). The choice of TP/4ATP mixed ligand

GNC was based on the fact that in chapter V we report the synthesis and characterization of the $[Au_{25}(4ATP)_x(TP)_{18-x}]^-$ cluster by adapting the method used in reference [3] and we aim to compare the experimental and computed UV – Vis spectra. The $S(CH_2)_5COOH$ ligand was also explored in the $[Au_{25}(TP)_x(S(CH_2)_5COOH)_{18-x}]^-$ set of clusters since we want to evaluate if having a more flexible and longer ligand than an aromatic TP or 4ATP will have an effect on the optical properties. Unfortunately, we were not able to obtain an equilibrium structure for the monoligand $[Au_{25}(S(CH_2)_5COOH)_{18}]^-$.

Our results show for the different TP/$S(CH_2)_5COOH$ and TP/4ATP ligand ratio investigated that the metal core does not suffer a significant distortion. In some cases, only a barely detectable expansion of the staple motif can be found. Our computations on the two sets of Janus $[Au_{25}(SR')_x(SR'')_{18-x}]^-$ clusters confirm the resemblance of their electronic structure to that of the bare Au_{13}^{5+} which, constitutes a superatomic unit. [31] Both sets of Janus $[Au_{25}(SR')_x(SR'')_{18-x}]^-$ clusters show a very close structure to the experimentally reported for the $Au_{25}(SCH_2CH_2Ph)_{18}^-$ [34]

Finally, our computations on both two – ligand protected GNCs ($[Au_{25}(TP)_x(S(CH_2)_5COOH)_{18-x}]^-$ and the $[Au_{25}(4ATP)_x(TP)_{18-x}]^-$) show that the position of the lowest energy bands do not vary linearly with the ligand ratio. No significant modification of the UV – Vis spectrum of the $[Au_{25}(TP)_x(S(CH_2)_5COOH)_{18-x}]^-$ was detected when comparing with the monoligand TP protected analogue. However, a blue shift is observed of the $[Au_{25}(4ATP)_x(TP)_{18-x}]^-$ with the less negative Au_{13} partial charge.

4.1 The monoligand protected $[Au_{25}(SR)_{18}]^-$ cluster

4.1.1 Structure and partial charge distribution of the monoligand protected $[Au_{25}(SR)_{18}]^-$

As a first step, the equilibrium geometries of the five different thiolate protected Au_{25} cluster have been determined. Two of them, the $[Au_{25}(SCH_3)_{18}]^-$ and the $[Au_{25}(TP)_{18}]^-$, were already investigating in chapter III and are used here for comparison. [7] The ligands used to protect the metal cores are: methylthiol (SCH_3), 4 – aminothiophenol (4ATP), phenylthiol (TP), biphenyl-4-thiol (SPhPh) and 1, 1′, 4′, 1″-terphenyl – 4 – thiol (SPhPhPh).

The $Au_{25}(SCH_2CH_2Ph)_{18}$ cluster structure has been resolved by X – ray crystallography and was used as starting point for our calculations by modifying the ligand shell. [1, 34]

Computations have been performed at the DFT / CAM – B3LYP level. The LANL2MB relativistic corrected pseudopotentials and basis sets [39, 40] for the gold atoms and the 6 – 31G(d) Gaussian basis set for the different ligands. For more details about the computational methodology consult the *computational details* section in chapter II.

The computed equilibrium structures of the bare Au_{25} and the five $[Au_{25}(SR)_{18}]^-$ clusters are displayed in figure 4. As found in other studies,[5, 19, 31, 38, 41] the *divide and protect* motif proposed by Häkkinen *et al*. [42] is followed; all of the clusters are composed of a small icosahedral core Au_{13} protected

by six – SR – Au – SR – Au – SR – *staple* oligomers. Figure 2 shows some of the staples in the $[Au_{25}(SPhPhPh)_{18}]^-$ cluster. In most of the cases, two out of three ligands in each staple are arranged in eclipsed orientation while the third one lies on the opposite side as can be seen in figure 2c.

We build a histogram of the Au – Au distances to get insight about how the gold atoms rearrange after ligand exchange. Figure 3 shows the histograms of the distances Au – Au for all the $[Au_{25}(SR)_{18}]^-$ computed structures, as well as for the icosahedral bare core shown in figure 1a. We can see that the exchange of thiolates does not induce a significant modification on the histogram of Au – Au distances. The formation of the '– SR – Au – SR – Au – SR –' staple is reflected -by the appearance of a new 'Au – Au distance' in the 9.8 – 11 Å range, which is absent from the histogram of the distances of the bare cluster (fig 3a).

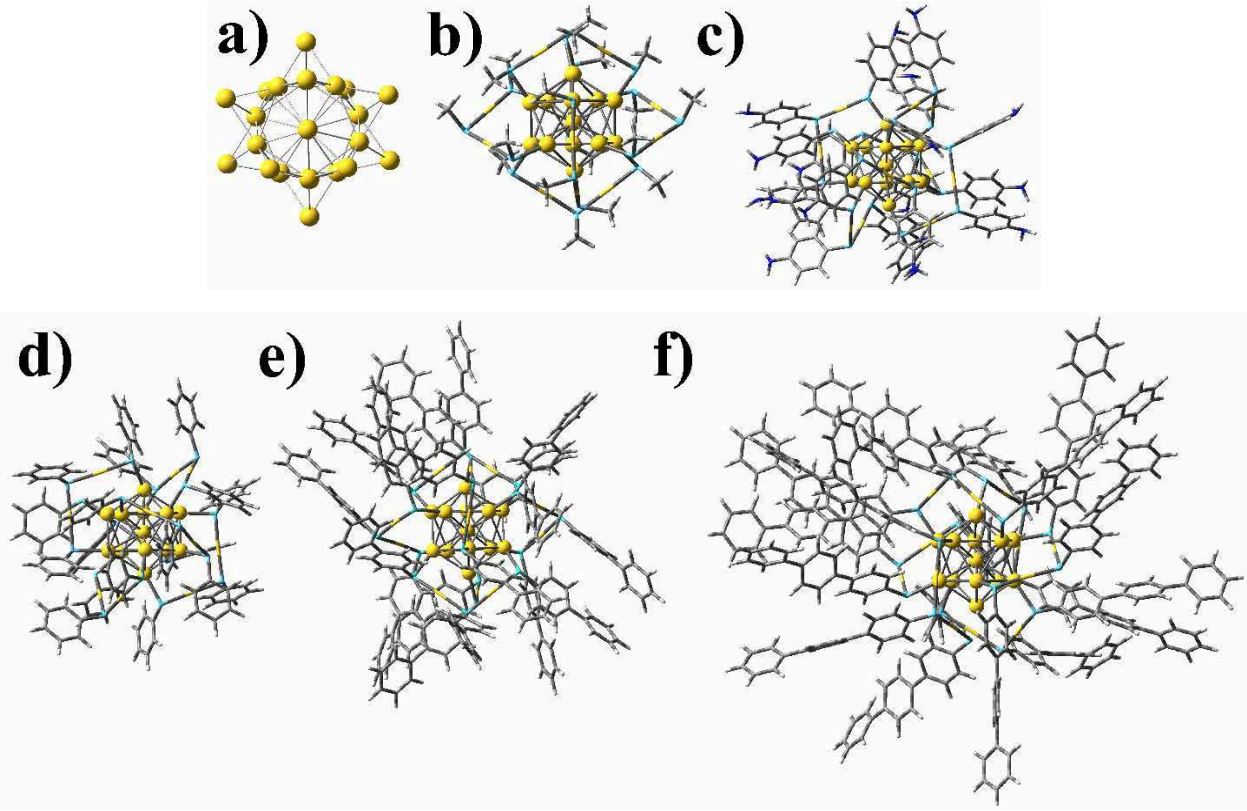

***Figure 1**. Computed equilibrium geometries of the bare Au_{25} core (a) and the $[Au_{25}(SR)_{18}]^-$ set of clusters: (b) $[Au_{25}(SCH_3)_{18}]^-$, (c) $[Au_{25}(4ATP)_{18}]^-$, (d) $[Au_{25}(TP)_{18}]^-$, (e) $[Au_{25}(SPhPh)_{18}]^-$ and (f) $[Au_{25}(SPhPhPh)_{18}]^-$. The Au atoms are shown in yellow, the C atoms in grey, the dark blue junctions stand for N, S is represented in navy blue and H is in white.*

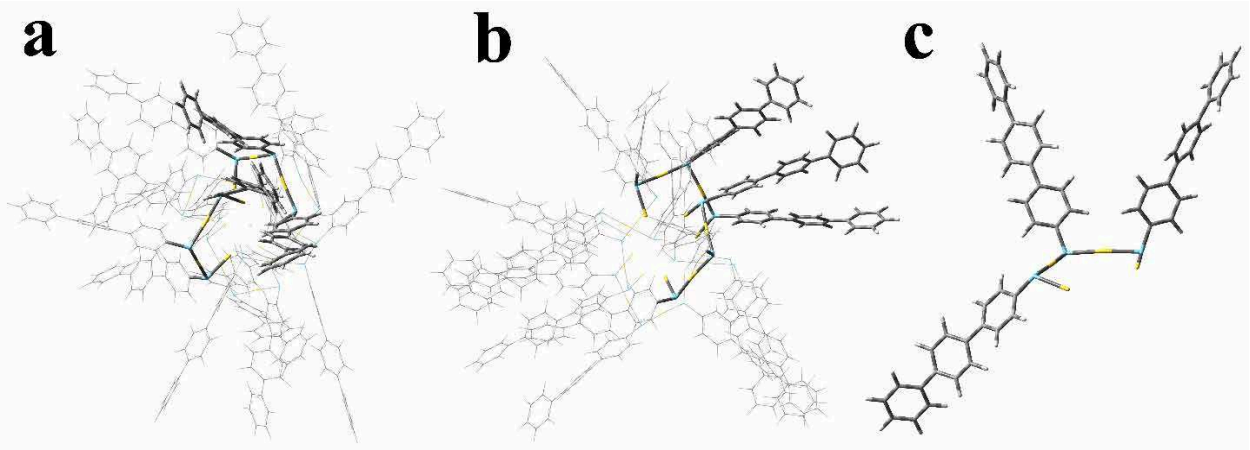

***Figure 2**. Computed equilibrium geometries of the bare Au_{25} core (a) and the $[Au_{25}(SPhPhPh)_{18}]^-$ highlighting three of the ligand interactions; panel a) the upside view, panel b) the side view and panel c) the staple.*

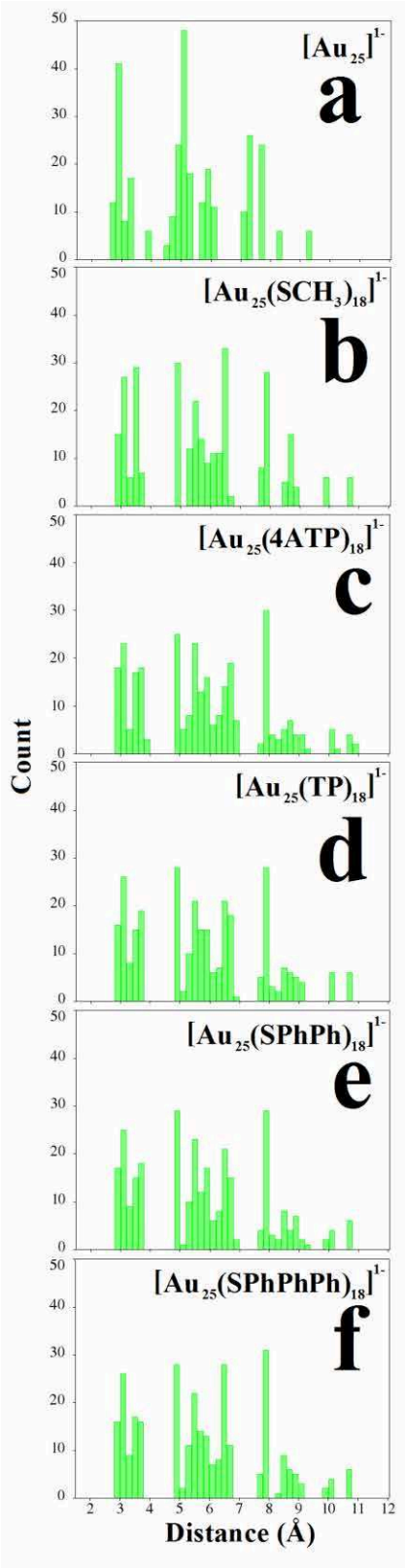

***Figure 3**. Histogram of the Au – Au distances of the bare Au_{25} core (a) and the $[Au_{25}(SR)_{18}]^-$ clusters: (b) $[Au_{25}(SCH_3)_{18}]^-$, (c) $[Au_{25}(4ATP)_{18}]^-$, (d) $[Au_{25}(TP)_{18}]^-$, (e) $[Au_{25}(SPhPh)_{18}]^-$ and (f) $[Au_{25}(SPhPhPh)_{18}]$.*

Counting the number of Au atoms within successive spheres centered on the central gold atom whose diameter differ by 1 Å allows us to build the histogram of radial distances of Au atoms for the $[Au_{25}(SR)_{18}]^-$ equilibrium structures. Figure 4 shows the histogram of radial distances of Au atoms of all the $[Au_{25}(SR)_{18}]^-$. The first and second blue bars represent the central Au and the twelve Au atoms, respectively, forming the icosahedral Au_{13} core. The last and third bar stands for the Au atoms in the staple. Again, as found in the Au – Au distance histogram in figure 3, comparison of figures 4a (bare Au_{25}) with 4b – f shows that protecting the core with thiolates leads to an expansion of the bare Au_{25} due to the formation of the staple motifs.

Figure 4 shows that the staple motif starts to deform when the phenyl group is used. A slight compression of the Au_{25} cluster is detected in figure 4 when SPhPhPh is protecting the metal cores (see the third bar in figure 4f). This can be due to the fact that ligands with phenyl groups tend to arrange in a way to interact among them by π– stacking (see figure 2a and 2b).

Table 1 shows the S – C, $Au_{(C)} – Au_{12}$ and $Au_{(C)} – Au_{staple}$ bond lengths for comparison. $Au_{(C)} – Au_{12}$ represents the distance between the central Au and the 12 Au atoms forming the icosahedral Au_{13} core and $Au_{(C)} – Au_{staple}$ stands for the distance between the central Au and the 12 Au in the staple oligomers. Table 1 shows very similar S – C, $Au_{(C)} – Au_{12}$ and $Au_{(C)} – Au_{staple}$ distances for all of the clusters independently on the ligand protecting the core, except for the $[Au_{25}(SCH_3)_{18}]^{1-}$ clusters where we have larger values. This confirms the stability of the Au_{25} core. [43]

Table 2 shows the partial charge distribution of the $[Au_{25}(SR)_{18}]^-$ clusters. The computed partial charge on Au_{25} cores is positive (+3 |e|) and does not vary significantly upon changing the nature of the R group in the ligand shell, except for the $[Au_{25}(SCH_3)_{18}]^{1-}$ for which it is slightly more positive. The positive partial charge on the Au_{25} core reflects the electron – attractor character of the sulfur atoms. The fact that the R = CH_3 ligand leads to a different charge distribution can be understood by its smaller polarizability. However, the partial charges on the Au_{13} core reported in table 2 are negative, leading to a polarization of the Au_{25} metallic core. [7] A partial negative charge of –0.53 |e| of Au_{13} core is computed for the $[Au_{25}(SCH_3)_{18}]^{1-}$ cluster while the $[Au_{25}(TP)_{18}]^{1-}$ cluster has a partial charge of –0.45 |e|, a value that is similar for the R substituents, which all involve phenyl rings. The $[Au_{25}(SPhPh)_{18}]^-$ cluster has the same partial charge as $[Au_{25}(TP)_{18}]^{1-}$ while the partial charge for $[Au_{25}(SPhPhPh)_{18}]^-$ is –0.46 |e|. The difference in partial charges reflects the electron – attractor character of the phenyl groups, which leads to a smaller polarization of the charge distribution inside the metallic core. Entries *d*, *e* and *f* in table 2 shows that, for these three protected clusters the charge is concentrated on the first ring in the SPhPh and the SPhPhPh ligands absorbed on the Au_{25} core. The less negative metal Au_{13} core reported in table 2 is found for the $[Au_{25}(4ATP)_{18}]^{1-}$ cluster. A total natural charge of –1.32 |e| is obtained for the NH_2 groups showing their electron withdrawing character.

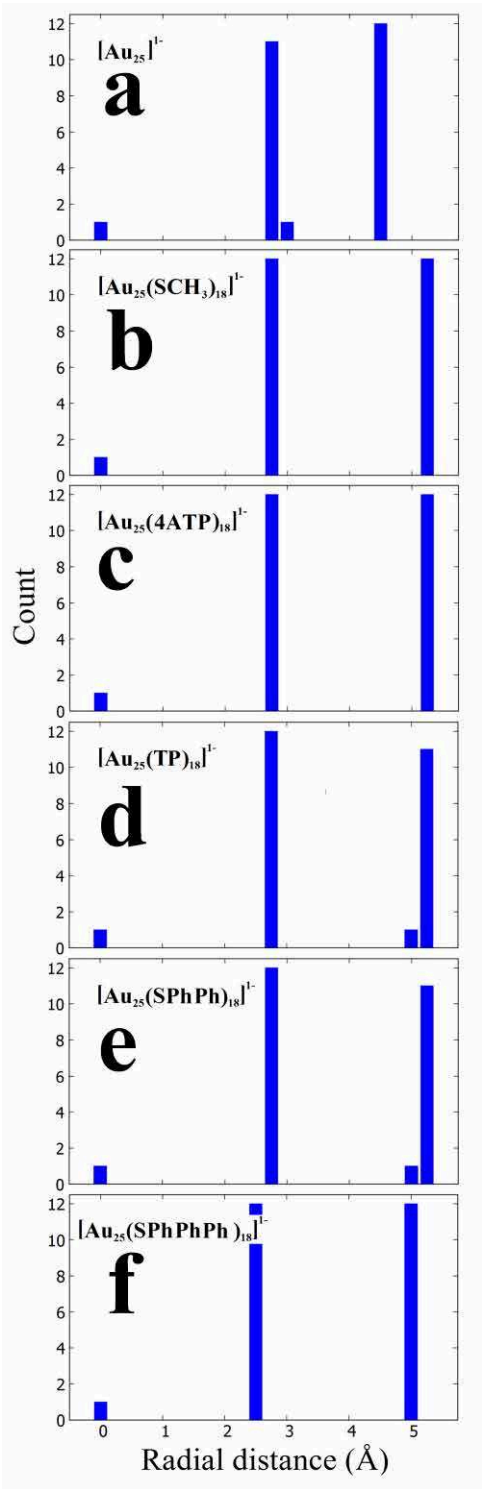

***Figure 4**. Histogram of the radial distances in the bare Au_{25}^- core in panel (a) and the $[Au_{25}(SR)_{18}]^-$ clusters: panel (b) $[Au_{25}(SCH_3)_{18}]^-$, panel (c) $[Au_{25}(4ATP)_{18}]^-$, panel (d) $[Au_{25}(TP)_{18}]^-$, panel (e) $[Au_{25}(SPhPh)_{18}]^-$ and panel (f) $[Au_{25}(SPhPhPh)_{18}]^-$.*

***Table 1**. Label, cluster stoichiometry and S – C, $Au_{(C)}$ – Au_{12} and $Au_{(C)}$ – Au_{staple} bond lengths in (Å) of the $[Au_{25}(SR)_{18}]^-$ clusters. $Au_{(C)}$ stands for the central atom in the icosahedral Au_{13} while Au_{12} represents the rest of the Au atoms. $Au_{staples}$ represent the Au atoms left which form the staple motif.*

Label	Cluster Stoichiometry	S – C (Å)	$Au_{(c)}$ – Au_{12} (Å)	$Au_{(c)}$ – Au_{staple} (å)
b	$[Au_{25}(SCH_3)_{18}]^{1-}$	1.829 – 1.833	2.875 – 2.926	5.272 – 5.372
c	$[Au_{25}(4ATP)_{18}]^{1-}$	1.789 – 1.797	2.879 – 2.958	5.317 – 5.489
d	$[Au_{25}(TP)_{18}]^{1-}$	1.791 – 1.797	2.877 – 2.948	5.236 – 5.431
e	$[Au_{25}(SPhPh)_{18}]^{1-}$	1.787 – 1.795	2.871 – 2.933	5.234 – 5.445
f	$[Au_{25}(SPhPhPh)_{18}]^{1-}$	1.788 – 1.795	2.880 – 2.938	5.210 – 5.429

***Table 2**. Label, cluster stoichiometry, partial charges of the different fragments in the clusters and HOMO – LUMO gap values (H – L gap) of the $[Au_{25}(SR)_{18}]^-$ clusters.*

Label	Cluster Stoichiometry	Partial charges |e|					H – L Gap (eV)
		Au_{25}	Au_{13}	S	C H	Substituent	
b	$[Au_{25}(SCH_3)_{18}]^{1-}$	3.10	-0.53	-3.29	-0.81	–	3.99
c	$[Au_{25}(4ATP)_{18}]^{1-}$	3.05	-0.40	-2.30	-0.44	-1.32 NH_2	3.99
d	$[Au_{25}(TP)_{18}]^{1-}$	3.06	-0.45	-2.19	-1.87	–	4.01
e	$[Au_{25}(SPhPh)_{18}]^{1-}$	3.04	-0.45	-2.12	-1.93	-1.78 (C_6H_4) -0.15 (C_6H_5)	3.97
f	$[Au_{25}(SPhPhPh)_{18}]^{1-}$	3.02	-0.46	-2.09	-1.93	-1.76 (C_6H_4) -0.044 (C_6H_4) -0.13 (C_6H_5)	3.96

Additionally, H – L gap values are reported for all the thiolate coated Au_{25} clusters. No significant modification of the H – L gap value was observed upon thiolate exchange. Since the H – L gap reported in table 2 are not significantly different we can say that the stability of the cluster is not affected by the organic group bearing the S atom among the thiolates studied here.

4.1.2 Optical properties

UV − Vis spectra were computed at the equilibrium geometry of the ground electronic state with the linear response TD – DFT method as implemented in Gaussian 09. The absorption spectrum was obtained by the calculation of the 70 lowest excited states.

Figure 5 and 6 show the computed UV – Vis spectra of the $[Au_{25}(SR)_{18}]^-$ set of clusters. Vertical bars stand for the transition energies whose heights correspond to the oscillator strength of the corresponding transition, and the spectra are obtained by convolution with Gaussian line shapes with σ = 0.085 eV.

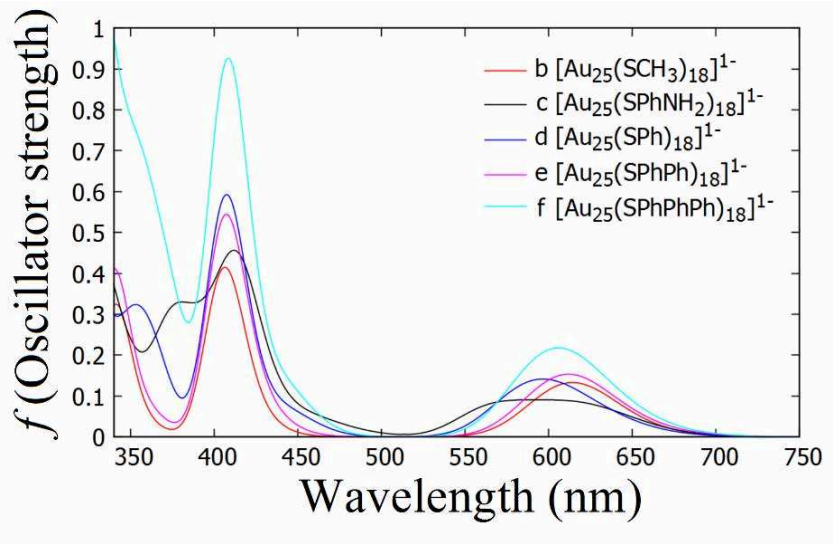

***Figure 5**. Computed UV−vis absorption spectra of the $[Au_{25}(SR)_{18}]^-$ clusters at the DFT/CAM – B3LYP level.*

Comparison of the UV – Vis spectra is shown in figure 6. It is possible to see that in all cases, as found in previous computational studies on the same cluster, [8, 12, 38] our computed absorption spectra are characterized by a tail – and – hump profile. Relative weak absorption are found in the visible region while the main bands can be found in the UV.

Table 3 shows the range (in nm) for each band for all the thiolate capped Au_{25} clusters and their character. We can see that the first band originates from excitations involving transitions from the 3 - fold quasidegenerate HOMO to the LUMO, LUMO + 1 quasidegenerate set.

In all cases, the 3 – fold quasi – degenerate set; HOMO, HOMO – 1 and HOMO − 2 and the virtual orbitals; LUMO to LUMO + 4 show a resemblance with the superatomic molecular orbitals (SAMO) that characterize the electronic structure of the icosahedral bare Au_{13}^{5+} core. [31, 38] For instance, figure 7 shows a schematic representation of the energy levels together with the isocontour of the corresponding orbitals (isovalue 0.02 $Å^{-3}$) of the $[Au_{25}(SPhPh)_{18}]^-$ cluster. However, compared to the Au_{13} electronic structure, the

d – SAMO in $[Au_{25}(SPhPh)_{18}]^-$ are split and as a consequence a splitting in the optical bands is observed. Figure 7 shows that the 3 – quasidegenerate p – SAMO (HOMO – 1, HOMO – 2 and HOMO – 3) and the d – SAMO (LUMO + 1 to LUMO +5) are highly localized on the metal Au_{13} core. We find that the contribution from the Au_{13} core to the frontier molecular orbitals is greater than 70%, except in the specific case of the $[Au_{25}(4ATP)_{18}]^-$ where the contribution is >60 %.

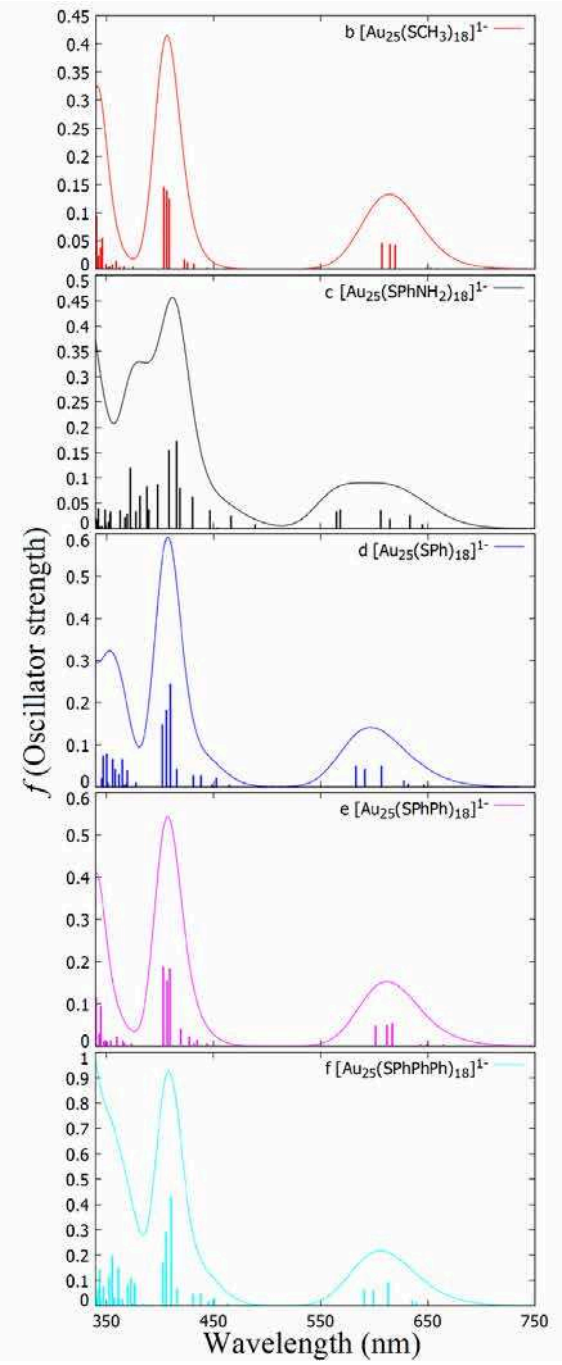

***Figure 6**. Computed UV−vis absorption spectra of the $[Au_{25}(SR)_{18}]^-$ clusters at the DFT/CAM – B3LYP level. The height of the vertical bars give the oscillator strength of each transition and the spectra are obtained by convolution with Gaussian line shapes (σ = 0.085 eV).*

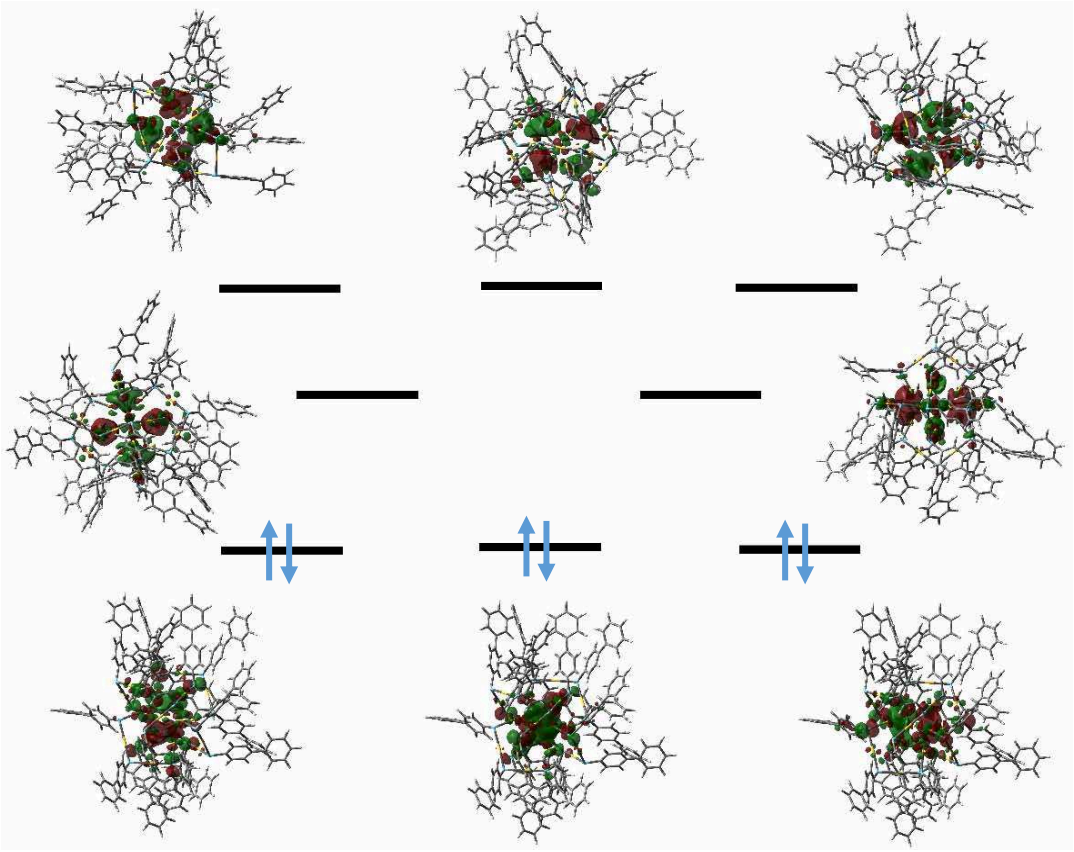

***Figure 7**. Schematic representation of the energy levels (with a degeneracy threshold of 0.13 eV) together with the isocontour of the corresponding orbitals (isovalue 0.02 Å^{-3}) of the $[Au_{25}(SPhPh)_{18}]^-$ cluster at the DFT/CAM – B3LYP level.*

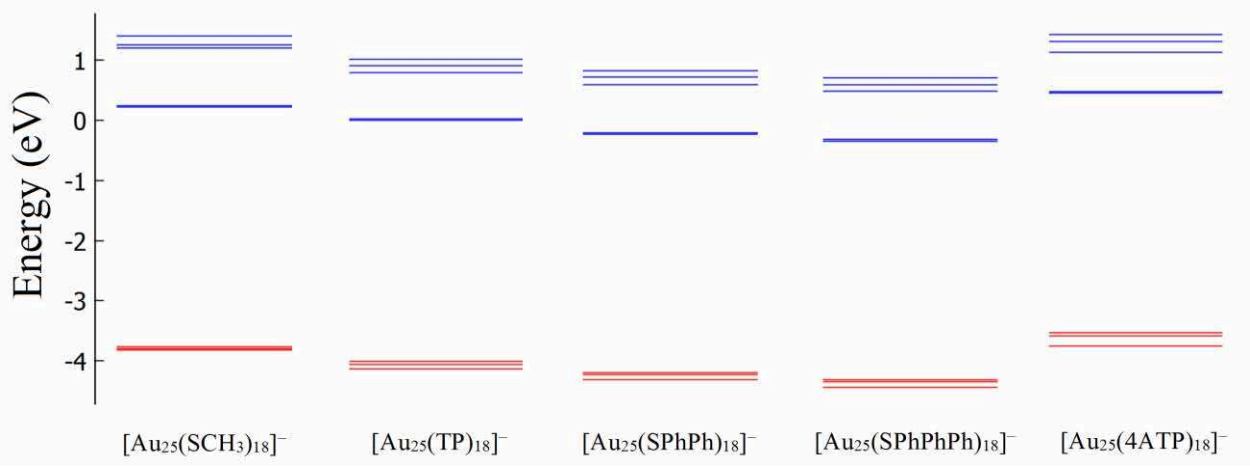

***Figure 8**. Molecular orbital diagram of the $[Au_{25}(SR)_{18}]^-$ clusters at the DFT/CAM – B3LYP level. The red bars are the p – SAMO 3 – fold quasi – degenerate HOMO (HOMO – 1, HOMO – 1 and HOMO – 2) and the blue bars stand for the five d – SAMO; the two degenerate LUMO and the 3 – fold quasi – degenerate LUMO + 1.*

***Table 3**. Label, cluster stoichiometry, partial charge on the Au_{13} core (NBO) and characteristics of the first and second band of the $[Au_{25}(SR)_{18}]^-$ set of clusters.*

Label	Cluster Stoichiometry	NBO Au_{13} |e|	First band Range (nm)	First band Character	Second band Range (nm)	Second band Character
b	$[Au_{25}(SCH_3)_{18}]^{1-}$	-0.53	607.09 – 658.76	H → L	403.49 – 444.56	H → L + 1
c	$[Au_{25}(4ATP)_{18}]^{1-}$	-0.40	546.43 – 645.14	H → L	398.10 – 488.96	H → L + 1 H → L + 2
d	$[Au_{25}(TP)_{18}]^{1-}$	-0.45	582.73 – 646.20	H → L	402.55 – 464.71	H → L + 1
e	$[Au_{25}(SPhPh)_{18}]^{1-}$	-0.45	593.15 – 656.74	H → L	404.60 – 462.49	H → L + 1
f	$[Au_{25}(SPhPhPh)_{18}]^{1-}$	-0.46	590.54 – 657.71	H → L	403.02 – 463.59	H → L + 1

Figure 8 shows the molecular orbital diagram of the $[Au_{25}(SR)_{18}]^-$ clusters. It is possible to see that the orbitals energies are affected by exchanging the organic group bearing the S atom but not a significant modification on the degeneracy landscape is observed. This is confirmed by the H-L gaps reported in table 2, which do not vary significantly.

Table 3 also shows that the second band originates from excitations involving transitions from the 3 - fold quasidegenerate HOMO to the d – SAMO set; LUMO + 1 and LUMO + 2. Notice that no significant modification on the optical absorption profile is experienced by modifying the organic group bearing the S atom in the thiolate. Figure 6 shows that, in all cases, the lowest energy band in centered ~600 nm while the one at higher energies is around 409 nm.

4.2 The Janus $[Au_{25}(SR')_x(SR'')_{18-x}]^-$ cluster (R' = Ph (TP) and R'' = 4ATP, $CH_3(CH_2)_4COOH$)

Taking the $[Au_{25}(TP)_{18}]^-$ as parent cluster, the equilibrium structure and the optical absorption profile of the $[Au_{25}(TP)_x(S(CH_2)_5COOH)_{18-x}]^-$ and the $[Au_{25}(TP)_x(4ATP)_{18-x}]^-$ Janus clusters have been determined for different SR'/SR'' ratios. We then analyze the computed UV – Vis spectra..

4.2.1 Structure and partial charge distribution of the Janus $[Au_{25}(TP)_x(S(CH_2)_5COOH)_{18-x}]^-$

The equilibrium geometries of anionic Au_{25} cluster protected by thiophenol (TP) and the 6 – mercaptohexanoic acid ($S(CH_2)_5COOH$) in Janus ligand – ordered domains have been studied for four ligand TP/$S(CH_2)_5COOH$)$_2$ ratios: $[Au_{25}(TP)_{16}(S(CH_2)_5COOH)_2]^-$, $[Au_{25}(TP)_{14}(S(CH_2)_5COOH)_4]^-$, $[Au_{25}(TP)_{12}(S(CH_2)_5COOH)_6]^-$ and $[Au_{25}(TP)_{10}(S(CH_2)_5COOH)_8]^-$. The ground state equilibrium geometries have been computed at the DFT/CAM – B3LYP level and the corresponding UV – Vis spectra with the linear response TD – DFT method. Unfortunately, we were not able to find the equilibrium structure of the $[Au_{25}(S(CH_2)_5COOH)_{18}]^-$ cluster. The crystallographic data of the $Au_{25}(SCH_2CH_2Ph)_{18}$ cluster are available and were used as starting point for our calculations by modifying the ligand shell as done for the monoligand protected Au_{25}. [1, 34]

The computed equilibrium structures of the four Janus $[Au_{25}(TP)_x(S(CH_2)_5COOH)_{18-x}]^-$ clusters are shown in figure 9 together with the $[Au_{25}(TP)_{18}]^-$. As expected, the addition of a second type of thiolate ($S(CH_2)_5COOH$) does not induce a significant rearrangement of the metal core. The Au_{13} + 6{– SR – Au – SR – Au – SR –} staple structure is preserved. [42]

Figure 10 shows the histograms of the Au–Au distances for the four Janus $[Au_{25}(TP)_x(S(CH_2)_5COOH)_{18-x}]^-$ clusters together with the $[Au_{25}(TP)_{18}]^-$. Different TP/$S(CH_2)_5COOH$ ratios do not induce a significant modification on the Au – Au distance histogram.

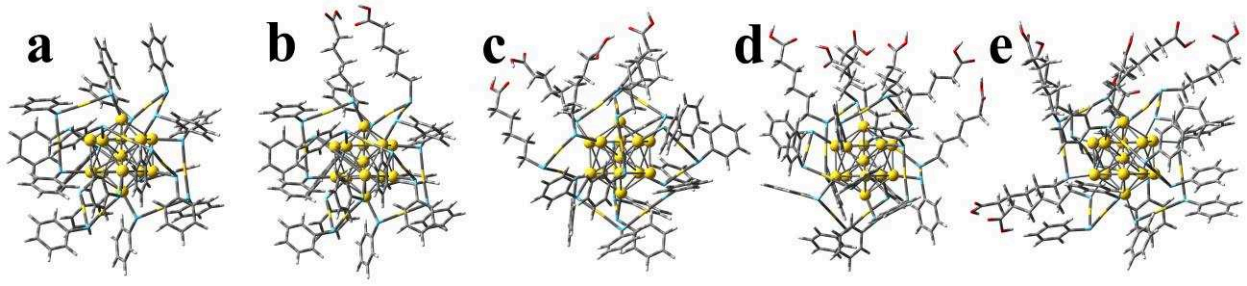

***Figure 9**. Computed equilibrium geometries of the $[Au_{25}(TP)_{18}]^-$ cluster in panel (a) and of the Janus $[Au_{25}(TP)_x(S(CH_2)_5COOH)_{18-x}]^-$ clusters: panel (b) $[Au_{25}(TP)_{16}(S(CH_2)_5COOH)_2]^-$ cluster, panel (c) $[Au_{25}(TP)_{14}(S(CH_2)_5COOH)_4]^-$, panel (d) $[Au_{25}(TP)_{12}(S(CH_2)_5COOH)_6]^-$ and (e) $[Au_{25}(TP)_{10}(S(CH_2)_5COOH)_8]^-$. The Au atoms are shown in yellow, the C atoms in grey, the dark blue junctions stand for N, S is represented in navy blue and H is in white.*

Figure 11 shows the histogram of the radial distances of all the $[Au_{25}(TP)_x(S(CH_2)_5COOH)_{18-x}]^-$ Janus clusters together with the $[Au_{25}(TP)_{18}]^-$. The staple motif keeps its structure with the exception of the Janus $[Au_{25}(TP)_{16}(S(CH_2)_5COOH)_2]^-$ cluster (figure 9b and 10b) where the $S(CH_2)_5COOH$ acids slightly distort the staples. For the $S(CH_2)_5COOH$ ligands, we observe the formation of hydrogen bond between the pairs of COOH groups.

Table 4 shows the S – C, $Au_{(C)}$ – Au_{12} and $Au_{(C)}$ – Au_{staple} distances for comparison. As in the monoligand capped anion Au_{25}, table 4 shows very similar S – C, $Au_{(C)}$ – Au_{12} and $Au_{(C)}$ – Au_{staple} distances for all of the clusters independently on the ligand TP/ $S(CH_2)_5COOH$ ratio. Again, the only exception is in the $[Au_{25}(TP)_{16}(S(CH_2)_5COOH)_2]^-$ cluster where the $Au_{(C)}$ – Au_{staple} distance is slightly larger than the other cases.

Furthermore, table 5 shows the natural charge distribution of the Janus $[Au_{25}(TP)_x(S(CH_2)_5COOH)_{18-x}]^-$ clusters. An overall positive charge for the Au_{25} core is reported highlighting the electron – attractor character of the thiolates ligands. Table 5 shows that the TP has stronger electron – attractor character than the $S(CH_2)_5COOH$ ligand. As a consequence, the larger the amount of TP ligands the less positive the Au_{25}

becomes. As observed in the monoligated case, the partial charge on the Au_{13} core cluster is negative. No correlation between the charge of the Au_{13} and the ligand ratio has been found.

All the Janus equilibrium structures shown in this section present practically the same Au_{25} core structure independently of the $S(CH_2)_5COOH$ / TP ligand.

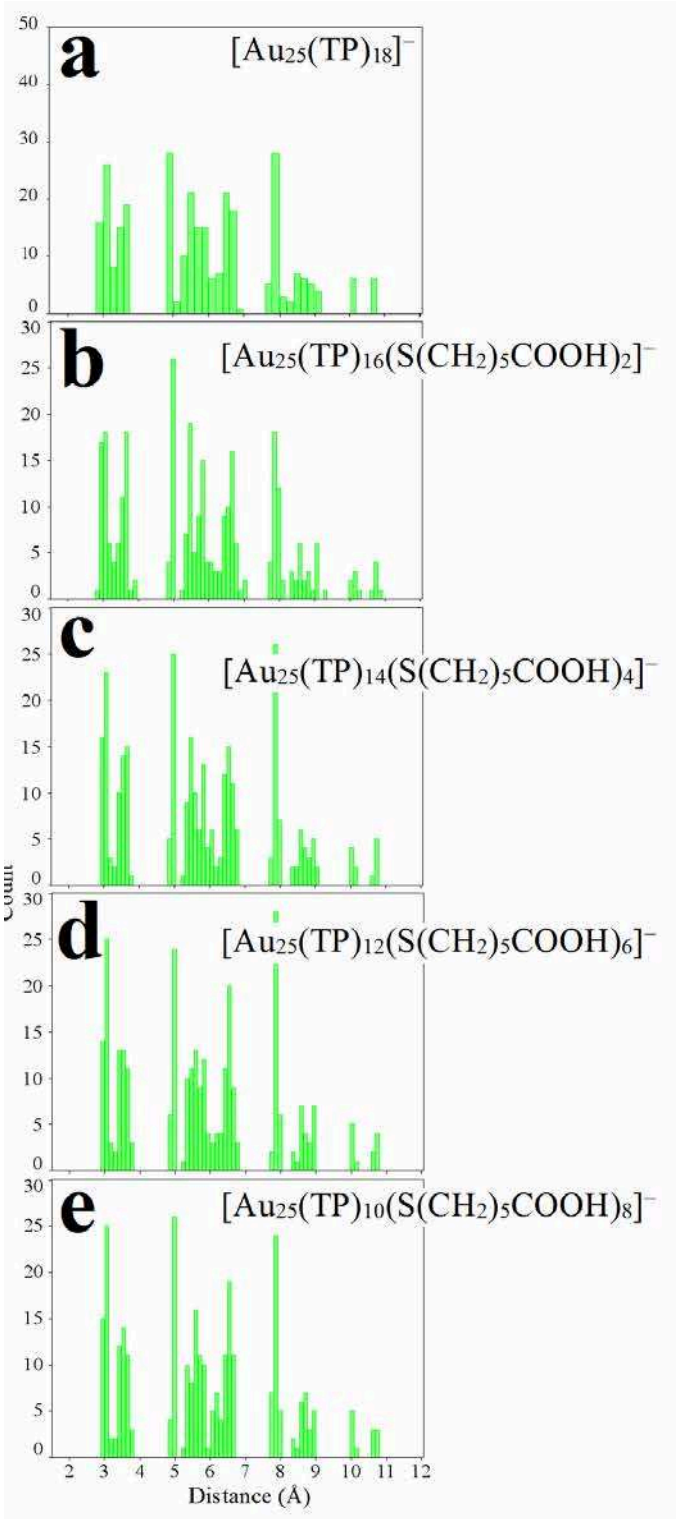

***Figure 10**. Histogram of the Au – Au distances of the $[Au_{25}(TP)_{18}]^-$ (in panel a) and the Janus $[Au_{25}(TP)_x(S(CH_2)_5COOH)_{18-x}]^-$ clusters: panel (b) $[Au_{25}(TP)_{16}(S(CH_2)_5COOH)_2]^-$, panel (c) $[Au_{25}(TP)_{14}(S(CH_2)_5COOH)_4]^-$, panel (d) $[Au_{25}(TP)_{12}(S(CH_2)_5COOH)_6]^-$ and panel (e) $[Au_{25}(TP)_{10}(S(CH_2)_5COOH)_8]^-$.*

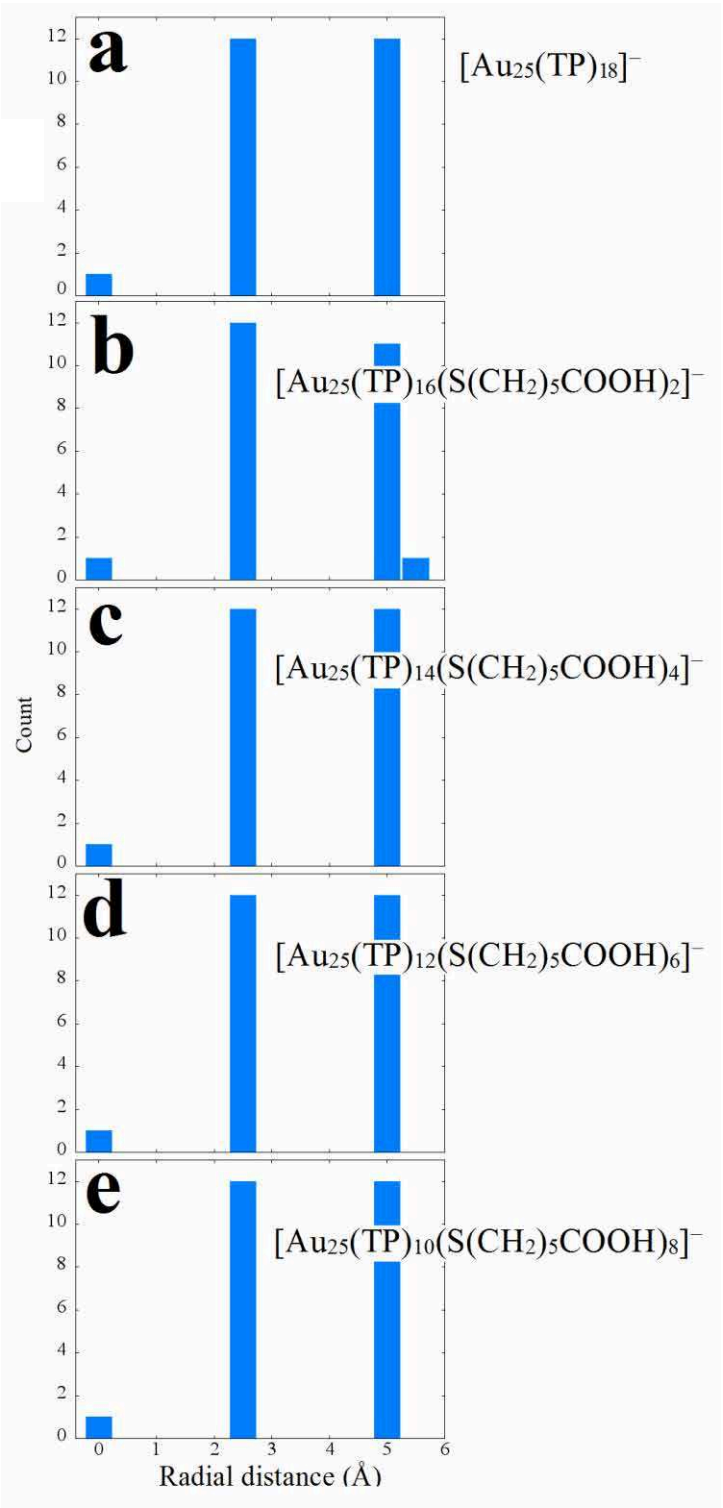

Figure 11. *Histogram of the radial distances of the $[Au_{25}(TP)_{18}]^-$ (in panel a) and the Janus $[Au_{25}(TP)_x(S(CH_2)_5COOH)_{18-x}]^-$ clusters: panel (b) $[Au_{25}(TP)_{16}(S(CH_2)_5COOH)_2]^-$, panel (c) $[Au_{25}(TP)_{14}(S(CH_2)_5COOH)_4]^-$, panel (d) $[Au_{25}(TP)_{12}(S(CH_2)_5COOH)_6]^-$ and panel (e) $[Au_{25}(TP)_{10}(S(CH_2)_5COOH)_8]^-$.*

***Table 4**. Label, cluster stoichiometry and S – C, $Au_{(C)}$ – Au_{12} and $Au_{(C)}$ – Au_{staple} distances in (Å) of the Janus $[Au_{25}(TP)_x(S(CH_2)_5COOH)_{18-x}]^-$ set of clusters together with the monoligand protected $[Au_{25}(TP)_{18}]^-$. $Au_{(C)}$ stands for the central atom in the icosahedral Au_{13} while Au_{12} represents the rest of the Au atoms. $Au_{staples}$ represent the Au atoms left which form the staple motif.*

Label	Cluster Stoichiometry	S – C TP (å)	S – C $S(CH_2)_5COOH$ (Å)	$Au_{(c)}$ – Au_{12} (Å)	$Au_{(c)}$ – Au_{staple} (å)
a	$[Au_{25}(TP)_{18}]^{1-}$	1.791 – 1.797	–	2.88 – 2.95	5.24 – 5.43
b	$[Au_{25}(TP)_{16}(S(CH_2)_5COOH)_2]^-$	1.791 – 1.798	1.831 – 1.839	2.87 – 2.95	5.27 – 5.50
c	$[Au_{25}(TP)_{14}(S(CH_2)_5COOH)_4]^-$	1.791 – 1.796	1.831 – 1.847	2.89 – 2.94	5.27 – 5.42
d	$[Au_{25}(TP)_{12}(S(CH_2)_5COOH)_6]^-$	1.790 – 1.796	1.831 – 1.847	2.88 – 2.94	5.28 – 5.43
e	$[Au_{25}(TP)_{10}(S(CH_2)_5COOH)_8]^-$	1.791 – 1.796	1.832 – 1.847	2.88 – 2.93	5.25 – 5.41

***Table 5**. Label, cluster stoichiometry, partial charge of the different fragments in the clusters and HOMO – LUMO gap (H – L gap) of the Janus $[Au_{25}(TP)_x(S(CH_2)_5COOH)_{18-x}]^-$ set of clusters together with the monoligand protected $[Au_{25}(TP)_{18}]^-$. The partial charges for TP and $S(CH_2)_5COOH$ represent the charge per ligand.*

Label	Cluster Stoichiometry	Partial charge |e|				H – L (eV)
		Au_{25}	Au_{13}	TP	$S(CH_2)_5COOH$	
a	$[Au_{25}(TP)_{18}]^{1-}$	3.06	-0.450	-4.062	–	4.01
b	$[Au_{25}(TP)_{16}(S(CH_2)_5COOH)_2]^-$	3.03	-0.430	-0.227	-0.199	4.062
c	$[Au_{25}(TP)_{14}(S(CH_2)_5COOH)_4]^-$	2.98	-0.416	-0.228	-0.199	3.947
d	$[Au_{25}(TP)_{12}(S(CH_2)_5COOH)_6]^-$	2.95	-0.423	-0.229	-0.200	3.944
e	$[Au_{25}(TP)_{10}(S(CH_2)_5COOH)_8]^-$	2.92	-0.425	-0.230	-0.203	3.924

4.2.2 Structure and partial charge distribution effects of thiolate ligands on the Janus $[Au_{25}(TP)x(4ATP)_{18-x}]^-$ cluster

The equilibrium geometries of the anion Au_{25} cluster protected by thiophenol (TP) and the 4 – aminothiophenol (4ATP) in Janus configuration have been studied for three different ligand TP/4ATP ratios: $[Au_{25}(4ATP)_4(TP)_{14}]^-$, $[Au_{25}(4ATP)_9(TP)_9]^-$ and the $[Au_{25}(4ATP)_{13}(TP)_5]^-$. The ground state equilibrium geometries have been computed at the DFT/CAM – B3LYP level and the corresponding UV – Vis spectra with the linear response TD – DFT method.

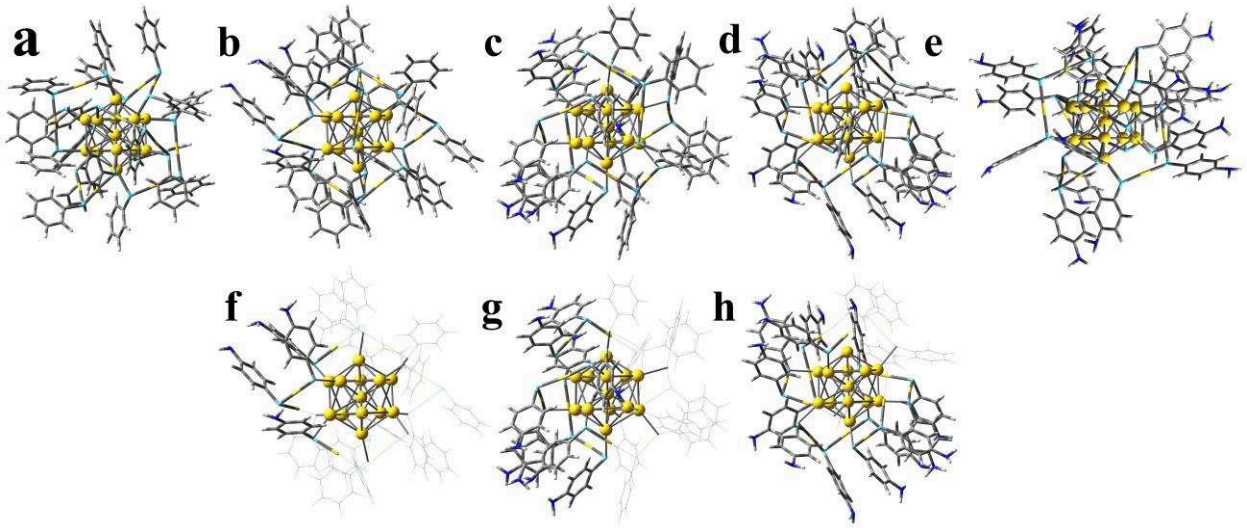

***Figure 12**. Computed equilibrium geometries of the monoligand protected $[Au_{25}(TP)_{18}]^-$ in panel (a) the Janus $[Au_{25}(4ATP)_x(TP)_{18-x}]^-$ clusters: panel (b) $[Au_{25}(4ATP)_4(TP)_{14}]^-$, panel (c) the $[Au_{25}(4ATP)_9(TP)_9]^-$ and panel (d) the $[Au_{25}(4ATP)_{13}(TP)_5]^-$ and the monoligand protected $[Au_{25}(4ATP)_{18}]^-$ cluster in panel (e). In panels (f), (g) and (h) the 4ATP ligands of (b), (c) and (d) are highlighted. The Au atoms are shown in yellow, the C atoms in grey, the dark blue junctions stand for N, S is represented in navy blue and H is in white.*

As in the monoligand protected case and the four Janus $[Au_{25}(TP)_x(S(CH_2)_5COOH)_{18-x}]^-$ set of clusters, our computed $[Au_{25}(4ATP)_x(TP)_{18-x}]^-$ equilibrium structures keeps the Au_{13} + 6{'– SR – Au – SR – Au – SR –} structure [42] as shown in figure 12. As expected, no significant rearrangement of the metal core was experienced by varying the TP/4ATP ligand ratio as can be seen in the histogram of Au – Au distances in figure 13. There is also no significant difference with the two monoligated clusters, $[Au_{25}(TP)_{18}]^-$ and $[Au_{25}(4ATP)_{18}]^-$ discussed above. This is confirmed by table 6.

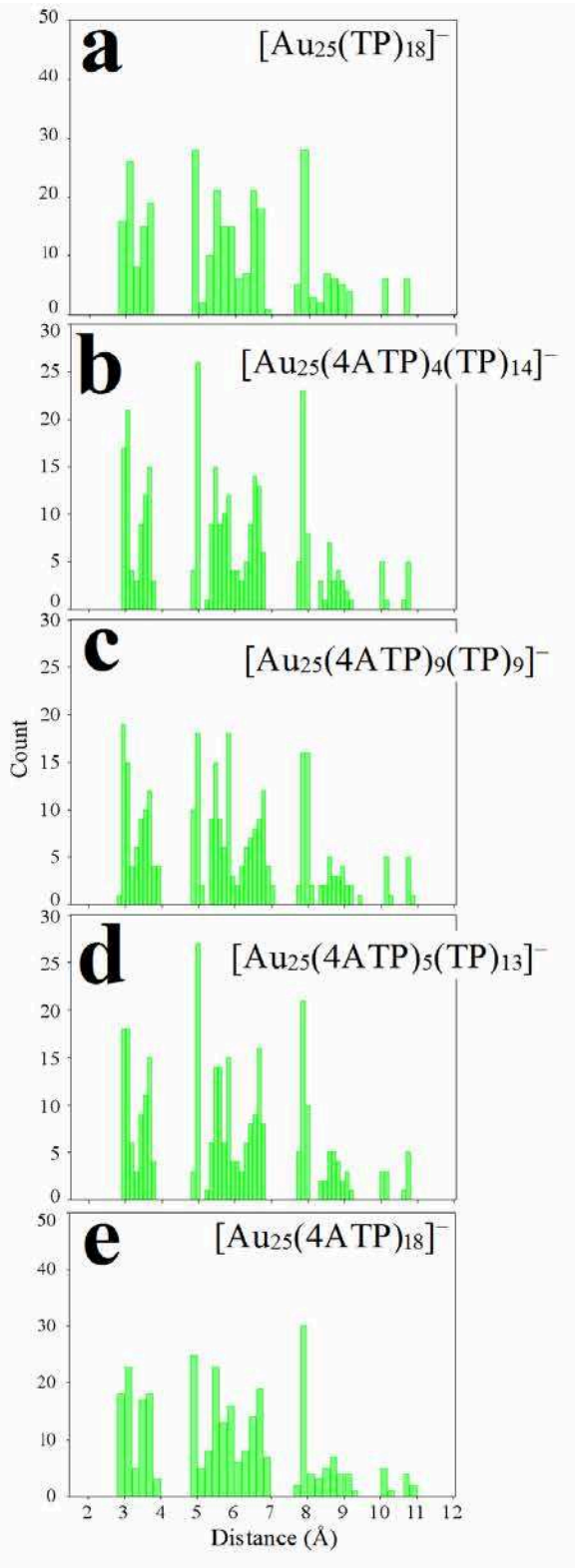

***Figure 13**. Histogram of the Au – Au distances of the monoligand protected $[Au_{25}(TP)_{18}]^-$ in panel (a), the Janus $[Au_{25}(4ATP)_x(TP)_{18-x}]^-$ clusters: panel (b) $[Au_{25}(4ATP)_4(TP)_{14}]^-$, (c) $[Au_{25}(4ATP)_9(TP)_9]^-$ and (d) the $[Au_{25}(4ATP)_{13}(TP)_5]^-$ cluster and the $[Au_{25}(TP)_{18}]^-$ in panel (e).*

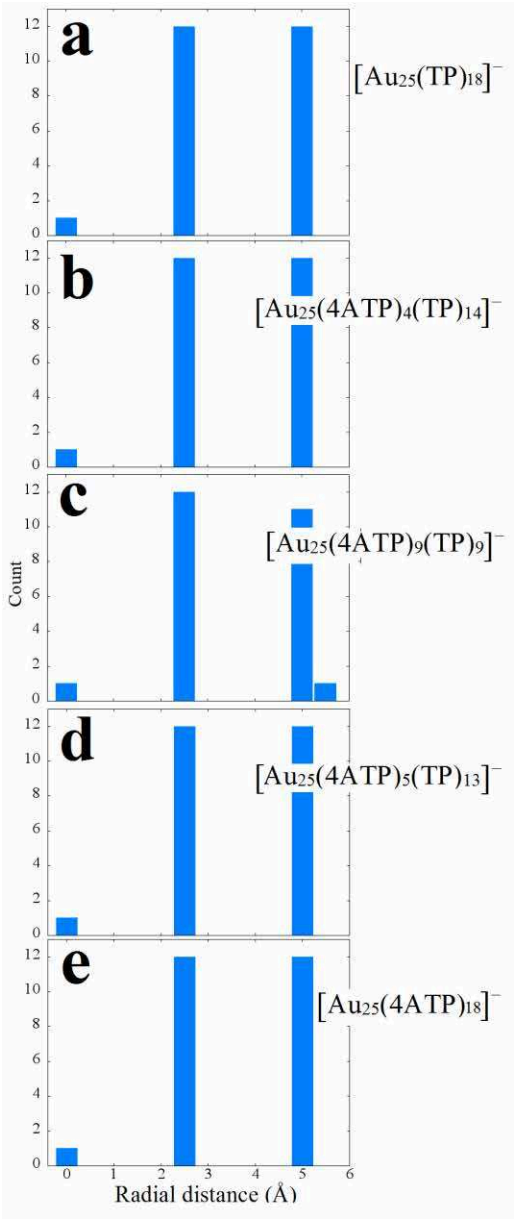

***Figure 14**. Histogram of the radial distances of the monoligand protected $[Au_{25}(TP)_{18}]^-$ in panel (a), the Janus $[Au_{25}(4ATP)_x(TP)_{18-x}]^-$ clusters: panel (b) $[Au_{25}(4ATP)_4(TP)_{14}]^-$, (c) $[Au_{25}(4ATP)_9(TP)_9]^-$ and (d) the $[Au_{25}(4ATP)_{13}(TP)_5]^-$ cluster and the $[Au_{25}(TP)_{18}]^-$ in panel (e).*

***Table 6**. Label, cluster stoichiometry, S – C, $Au_{(C)}$ – Au_{12} and $Au_{(C)}$ – Au_{staple} distances in (Å) of the Janus $[Au_{25}(4ATP)_x(TP)_{18-x}]^-$ clusters: (a) shows the $[Au_{25}(4ATP)_4(TP)_{14}]^-$, (c) the $[Au_{25}(4ATP)_9(TP)_9]^-$ and (e) the $[Au_{25}(4ATP)_{13}(TP)_5]^-$ cluster for the two different ligands. $Au_{(C)}$ stands for the central atom in the icosahedral Au_{13} while Au_{12} represents the rest of the Au atoms. $Au_{staples}$ represent the Au atoms left which form the staple motif.*

Label	Cluster Stoichiometry	S – C TP (Å)	S – C 4ATP (Å)	$Au_{(c)}$ – Au_{12} (Å)	$Au_{(c)}$ – Au_{staple} (Å)
a	$[Au_{25}(TP)_{18}]^{1-}$	1.791 – 1.797	–	2.88 – 2.95	5.24 – 5.43
b	$[Au_{25}(4ATP)_4(TP)_{14}]^-$	1.792 – 1.797	1.790 – 1.795	2.89 – 2.95	5.25 – 5.44
c	$[Au_{25}(4ATP)_9(TP)_9]^-$	1.791 – 1.797	1.791 – 1.797	2.86 – 2.97	5.30 – 5.52
d	$[Au_{25}(4ATP)_{13}(TP)_5]^-$	1.792 – 1.797	1.789 – 1.797	2.89 – 2.95	5.27 – 5.44
e	$[Au_{25}(4ATP)_{18}]^{1-}$	–	1.789 – 1.797	2.88 – 2.96	5.32 – 5.45

Furthermore, table 7 shows the natural charge distribution of the Janus $[Au_{25}(TP)_x(4ATP)_{18-x}]^-$ clusters. Again, a positively charged Au_{25} core is reported. Table 7 shows that the TP has stronger electron – attractor character than the 4ATP ligand. However, no specific relation between the ligand TP/4ATP ratio and the charge of the Au_{13} or the Au_{25} has been found. It is possible to see that for the $[Au_{25}(4ATP)_9(TP)_9]^-$ (1:1 TP:4ATP) we obtain a larger polarization of the metallic core with the less negative Au_{13} core and the more positive Au_{25}.

***Table 7**. Label, cluster stoichiometry, partial charges of the different fragments in the clusters and HOMO – LUMO gap (H – L gap) of the Janus $[Au_{25}(4ATP)_x(TP)_{18-x}]^-$ clusters: (a) shows the $[Au_{25}(4ATP)_4(TP)_{14}]^-$, (c) the $[Au_{25}(4ATP)_9(TP)_9]^-$ and (e) the $[Au_{25}(4ATP)_{13}(TP)_5]^-$ cluster. The partial charge for TP and $S(CH_2)_5COOH$ represent the charge per ligand.*

Label	Cluster Stoichiometry	Partial charge |e|				H – L (eV)
		Au_{25}	Au_{13}	TP	4ATP	
a	$[Au_{25}(TP)_{18}]^{1-}$	3.06	-0.45	-0.23	–	4.01
b	$[Au_{25}(4ATP)_4(TP)_{14}]^-$	3.04	-0.45	-0.24	-0.19	3.99
c	$[Au_{25}(4ATP)_9(TP)_9]^-$	3.09	-0.38	-0.24	-0.22	4.05
d	$[Au_{25}(4ATP)_{13}(TP)_5]^-$	3.04	-0.44	-0.23	-0.22	3.96
e	$[Au_{25}(4ATP)_{18}]^{1-}$	3.05	-0.40	–	-0.23	3.99

4.2.3 Optical properties

The UV – Vis spectra of the two types of Janus cluster, $[Au_{25}(TP)_x(S(CH_2)_5COOH)_{18-x}]^-$ and the $[Au_{25}(4ATP)_x(TP)_{18-x}]^-$, were computed at the TD – DFT / CAM – B3LYP level and analyzed through features of the MO involved in the excitations.

4.2.3.1 Computed UV – Vis spectra of the $[Au_{25}(TP)_x(S(CH_2)_5COOH)_{18-x}]^-$ Janus clusters

Figure 15 shows the UV – vis absorption spectra of the Janus $[Au_{25}(TP)_x(S(CH_2)_5COOH)_{18-x}]^-$ clusters. The tails – and – hump pattern typical spectrum of a small cluster is obtained. In Figure 16 the vertical bars representing the transition energies whose heights correspond to the oscillator strength of the corresponding transition is shown.

Figures 15 and 16 clearly show that in most of the cases no significant modification of the UV – Vis spectrum is experienced by varying the TP/$S(CH_2)_5COOH$ ratio. The UV – Vis spectra of the Janus $[Au_{25}(TP)_x(S(CH_2)_5COOH)_{18-x}]^-$ clusters look very similar to the one of the $[Au_{25}(TP)_{18}]^-$. The lowest energy band for $[Au_{25}(TP)_{18}]^-$ is centered at ~600 nm (2.03 eV) whereas it is found ~590 nm (2.10 eV) for $[Au_{25}(TP)_{16}(S(CH_2)_5COOH)_2]^-$ and ~610 nm (2.06 eV) for $[Au_{25}(TP)_{14}(S(CH_2)_5COOH)_4]^-$, $[Au_{25}(TP)_{12}(S(CH_2)_5COOH)_6]^-$ and $[Au_{25}(TP)_{10}(S(CH_2)_5COOH)_8]^-$. Even though the $[Au_{25}(TP)_{16}(S(CH_2)_5COOH)_2]^-$ shows a slight blue shift compared to the monoligand $[Au_{25}(TP)_{18}]^-$ and the rest of the Janus, the difference in position of the band is no significant. This correlates well with the fact that the structure does not experience significant distortion upon TP exchange by the $S(CH_2)_5COOH$ ligand. Table 5 does not show any relation between the ligand TP/ $S(CH_2)_5COOH$ and the partial charge on the metal core Au_{13}.

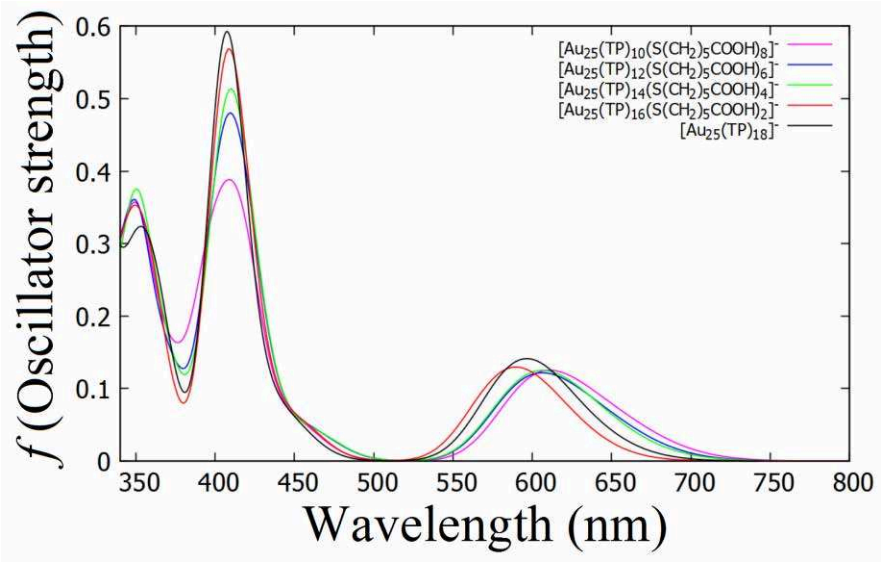

***Figure 15**. Computed UV−vis absorption spectra of the monoligand protected $[Au_{25}(TP)_{18}]^-$ and the Janus $[Au_{25}(TP)_x(S(CH_2)_5COOH)_{18-x}]^-$ clusters at the DFT/CAM – B3LYP level.*

Table 8 shows that, as observed in the monoligand protected clusters discussed here and in chapter III, the first band originates from excitations involving transitions from the 3 – fold quasidegenerate HOMO to the 2 – fold quasidegenerate LUMO superatomic orbitals. The second band originates from excitations

involving transitions from the 3 - fold quasidegenerate HOMO to the *d* – SAMO set; LUMO + 3, LUMO + 4 and LUMO +5.

Figure 17 shows the molecular orbital diagram of the Janus $[Au_{25}(TP)_x(S(CH_2)_5COOH)_{18-x}]^-$ set of clusters. Notice that, compared to figure 8 in the monoligand protected case, the molecular orbital energies are not highly affected by the substitution of the TP by $S(CH_2)_5COOH$ acid ligands which supports the significant resemblance in the UV – Vis spectra of the Janus $[Au_{25}(TP)_x(S(CH_2)_5COOH)_{18-x}]^-$.

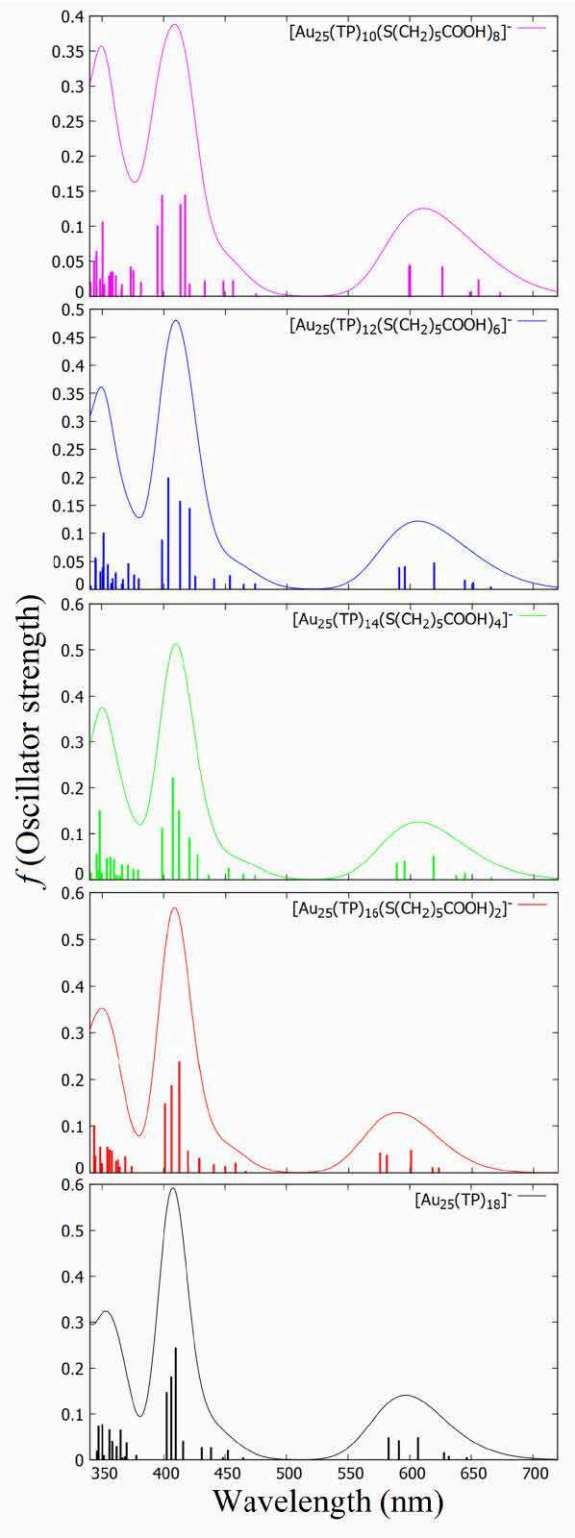

***Figure 16**. Computed UV−vis absorption spectra of the monoligand protected $[Au_{25}(TP)_x]^-$ and the Janus $[Au_{25}(TP)_x(S(CH_2)_5COOH)_{18-x}]^-$ clusters at the DFT/CAM – B3LYP level. The height of the vertical bars give*

the oscillator strength of each transition and the spectra are obtained by convolution with Gaussian line shapes (σ = 0.085 eV).

***Table 8**. Label, cluster stoichiometry and characteristics of the first and second band of the Janus $[Au_{25}(TP)_x(S(CH_2)_5COOH)_{18-x}]^-$ clusters*

Label	Cluster Stoichiometry	First band		Second band	
		Range (nm)	Character	Range (nm)	Character
a	$[Au_{25}(TP)_{18}]^{1-}$	582.73 – 646.20	H → L	402.55 – 464.71	H → L + 1
b	$[Au_{25}(TP)_{16}(S(CH_2)_5COOH)_2]^-$	575.93 – 630.71	H → L	401.18 – 466.28	H → L + 1
c	$[Au_{25}(TP)_{14}(S(CH_2)_5COOH)_4]^-$	589.03 – 665.74	H → L	398.88 – 474.11	H → L + 1 H → L + 2
d	$[Au_{25}(TP)_{12}(S(CH_2)_5COOH)_6]^-$	591.06 – 665.37	H → L	398.41 – 474.00	H → L + 1 H → L + 2
e	$[Au_{25}(TP)_{10}(S(CH_2)_5COOH)_8]^-$	599.34 – 673.28	H → L	394.99 – 475.01	H → L + 1 H → L + 2 H → L + 3

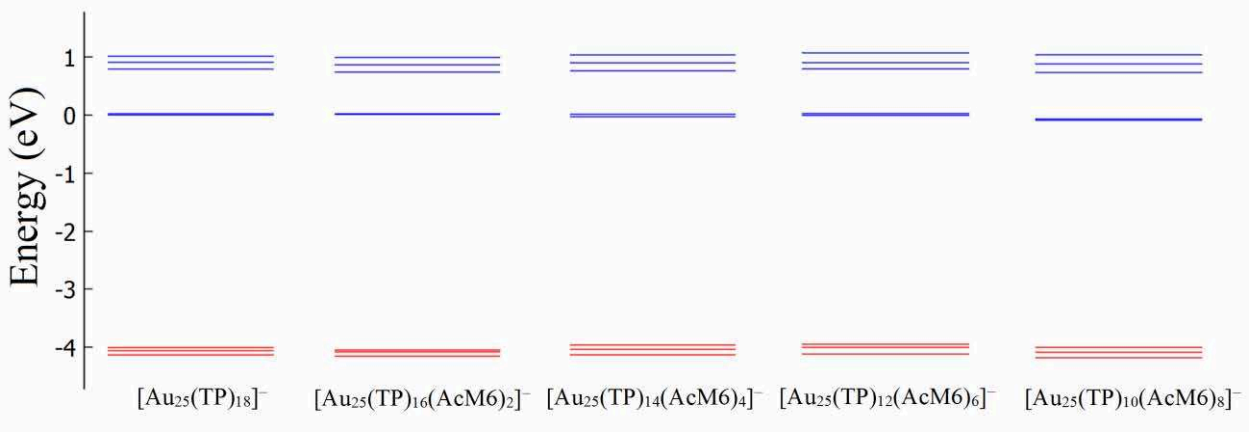

***Figure 17**. Molecular orbital diagram of the Janus $[Au_{25}(TP)_x(S(CH_2)_5COOH)_{18-x}]^-$ clusters at the DFT/CAM – B3LYP level. The red bars are the p – SAMO three – fold quasi – degenerate HOMO (HOMO – 1, HOMO – 1 and HOMO – 2) and the blue bars stand for the 5 d – SAMO; the two degenerate LUMO and the 3 – fold quasi – degenerate LUMO + 1. The AcM6 label was used for $S(CH_2)_5COOH$ ligand.*

The barely modified electronic structure of the Janus $[Au_{25}(TP)_x(S(CH_2)_5COOH)_{18-x}]^-$ clusters is confirmed in table 7 by the H – L gaps. No significant modification of the H – L gap is experienced upon TP exchange by $S(CH_2)_5COOH$.

4.2.3.2 Computed UV – Vis spectra of the $[Au_{25}(TP)x(4ATP)_{18-x}]^-$ Janus clusters

Figure 18 shows the UV – vis absorption spectra of the Janus $[Au_{25}(TP)_x(4ATP)_{18-x}]^-$ clusters and figure 19 shows the computed spectrum together with the vertical bars representing the transition energies whose heights correspond to the oscillator strength of the corresponding transition.

Figures 18 and 19 clearly shows that, for $[Au_{25}(4ATP)_4(TP)_{14}]^-$ and $[Au_{25}(4ATP)_{13}(TP)_5]^-$ no significant modification of the UV – Vis spectrum is experienced compared to both monoligand protected $[Au_{25}(4ATP)_{18}]^-$ and $[Au_{25}(TP)_{18}]^-$. This is confirmed by table 12; the lowest energy band of $[Au_{25}(4ATP)_4(TP)_{14}]^-$ and $[Au_{25}(4ATP)_{13}(TP)_5]^-$ is centered ~600 nm (2.06 eV) as for both monoligand protected clusters while a small blue shift can be seen for the $[Au_{25}(4ATP)_9(TP)_9]^-$ cluster (see figure 18) which is centered ~552 nm (2.25 eV). By comparing the charge in table of the Au_{13} core we find that the charge of the Janus $[Au_{25}(4ATP)_9(TP)_9]^-$ is the more negative (-0.38 |e|) among the rest of the TP/4ATP Janus (approximately -0.45 |e|) and also both monoligand protected $[Au_{25}(4ATP)_{18}]^-$ and $[Au_{25}(TP)_{18}]^-$ (-0.40 and -0.45 |e|, respectively). We find that the Janus $[Au_{25}(4ATP)_x(TP)_{18-x}]^-$ clusters follow the trend discussed in chapter III *the more negative the metal core, the more the UV – Vis spectrum is red shifted.*

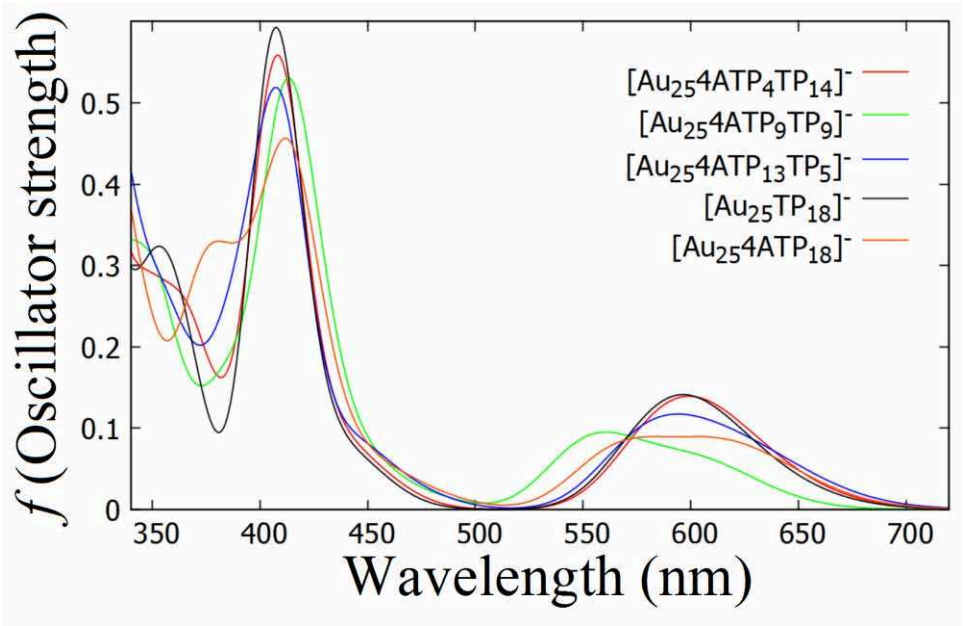

***Figure 18**. Computed UV−vis absorption spectra of the Janus $[Au_{25}(4ATP)_x(TP)_{18-x}]^-$ clusters together with the monoligand protected $[Au_{25}(4ATP)_{18}]^-$ and the $[Au_{25}(TP)_{18}]^-$ at the DFT/CAM – B3LYP level.*

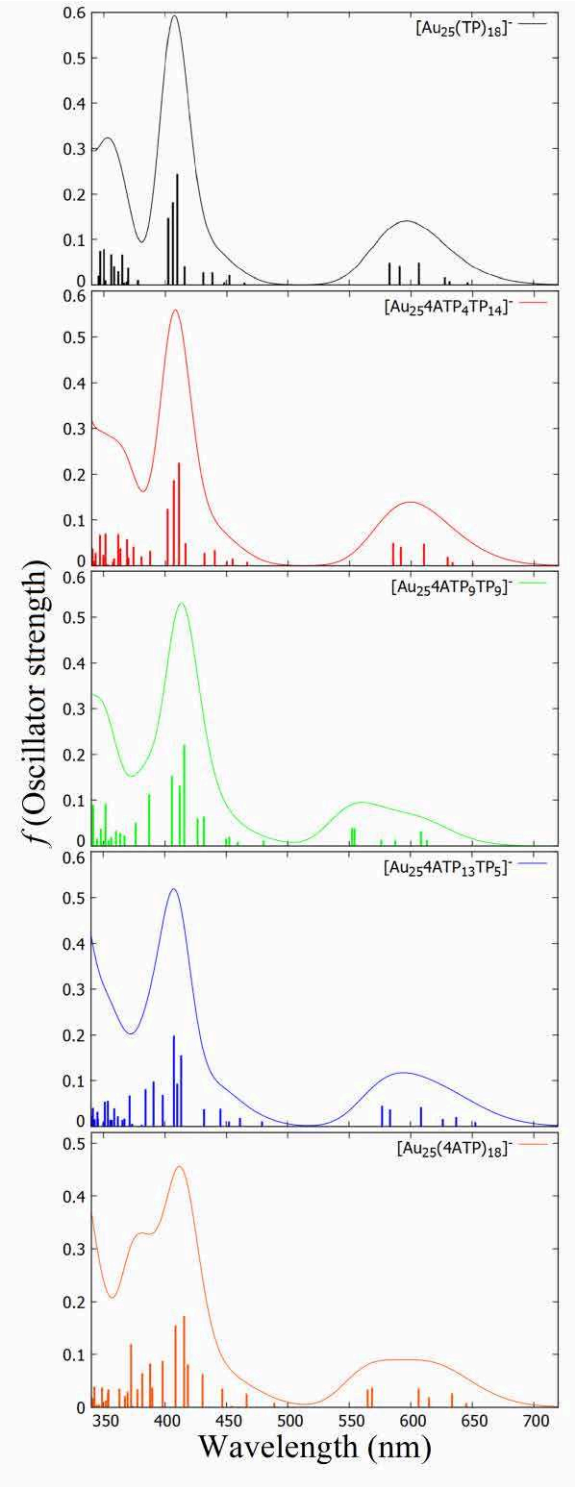

***Figure 19**. Computed UV−vis absorption spectra of the Janus $[Au_{25}(4ATP)_x(TP)_{18-x}]^-$ clusters together with the monoligand protected $[Au_{25}(4ATP)_{18}]^-$ and the $[Au_{25}(TP)_{18}]^-$ at the DFT/CAM – B3LYP level. The height of the vertical bars give the oscillator strength of each transition and the spectra are obtained by convolution with Gaussian line shapes (σ = 0.085 eV).*

***Table 9**. Label, cluster stoichiometry and characteristics of the first and second band of the Janus $[Au_{25}(4ATP)_x(TP)_{18-x}]^-$ clusters.*

Label	Cluster Stoichiometry	First band		Second band	
		Range (nm)	Character	Range (nm)	Character
a	$[Au_{25}(TP)_{18}]^{1-}$	582.73 – 646.20	H → L	402.55 – 464.71	H → L + 1
b	$[Au_{25}(4ATP)_4(TP)_{14}]^-$	585.41 – 650.20	H → L	401.88 – 466.58	H → L + 1
c	$[Au_{25}(4ATP)_9(TP)_9]^-$	552.20 – 613.17	H → L	387.17 – 480.35	H → L + 1
d	$[Au_{25}(4ATP)_{13}(TP)_5]^-$	576.95 – 652.82	H → L	384.50 – 479.23	H → L + 1 H → L + 2 H → L + 3
e	$[Au_{25}(4ATP)_{18}]^{1-}$	546.43 – 645.14	H → L	398.10 – 488.96	H → L + 1 H → L + 2

Table 9 confirm that the same character analysis can be applied as in the monoligand and the previous Janus cluster.

Figure 20 shows the molecular orbital diagram of the Janus $[Au_{25}(4ATP)_x(TP)_{18-x}]^-$ clusters. We can see that, by increasing the amount of 4ATP/TP ratio on the gold surface the degeneracy landscape resembles to the monoligated $[Au_{25}(4ATP)_{18}]^-$ cluster. The trends also applies on the other sense. Figure 21 confirms that the p – and d – SAMO shape is preserved in the mixed ligand shell protected anion Au_{25}.

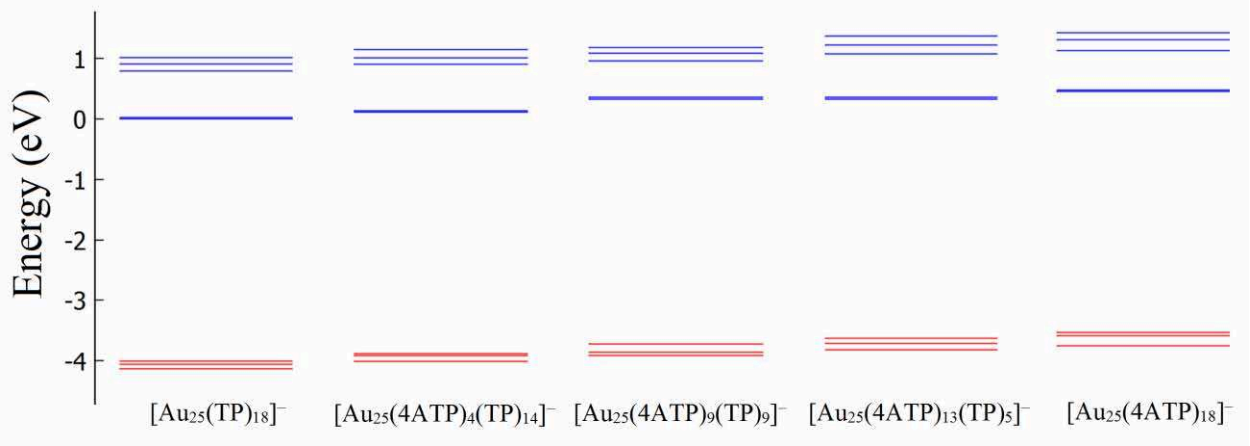

***Figure 20**. Molecular orbital diagram of the Janus $[Au_{25}(4ATP)_x(TP)_{18-x}]^-$ clusters at the DFT/CAM – B3LYP level. The red bars are the p – SAMO three – fold quasi – degenerate HOMO (HOMO – 1, HOMO – 1 and HOMO – 2) and the blue bars stand for the 5 d – SAMO; the two degenerate LUMO and the 3 – fold quasi – degenerate LUMO + 1.*

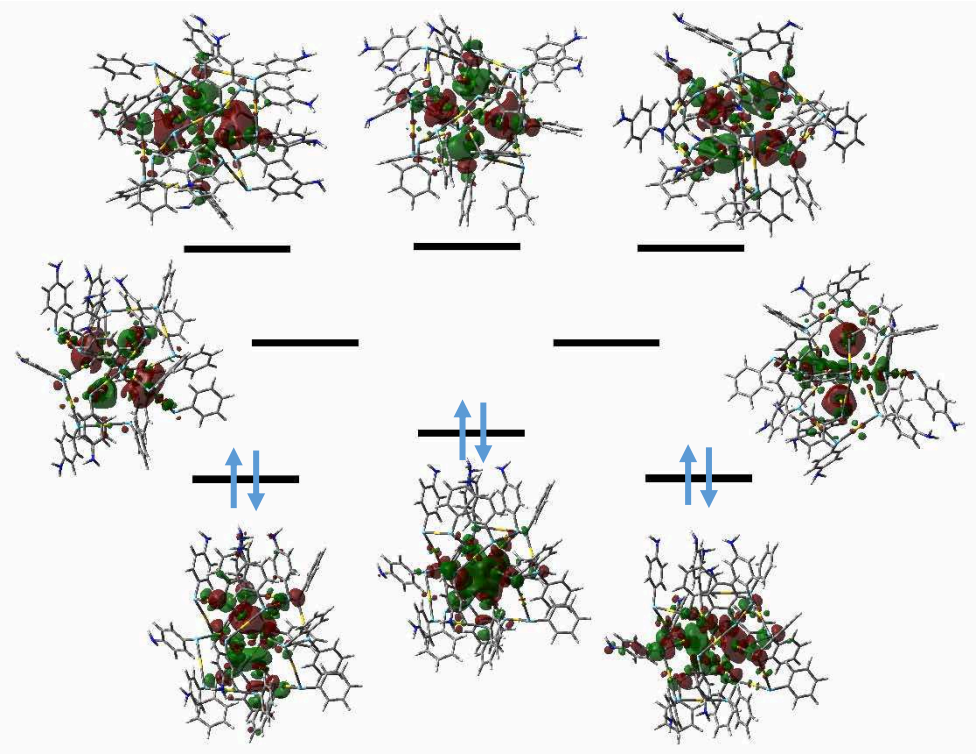

***Figure 21**. Schematic representation of the energy levels (with a degeneracy threshold of 0.13 eV) together with the isocontour of the corresponding orbitals (isovalue 0.02 $Å^{-3}$) of the Janus $[Au_{25}(4ATP)_9(TP)_9]^-$ cluster at the DFT/CAM – B3LYP level.*

4.3 Conclusion

We employed density functional theory to study the effect of different ligands on the geometric structure and optical properties of the thiolate – protected 25 – atom gold nanocluster in its anionic charge state. The two thiolate – ligand protected anion Au_{25} was also explored at different ligand ratios.

Our study shows that the exchange of thiolate ligands as well the used a mixed ligand shell to protect the metal core does not induce a significant distortion on it which confirms the stability of the Au_{25} structure. In the monoligand capped case, the molecular orbitals energies are highly affected by the exchange of thiolates however the general landscape is not modified.

Our computations confirm that the Janus mixed ligand capped 25 – gold cluster preserves its electronic structure. It is possible to see that in both Janus set of clusters studied here ($[Au_{25}(TP)_{16}(S(CH_2)_xCOOH)_{18-x}]^-$ and $[Au_{25}(4ATP)_x(TP)_{18-x}]^-$) the position of the lowest energy band does not vary linearly with the ligand ratio. No trends has been found either for the partial charge on the Au_{13} core. However, the blue shift in the $[Au_{25}(4ATP)_9(TP)_{9x}]^-$ and the fact that it shows the less negative Au_{13} core partial charge show that the trend discussed in chapter III is valid.

4.4 References

1. Zhu, M., C.M. Aikens, F.J. Hollander, G.C. Schatz, and R. Jin, *Correlating the Crystal Structure of A Thiol-Protected Au25 Cluster and Optical Properties.* Journal of the American Chemical Society, 2008. **130**(18): p. 5883-5885.
2. Shichibu, Y. and K. Konishi, *HCl-Induced Nuclearity Convergence in Diphosphine-Protected Ultrasmall Gold Clusters: A Novel Synthetic Route to "Magic-Number" Au13 Clusters.* Small, 2010. **6**(11): p. 1216-1220.
3. Lavenn, C., F. Albrieux, G. Bergeret, R. Chiriac, P. Delichere, A. Tuel, and A. Demessence, *Functionalized gold magic clusters: Au25(SPhNH2)17.* Nanoscale, 2012. **4**(23): p. 7334-7337.
4. Shichibu, Y., K. Suzuki, and K. Konishi, *Facile synthesis and optical properties of magic-number Au13 clusters.* Nanoscale, 2012. **4**(14): p. 4125-4129.
5. Pei, Y., Y. Gao, and X.C. Zeng, *Structural Prediction of Thiolate-Protected Au38: A Face-Fused Bi-icosahedral Au Core.* Journal of the American Chemical Society, 2008. **130**(25): p. 7830-7832.
6. Guo, R. and R.W. Murray, *Substituent Effects on Redox Potentials and Optical Gap Energies of Molecule-like Au38(SPhX)24 Nanoparticles.* Journal of the American Chemical Society, 2005. **127**(34): p. 12140-12143.
7. Lugo, G., V. Schwanen, B. Fresch, and F. Remacle, *Charge Redistribution Effects on the UV–Vis Spectra of Small Ligated Gold Clusters: a Computational Study.* The Journal of Physical Chemistry C, 2015.
8. Tlahuice-Flores, A., R.L. Whetten, and M. Jose-Yacaman, *Ligand Effects on the Structure and the Electronic Optical Properties of Anionic Au25(SR)18 Clusters.* The Journal of Physical Chemistry C, 2013. **117**(40): p. 20867-20875.
9. Goel, S., K.A. Velizhanin, A. Piryatinski, S.A. Ivanov, and S. Tretiak, *Ligand Effects on Optical Properties of Small Gold Clusters: A TDDFT Study.* The Journal of Physical Chemistry C, 2012. **116**(5): p. 3242-3249.
10. Wu, Z. and R. Jin, *On the Ligand's Role in the Fluorescence of Gold Nanoclusters.* Nano Letters, 2010. **10**(7): p. 2568-2573.
11. Weerawardene, K.L.D.M. and C.M. Aikens, *Effect of Aliphatic versus Aromatic Ligands on the Structure and Optical Absorption of Au20(SR)16.* The Journal of Physical Chemistry C, 2016. **120**(15): p. 8354-8363.
12. Aikens, C.M., *Effects of Core Distances, Solvent, Ligand, and Level of Theory on the TDDFT Optical Absorption Spectrum of the Thiolate-Protected Au25 Nanoparticle.* The Journal of Physical Chemistry A, 2009. **113**(40): p. 10811-10817.
13. Zeng, C., C. Liu, Y. Pei, and R. Jin, *Thiol Ligand-Induced Transformation of Au38(SC2H4Ph)24 to Au36(SPh-t-Bu)24.* ACS Nano, 2013. **7**(7): p. 6138-6145.
14. Si, S., C. Gautier, J. Boudon, R. Taras, S. Gladiali, and T. Bürgi, *Ligand Exchange on Au25 Cluster with Chiral Thiols.* The Journal of Physical Chemistry C, 2009. **113**(30): p. 12966-12969.
15. Shichibu, Y., Y. Negishi, T. Tsukuda, and T. Teranishi, *Large-Scale Synthesis of Thiolated Au25 Clusters via Ligand Exchange Reactions of Phosphine-Stabilized Au11 Clusters.* Journal of the American Chemical Society, 2005. **127**(39): p. 13464-13465.
16. Johnson, G.E., T. Priest, and J. Laskin, *Synthesis and Characterization of Gold Clusters Ligated with 1,3-Bis(dicyclohexylphosphino)propane.* ChemPlusChem, 2013. **78**(9): p. 1033-1039.
17. Chen, Y., C. Zeng, D.R. Kauffman, and R. Jin, *Tuning the Magic Size of Atomically Precise Gold Nanoclusters via Isomeric Methylbenzenethiols.* Nano Letters, 2015. **15**(5): p. 3603-3609.

18. Shibu, E.S., M.A.H. Muhammed, T. Tsukuda, and T. Pradeep, *Ligand Exchange of Au25SG18 Leading to Functionalized Gold Clusters: Spectroscopy, Kinetics, and Luminescence.* The Journal of Physical Chemistry C, 2008. **112**(32): p. 12168-12176.
19. Pichugina, D.A., N.E. Kuz'menko, and A.F. Shestakov, *Ligand-protected gold clusters: the structure, synthesis and applications.* Russian Chemical Reviews, 2015. **84**(11): p. 1114.
20. Bergeron, D.E., O. Coskuner, J.W. Hudgens, and C.A. Gonzalez, *Ligand Exchange Reactions in the Formation of Diphosphine-Protected Gold Clusters.* The Journal of Physical Chemistry C, 2008. **112**(33): p. 12808-12814.
21. Beqa, L., D. Deschamps, S. Perrio, A.-C. Gaumont, S. Knoppe, and T. Bürgi, *Ligand Exchange Reaction on Au38(SR)24, Separation of Au38(SR)23(SR')1 Regioisomers, and Migration of Thiolates.* The Journal of Physical Chemistry C, 2013. **117**(41): p. 21619-21625.
22. Wang, B., B. Li, B. Zhao, and C.Y. Li, *Amphiphilic Janus Gold Nanoparticles via Combining "Solid-State Grafting-to" and "Grafting-from" Methods.* Journal of the American Chemical Society, 2008. **130**(35): p. 11594-11595.
23. Glaser, N., D.J. Adams, A. Böker, and G. Krausch, *Janus Particles at Liquid–Liquid Interfaces.* Langmuir, 2006. **22**(12): p. 5227-5229.
24. Vilain, C., F. Goettmann, A. Moores, P. Le Floch, and C. Sanchez, *Study of metal nanoparticles stabilised by mixed ligand shell: a striking blue shift of the surface-plasmon band evidencing the formation of Janus nanoparticles.* Journal of Materials Chemistry, 2007. **17**(33): p. 3509-3514.
25. Kim, H., R.P. Carney, J. Reguera, Q.K. Ong, X. Liu, and F. Stellacci, *Synthesis and Characterization of Janus Gold Nanoparticles.* Advanced Materials, 2012. **24**(28): p. 3857-3863.
26. Lattuada, M. and T.A. Hatton, *Synthesis, properties and applications of Janus nanoparticles.* Nano Today, 2011. **6**(3): p. 286-308.
27. Carney, R.P., G.A. DeVries, C. Dubois, H. Kim, J.Y. Kim, C. Singh, P.K. Ghorai, J.B. Tracy, R.L. Stiles, R.W. Murray, S.C. Glotzer, and F. Stellacci, *Size Limitations for the Formation of Ordered Striped Nanoparticles.* Journal of the American Chemical Society, 2008. **130**(3): p. 798-799.
28. Cesbron, Y., C.P. Shaw, J.P. Birchall, P. Free, and R. Lévy, *Stripy Nanoparticles Revisited.* Small, 2012. **8**(24): p. 3714-3719.
29. Jackson, A.M., Y. Hu, P.J. Silva, and F. Stellacci, *From Homoligand- to Mixed-Ligand- Monolayer-Protected Metal Nanoparticles: A Scanning Tunneling Microscopy Investigation.* Journal of the American Chemical Society, 2006. **128**(34): p. 11135-11149.
30. Jackson, A.M., J.W. Myerson, and F. Stellacci, *Spontaneous assembly of subnanometre-ordered domains in the ligand shell of monolayer-protected nanoparticles.* Nat Mater, 2004. **3**(5): p. 330-336.
31. Fresch, B., E. Hanozin, F. Dufour, and F. Remacle, *Interplay of structural and electronic stabilizing factors in neutral and cationic phosphine protected Au13 clusters.* The European Physical Journal D, 2012. **66**(12): p. 1-9.
32. Aikens, C.M., *Geometric and Electronic Structure of Au25(SPhX)18− (X = H, F, Cl, Br, CH3, and OCH3).* The Journal of Physical Chemistry Letters, 2010. **1**(17): p. 2594-2599.
33. Jin, R., *Quantum sized, thiolate-protected gold nanoclusters.* Nanoscale, 2010. **2**(3): p. 343-362.
34. Heaven, M.W., A. Dass, P.S. White, K.M. Holt, and R.W. Murray, *Crystal Structure of the Gold Nanoparticle [N(C8H17)4][Au25(SCH2CH2Ph)18].* Journal of the American Chemical Society, 2008. **130**(12): p. 3754-3755.
35. Zeng, C., T. Li, A. Das, N.L. Rosi, and R. Jin, *Chiral Structure of Thiolate-Protected 28-Gold-Atom Nanocluster Determined by X-ray Crystallography.* Journal of the American Chemical Society, 2013. **135**(27): p. 10011-10013.

36. Qian, H., W.T. Eckenhoff, Y. Zhu, T. Pintauer, and R. Jin, *Total Structure Determination of Thiolate-Protected Au38 Nanoparticles.* Journal of the American Chemical Society, 2010. **132**(24): p. 8280-8281.
37. Hakkinen, H., *Atomic and electronic structure of gold clusters: understanding flakes, cages and superatoms from simple concepts.* Chemical Society Reviews, 2008. **37**(9): p. 1847-1859.
38. Aikens, C.M., *Origin of Discrete Optical Absorption Spectra of M25(SH)18− Nanoparticles (M = Au, Ag).* The Journal of Physical Chemistry C, 2008. **112**(50): p. 19797-19800.
39. Hay, P.J. and W.R. Wadt, *Ab initio effective core potentials for molecular calculations. Potentials for the transition metal atoms Sc to Hg.* The Journal of Chemical Physics, 1985. **82**(1): p. 270-283.
40. Hay, P.J. and W.R. Wadt, *Ab initio effective core potentials for molecular calculations. Potentials for K to Au including the outermost core orbitals.* The Journal of Chemical Physics, 1985. **82**(1): p. 299-310.
41. Knoppe, S., S. Malola, L. Lehtovaara, T. Bürgi, and H. Häkkinen, *Electronic Structure and Optical Properties of the Thiolate-Protected Au28(SMe)20 Cluster.* The Journal of Physical Chemistry A, 2013. **117**(40): p. 10526-10533.
42. Häkkinen, H., M. Walter, and H. Grönbeck, *Divide and Protect: Capping Gold Nanoclusters with Molecular Gold−Thiolate Rings.* The Journal of Physical Chemistry B, 2006. **110**(20): p. 9927-9931.
43. Shichibu, Y., Y. Negishi, H. Tsunoyama, M. Kanehara, T. Teranishi, and T. Tsukuda, *Extremely High Stability of Glutathionate-Protected Au25 Clusters Against Core Etching.* Small, 2007. **3**(5): p. 835-839.

Chapter V. Experimental approach to gold nanocluster synthesis and characterization

Introduction

It is well known that gold nanoclusters are not stable in their bare configuration while presenting size dependent properties. [1-3] Ligand protection is therefore required to preserve their structure and properties. Synthesis of gold nanocluster (GNC) is a very challenging task since their size, nuclearity, shape and stability are highly dependent on the reaction conditions and the ligand used to limit the core growth and to protect the metal core.[4-6]

Extensive work on the synthesis of ligand protected GNCs has been done in recent years yielding ultra-small stable particles characterized by defined stoichiometries and sizes. For instance, Jin *et al.* reported the synthesis of the $Au_{25}(GSH)_{18}$ (GSH being glutathione ligand) in organic solvent [7] as well as the large scale synthesis of $Au_{38}(GSH)_{24}$ cluster. [8] The $[Au_{13}dppe_5Cl_2]^{3+}$ and the family of $[Au_{13}P_8Cl_4]^{+}$ clusters were also obtained by Konishi and co – workers (dppe being $Ph_2P{-}(CH_2)_2{-}PPh_2$ ligand). [9] Synthesis of other ligand protected GNCs with different nuclearities can be reproduced, for instance; $Au_{55}(PPh_3)_{12}Cl_6$,[10] $Au_{102}(SR)_{44}$,[11] $Au_{144}(SR)_{60}$,[12] (with SR representing a thiolate ligand).

Due to their ultra – small size intermediate between nanoparticles and molecular organometallic species, complete GNCs characterization is very difficult to achieve. For instance, ligand organization on the metal surface which has a significant impact on the surface and optical properties of GNCs [9, 13-16] remains in most cases elusive. Fortunately, techniques such as electrospray ionization (ESI – MS), matrix – assisted laser desorption/ionization (MALDI – ToF) and ion mobility (IMS – MS) mass spectrometry, X – Ray diffraction, UV – Vis and FT – IR spectroscopy together with small – angle X – Ray scattering (SAXS) offer very good insights on the structure determination of metal clusters.[9, 16-27]

It is the versatility of the gold nanocluster surface which motivates the study of the effect of the ligand shell on the structural and optical properties of the GNC structure. Not only the use of different ligands leads to a wide range of potential applications but also the combination of different ligands can be used to tune the surface and optical properties of GNCs. Moreover, as mentioned above, mixtures of different ligands protecting the metal surface can form different ligand domains (Janus, [28-31] stripe [32, 33] or pitchy/randomly organized) raising the possibility of further controlling the properties of the nanocluster by engineering the ligand shell. [34]

Even though the systems discussed here are typically described from the synthetic and characterization point of view as ultra – small, from a computational perspective they are huge systems to deal with. In the present work, I nonetheless show that experimental and computational methodologies can

be used in a complementary way to shed light on the structure and to understand the relation between the structure and physicochemical properties of GNCs.

Among the already mentioned GNCs, the $[Au_{25}(SR)_{18}]^-$ cluster (SR being a thiolate ligand) have been studied in great details. This cluster has been found to be stable [35, 36] with protocols of synthesis available for various thiolate ligands, [23, 36-41]. Many are well characterized [17, 27, 42-44] and display potential for applications. [35, 45-50]

On the other hand, two different ligand – protected GNCs have been synthesized in recent years using ligand – exchange reaction.[18, 36, 51, 52] Experimental and computational work show that it is possible to modify the optical, [50] chemical reactivity, [53] and surface properties of gold clusters by substituting all or some of the ligands on the metal surface while keeping the cluster nuclearity. Bürgi *et al.* showed strong optical activity at very short ligand-exchange reaction times and also that the amount of ligands exchanged depends on the structure of the staple moiety in the Au_{38} and Au_{40} clusters. [18] Other studies show that the optical profile of GNC is highly dependent on the organization of the ligands on the metal surface and on the ratio between ligands (i.e. ligand A / ligand B) [9, 13, 54] Therefore understanding the mechanism of this process, the effect of the nature and organization of ligands, the core morphology and the interaction among ligands are essential for the rational design of materials and devices based on gold clusters.

In this chapter, we aim to synthesize the Au_{25} cluster using different ligands: 4 – aminothiophenol (4ATP), thiophenol (TP), 2 – naphthalenethiol (2NT), 1 – dodecanethiol (DDT), phenylethylthiol (PETH) and 4 – mercaptobenzoic acid (4MA)using the technique developed by Demessence *et al*. [23] as well as to perform the characterization of their structural and optical properties.

As a first step, the single-ligand capped Au_{25} cluster synthesis was carried out by adapting the Demessence's protocol to the 4ATP, TP, 2NT, DDT, PETH and 4MA ligands. In a second step, dual – ligand protected Au_{25} clusters were synthesized by combining 4ATP, TP and DDT and adding them simultaneously to the reaction solution. The three different combinations were investigated (4ATP/TP, TP/DDT and 4ATP/DDT). ESI – MS evidences that, by adding 4ATP and TP to the reaction solution the Au_{25} nuclearity is preserved and we obtain a set of $Au_{25}(4ATP)_x(TP)_{18-x}$ clusters with different 4ATP/TP ratio. In the case of the other two combinations where DDT is involved, instable GNCs were obtained leading to aggregation and the formation of nanoparticles.

Finally, ESI-MS, IMS-MS, UV-Vis and FT-IR spectroscopy, TEM and SAXS techniques were used to characterize clusters synthesized.

5.1 Synthesis and characterisation of the $Au_{25}(TP)_{18}$ and $Au_{25}(4ATP)_{18}$ nanoclusters

5.1.1 Synthesis protocol of the $Au_{25}(TP)_{18}$ and $Au_{25}(4ATP)_{18}$ nanoclusters

Demessence's synthesis methodology [23] was used to obtain the $Au_{25}(4ATP)_{18}$ cluster and also adapted to other ligands shown in table 1. Gold (III) chloride trihydrate ($HAuCl_4 – 3H_2O$), a reducing agent ($LiBH_4$) and tetrahydrofuran (THF) as solvent have been used in the synthesis process.

All ligand protected cluster syntheses follow the same methodology pattern except in the thiophenol case where longer stirring time (24 hours) and solution A and C addition rates of 45 ml / h have been used. Figure 1 shows a scheme of the cluster synthesis and the quantity of every substance used in the process is reported in tale 1. The reaction was carried below room temperature.

Among all single ligand protected cluster synthesized only three presented a black/brownish coloration (4ATP, TP and DDT protected clusters) which is an indication of GNC formation.[55] The others ligands did not lead to this trend. For the other ligands (4MA, 2NT, and PETH) nanoclusters were not obtained therefore, we are only going to describe the results for 4ATP, TP and DDT.

The protocol used is the following:

1. Preparation of solution **A, B** and **C**:

    - **Solution A.** 60 mg of lithium borohydride ($LiBH_4$) are dissolved in 25 ml of tetrahydrofuran (THF) and let under stirring for 30 min.
    - **Solution B.** In a 100 ml flask, the indicated ligand mass (in table 1) is dissolved in 20 ml of THF and let under stirring at 500 rpm. Solution B (still under stirring) is put in an ice bath. Tempeture has to be below 25° C.
    - **Solution C.** The indicated mass of $HAuCl_4 – 3H_2O$ is dissolved (in table 1) in 25 ml of THF.

2. Reaction: 20 ml of solutions A and C, are added in solution B at a rate of 60 ml / h (45 ml / h only for TP) under stirring. Figure 1 shows a scheme of the syntesis procedure. After solutions A and C have been added, we let the reaction 5 hours under stirring at 500 rpm keeping the temperature below 25° C. (Only, in the TP coated cluster synthesis, the reaction was kept 24 h under stirring). A black / brownish solution will be produced. In the case of 4ATP a black precipitate is formed.
3. Purification: the THF is eliminated under reduce pressure at 40 °C and 300 mbar. Next, the black solid is centrifugated 3 times and watched using ethanol at 8000 rpm for 15 min. Finally, the solid is dried with air.

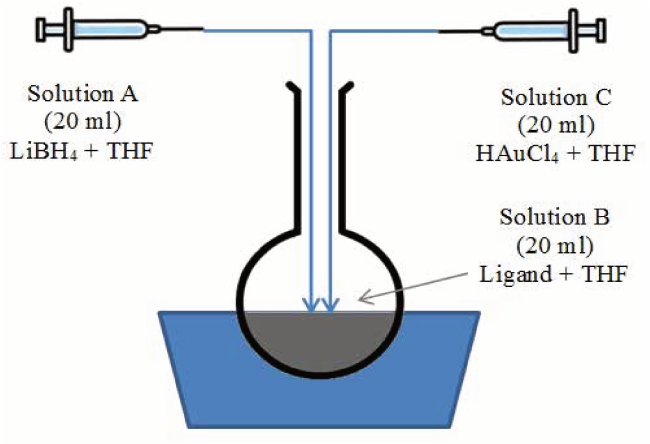

Figure 1. *Scheme of the synthesis of ligated Au_{25} cluster. Rate of addition of solution A and C was 60 ml/ h except for TP for which a rate of 45 ml / h was used. Stirring rate was 500 rpm. Quantities of ligand, reductant agent and the $HAuCl_4$– $3H_2O$ are specified in table 1.*

Table 1. *Substance used in the synthesis of the single ligated Au_{25}, quantities in mmol and mg, structural formula of every ligand and the mass of solvent (THF) is shown.*

Substance	Label	Mass		Structural	Solvent: THF
		(mmol)	(mg)	Formula	(ml)
$HAuCl_4 – 3H_2O$	–	0.53	260	–	25
$LiBH_4$	–	2.11	60	–	25
4 – Mercaptobenzoic acid	4MA	2.11	293	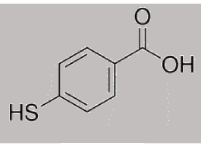	20
4 – Aminothiophenol	4ATP	1.06	128.2	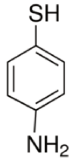	20
2 – Naphthalenethiol	2NT	2.11	335.1	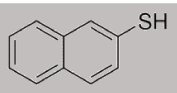	20
Thiophenol	TP	2.11	227	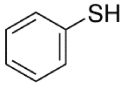	20
Phenylethylthiol	PETH	2.11	286	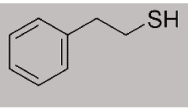	20
Dodecanethiol	DDT	2.11	419	$CH_3(CH_2)_{10}CH_2SH$	20

Reduction of the Au(III) precursor was quite fast. The solution started to change color after 1 – 3 min.[23] Due to the fast reduction rate, the nucleation process could not be monitored in real time.

5.1.2 Characterization of the $Au_{25}(TP)_{18}$ and $Au_{25}(4ATP)_{18}$ nanoclusters

Characterization of the clusters synthesized have been performed at the Laboratoire de la chimie de la matière condensée de Paris (LCMCP) at the UPMC except for the ESI – MS and the IMS – MS measurements which have been done at the Karlsruhe Institute of Technology, Germany under the supervision of Prof. B. Leyh (ULg) and Dr. J.-F Greisch (KIT).

5.1.2.1 FT – IR spectroscopy

The infrared spectra were obtained on a Perkin Elmer spectrum 400 FT – IR / FT – NIR spectrometer with KBr pellets at room temperature in a transmittance range between 500 and 4000 cm^{-1}. In figure 2 we present the FT – IR spectra of the single ligand coated clusters. FT – IR spectra confirm that all thiolate ligands are coordinated to the gold atoms by the disappearance of the S – H stretching band (2535 – 2564 cm^{-1}). [27] Figure 2a, 2b and 2c show the infrared spectra of the synthesized clusters protected only by 4ATP, TP and DDT respectively.

Comparison of the spectra of the GNCs synthesized with those measured for the ligands (alone) allows us to identify and interpret the signals found. In figure 2a (gold clusters protected by 4ATP) we observe the characteristic signal of the **N – H stretching** at 3343.59 cm^{-1} indicating the presence of the NH_2 group in the 4ATP absorbed on the gold surface. The presence of the **C – C stretching** at 1488.98 cm^{-1} confirms the existence of benzene rings, as well as the **C – H stretching** of the aromatic ring at 2962.74 cm^{-1}. We can also observe at 1614.75 cm^{-1} the **bending** of the N – H bond proving again the presence of the NH_2 and therefore the 4ATP coordinating the gold core.

Figure 2b shows the single TP protected cluster FT – IR spectrum. It is possible to see at 3051.53 cm^{-1} the **(sp^2) C – H stretching** mode, the **double C – C bond stretching** at 1576.26 cm^{-1} and 1472.60 cm^{-1} which indicate the presence of benzene rings.

Finally, figure 2c shows the infrared spectrum of the gold clusters coordinated by DDT. At 2919.11 cm^{-1} we have the characteristic **C – H asymmetric stretching** of an aliphatic organic chain. While at 2848.69 cm^{-1} we can see the **symmetric stretching** of the same bonds. At 1468.15 cm^{-1} we have the signal of the **C – H bending** and finally we can observe the **C – H rocking** at 801.92 cm^{-1}.

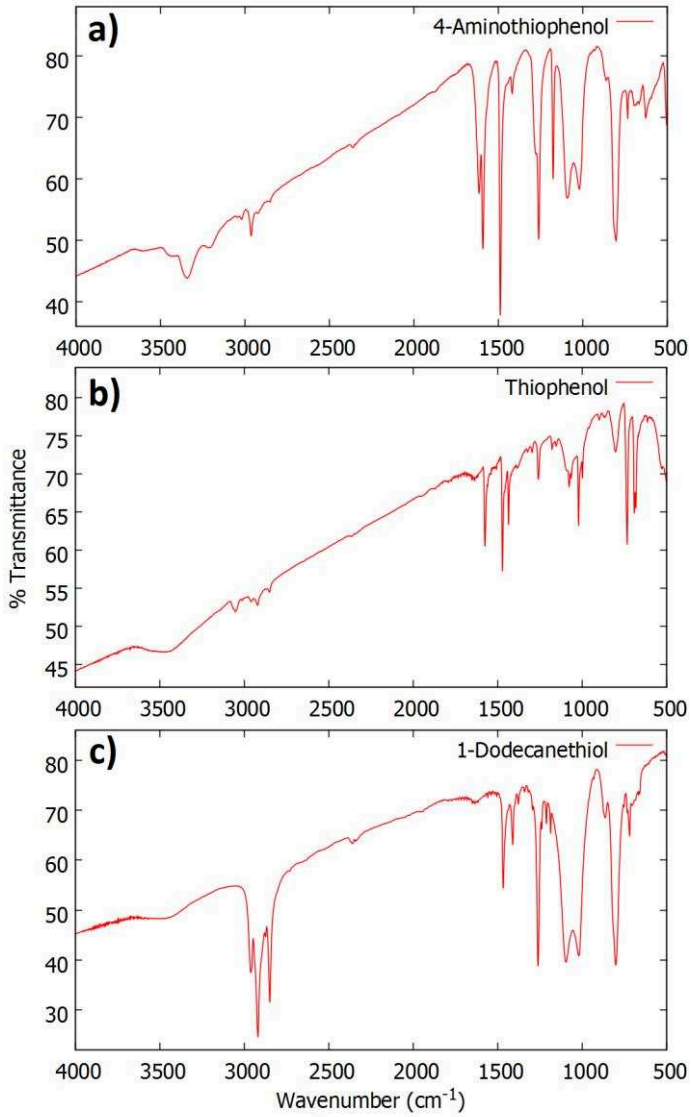

Figure 2. *FT – IR spectra of the single ligand protected gold clusters by 4ATP (a), TP (b) and DDT (c). The ligand used for cluster protection is indicated at the top right of every spectrum. 4ATP stands for 4 – aminothiophenol, TP for thiophenol and DDT for 1 – dodecanethiol.*

5.1.2.2 Transmission electron microscopy (MET)

Transmission electron microscopy (TEM) characterisation was carried out using a FEI Tecnai G2 Spirit instrument operating on acceleration tension of 120 kV. The measurements were performed under the supervision of Dr. Patrick Legriel. TEM samples were prepared by dispersing the gold clusters in formaldehyde or tetrahydrofuran (THF) and then placing a drop of the suspension on a carbon coated Cu grid. After solvent evaporation the samples were ready.

Figure 3 shows the TEM micrograph of the TP protected gold clusters synthesized by the Demessence's method. We can see the formation of aggregates larger than 10 nm. Figure 3 (right) also shows the cluster size distribution. Particle diameter ranges from 0.63 to 4.91 nm, with an average diameter of 1.10 ± 0.51 nm. It is worth to mention that the aggregates make the determination of the size distribution very complicated.

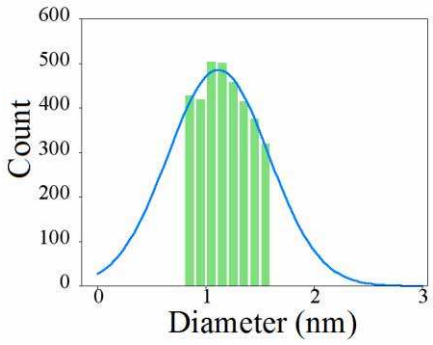

Figure 3. *TEM images of TP gold clusters synthesized by the Demessence method. The cluster size distribution is shown at the right. The average diameter is 1.10 ± 0.51 nm. 480 clusters were taken into account to obtain the size distribution in THF.*

TEM images in figure 4 shows the formation of large aggregate for the 4ATP coated gold clusters (as for the TP protected ones). In the 4ATP protected cluster case, the average particle diameter is 1.23 ± 0.20 nm. 1.08 nm and 2.35 nm have been found in computations at the DFT CAM – B3LYP level for the Au_{25} core and the cluster with ligands included, respectively. Again, the presence of these aggregates makes very challenging the performance of the statistics on the TEM micrographs.

TEM images of the DDT protected cluster synthesized are shown in figure 5. The particle has an average value of 1.05 ± 0.68 nm.

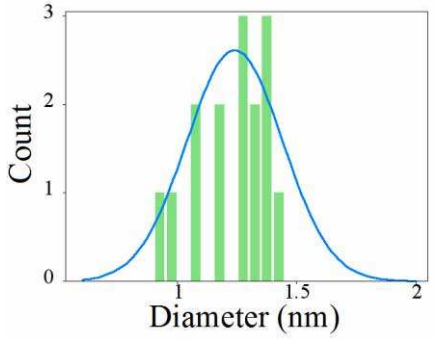

Figure 4. *TEM image of 4ATP gold clusters synthesized by the Demessence method. The cluster size distribution is shown at the right. The average diameter is 1.23 ± 0.20 nm. Only 74 clusters were taken into account to obtain the size distribution due to the aggregates formed.*

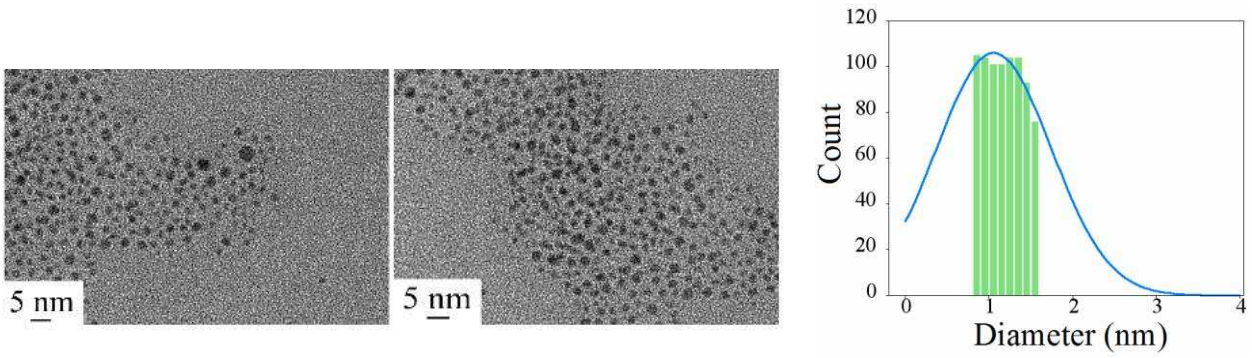

Figure 5. *TEM image of DDT gold clusters synthesized by the Demessence method. The cluster size distribution is shown at the right. The average diameter is 1.05 ± 0.68 nm. 1443 clusters were taken into account to obtain the size distribution.*

5.1.2.3 Small – angle X – ray scattering (SAXS)

Small-angle X-ray scattering (SAXS) characterization was performed to study the size of the single-ligand capped clusters synthesized under the supervision of Dr. Mohamed Selmane at UPMC. The SAXS profiles of the sample powders were collected in transmission mode using a Rigaku S – Max 3000 diffractometer (0.45 kV; Cu−Kα radiation; λ = 1.54056 Å) with a 2D gas detector Gabriel type. Sample alignment and premeasurement scan were carried out before each SAXS measurement. The maximum time taken for each SAXS data acquisition was 60 min. The SAXSGUI software of Rigaku was used to solve the SAXS profiles. Data collected from SAXS measurements are summarized in table 2 and shown in figure 7. The distance measure by SAXS corresponds to that between the two central gold atoms as can be seen in figure 6. It can be seen that different ligand protection leads to a different distances, as expected.

Table 2. *q Vector and calculated distance (d) between to gold clusters collected from SAXS analysis of the clusters synthesized.*

Cluster Stoichiometry	q ($Å^{-1}$)	d (nm)
$Au_n(TP)_{18}$	0.46	1.38
Au_n $(4ATP)_{18}$	0.42	1.51
Au_n $(DDT)_n$	0.37	1.70

The obtained *q* vectors values are used to calculate the interparticle distance as shown in table 2. Crystallographic data reported a gold core diameter of 0.98 nm in the well – known $Au_{25}(SCH_2CH_2Ph)_{18}$ cluster. [43] Our computations for the single ligand capped GNCs at the DFT level in the gas phase (in chapter IV, section 4.1) show in the case of $Au_{25}(4ATP)_{18}$ a core diameter of 1.08 nm, 1.06 nm for the $Au_{25}(SCH_3)_{18}$ and 1.08 nm for the $Au_{25}(TP)_{18}$, $Au_{25}(SPhPh)_{18}$ and the $Au_{25}(SPhPhPh)_{18}$ clusters. Our computations show that the size of the cluster does not experiences a significant distortion when the ligand

is replaced (as far as we used the already mentioned thiolates). Using the computational assumption to the SAXS measurements and then, taking the 0.98 nm found for the $Au_{25}(SCH_2CH_2Ph)_{18}$ cluster as a reference, it is possible to calculate the width of the ligand shell. We obtain a 0.53 nm ligand layer for the $Au_{25}(4ATP)_{18}$ cluster, which is in good agreement with Demessence *et al.* [23] And 0.40 nm for the $Au_{25}(TP)_{18}$ cluster. As expected, the thickness of the ligand layer is larger in the $Au_{25}(4ATP)_{18}$ cluster which can be attributed to the presence of the NH_2 group in 4ATP.

The DDT protected cluster was also explored by SAXS. Table 2 shows an interparticle distance of 1.70 nm which leads to a 0.72 nm shell width between two GNCs. It is possible to see that SAXS shows good agreement between the size of the ligand and the interparticle distance.

Our computations (in chapter IV, section 4.1) show that the total diameter for the $Au_{25}(TP)_{18}$ cluster (i.e. ligand layer included) is 2.16 nm which leads to a 0.54 nm TP layer. For the $Au_{25}(4ATP)_{18}$ a 2.35 nm total diameter is found which leads to a 0.64 nm 4ATP layer width. Demessence *et al.* suggest that ligands shell on GNCs can interpenetrate each other.[23] We have to recall the fact that our calculations are performed in the gas phase which could explain the differences in the calculated sizes and those measured by SAXS.

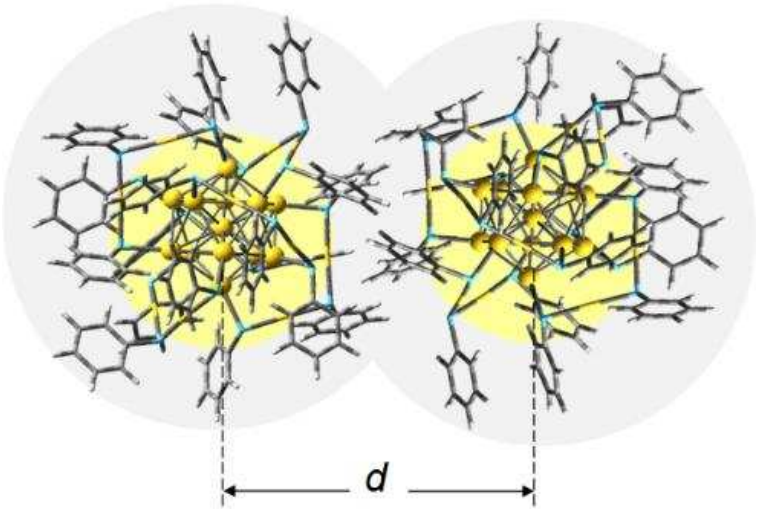

Figure 6. *Schematic representation of the distance measure by the SAXS technique.*

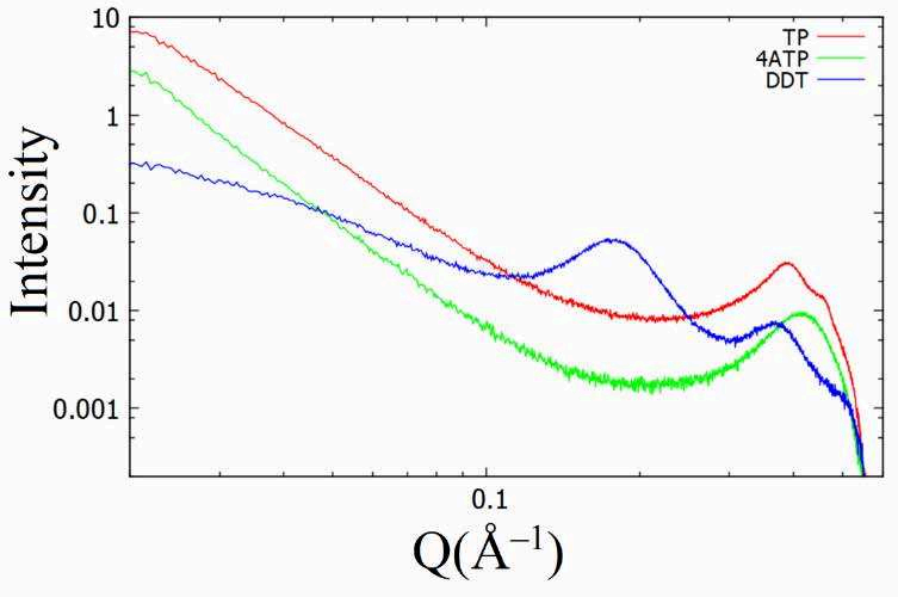

Figure 7. SAXS profiles of the $Au_{25}(TP)_{18}$ (in red), $Au_{25}(4ATP)_{18}$ (green) and the $Au_n(4ATP)_m$ synthesized. SAXS measurements were performed in powder using a potential difference of 0.45 kV and an electrical current of 0.5 mA. Figure provided by Dr. Mohamed Selmane.

The nuclearity of the $Au_{25}(TP)_{18}$ and the Au25$(4ATP)_{18}$ was confirmed by ESI – MS measurements done by Prof. B. Leyh (ULg) and Dr. J.-F Greisch (KIT), see next section. No specific stoichiometry was found for $Au_n(4ATP)_m$.

5.1.2.4 Electrospray – Ionization (ESI – MS) and ion – mobility (IMS – MS) mass Spectrometry

In this section we report the ESI and IMS mass spectra data for the two $Au_{25}(TP)_{18}$ and $Au_{25}(4ATP)_{18}$ nanoclusters synthesized. The ESI – MS and the IMS – MS data and the arrival time distributions in negative mode were measured using a SYNAPT G2S – HDMS (Waters) mass spectrometer equipped with an electrospray ionization source. The gas used for ion separation was N_2. The experiments were done at the Karlsruhe Institute of Technology, Germany under the supervision of Prof. B. Leyh (ULg) and Dr. J.-F Greisch (KIT).

The analysis on the mass spectrometry results have been carried out by Prof. B. Leyh (ULg) and Dr. J.-F Greisch (KIT). The computation of the TWIMS converted cross – section have been done by Dr. J.-F Greisch (KIT) by using the Mobcal software. [56, 57]

Figure 8 shows the ESI – MS spectrum of the $Au_{25}(TP)_{18}$ cluster acquired in negative mode by dissolving the nanoclusters in dichloromethane (DCM) to a final concentration about 1mg/ml. The negative – ion mass spectrum of $[Au_{25}(TP)_{18}]^-$ is dominated by 2 peaks, the first one near *m/z* = 6890. The splitting between the different isotopes verifies that the core charge state is 1–. A higher negative charge state has

been found as well in figure 8. The $[Au_{25}(TP)_{18}]^{2-}$ cluster is found near *m/z* = 3444. The low mass peaks can be due to impurities in the sample.

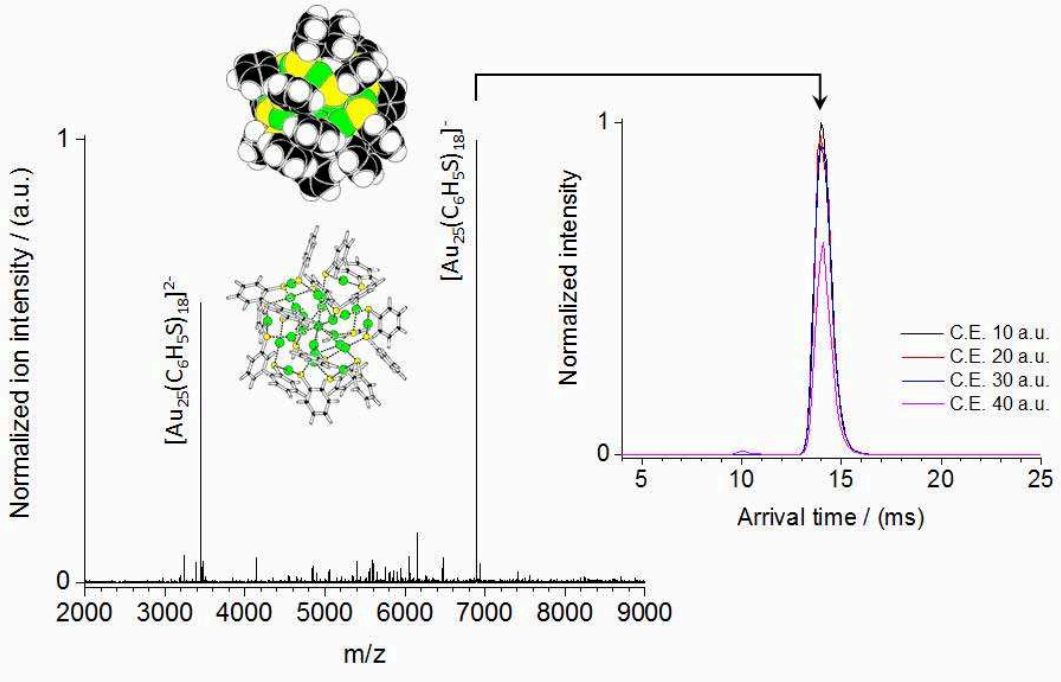

Figure 8. *Negative – mode ESI – MS spectrum of the $[Au_{25}(TP)_{18}]^-$ cluster. The arrival time distribution is shown on the right as an inset. Clusters were analyzed in DCM. Figure provided by Dr. J.-F Greisch (KIT).*

IMS – MS characterization technique was also used to analyze the clusters synthesized. IMS – MS measures the time it takes for an ion to travel to a pressurized cell under the influence of a weak electric field. The speed by which the ions traverse the drift region depends on their size since, shape, charge and *m/z* ratio. Large ions will experience a greater number of collisions with the background gas and thus travel more slowly though the IMS equipment than those ions having a smaller cross-section. Figure 8 also shows (as inset) the arrival time distribution. Here we can see a narrow, symmetric drift time distribution that evidences the presence of only one structure. This indicates that the clusters do not aggregate.

Additionally, in figure 9 the survival yield fragmentation pattern for the $Au_{25}(TP)_{18}$ cluster is shown. It is possible to see that the $[Au_{25}(TP)_{18}]^-$ cluster begins to fragment at collision energies around 40 a.u. (where a.u. stands for arbitrary units) The survival yield fragmentation pattern is characterized by the loss of a $Au_4(TP)_4$ fragment which was observed in the MALDI – ToF – MS spectra and IMS-MS measurements of the $Au_{25}(SCH_2CH_2Ph)_{18}$ [17, 58].

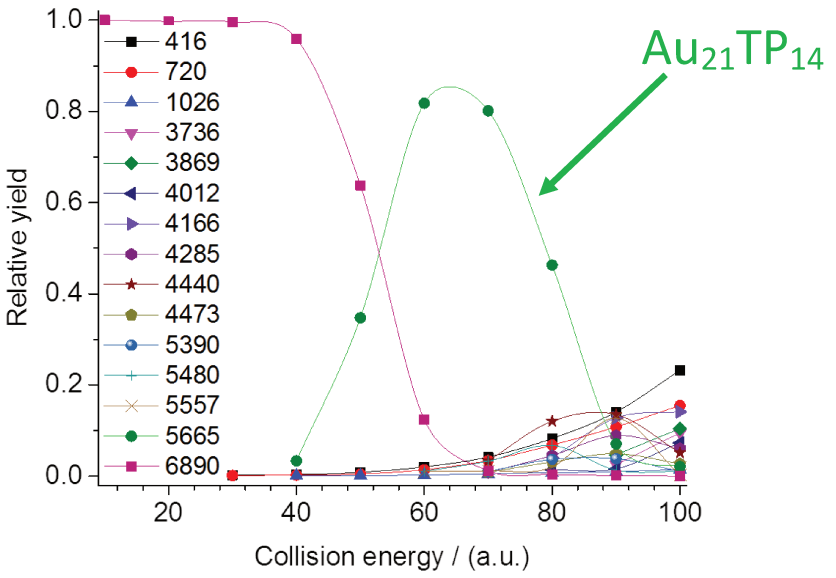

Figure 9. *Survival yield fragmentation pattern for the $[Au_{25}(TP)_{18}]^-$ cluster as a function of the collision energy in arbitrary units (a.u.). Clusters were analyzed in DCM. The inset at the left shows the masses of the different fragments. The purple curve stands for the $[Au_{25}(TP)_{18}]^-$ cluster (6890 Da) while the green curve (5665 Da) represents the $Au_{21}(TP)_{14}$ (i.e. $Au_{25}(TP)_{18} – Au_{21}(TP)_{14}$). The maximum relative yield of the for the $Au_{21}(TP)_{14}$ clusters is found at a collision energy of 64 a.u. Figure provided by Dr. J.-F Greisch (KIT).*

Figure 10 shows the ESI – MS spectrum of the $[Au_{25}(4ATP)_{18}]^-$ cluster acquired in negative mode by dissolving the nanoclusters in dimethyl sulfoxide (DMSO) to a final concentration about 1mg / ml. The negative – ion mass spectrum of $[Au_{25}(4ATP)_{18}]^-$ is dominated by 2 sets of peaks with high intensity, the first one near *m/z* = 7160 which corresponds to the $[Au_{25}(4ATP)_{18}]^-$ and its multicharged multimers (e.g. doubly charged dimer) and the second one (nature unknown) around *m/z* = 3600. The mass to charge interval between the different isotopic peaks confirm that the core charge state is 1– as shown in the inset in figure 10. Other low intensity charge states can also be observed in the ESI – MS spectrum of the $[Au_{25}(4ATP)_{18}]^-$ cluster.

The survival yield fragmentation pattern for the $[Au_{25}(4ATP)_{18}]^-$ cluster is shown in Figure 11. As in the $[Au_{25}(TP)_{18}]^-$ cluster, the loss of a $Au_4(4ATP)_4$ fragment is detected. By comparing the two survival yield fragmentation patterns (in figure 9 and 11), we can observe that, in both cases, around 64 a.u. the Au_4L_4 (L being TP or 4ATP) fragment is liberated indicating that the presence of an amine (NH_2) group does not change significantly the stability of the metal core.

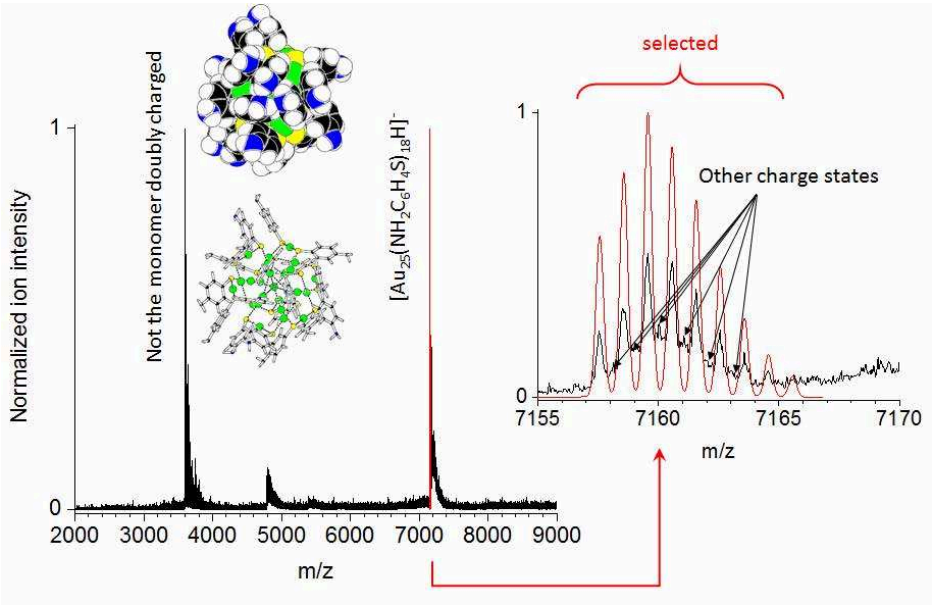

Figure 10. *Negative – mode ESI – MS spectrum of the $[Au_{25}(4ATP)_{18}]^-$ cluster. The inset shows the isotopomer splitting highlighting the presence of other charge states (other than one) in very low intensities. Clusters were analyzed in DMSO. Figure provided by Dr. J.-F Greisch (KIT).*

However, by comparing both survival yield fragmentation patterns (figures 9 and 11) it is possible to notice that for the $Au_{25}(4ATP)_{18}$ cluster (figure 11) the relative yield starts to decrease around 20 a.u. together with an increase of the different fragments population. On the other side, figure 9 shows for the $Au_{25}(TP)_{18}$ cluster that the relative yield remains practically constant until we reach 40 a.u. of collision energy where the different population of different fragments start increasing. This indicates that, in the $Au_{25}(4ATP)_{18}$ cluster solution less stable species with the same m/z are present.

The arrival time distribution for the $[Au_{25}(4ATP)_{18}]^-$ cluster is shown in figure 12. Unlike the $[Au_{25}(TP)_{18}]^-$ different signals can be seen. They correspond to different $[Au_{25}(4ATP)_{18}]_x^{x-}$ aggregates. Notice that at relatively low collision energies (10 a.u.) several aggregates can be found, x ranging from 1 to 6. And, when increasing the collision energy, the intensity of these big aggregates (x = 4, 5 and 6) decreases while that of the trimer, dimer and the cluster itself increase.

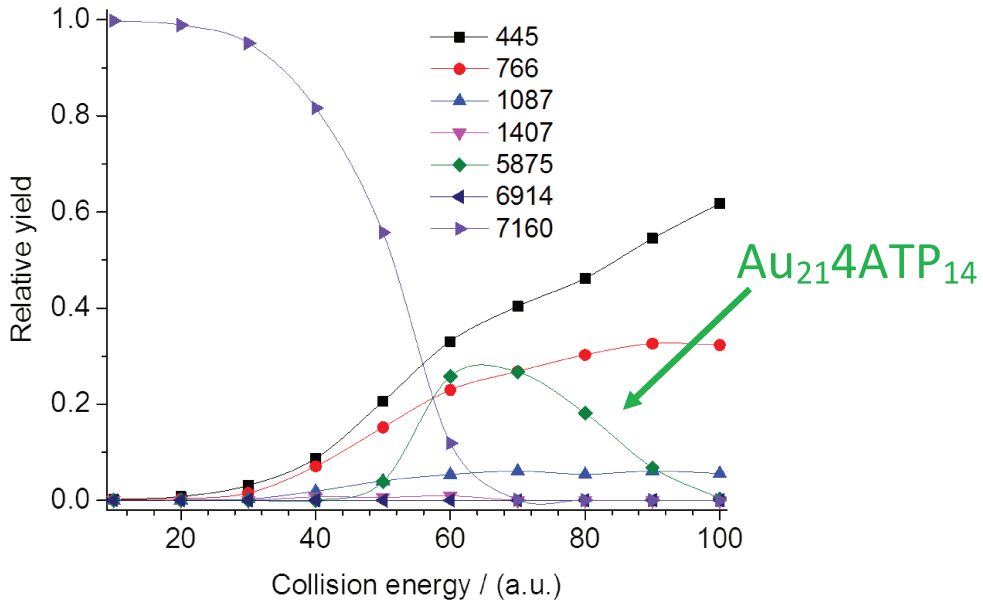

Figure 11. *Survival yield fragmentation pattern of the $[Au_{25}(4ATP)_{18}]^-$ cluster. Clusters were analyzed in DMSO. The legend reports the masses of the different fragments. The purple curve stands for the $Au_{25}(4ATP)_{18}$ cluster (7160 Da) while the green curve (5875 Da) represents the $Au_{21}(TP)_{14}$ (i.e. $Au_{25}(4ATP)_{18}$ – $Au_4(TP)_4$). The maximum relative yield of the for the $Au_{21}(TP)_{14}$ clusters is found at 64 a.u. Figure provided by Dr. J.-F Greisch (KIT).*

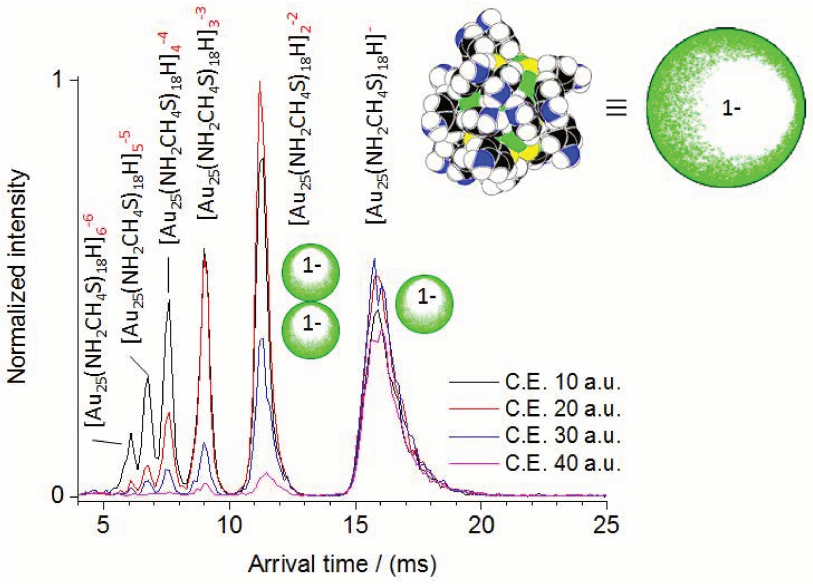

Figure 12. *Separation according to cross section (and charge) of selected clusters for the $[Au_{25}(4ATP)_{18}]^-$ cluster. Arrival time profile for the $[Au_{25}(4ATP)_{18}]_x^{x-}$ cluster aggregates. Clusters were analyzed in DCM. Figure provided by Dr. J.-F Greisch (KIT).*

By performing IMS – MS measurements we can observe that the presence of the amine group has a significant impact on the interaction of the clusters in solution. The coalesced clusters ($[Au_{25}(4ATP)_{18}]^-$) form aggregates. Unfortunately, detection of the GNCs protected by DDT was not achieved.

Now that we know the $[Au_{25}(4ATP)_{18}]^-$ form aggregates, Traveling Wave Ion Mobility Spectrometry (TW IMS)[59] can be very helpful to understand how these clusters pack in solution. For this purpose, the Mobcal [56, 57] software was used to compute He the cross section of the $Au_{25}(4ATP)_{18}]^-$ cluster. Within the hard – sphere limit the cross – section of a particle colliding with a buffer gas can be defined as the area of the base of a cylinder aligned along the velocity vector of the particle. [60]

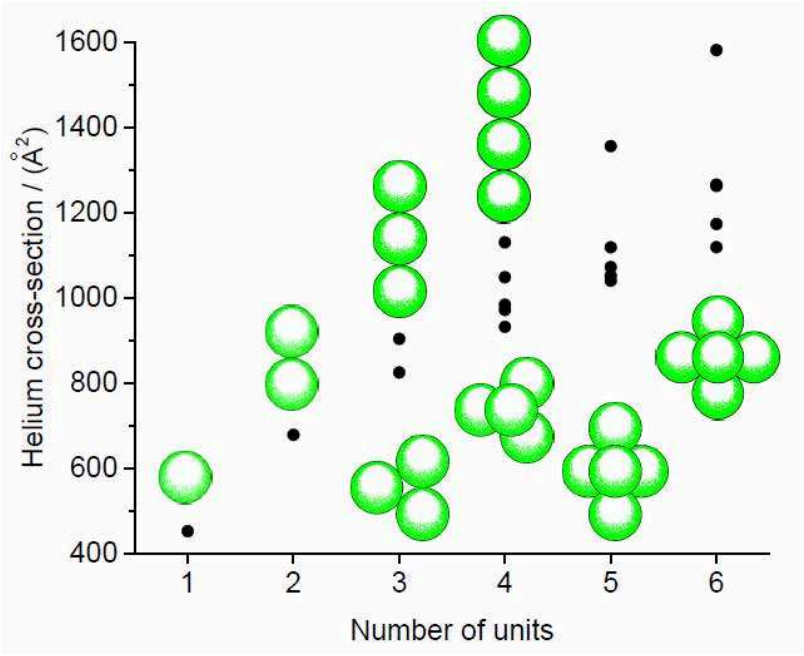

***Figure 13**. Computed IMB He cross – sections for the $[Au_{25}(4ATP)_{18}]_x^{x-}$ aggregates by Mobcal as a function of the number of units. Figure provided by Dr. J.-F Greisch (KIT).*

Figure 13 shows some of the different packing configuration the $[Au_{25}(4ATP)_{18}]_x^{x-}$ aggregates can take. It also illustrates the relation between the different computed Helium cross – sections and the number of units forming the aggregate.

The correlation between the measured drift time values and the collision cross-section is typically calculated by using a calibration curve generated from peptides or proteins with defined cross – sections as done by Lange and co – workers [61] based on the calibration performed by Smith et al. [62] Due to limitations in the number of reference systems available to us with cross-sections suitably covering the

experimental range probed here, we used for the 4ATP the computed structure for the monomer and dimer to compute "reference" cross-sections using the Mobcal software. [56, 57]

Unlike IMS – MS, TWIMS uses a non-constant and non-uniform electric field. We therefore use here the "corrected" classical cross – section (Ω) deduced by Smith et al. [62]

$$\Omega = \frac{\sqrt{18\pi}}{16}\frac{ze}{\sqrt{k_B T}}\sqrt{\left(\frac{1}{m_i}+\frac{1}{m_n}\right)}\frac{760}{P}\frac{T}{273.2}\frac{1}{N}At_D^B \quad (1)$$

Here, z is the ion charge, e is the elementary charge (in C), k_B is the Boltzmann constant, T represents the gas temperature, m_i and m_n are the ion and gas masses, respectively, P stands for the gas pressure (in Torr), t_D is the drift time of the ion and N is the gas number density (in m^{-3}). The correction for the electric field variation and a non – linear effect compensation are included in the A and B, respectively. The corrections for the electric field variation, temperature and pressure can be incorporated in constant A' as follows:

$$\Omega' = \frac{\Omega}{ze}\left(\frac{1}{m_i}+\frac{1}{m_n}\right)^{-1/2} = A' t_D^B \quad (2)$$

Notice that now Ω' is independent of mass and charge since in equation 2, Ω is divided by the terms ze and $\left(\frac{1}{m_i}+\frac{1}{m_n}\right)^{-1/2}$. Figure 14 plots the relation between the TWIMS converted cross – section (Ω') and the number of units in the $[Au_{25}(4ATP)_{18}]_x^{x-}$ aggregates by using the relation deduced by Smith et al. [62].

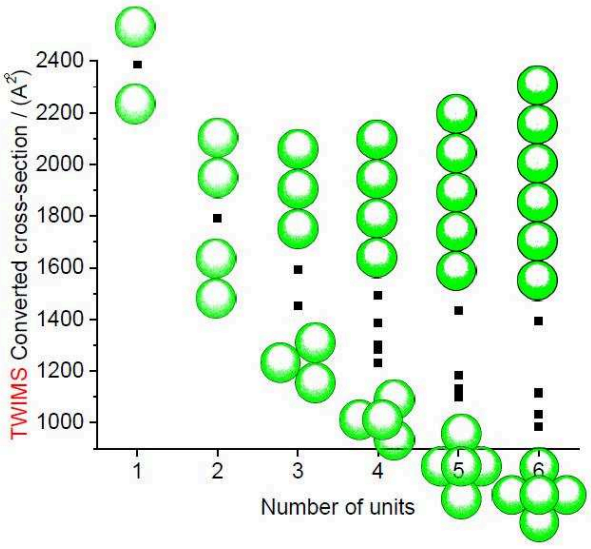

Figure 14. Converted TWI – MS cross – section of the for the $[Au_{25}(4ATP)_{18}]_x^{x-}$ aggregates. Figure provided by Dr. J.-F Greisch (KIT).

Figure 15 shows the TWIMS converted cross – section of the different $Au_{25}(4ATP)_{18}]_x^{x-}$ aggregates as a function of the drift time t_D (see equation 2). Equation 2 can be used to obtain structural information about the aggregates.

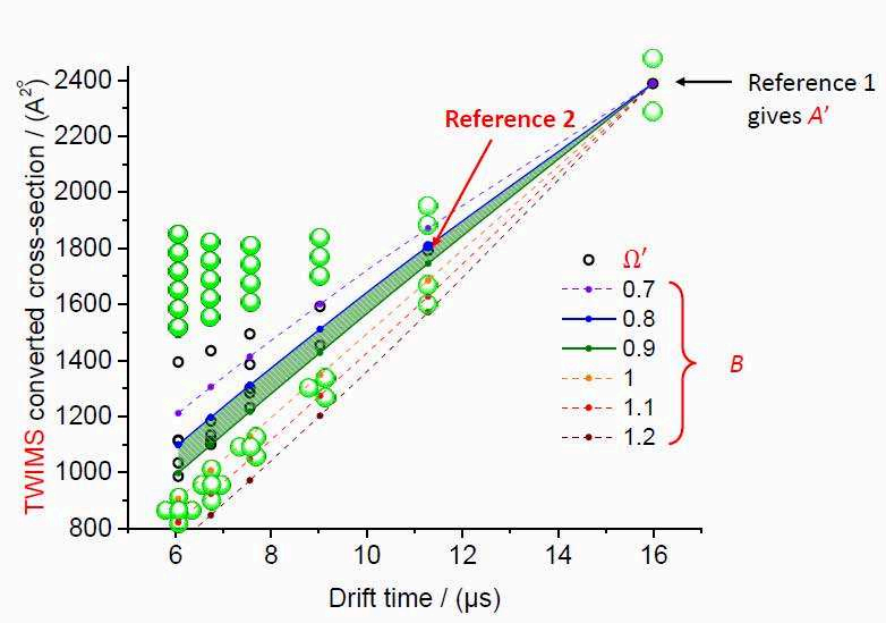

***Figure 15**. TWIMS converted cross – section of the $[Au_{25}(4ATP)_{18}]_x^{x-}$ aggregates as a function of the drift time (t_D). The black circles stand for the model and the lines represent the experimental results. Figure provided by Dr. J.-F Greisch (KIT).*

By measuring a series of drift times for our $[Au_{25}(4ATP)_{18}]^{1-}$ cluster and the $[Au_{25}(4ATP)_{18}]_2^{2-}$ dimers is possible to obtain two points in figure 15 (called reference 1 and 2) to calibrate equation 2 by obtaining A' and B. Figure 15 shows for which values of B there is an overlap between the curve and TWIMS cross-sections for all the aggregates. The determined values support the observation of compact aggregates.

5.1.2.5 Thermogravimetric Analysis (TGA)

TGA analysis was carried out for the $[Au_{25}(4ATP)_{18}]^-$ and $[Au_{25}(TP)_{18}]^-$ clusters. TGA was performed in a S – MAX3000 Rigaku thermal analysis system on samples of 8.51 and 10.85 mg accurately weighed, dried clusters, under air. Temperatures were controlled from 30 to 1150 °C at 5 °C/min. Under thermal decomposition the clusters result in the formation of pure gold due to the loss of solvent and ligand protecting the core.

TGA profiles of the $[Au_{25}(4ATP)_{18}]^-$ and $[Au_{25}(TP)_{18}]^-$ clusters are given in figure 16. The inset upside at the right indicates the ligand used to protect the Au_{25} anion. Notice that this clusters are thermally stable

since the volatilization of the organic layer begins around 200 °C. Also, we can see that the loss of the TP shell in $[Au_{25}(TP)_{18}]^-$ is well – defined. We have almost a vertical mass % decrease for $[Au_{25}(TP)_{18}]^-$ around 200 °C while for the $[Au_{25}(4ATP)_{18}]^-$ cluster the loss of the 18 4ATPs ligands begins at 200 °C and finished around 600 °C. This could be attributed to the presence of aggregates in the $[Au_{25}(4ATP)_{18}]^-$ solution (see section 4.1.2.4. on the ESI – MS and IMS – MS GNC characterization).

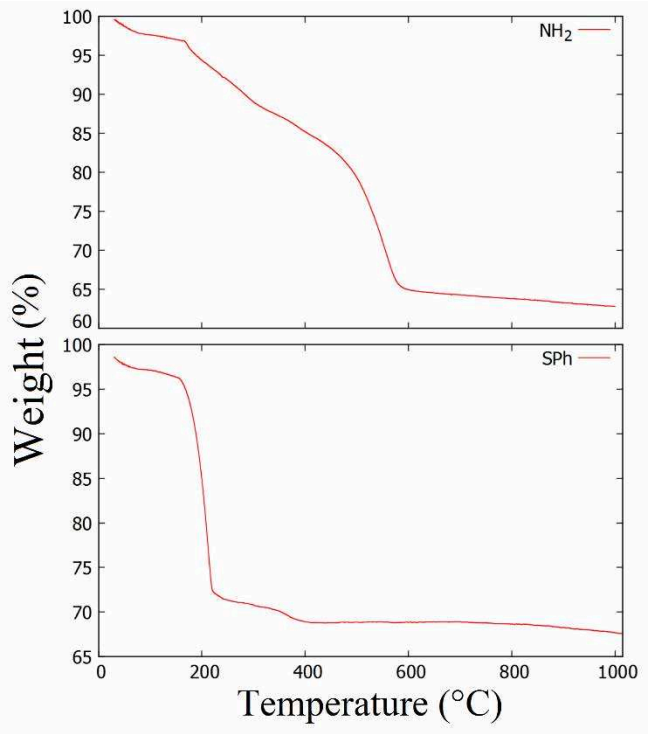

***Figure 16**. TGA of the single thiolate - capped clusters in air: at the top, the $Au_{25}(4ATP)_{18}$ indicated with the NH_2 group and at the bottom the $Au_{25}(TP)_{18}$ cluster (SPh).*

Additionally, table 3 shows the metal / ligand ration calculated based on the TGA data for the $[Au_{25}(4ATP)_{18}]^-$ and $[Au_{25}(TP)_{18}]^-$ clusters.

Table 3. *Sample table, total mass of the sample, residual mass, mast loss and the metal – to – ligand ratio for the 4ATP and the TP single ligand protected clusters synthesized.*

Sample Label	Total mass (mg)	Residual mass (Au) (%)	Residual mass (Au) (mg)	Mass lost (%)	Mass lost (mg)	Metal / ligand Ratio
$[Au_{25}(TP)_{18}]^-$	8.51	66.62	5.67	27.41	2.33	2.43
$[Au_{25}(4ATP)_{18}]^-$	10.85	62.79	6.81	30.01	3.26	2.09

The metal – to – ligand ratio is calculated as follow: residual mass (Au) / total ligand mass.

Here, we define the metal – to – ligand ratio as the residual mass (Au) divided by the total ligand mass. By talking as a reference 1 mol of $[Au_{25}(4ATP)_{18}]^-$ and $[Au_{25}(TP)_{18}]^-$ clusters we can calculate the *theoretical* metal – to – ligand ratio in both cases. The *theoretical* metal – to – ligand ratio for the $Au_{25}(4ATP)_{18}]^-$ and $[Au_{25}(TP)_{18}]^-$ clusters are 2.20 and 2.51, respectively. Table 3 shows that, based on the TGA profiles we obtain 2.09 and 2.43 experimental ratios for the $Au_{25}(4ATP)_{18}]^-$ and $[Au_{25}(TP)_{18}]^-$ clusters, respectively which are in good agreement with the theoretical ratios.

5.1.2.6 UV – Vis spectroscopy

UV – Vis spectra were measured in solution by using an Agilent Cary 5000 UV – Vis – NIR spectrophotometer. Figure 17 shows the optical profiles collected for the $Au_{25}(4ATP)_{18}$ (in green) and the $Au_{25}(TP)_{18}$ (in red) clusters measured in DMF (dimethylformamide) and DCM (dichloromethane), respectively.

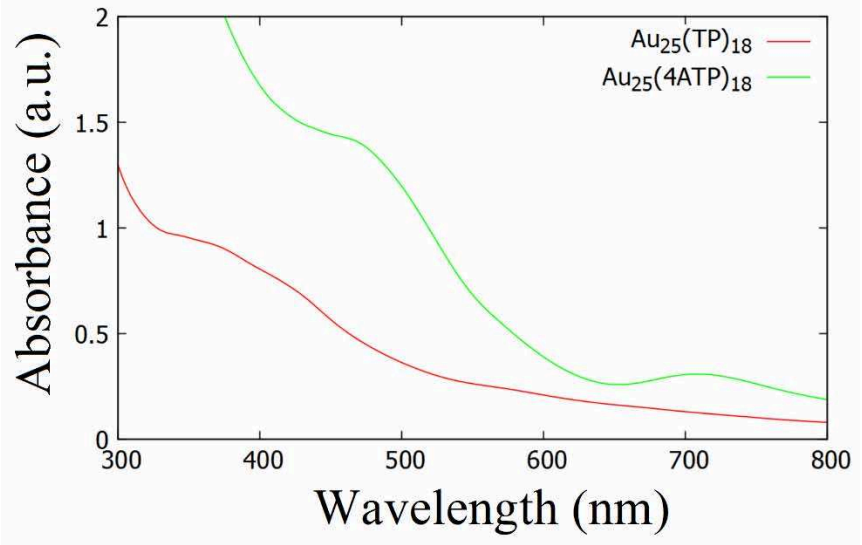

Figure 17*. UV – vis spectra of the $Au_{25}(4ATP)_{18}$ (in green) and the $Au_{25}(TP)_{18}$ (in red) clusters measured in DMF and DCM, respectively.*

Both UV – Vis spectra show the characteristic optical profile of a small cluster. This is confirmed by the absence of a surface plasmon resonance. The $Au_{25}(4ATP)_{18}$ UV – Vis spectrum shows the typical HOMO – LUMO transition band centered around 710 nm (1.75 eV) and an absorption peak at 470 nm (2.64 eV) which is in very good agreement with Demessence [23]. Additionally, our computations show that the lowest energy band for the $[Au_{25}(4ATP)_{18}]^-$ ranges from 546.43 to 645.14 nm (1.92 to 2.67 eV), centered approximatively at 600 nm (2 eV) and the second one at ~415 nm (2.98 eV). Notice that for the $[Au_{25}(4ATP)_{18}]^-$ the computed spectrum is blue shifted by ~0.25 eV respect to the experimental one.

Unfortunately, the $Au_{25}(TP)_{18}$ UV – Vis spectrum does not show the H – L band signal which can be attributed to the presence of impurities. A band can be localized at 430 nm (2.88 eV) and the last one ~370 nm (3.35 eV). However, the $Au_{25}(TP)_{18}$ cluster has been previously synthesized and its UV – Vis spectrum is available. [63] The lowest energy band is found ~ 688 nm (1.8 eV) together a shoulder at 427 nm (2.9 eV). Our computations show that, for the $[Au_{25}(TP)_{18}]^-$ the lowest energy band ranges from 582.73 to 646.20 nm (1.92 to 2.13 eV) and from 402.55 to 464.71 nm (2.67 to 3.08 eV), centered at ~409 nm (3.03 eV) for the second one.

5.2 The $Au_{25}(SR)_{18}(SR')_{18-x}$ cluster synthesis protocol by simultaneous ligand addition

5.2.1 Synthesis protocol of the $Au_{25}(SR)_{18}(SR')_{18-x}$ nanoclusters

Three different ligands (4ATP, DDT and TP) were used in order to obtain two different ligand protected clusters. The standard synthesis protocol [23] was modified by preparing a new **B** solution by mixing two different ligands at the ratio 1:1 in THF. The ligand quantities used are shown in table 4. The $HAuCl_4 – 3H_2O$ and the solvent (THF) mass are the same as in the single ligand case.

The protocol used is the following:

1. Preparation of solution **A, B** and **C**:

    - **Solution A.** 60 mg of lithium borohydride ($LiBH_4$) are dissolved in 25 ml of tetrahydrofuran (THF) and let under stirring for 30 min.
    - **New solution B.** In a 100 ml flask, both ligands are dissolved using the indicated ligand mass (in table 4) in 20 ml of THF and let under stirring at 500 rpm. Solution B (still under stirring) is cooled in an ice bath. Tempeture has to be under 25° C.
    - **Solution C.** the indicated mass (in table 1) is dissolved of $HAuCl_4 – 3H_2O$ in 25 ml of THF.

2. Reaction: 20 ml of both solutions, A and C, are added in solution B at a rate of 60 ml / h. After the mixture is let 24 hours under stirring at 500 rpm keeping the temperature under 25° C. A black / brownish solution should be produced.
3. Purification: the THF is eliminated under reduce pressure at 40 °C and 300 mbar. Next, the black solid is centrifugated 3 times using ethanol at 8000 rpm for 15 min. Finally, the solid is dried with air.

Table 4. *Quantities of different substances used in the two ligand synthesis of protected gold clusters. The THF used was anhydrous.*

Substance	Mass				Solvent
	A		B		(THF)
	(mmol)	(mg)	(mmol)	(mg)	(ml)
(A) DDT + (B) 4ATP	1.06	209.5	0.53	64.1	20
(A) DDT + (B) Thiophenol	1.06	209.5	1.06	113.5	20
(A) 4ATP + (B) Thiophenol	0.53	64.1	1.06	113.5	20

5.2.2 Characterization of the $Au_{25}(SR)_{18}(SR')_{18-x}$ clusters

5.2.2.1 FT – IR spectroscopy

The infrared spectra of the hypothetical $Au_{25}(SR)_{18}(SR')_{18-x}$ synthesized were obtained on a Perkin Elmer spectrum 400 FT – IR / FT – NIR spectrometer in powder at room temperature in a transmittance range between 500 and 4000 cm^{-1}.

In the three different combinations, FT – IR spectra shows that both ligands are attached to the gold surface. FT – IR spectra confirm that all thiolate ligands are coordinated to the gold atoms through the S atom by the disappearance of the S – H stretching band (2535 – 2564 cm^{-1}). [27] Comparison of the spectra of the ligand capped GNCs synthesized with those measured for the ligands (not shown here) allows us to identify and interpret the signals found. At the top of figure 18 (gold clusters protected by 4ATP) we observe the characteristic signal of the **N – H stretching** at 3343.59 cm^{-1} indicating the presence of the NH_2 group in the product. The appearance of the **C – C stretching** at 1488.98 cm^{-1} confirms the existence of benzene rings, as well as the **C – H stretching** of the aromatic ring at 2962.74 cm^{-1}. We can also observe at 1614.75 cm^{-1} the **bending** of the N – H bond proving again the presence of the NH_2 and therefore the 4ATP coordinating the gold core. At the bottom of figure 18 is the infrared spectrum of the gold clusters coordinated by DDT. At 2919.11 cm^{-1} we have the characteristic **C – H asymmetric stretching** of an aliphatic organic chain. While at 2848.69 cm^{-1} we can see the **symmetric stretching** of the same bonds. At 1468.15 cm^{-1} we have the signal of the **C – H bending** and finally we can observe the **C – H rocking** at 801.92 cm^{-1}. Infrared spectrum of the biligand (4ATP / DDT in figure 18b) protected gold cluster has been measured as

well. Comparison of figure 18a and 18b shows that the peaks at 3343.59, 1614.75 and 804.28 cm^{-1} in the spectrum of 4ATP (figure 18a) have disappeared in the 4ATP + DDT spectrum indicating that no 4ATP has attached to the metallic core. This could suggests that the DDT has a larger binding strength that the 4ATP.

On the other hand, figure 19 shows the infrared spectra of the DDT protected clusters at the top (figure 19a), the TP coated GNCs (in figure 19c) and the two – ligand protected GNCs at the middle (figure 19b). Figure 19c shows at 3051.53 cm^{-1} the **(sp^2) C – H stretching** mode, the **double C – C bond stretching** at 1576.26 cm^{-1} and 1472.60 cm^{-1} indicate the presence of benzene rings. Also, we can see that there is no peak in the range 2535 – 2564 cm^{-1} confirming the disappearance of the S – H stretching suggesting that the ligands have attached to the metallic core through the S atom. Comparison of figures 19 suggests again that DDT has larger binding strength than TP since there is no big difference between figure 19a and 19b. We can observe in figure 19b at 2919.38 cm^{-1} the characteristic C – H asymmetric stretching of an aliphatic organic chain. While at 2848.36 cm^{-1} we can see the symmetric stretching of same bonds. At 1467.95 cm^{-1} we have the signal of the C – H bending and finally we can observe the C – H rocking at 801.95 cm^{-1}. A small signal at 1577.49 cm^{-1} appeared in figure 19b (DDT and TP coated GNCs) which is not in the DDT capped cluster spectrum (figure 19a). This new signal could be attributed to the **double C – C bond stretching** in the benzene ring (at 1576.26 cm^{-1}; see the TP protected GNC spectrum in figure 19b). Figure 19b also shows at 3051.53 cm^{-1} the **(sp^2) C – H stretching** mode which is not present in figure 19a (DDT capped GNCs). This suggests that a small quantity of thiophenol ligands have succeeded to attach the gold core.

Finally, figure 20b shows a very weak absorption signal at 3382.5 cm^{-1} that can be associated to the **N – H stretching vibration** found in figure 18a at 3343.59 cm^{-1}. In figure 20b, at 1602.29 cm^{-1} an absorption signal is found which can be attributed to the presence of a **benzene ring** as well the one found at 1489.34 cm^{-1}. These two last peaks can also be seen slightly moved to smaller wavenumbers in figure 20c (spectrum of TP). An interesting fact, comparing the three spectra in figure 20, is that the absorption due to the **N – H bending** (at 1614.75 cm^{-1}) in figure 20a seems to appear also in figure 20b. Also, the absorption signal found at 1261.85 cm^{-1} in figure 20a and found as well in figure 20b at 1261.84 cm^{-1} could be attributed to the **C – N stretch vibration**. This could indicate the presence of the group NH_2, and therefore the 4ATP ligand. However, also an absorption peak at 1260.24 cm^{-1} is detected in figure 20c. Figure 20b looks like a combination of both figures; 20a and 20c however, because of the similarities on the 4ATP and TP ligand structures it is not very clear if the two ligands succeeded to attach to the metallic core.

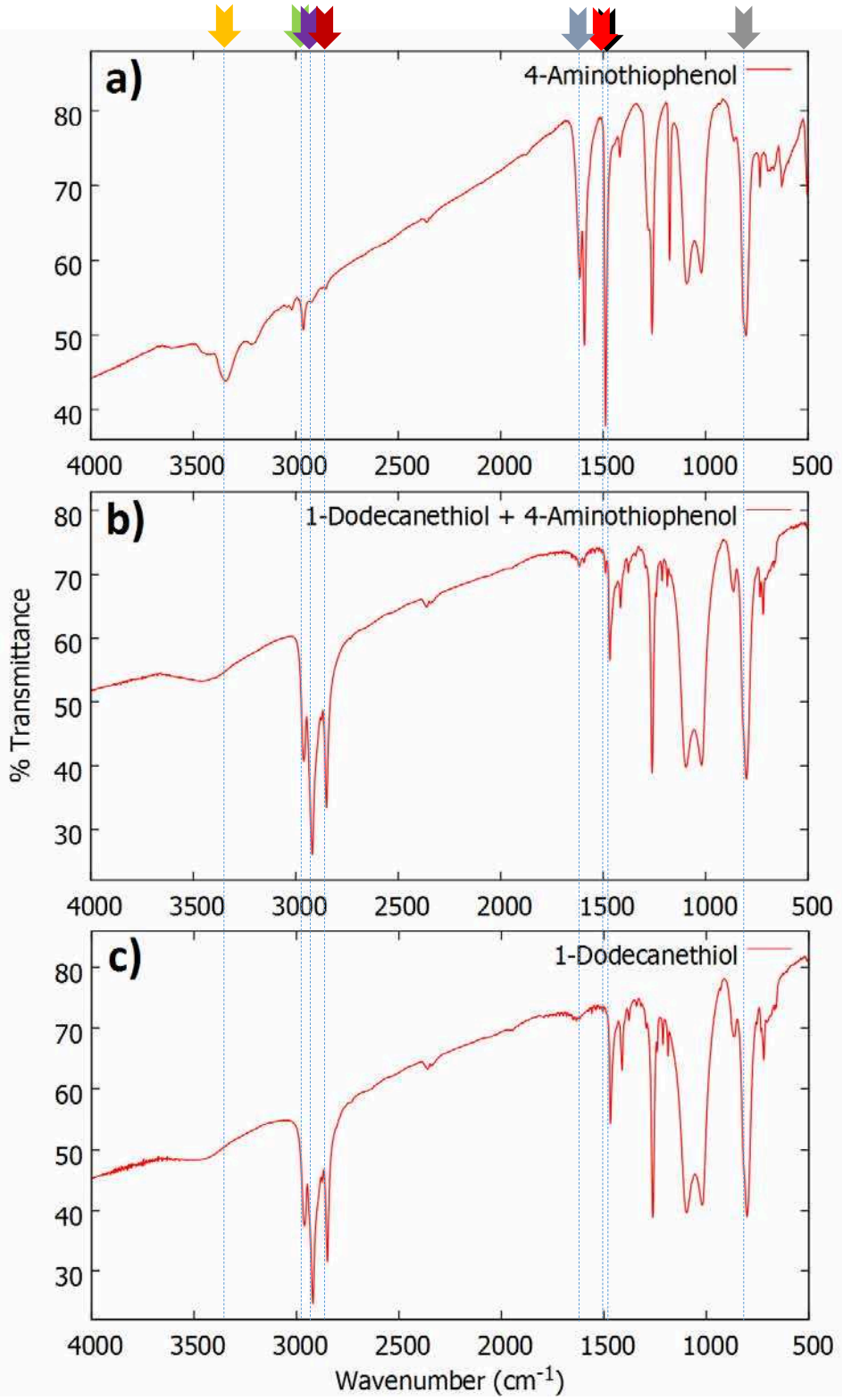

***Figure 18**. FT – IR spectra of the single ligand protected gold clusters by 4ATP (a) and DDT (c) and also the two different ligand capped clusters by 4ATP and DDT (b). The ligand used is indicated at the top right of every spectrum. 4ATP stands for 4 –aminothiophenol and DDT for 1 – dodecanethiol.*

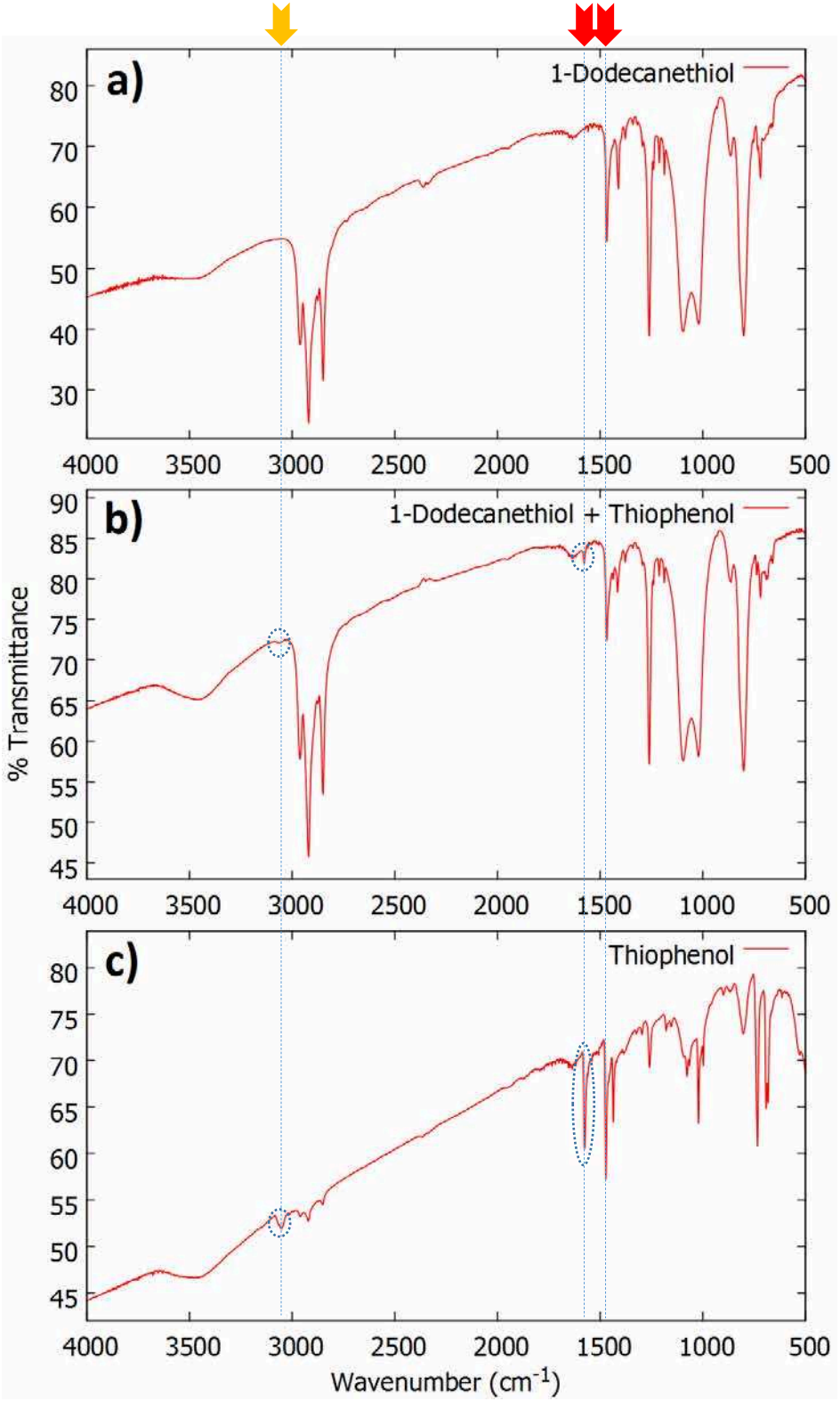

Figure 19. *FT – IR spectra of the single ligand protected gold clusters by DDT(a) and TP (c) and also the two different ligand capped clusters (in b). The ligand used is indicated at the top right of every spectrum. The dotted circle in (b) highlights the* ***double C – C bond stretching*** *at 1577.49 cm^{-1} and the* ***(sp^2) C – H stretching at*** *3051.53 cm^{-1} the of the benzene ring in TP.*

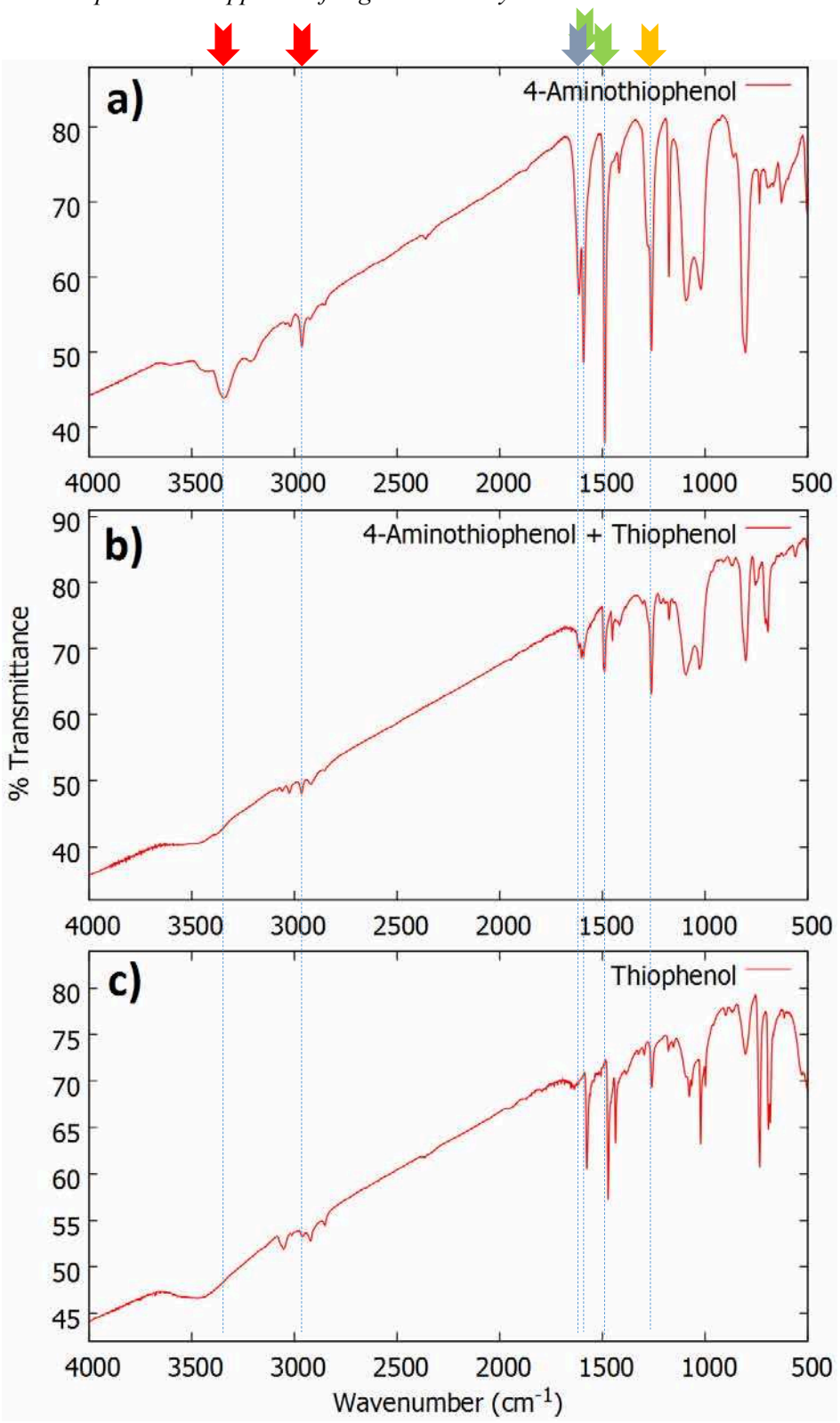

***Figure 20**. FT – IR spectra of the single ligand protected gold clusters by 4ATP (a) and TP (c) and also the two different ligand capped clusters in (c). The ligand used is indicated at the top right of every spectrum. 4ATP stands for 4 –aminothiophenol and TP for thiophenol.*

5.2.2.2 Transmission electron microscopy (MET)

It is possible to see in figures 21 to 23 that the two ligand protected cases, that the presence of the DDT does not prevents completely the formation of big aggregates (see section 4.1.2.2. TEM). 0.92 ± 0.10 nm, 1.33 ± 0.37 nm and 1.33 ± 0.36 nm diameter average size is found for $Au_z(4ATP)_x(DDT)_y$, $Au_{z'}(TP)_{x'}(4ATP)_{y'}$ and $Au_{z''}(TP)_{x''}(DDT)_{y''}$, respectively. The addition of two different ligands in the synthesis process results in the change of particle size. That is the reason we used the subscripts "z", "x" and "y" in the GNC stoichiometry.

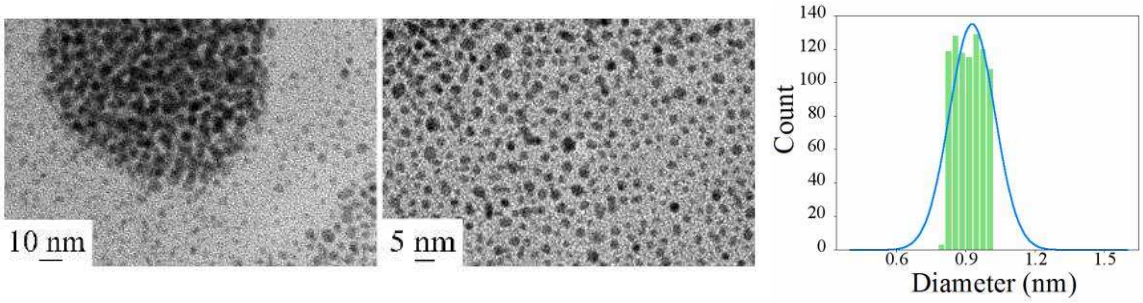

Figure 21. *TEM image of $Au_z(4ATP)_x(DDT)_y$ clusters synthesized by the Demessence method. The cluster size distribution is shown at the right. The average diameter is 0.92 ± 0.10 nm. 6852 clusters were taken into account to obtain the size distribution.*

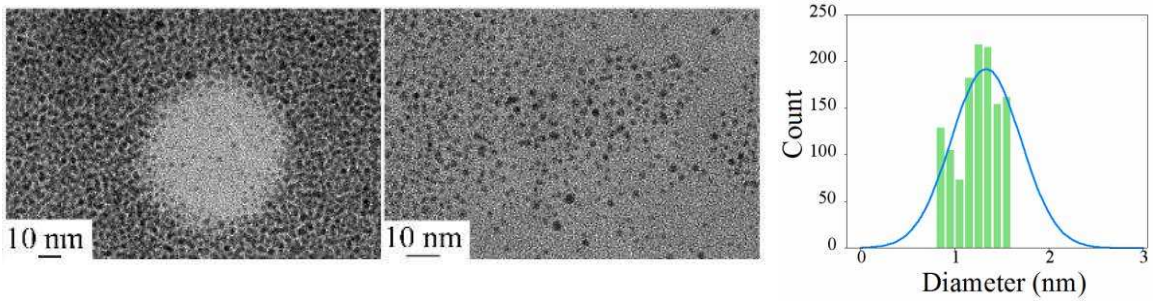

Figure 22. *TEM image of $Au_{z'}(TP)_{x'}(4ATP)_{y'}$ clusters synthesized by the Demessence method. The cluster size distribution is shown at the right. The average diameter is 1.33 ± 0.37 nm. 6852 clusters were taken into account to obtain the size distribution.*

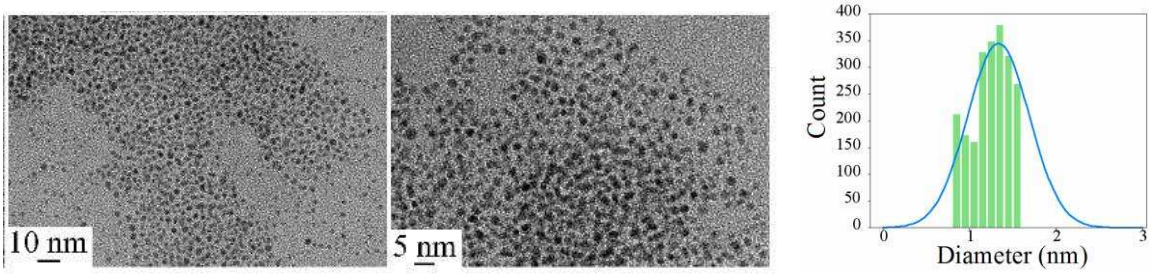

Figure 23. *TEM image of $Au_{z''}(TP)_{x''}(DDT)_{y''}$ clusters synthesized by the Demessence method. The cluster size distribution is shown at the right. The average diameter is 1.33 ± 0.36 nm. 5432 clusters were taken into account to obtain the size distribution.*

Given the ultra – small size of the nanoclusters synthesized and the TEM resolution, these results can only be used to show the presence of GNCs. ESI – MS and IMS – MS provide more accurate information about the nuclearity of the metal core and the ligand shell stoichiometry.

In the next section (4.2.2.3 Electrospray – Ionization (ESI – MS) and ion – mobility (IMS – MS) mass Spectrometry) we confirm by ESI – MS the formation of $Au_{25}(4ATP)_x(TP)_{18-x}$ series of cluster. Unfortunately, no specific nuclearity was found for those GNC where DDT has been used as protecting ligand.

5.2.2.3 Electrospray – Ionization (ESI – MS) and ion – mobility (IMS – MS) mass spectrometry

Figure 24 shows the ESI – MS spectrum of the $Au_{25}(4ATP)_x(TP)_{18-x}$ series of cluster obtained by the simultaneous ligand addition protocol. The ESI – MS spectrum was acquired in negative mode by dissolving the nanoclusters in dichloromethane (DCM) to a final concentration of 1mg/ml.

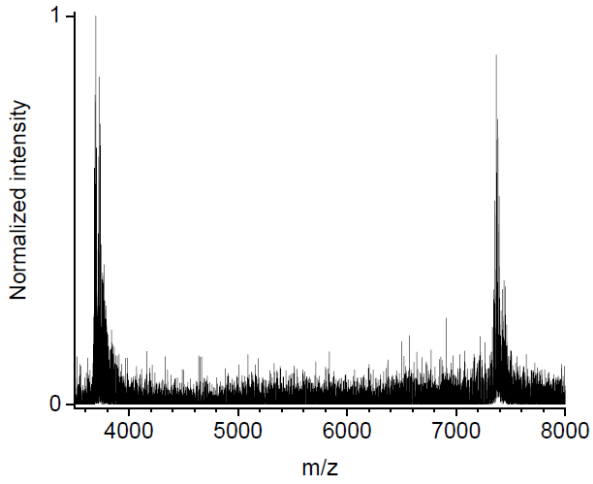

***Figure 24**. Positive – mode ESI – MS spectrum of the $[Au_{25}(4ATP)_x(TP)_{18-x}]^-$ set of clusters. The arrival time distribution is shown at the right as an inset. Clusters were analyzed in DCM. Figure provided by Dr. J.-F Greisch (KIT).*

The mass spectrum in figure 24 is dominated by two intense picks; the one around m/z = 3800 is attributed to the doubly charged species while the one around m/z = 7370 corresponds to monocharged clusters. Figure 25 shows the two peaks found in figure 24. It is possible to see (in the zoomed) peaks in figure 25 that they are composed of a series of signals. The isotopic patters are consistent a 25 – gold cluster confirming that the Au_{25} nuclearity is preserved even if two different ligands have been simultaneously added to the reaction solution. Unfortunately, no specific pattern has been found in the two cases where DDT has been added. Figure 25 shows a good agreement between the experimental and theoretical patters.

The composition of the ligand layer of these Au_{25} series of clusters has been determined. Figures 25 and 26 show the composition of the $[Au_{25}(4ATP)_x(TP)_{18-x}]^-$ set of clusters for the monocharged and the dicharged state, respectively.

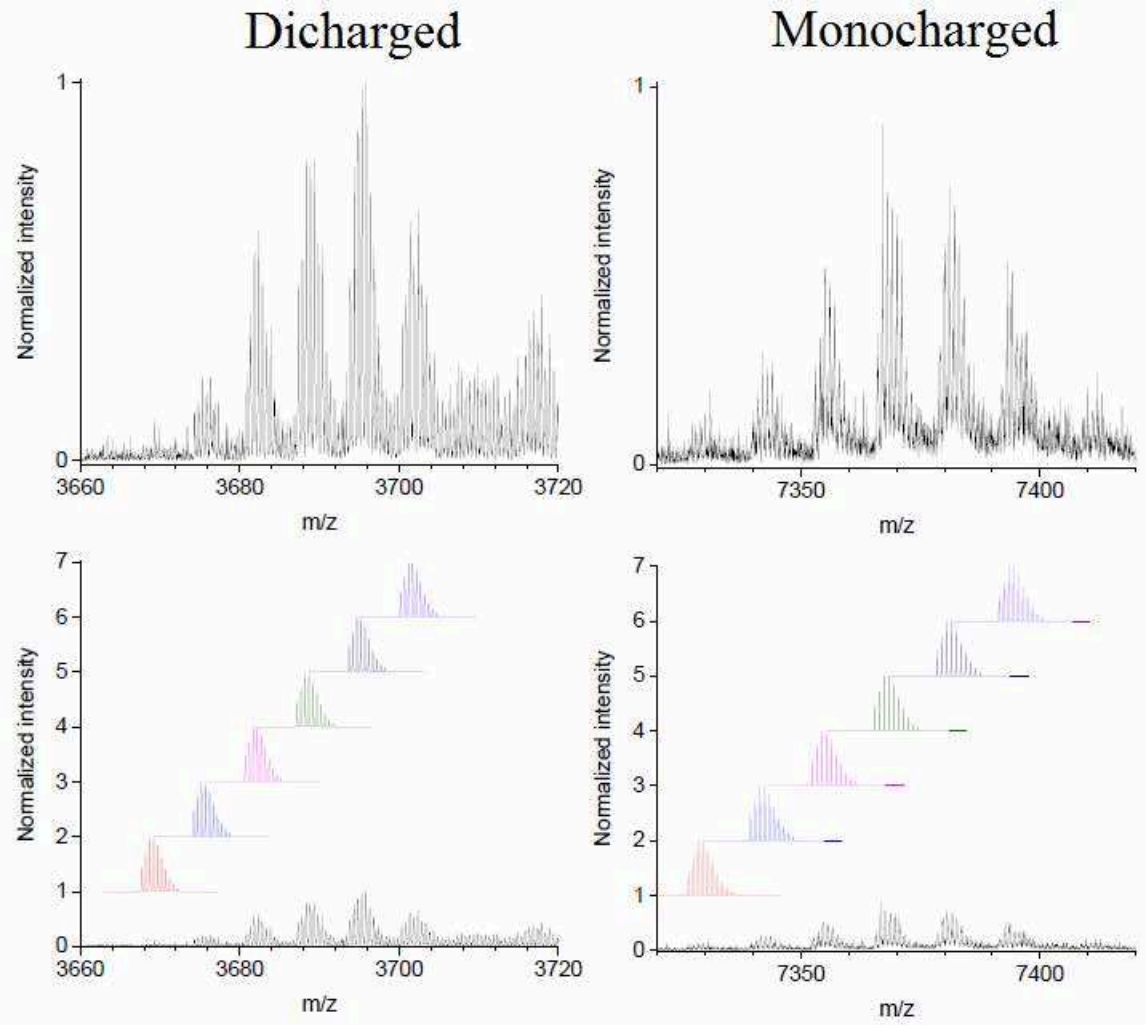

***Figure 25**. Positive – mode ESI – MS spectrum of the $[Au_{25}(4ATP)_x(TP)_{18-x}]^-$ set of clusters. Upside the dicharged and the monocharged mass spectra are shown while below the comparison between the experimental and the theoretical (in different colors) are presented. Figure provided by Dr. J.-F Greisch (KIT).*

It is possible to see that the Au_{25} is now capped by both; the 4ATP and the TP ligands in different 4ATP/TP ligand ratio. The ESI – MS spectra show that all the patterns are consistent with a Au_{25} core coated by 18 ligands. However, 21 ligands in total have been detected, suggesting that the 4ATP can form N = N interligand bridges between two 4ATP.[23, 64-68] However, further work has to be done in order to evidence the presence of the N = N bridges. The two hypothetical conformations of the interligand 4ATP bridges are

shown in figure 28. Figure 26 and 27 show the proposed GNCs stoichiometries which match very well with the isotopic pattern found.

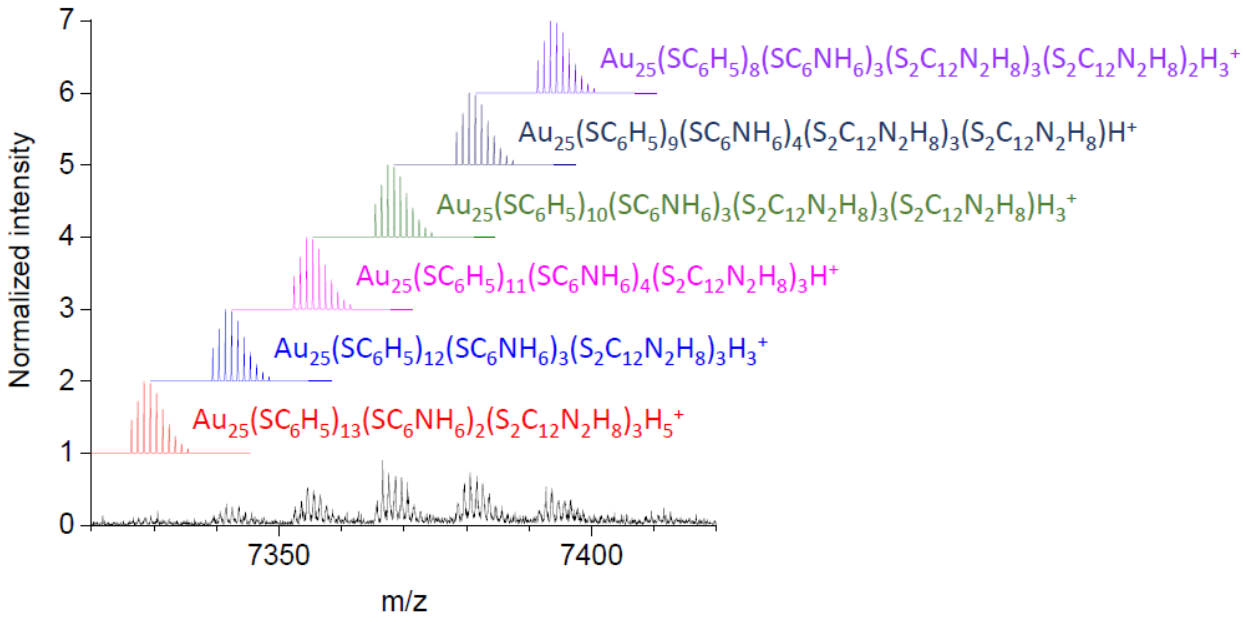

***Figure 26**. Positive – mode ESI – MS spectrum of the monocharged $[Au_{25}(4ATP)_x(TP)_{18-x}]^-$ set of clusters. The composition of the ligand layer is shown for the different protected clusters obtained. A detailed description of the ligand interaction proposed by Dr. J.-F Greisch is shown in figure 28. Figure provided by Dr. J.-F Greisch (KIT).*

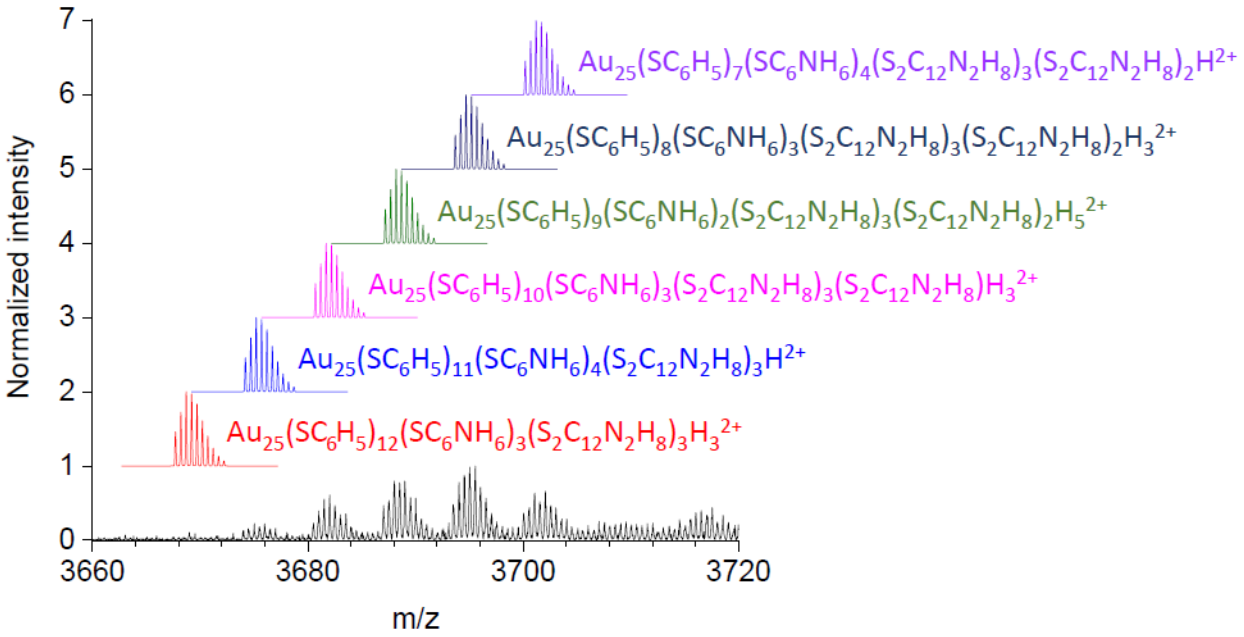

Figure 27. *Positive – mode ESI – MS spectrum of the dicharged $[Au_{25}(4ATP)_x(TP)_{18-x}]^-$ set of clusters. The composition of the ligand layer is shown for the different protected clusters obtained. A detailed description of the ligand interaction proposed by Dr. J.-F Greisch is shown in figure 28. Figure provided by Dr. J.-F Greisch (KIT).*

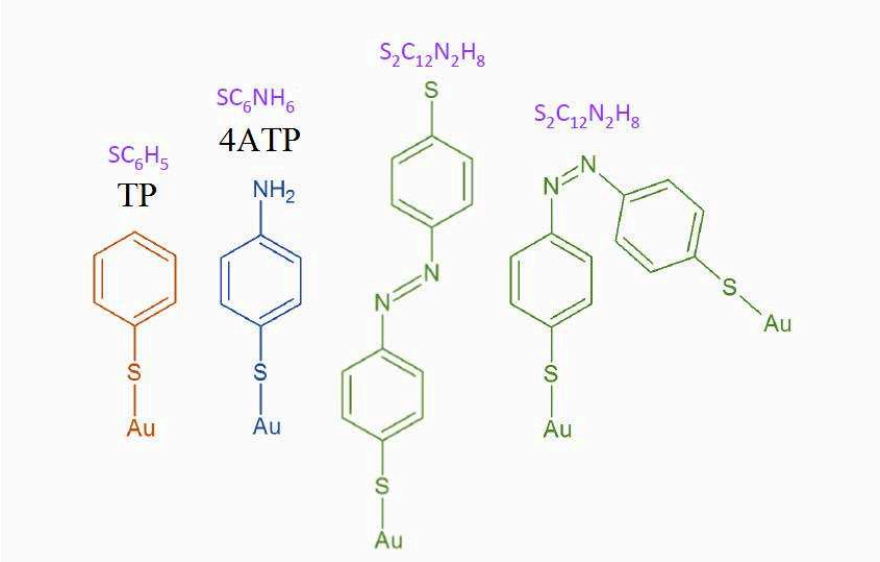

Figure 28. *The TP and the 4ATP ligands and the two different hypothetical conformations of the N = N interligand bridges can take. In the case of a bridging conformation of the dimer without gold at one end the sulfur is likely deprotonated. In purple we show the stoichiometry of the ligand/dimer as used in figure 26 and 27.*

5.2.2.4 UV – Vis spectroscopy

Figure 29 shows the UV – Vis spectrum of the $Au_{25}(4ATP)_x(TP)_{18-x}$ measured in DMF for the simultaneous 4ATP and TP ligand addition GNC synthesis.

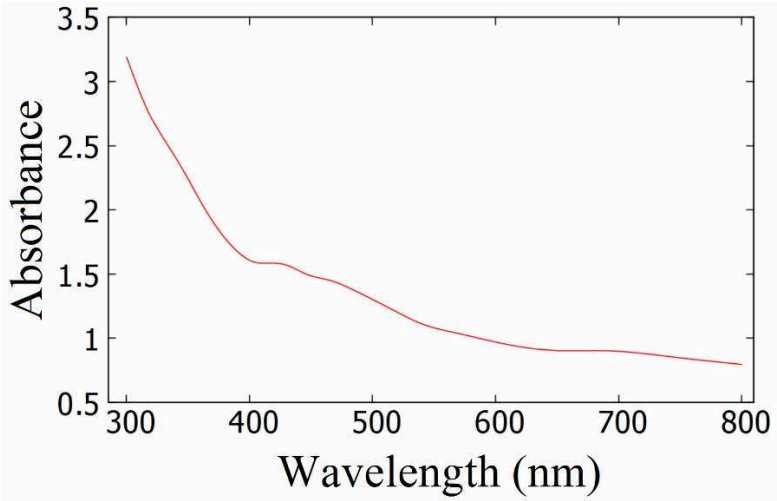

***Figure 29**. UV – vis spectra of the $Au_{25}(4ATP)_x(TP)_{18-x}$ measured in DMF.*

UV – Vis spectrum in figure 29 confirms the presence of the Au_{25} metal core by the presence of a band at ~685 nm. Interestingly, the band found at 710 nm for the $Au_{25}(4ATP)_{18}$ (see figure 17) is shifted to higher energies. This effect has been found while comparing the $[Au_{25}(4ATP)_{18}]^-$ and the Janus $[Au_{25}(4ATP)_9(TP)_9]^-$ cluster computed at the DFT level (see chapter IV, section 4.2.3 on the optical properties). The lowest energy band found in the computed UV – Vis spectrum for the Janus $[Au_{25}(4ATP)_9(TP)_9]^-$ cluster ranges from 552.20 to 613.17 nm (2.02 to 2.25 eV), centered at ~ 552 nm (2.25 eV) while it ranges from 546.43 to 645.14 nm (1.92 to 2.67 eV) centered ~ 600 nm (2.07 eV) for $[Au_{25}(4ATP)_{18}$.

5.3 Conclusions

The $[Au_{25}(4ATP)_{18}]^-$ and the $[Au_{25}(TP)_{18}]^-$ have been successfully detected by ESI – MS. IMS – MS measures the time taken for an ion to travel to a pressurized cell under the influence of a weak electric field. The speed by which the ions traverse the drift region depends on their size since, shape, charge and *m/z* ratio which allows us to separate them. IMS – MS for the $[Au_{25}(TP)_{18}]^-$ cluster shows a narrow, symmetric drift time distribution that evidences the presence of only one structure. However, several peaks can be seen in the $[Au_{25}(4ATP)_{18}]^-$ drift time distribution, showing the formation of aggregates in solution. IMS – MS could help to understand the formation of GNCs super lattices in solution.

Comparison of both survival yield fragmentation patterns ($[Au_{25}(4ATP)_{18}]^-$ and the $[Au_{25}(TP)_{18}]^-$ clusters) indicates that in the $[Au_{25}(4ATP)_{18}]^-$ cluster fragmentation analysis less stable species are present.

ESI – MS of the two ligand protected clusters synthesized by the simultaneous ligand addition protocol using 4ATP and TP evidences the presence of a set of $[Au_{25}(4ATP)_x(TP)_{18-x}]^-$ clusters with different 4ATP/TP ligand ratio. The mass spectra show that all the pattern are consistent with a Au_{25} core coated by 18 ligands. However, 21 ligands in total have been detected, suggesting that the 4ATP can form N = N interligand bridges between two NH_2 groups. However, further work has to be done in order to evidence the presence of the hypothetical N = N bridges. Moreover, TWIMS evidences the formation of compact aggregates.

Additionally, FT – IR spectroscopy confirm that all ligands are successfully attached to the metal surface by the characteristic normal mode signal in the spectra and the by the disappearance of the S – H stretching band (2535 – 2564 cm^{-1}). [27] The results for the two different ligand protected clusters show the same trend.

The TEM characterization turned to be very challenging since in most of the cases the obtained clusters form aggregates larger than 10 nm.

Finally, our results show confirm that ESI and IMS mass spectrometry are highly informative techniques to understand the ligand protection mode on thiolated GNC.

5.4 References

1. Jin, R., *Quantum sized, thiolate-protected gold nanoclusters.* Nanoscale, 2010. **2**(3): p. 343-362.
2. Konishi, K., *Phosphine-Coordinated Pure-Gold Clusters: Diverse Geometrical Structures and Unique Optical Properties/Responses*, in *Gold Clusters, Colloids and Nanoparticles I*, P.D.M. Mingos, Editor. 2014, Springer International Publishing: Cham. p. 49-86.
3. Yamazoe, S., K. Koyasu, and T. Tsukuda, *Nonscalable Oxidation Catalysis of Gold Clusters.* Accounts of Chemical Research, 2014. **47**(3): p. 816-824.
4. Rodriguez-Castillo, M., D. Laurencin, F. Tielens, A. van der Lee, S. Clement, Y. Guari, and S. Richeter, *Reactivity of gold nanoparticles towards N-heterocyclic carbenes.* Dalton Transactions, 2014. **43**(16): p. 5978-5982.
5. Vignolle, J. and T.D. Tilley, *N-Heterocyclic carbene-stabilized gold nanoparticles and their assembly into 3D superlattices.* Chemical Communications, 2009(46): p. 7230-7232.
6. de Silva, N., J.-M. Ha, A. Solovyov, M.M. Nigra, I. Ogino, S.W. Yeh, K.A. Durkin, and A. Katz, *A bioinspired approach for controlling accessibility in calix[4]arene-bound metal cluster catalysts.* Nat Chem, 2010. **2**(12): p. 1062-1068.
7. Qian, H., M. Zhu, E. Lanni, Y. Zhu, M.E. Bier, and R. Jin, *Conversion of Polydisperse Au Nanoparticles into Monodisperse Au25 Nanorods and Nanospheres.* The Journal of Physical Chemistry C, 2009. **113**(41): p. 17599-17603.
8. Qian, H., M. Zhu, U.N. Andersen, and R. Jin, *Facile, Large-Scale Synthesis of Dodecanethiol-Stabilized Au38 Clusters.* The Journal of Physical Chemistry A, 2009. **113**(16): p. 4281-4284.
9. Shichibu, Y., K. Suzuki, and K. Konishi, *Facile synthesis and optical properties of magic-number Au13 clusters.* Nanoscale, 2012. **4**(14): p. 4125-4129.
10. Lotz, A.R. and M. Fröba, *Synthesis and Characterization of Au55 Clusters within Mesoporous Silica.* Zeitschrift für anorganische und allgemeine Chemie, 2005. **631**(13-14): p. 2800-2805.
11. Levi-Kalisman, Y., P.D. Jadzinsky, N. Kalisman, H. Tsunoyama, T. Tsukuda, D.A. Bushnell, and R.D. Kornberg, *Synthesis and Characterization of Au102(p-MBA)44 Nanoparticles.* Journal of the American Chemical Society, 2011. **133**(9): p. 2976-2982.
12. Qian, H. and R. Jin, *Ambient Synthesis of Au144(SR)60 Nanoclusters in Methanol.* Chemistry of Materials, 2011. **23**(8): p. 2209-2217.
13. Lugo, G., V. Schwanen, B. Fresch, and F. Remacle, *Charge Redistribution Effects on the UV–Vis Spectra of Small Ligated Gold Clusters: a Computational Study.* The Journal of Physical Chemistry C, 2015.
14. Goel, S., K.A. Velizhanin, A. Piryatinski, S.A. Ivanov, and S. Tretiak, *Ligand Effects on Optical Properties of Small Gold Clusters: A TDDFT Study.* The Journal of Physical Chemistry C, 2012. **116**(5): p. 3242-3249.
15. Tlahuice-Flores, A., R.L. Whetten, and M. Jose-Yacaman, *Ligand Effects on the Structure and the Electronic Optical Properties of Anionic Au25(SR)18 Clusters.* The Journal of Physical Chemistry C, 2013. **117**(40): p. 20867-20875.
16. Pichugina, D.A., N.E. Kuz'menko, and A.F. Shestakov, *Ligand-protected gold clusters: the structure, synthesis and applications.* Russian Chemical Reviews, 2015. **84**(11): p. 1114.
17. Angel, L.A., L.T. Majors, A.C. Dharmaratne, and A. Dass, *Ion Mobility Mass Spectrometry of Au25(SCH2CH2Ph)18 Nanoclusters.* ACS Nano, 2010. **4**(8): p. 4691-4700.
18. Knoppe, S., A.C. Dharmaratne, E. Schreiner, A. Dass, and T. Bürgi, *Ligand Exchange Reactions on Au38 and Au40 Clusters: A Combined Circular Dichroism and Mass Spectrometry Study.* Journal of the American Chemical Society, 2010. **132**(47): p. 16783-16789.

19. Dass, A., K. Holt, J.F. Parker, S.W. Feldberg, and R.W. Murray, *Mass Spectrometrically Detected Statistical Aspects of Ligand Populations in Mixed Monolayer Au25L18 Nanoparticles.* The Journal of Physical Chemistry C, 2008. **112**(51): p. 20276-20283.
20. Fields-Zinna, C.A., J.F. Parker, and R.W. Murray, *Mass Spectrometry of Ligand Exchange Chelation of the Nanoparticle [Au25(SCH2CH2C6H5)18]1− by CH3C6H3(SH)2.* Journal of the American Chemical Society, 2010. **132**(48): p. 17193-17198.
21. Harkness, K.M., L.S. Fenn, D.E. Cliffel, and J.A. McLean, *Surface Fragmentation of Complexes from Thiolate Protected Gold Nanoparticles by Ion Mobility-Mass Spectrometry.* Analytical Chemistry, 2010. **82**(7): p. 3061-3066.
22. Johnson, G.E., A. Olivares, D. Hill, and J. Laskin, *Cationic gold clusters ligated with differently substituted phosphines: effect of substitution on ligand reactivity and binding.* Physical Chemistry Chemical Physics, 2015. **17**(22): p. 14636-14646.
23. Lavenn, C., F. Albrieux, G. Bergeret, R. Chiriac, P. Delichere, A. Tuel, and A. Demessence, *Functionalized gold magic clusters: Au25(SPhNH2)17.* Nanoscale, 2012. **4**(23): p. 7334-7337.
24. Zeng, C., T. Li, A. Das, N.L. Rosi, and R. Jin, *Chiral Structure of Thiolate-Protected 28-Gold-Atom Nanocluster Determined by X-ray Crystallography.* Journal of the American Chemical Society, 2013. **135**(27): p. 10011-10013.
25. Menard, L.D., H. Xu, S.-P. Gao, R.D. Twesten, A.S. Harper, Y. Song, G. Wang, A.D. Douglas, J.C. Yang, A.I. Frenkel, R.W. Murray, and R.G. Nuzzo, *Metal Core Bonding Motifs of Monodisperse Icosahedral Au13 and Larger Au Monolayer-Protected Clusters As Revealed by X-ray Absorption Spectroscopy and Transmission Electron Microscopy.* The Journal of Physical Chemistry B, 2006. **110**(30): p. 14564-14573.
26. MacDonald, M.A., P. Zhang, N. Chen, H. Qian, and R. Jin, *Solution-Phase Structure and Bonding of Au38(SR)24 Nanoclusters from X-ray Absorption Spectroscopy.* The Journal of Physical Chemistry C, 2011. **115**(1): p. 65-69.
27. Farrag, M., M. Tschurl, A. Dass, and U. Heiz, *Infra-red spectroscopy of size selected Au25, Au38 and Au144 ligand protected gold clusters.* Physical Chemistry Chemical Physics, 2013. **15**(30): p. 12539-12542.
28. Wang, B., B. Li, B. Zhao, and C.Y. Li, *Amphiphilic Janus Gold Nanoparticles via Combining "Solid-State Grafting-to" and "Grafting-from" Methods.* Journal of the American Chemical Society, 2008. **130**(35): p. 11594-11595.
29. Glaser, N., D.J. Adams, A. Böker, and G. Krausch, *Janus Particles at Liquid–Liquid Interfaces.* Langmuir, 2006. **22**(12): p. 5227-5229.
30. Kim, H., R.P. Carney, J. Reguera, Q.K. Ong, X. Liu, and F. Stellacci, *Synthesis and Characterization of Janus Gold Nanoparticles.* Advanced Materials, 2012. **24**(28): p. 3857-3863.
31. Lattuada, M. and T.A. Hatton, *Synthesis, properties and applications of Janus nanoparticles.* Nano Today, 2011. **6**(3): p. 286-308.
32. Carney, R.P., G.A. DeVries, C. Dubois, H. Kim, J.Y. Kim, C. Singh, P.K. Ghorai, J.B. Tracy, R.L. Stiles, R.W. Murray, S.C. Glotzer, and F. Stellacci, *Size Limitations for the Formation of Ordered Striped Nanoparticles.* Journal of the American Chemical Society, 2008. **130**(3): p. 798-799.
33. Cesbron, Y., C.P. Shaw, J.P. Birchall, P. Free, and R. Lévy, *Stripy Nanoparticles Revisited.* Small, 2012. **8**(24): p. 3714-3719.
34. Harkness, K.M., A. Balinski, J.A. McLean, and D.E. Cliffel, *Nanoscale Phase Segregation of Mixed Thiolates on Gold Nanoparticles.* Angewandte Chemie International Edition, 2011. **50**(45): p. 10554-10559.
35. Shivhare, A., S.J. Ambrose, H. Zhang, R.W. Purves, and R.W.J. Scott, *Stable and recyclable Au25 clusters for the reduction of 4-nitrophenol.* Chemical Communications, 2013. **49**(3): p. 276-278.

36. Shichibu, Y., Y. Negishi, T. Tsukuda, and T. Teranishi, *Large-Scale Synthesis of Thiolated Au25 Clusters via Ligand Exchange Reactions of Phosphine-Stabilized Au11 Clusters.* Journal of the American Chemical Society, 2005. **127**(39): p. 13464-13465.
37. Shichibu, Y., Y. Negishi, H. Tsunoyama, M. Kanehara, T. Teranishi, and T. Tsukuda, *Extremely High Stability of Glutathionate-Protected Au25 Clusters Against Core Etching.* Small, 2007. **3**(5): p. 835-839.
38. Zhu, M., E. Lanni, N. Garg, M.E. Bier, and R. Jin, *Kinetically Controlled, High-Yield Synthesis of Au25 Clusters.* Journal of the American Chemical Society, 2008. **130**(4): p. 1138-1139.
39. Yu, Y., Z. Luo, Y. Yu, J.Y. Lee, and J. Xie, *Observation of Cluster Size Growth in CO-Directed Synthesis of Au25(SR)18 Nanoclusters.* ACS Nano, 2012. **6**(9): p. 7920-7927.
40. Yuan, X., Y. Yu, Q. Yao, Q. Zhang, and J. Xie, *Fast Synthesis of Thiolated Au25 Nanoclusters via Protection–Deprotection Method.* The Journal of Physical Chemistry Letters, 2012. **3**(17): p. 2310-2314.
41. Yu, Y., X. Chen, Q. Yao, Y. Yu, N. Yan, and J. Xie, *Scalable and Precise Synthesis of Thiolated Au10–12, Au15, Au18, and Au25 Nanoclusters via pH Controlled CO Reduction.* Chemistry of Materials, 2013. **25**(6): p. 946-952.
42. Zhu, M., C.M. Aikens, F.J. Hollander, G.C. Schatz, and R. Jin, *Correlating the Crystal Structure of A Thiol-Protected Au25 Cluster and Optical Properties.* Journal of the American Chemical Society, 2008. **130**(18): p. 5883-5885.
43. Heaven, M.W., A. Dass, P.S. White, K.M. Holt, and R.W. Murray, *Crystal Structure of the Gold Nanoparticle [N(C8H17)4][Au25(SCH2CH2Ph)18].* Journal of the American Chemical Society, 2008. **130**(12): p. 3754-3755.
44. Lopez-Acevedo, O. and H. Häkkinen, *Derivatives of the thiolate-protected gold cluster Au25(SR)18 -1.* The European Physical Journal D, 2011. **63**(2): p. 311-314.
45. Kwak, K., S.S. Kumar, K. Pyo, and D. Lee, *Ionic Liquid of a Gold Nanocluster: A Versatile Matrix for Electrochemical Biosensors.* ACS Nano, 2013. **8**(1): p. 671-679.
46. Chong, H., P. Li, S. Wang, F. Fu, J. Xiang, M. Zhu, and Y. Li, *Au25 Clusters as Electron-Transfer Catalysts Induced the Intramolecular Cascade Reaction of 2-nitrobenzonitrile.* Sci. Rep., 2013. **3**.
47. Kawasaki, H., S. Kumar, G. Li, C. Zeng, D.R. Kauffman, J. Yoshimoto, Y. Iwasaki, and R. Jin, *Generation of Singlet Oxygen by Photoexcited Au25(SR)18 Clusters.* Chemistry of Materials, 2014. **26**(9): p. 2777-2788.
48. Kauffman, D.R., D. Alfonso, C. Matranga, H. Qian, and R. Jin, *Experimental and Computational Investigation of Au25 Clusters and CO2: A Unique Interaction and Enhanced Electrocatalytic Activity.* Journal of the American Chemical Society, 2012. **134**(24): p. 10237-10243.
49. Shivhare, A., D.M. Chevrier, R.W. Purves, and R.W.J. Scott, *Following the Thermal Activation of Au25(SR)18 Clusters for Catalysis by X-ray Absorption Spectroscopy.* The Journal of Physical Chemistry C, 2013. **117**(39): p. 20007-20016.
50. Shibu, E.S., M.A.H. Muhammed, T. Tsukuda, and T. Pradeep, *Ligand Exchange of Au25SG18 Leading to Functionalized Gold Clusters: Spectroscopy, Kinetics, and Luminescence.* The Journal of Physical Chemistry C, 2008. **112**(32): p. 12168-12176.
51. Bergeron, D.E., O. Coskuner, J.W. Hudgens, and C.A. Gonzalez, *Ligand Exchange Reactions in the Formation of Diphosphine-Protected Gold Clusters.* The Journal of Physical Chemistry C, 2008. **112**(33): p. 12808-12814.
52. Beqa, L., D. Deschamps, S. Perrio, A.-C. Gaumont, S. Knoppe, and T. Bürgi, *Ligand Exchange Reaction on Au38(SR)24, Separation of Au38(SR)23(SR')1 Regioisomers, and Migration of Thiolates.* The Journal of Physical Chemistry C, 2013. **117**(41): p. 21619-21625.

53. Guo, R., Y. Song, G. Wang, and R.W. Murray, *Does Core Size Matter in the Kinetics of Ligand Exchanges of Monolayer-Protected Au Clusters?* Journal of the American Chemical Society, 2005. **127**(8): p. 2752-2757.
54. Dufour, F., B. Fresch, O. Durupthy, C. Chaneac, and F. Remacle, *Ligand and Solvation Effects on the Structural and Electronic Properties of Small Gold Clusters.* The Journal of Physical Chemistry C, 2014. **118**(8): p. 4362-4376.
55. Martin, M.N., D. Li, A. Dass, and S.-K. Eah, *Ultrafast, 2 min synthesis of monolayer-protected gold nanoclusters (d < 2 nm).* Nanoscale, 2012. **4**(14): p. 4091-4094.
56. Mesleh, M.F., J.M. Hunter, A.A. Shvartsburg, G.C. Schatz, and M.F. Jarrold, *Structural Information from Ion Mobility Measurements: Effects of the Long-Range Potential.* The Journal of Physical Chemistry, 1996. **100**(40): p. 16082-16086.
57. Shvartsburg, A.A. and M.F. Jarrold, *An exact hard-spheres scattering model for the mobilities of polyatomic ions.* Chemical Physics Letters, 1996. **261**(1): p. 86-91.
58. Dass, A., A. Stevenson, G.R. Dubay, J.B. Tracy, and R.W. Murray, *Nanoparticle MALDI-TOF Mass Spectrometry without Fragmentation: Au25(SCH2CH2Ph)18 and Mixed Monolayer Au25(SCH2CH2Ph)18−x(L)x.* Journal of the American Chemical Society, 2008. **130**(18): p. 5940-5946.
59. Shvartsburg, A.A. and R.D. Smith, *Fundamentals of Traveling Wave Ion Mobility Spectrometry.* Analytical Chemistry, 2008. **80**(24): p. 9689-9699.
60. Wyttenbach, T., C. Bleiholder, and M.T. Bowers, *Factors Contributing to the Collision Cross Section of Polyatomic Ions in the Kilodalton to Gigadalton Range: Application to Ion Mobility Measurements.* Analytical Chemistry, 2013. **85**(4): p. 2191-2199.
61. Maire, F., G. Coadou, L. Cravello, and C.M. Lange, *Traveling Wave Ion Mobility Mass Spectrometry Study of Low Generation Polyamidoamine Dendrimers.* Journal of The American Society for Mass Spectrometry, 2013. **24**(2): p. 238-248.
62. Smith, D., T. Knapman, I. Campuzano, R. Malham, J. Berryman, S. Radford, and A. Ashcroft, *Deciphering drift time measurements from travelling wave ion mobility spectrometry-mass spectrometry studies.* European Journal of Mass Spectrometry, 2009. **15**(2): p. 113-130.
63. Guo, R. and R.W. Murray, *Substituent Effects on Redox Potentials and Optical Gap Energies of Molecule-like Au38(SPhX)24 Nanoparticles.* Journal of the American Chemical Society, 2005. **127**(34): p. 12140-12143.
64. Xu, P., L. Kang, N.H. Mack, K.S. Schanze, X. Han, and H.-L. Wang, *Mechanistic understanding of surface plasmon assisted catalysis on a single particle: cyclic redox of 4-aminothiophenol.* Scientific Reports, 2013. **3**: p. 2997.
65. Liu, X., L. Tang, R. Niessner, Y. Ying, and C. Haisch, *Nitrite-Triggered Surface Plasmon-Assisted Catalytic Conversion of p-Aminothiophenol to p,p′-Dimercaptoazobenzene on Gold Nanoparticle: Surface-Enhanced Raman Scattering Investigation and Potential for Nitrite Detection.* Analytical Chemistry, 2015. **87**(1): p. 499-506.
66. Zhao, L.-B., M. Zhang, B. Ren, Z.-Q. Tian, and D.-Y. Wu, *Theoretical Study on Thermodynamic and Spectroscopic Properties of Electro-Oxidation of p-Aminothiophenol on Gold Electrode Surfaces.* The Journal of Physical Chemistry C, 2014. **118**(46): p. 27113-27122.
67. Üzer, A., Z. Can, İ. Akın, E. Erçağ, and R. Apak, *4-Aminothiophenol Functionalized Gold Nanoparticle-Based Colorimetric Sensor for the Determination of Nitramine Energetic Materials.* Analytical Chemistry, 2014. **86**(1): p. 351-356.
68. Hu, X., T. Wang, L. Wang, and S. Dong, *Surface-Enhanced Raman Scattering of 4-Aminothiophenol Self-Assembled Monolayers in Sandwich Structure with Nanoparticle Shape Dependence: Off-Surface Plasmon Resonance Condition.* The Journal of Physical Chemistry C, 2007. **111**(19): p. 6962-6969.

Chapter VI. Experimental and theoretical study of the reactivity of gold nanoparticles towards benzimidazole – 2 – ylidene ligand

Introduction

N – Heterocyclic carbenes (NHC) have received a lot of attention in recent years due to their wide range of applications in areas such as; catalysis, [1-3] light – emitting materials, [4, 5] and biology. [6, 7] Moreover, studies have shown that they also represent valid candidates for GNC passivation [8, 9] offering a new option on the gold cluster functionalization area.

Several studies on the synthesis of NHC protected gold nanoparticles (AuNP) point out that the size, shape and stability of the NHC capped AuNPs strongly depend on the morphology of the NHC ligand and the synthesis reaction conditions. [8, 10-12] For instance, Tilley and Vignolle [8] showed that different NHC with different N substituent lead to different gold nanoparticle size distribution. They found that, very small AuNPs are obtained – around 2 nm of diameter – when the bulky and rigid isopropyl substituent was bearing the N atoms while 6 – 7 nm AuNPs were found with a long alkyl chain.

However, there is still a lot of work to do in order to understand the role of interligand interactions on the stability of NHC coated GNCs since they show poor stability in solution [10, 13] even though NHC show a stronger bond with gold than thiolates and phosphine ligands. [14, 15] This suggests that the Au – ligand bond strength it is not the only parameter to take into account on the GNC stability. Therefore, the investigation of the mechanisms of NHC – capped GNCs and AuNPs formation, the mode of NHC grafting on the gold nanosurface and the effect of the substituent exchange bearing the N atoms are of great interest in order to understand NHC reactivity on GNCs.

Here, we study the reactivity of gold nanoparticles (AuNPs) and GNCs towards benzimidazole – 2 – ylidene ligands through a joint experimental – computational work. The experimental investigation was performed at the Institut Charles Gerhardt in the Université de Montpellier, France by Dr. M. Rodriguez Castillo, Dr. D. Laurencin, Dr. S. Clement, Dr. Y. Guari and Dr. S. Richeter together with a solid state DFT study considering a single NHCa (NHC bearing CH_3 on the N atoms: 1, 3 – dimethyl – 1H – benzimidazolium, called here NHCa) absorbed on a planar Au(111) surface in order to simulate a large AuNP performed by Prof. Tielens at the Laboratory of Condensed Matter of Paris at the UPMC. We carried out complementary computational modeling of the absorption of NHCa on GNCs using the quantum chemistry implementation of DFT. We chose the NHCa – Au_{38} set of complexes as a model. The computed binding energies are in agreement with DFT solid state computations where the carbene binds on a gold surface. We also computed the NMR spectra on $Au_{38}(NHCa)_9$ cluster which are in good agreement with the experimental ones.

Experimental results show that different NHCs ligands with different groups bearing the N atoms exhibit similar reactivity. The exchange ligand reaction is followed by the erosion of the AuNP under the effect of the NHC and the formation of bis(NHC) gold complexes ($[NHC - Au - NHC]^+$) was also demonstrated confirming the strong C – Au bond. [9]

Our computational results show that, single NHCa ligand absorption on 12 different Au type atoms (classified by their natural charge) on the Au_{38} surface produces a significant distortion of the cluster backbone, of the natural charge distribution of the gold atoms and also of the electronic structure of the complex. In most of the cases, the presence of the NHCa ligand triggers a distortion of the 38 gold core by pulling the gold atoms. Also, we confirm that, the bonding of the NHCa on the Au_{38} is even stronger than that of thiolates and characterized by a charge transfer from the ligand shell to the metal core, as for phosphine ligands.

Additionally, NMR spectra calculations were performed in order to interpret experimental data. First, the ^{13}C NMR chemical shifts of the molecular complex $[NHCa - Au - NHCa]^+$ were computed in a polarizable continuum model [16, 17] mimicking the effect of d_6 – DMSO solvent. Additionally, computation of the ^{13}C NMR spectrum was also performed on the NHCa – Au_{38} complex.

Furthermore, in order to analyze the effect of the chemical environment on the NMR signal we added several NHCa ligands on the NHCa – Au_{38} leading to the $(NHCa)_2 - Au_{38}$ complex and the $Au_{38}(NHCa)_9$ cluster. Calculation of the ^{13}C NMR spectrum of the bi – and fully – NHC coated clusters were also carried out. The computed ^{13}C NMR signals were now split because the NHCa carbon atoms become nonequivalent at the gold surface due to the different chemical environment. Our results show a good agreement with the experimental ^{13}C NMR spectra.

Finally, by combining the experimental data and the computations a possible mechanism to explain the formation of $[NHC - Au - NHC]^+$ complexes and the NHC – coated AuNPs is proposed. The computation of ^{13}C NMR spectra turned to be particularly useful to understand how the NMR signals are altered upon ligation of the AuNP surface.

6.1 Publication 2

Experimental and Theoretical Study of the Reactivity of Gold Nanoparticles towards Benzimidazole-2-ylidene Ligands

María Rodriguez – Castillo, [a] Gustavo Lugo – Preciado, [b] Danielle Laurencin, [a] Frederik Tielens,*[c] Arie van der Lee, [d] Sébastien Clement, [a] Yannick Guari, [a] José M. López – de – Luzuriaga,[e] Miguel Monge,[e] Françoise Remacle,*[b] and Sébastien Richeter*[a]

Chem. Eur. J. 2016, 22, 10446 – 10458

[a]. Institut Charles Gerhardt, UMR 5253 CNRS-ENSCM-UM, CC 1701, Université de Montpellier, Place E. Bataillon, 34095, Montpellier Cedex 05 (France). E-mail: sebastien.richeter@umontpellier.fr
[b]. Chemistry Department, B6c, University of Liège, 4000, Liège (Belgium). E-mail: fremacle@ulg.ac.be
[c]. Sorbonne Université, UPMC Université Paris 06, UMR 7574. Laboratoire Chimie de la Matière Condensée de Paris, Collège de France. 11 place M. Berthelot, 7523, Paris Cedex 05 (France). E-mail: frederik.tielens@upmc.fr
[d]. Institut Européen des Membranes, UMR 5635 CNRS – ENSCM – UM. Université de Montpellier, Place E. Bataillon, 34095, Montpellier Cedex 05 (France).
[e]. Departamento de Química, Grupo de Síntesis Química de la Rioja. UA-CSIC, Complejo Científico – Tecnológico, Universidad de La Rioja, 26004 *Logroño* (Spain).

Appendix 2: Supporting information. Experimental and Theoretical Study of the Reactivity of Gold Nanoparticles towards Benzimidazole-2 – ylidene Ligands.

ChemPubSoc Europe

DOI: 10.1002/chem.201601253

CHEMISTRY A European Journal Full Paper

Nanotechnology | *Hot Paper*

Experimental and Theoretical Study of the Reactivity of Gold Nanoparticles Towards Benzimidazole-2-ylidene Ligands

María Rodríguez-Castillo,[a] Gustavo Lugo-Preciado,[b] Danielle Laurencin,[a] Frederik Tielens,*[c] Arie van der Lee,[d] Sébastien Clément,[a] Yannick Guari,[a] José M. López-de-Luzuriaga,[e] Miguel Monge,[e] Françoise Remacle,*[b] and Sébastien Richeter*[a]

Abstract: The reactivity of benzimidazol-2-ylidenes with respect to gold nanoparticles (AuNPs) has been investigated using a combined experimental and computational approach. First, the grafting of benzimidazol-2-ylidenes bearing benzyl groups on the nitrogen atoms is described, and comparisons are made with structurally similar N-heterocyclic carbenes (NHCs) bearing other N-groups. Similar reactivity was observed for all NHCs, with 1) the erosion of the AuNPs under the effect of the NHC and 2) the formation of bis(NHC) gold complexes. DFT calculations were performed to investigate the modes of grafting of such ligands, to determine adsorption energies, and to rationalize the spectroscopic data. Two types of computational models were developed to describe the grafting onto large or small AuNPs, with either periodic or cluster-type DFT calculations. Calculations of NMR parameters were performed on some of these models, and discussed in light of the experimental data.

Introduction

Metal nanoparticles (MNPs) are an important class of nanomaterials that have found numerous applications, notably in catalysis[1] and medicine.[2] During the last decade, many synthetic pathways have been reported to give MNPs of controlled size and shape, both of these criteria being critical for specific applications such as catalysis.[1] As well-documented in the literature, the nature of the coating agents and experimental conditions used for the synthesis of MNPs have a significant impact on their morphology, reactivity, and solubility.[3]

N-Heterocyclic carbenes (NHCs) have become an ubiquitous class of ligands in the field of organometallic chemistry.[4] As NHCs are singlet carbenes, they are considered as phosphine analogues (i.e. two-electron σ-donor ligands), which can form very stable bonds with a wide range of metals in low and high oxidation states, including noble metals such as Ru,[5] Pd,[6] or Au.[7] Since their steric and electronic properties can be finely tuned according to the substituents present on the nitrogen atoms and heterocycle backbone, respectively, NHCs are now extensively used in the field of catalysis either as ligands of transition-metal complexes[4] or as organocatalysts.[8] The use of NHCs as coatings and stabilizing agents of metal nanoparticles (MNPs), and more generally metal surfaces, is also an emerging field of research with promising applications. NHC-coated Pd,[9] Ag,[10] Ru,[11] and Pt[12] nanoparticles have indeed been described in the literature: it was shown that such NHC-coated MNPs are often stable, and that they can sometimes be used as catalysts.[9,11,12]

Among MNPs, gold nanoparticles (AuNPs) are probably one of the most investigated metal-based nanoparticles.[13–17] Surface stabilization of AuNPs is routinely performed with thiols.[13] However, more labile ligands such as thioethers,[14] phosphines,[15] amines,[16] or carboxylates[17] can also be used. In the last few years, the use of NHCs to stabilize AuNPs has also been looked into.[9b,18–25] The stability of NHC-coated AuNPs strongly depends on the structure of the NHCs, that is, their size and rigidity. To ensure an efficient stabilization, they should be small or flexible to minimize steric repulsion between the NHC and the AuNP surface. In particular, small groups such as methyls or long flexible alkyl chains are

[a] Dr. M. Rodríguez-Castillo, Dr. D. Laurencin, Dr. S. Clément, Dr. Y. Guari, Dr. S. Richeter
Institut Charles Gerhardt, UMR 5253 CNRS-ENSCM-UM, CC 1701
Université de Montpellier, Place E. Bataillon
34095, Montpellier Cedex 05 (France)
E-mail: sebastien.richeter@umontpellier.fr

[b] G. Lugo-Preciado, Dr. F. Remacle
Chemistry Department, B6c, University of Liège, 4000, Liège (Belgium)
E-mail: fremacle@ulg.ac.be

[c] Dr. F. Tielens
Sorbonne Université, UPMC Université Paris 06, UMR 7574
Laboratoire Chimie de la Matière Condensée de Paris, Collège de France
11 place M. Berthelot, 7523, Paris Cedex 05 (France)
E-mail: frederik.tielens@upmc.fr

[d] Dr. A. van der Lee
Institut Européen des Membranes, UMR 5635 CNRS-ENSCM-UM
Université de Montpellier, Place E. Bataillon
34095, Montpellier Cedex 05 (France)

[e] Dr. J. M. López-de-Luzuriaga, Dr. M. Monge
Departamento de Química, Grupo de Síntesis Química de la Rioja
UA-CSIC, Complejo Científico-Tecnológico, Universidad de La Rioja
26004 Logroño (Spain)

Supporting information and the ORCID identification number(s) for the author(s) of this article can be found under http://dx.doi.org/10.1002/chem.201601253.

© 2016 Wiley-VCH Verlag GmbH & Co. KGaA, Weinheim

ChemPubSoc Europe

CHEMISTRY A European Journal Full Paper

suitable N-substituents. More surprisingly, the stability of NHC-coated AuNPs strongly depends on the experimental procedures used for their synthesis. To date, stable AuNPs coated by NHCs have mainly been prepared by chemical reduction[18,19] or thermolysis[20] of molecular species. Preparations using ligand exchange reactions have also been reported. In this case, starting materials are AuNPs coated by weakly coordinated molecules such as thioethers. Chechik et al. showed that the substitution of thioethers by NHCs is feasible, but they observed that the obtained AuNPs were not very stable and aggregated within a few hours.[21] In contrast, Glorius, Ravoo et al. showed that stable NHC-coated MNPs (M = Au or Pd) could be obtained by ligand exchange reactions using NHCs bearing long alkyl chains on their backbone (in positions 3 and 4 of imidazol-2-ylidenes).[9b] The improved stability of the NHC-coated AuNPs can be explained by the chemisorption of the NHC at the AuNPs surface and by the interactions between the long alkyl chains that occur simultaneously.[9b,19]

To date, most studies on the functionalization of AuNPs by NHCs have been performed using imidazol-2-ylidenes. However, to have a better comprehension of the interaction between NHCs and AuNPs, and to extend the types of coating agents that could be used, we, and others, have more recently started to study benzimidazol-2-ylidenes as stabilizing agents of AuNPs.[19,22,23] Crudden et al. showed that stable self-assembled monolayers of benzimidazol-2-ylidenes can be anchored on planar gold surfaces by exchange of thioether molecules.[22] In comparison to imidazol-2-ylidenes, the presence of the benzene ring fused to the positions 3 and 4 thus appears as a suitable option for further stabilization through π–π stacking at the surface of AuNPs.[26] These additional inter-NHC interactions seem to be of importance to give stable NHC-coated planar gold surfaces. Concurrently, we demonstrated that ligand exchange reactions between thioethers and benzimidazol-2-ylidenes bearing methyl or *n*-hexyl groups on the N atoms (Figure 1, **NHCa** and **NHCb**) occurred at the surface of AuNPs,[23] and ^{13}C solid-state NMR spectroscopy was used to characterize the grafted NHCs. We also showed that the reactivity of these benzimidazol-2-ylidenes was actually complex, because in addition to the ligand exchange reaction, the formation of bis(NHC) Au^{I} complexes was clearly evidenced (Figure 1, **3a** and **3b**). Moreover, Au^{I} complexes used as starting materials or generated during the reaction also appeared to be able to remove thioether molecules from the surface of AuNPs.[22]

Due to the apparent complexity of the reactivity of NHCs towards Au surfaces, and given the difficulties in characterizing experimentally their exact mode of grafting, computational studies have been initiated.[22,23,25] In particular, DFT calculations have been carried out using both periodic[22,23] and cluster approaches.[22,25] To date, these computational studies have mainly been performed to gain insight into the nature of the binding between the NHC and the Au surface, and to calculate the binding energy of the NHC ligand. However, the calculations so-far have been carried out on relatively simple models of Au surfaces, meaning that more complex simulations still need to be performed to get a better grasp of the potential differences in binding of NHCs on different Au surfaces, and hence, on AuNPs of different size and shape.

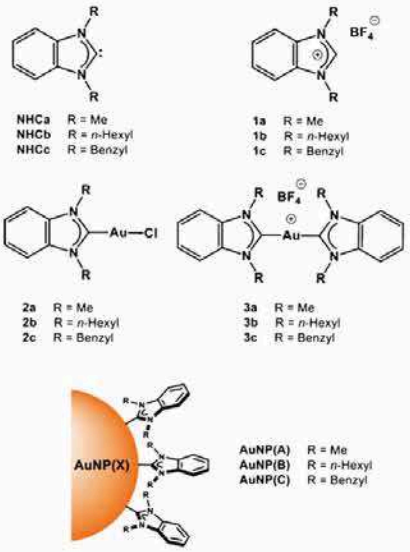

Figure 1. Structure of the NHC ligands, benzimidazolium salts, NHC–Au^{I} complexes, and NHC-functionalized AuNPs discussed in this work.

The purpose of this work is thus to provide a deeper insight into the reactivity and the grafting of benzimidazol-2-ylidenes at AuNP surfaces. In the first part, an overview of the experimental observations concerning the reactivity of benzimidazol-2-ylidenes onto AuNPs is provided. In particular, the grafting of a carbene bearing benzyl groups on the N atoms (**NHCc**) is discussed. Benzyl groups were chosen because they are flexible substituents that may contribute to further stabilize AuNPs through π-interactions with the gold surface.[11a,25] Here, the reactivity of this new system is compared with the previously studied NHCs involving methyl or *n*-hexyl substituents (**NHCa** and **NHCb**, respectively),[23] and the challenges related to the characterization of the functionalized nanoparticles are underscored. In a second part, a computational study of the binding of benzimidazol-2-ylidene ligands at AuNP surfaces is provided through DFT calculations. Different approaches (periodic and finite model DFT) to the modeling of gold surfaces functionalized by benzimidazol-2-ylidenes are presented, by looking at their grafting either onto "flat" Au surfaces or onto small nanoparticles, providing complementary insight into the strength and mode of binding benzimidazol-2-ylidenes onto Au surfaces. In the latter case, DFT calculations of NMR parameters were also performed, and results were discussed in view of the experimental data.

© 2016 Wiley-VCH Verlag GmbH & Co. KGaA, Weinheim

ChemPubSoc Europe

CHEMISTRY A European Journal Full Paper

Results and Discussion

Reactivity of NHCc towards thioether-coated AuNPs

The starting AuNPs used for the grafting were synthesized by following the procedure described by Reinhoudt et al.[27] They are well-dispersed, spherical AuNPs coated with di-*n*-dodecylthioether, and have a mean size of 5.8 (±1.2) nm.[23] The grafting of **NHCc** was performed in a similar way as previously described for **NHCa** and **NHCb**.[23] First, the di-*n*-dodecylthioether-coated AuNPs were mixed with the benzimidazolium salt **1c**. Then, NaOtBu was added to deprotonate **1c** and generate **NHCc** in situ. This led to the quick appearance of a dark precipitate in the reaction medium. Before complete precipitation, the UV/Vis spectrum of the suspension was collected, in order to monitor the change in the surface plasmon resonance (SPR) of the AuNPs. Compared to the spectrum of the starting di-*n*-dodecylthioether-coated AuNPs (λ_{max} ~ 510 nm), the SPR absorption band of the crude **AuNPs(C)** was bathochromically shifted to λ_{max} ~ 520 nm, suggesting that NHC-coated nanoparticles tend to aggregate.

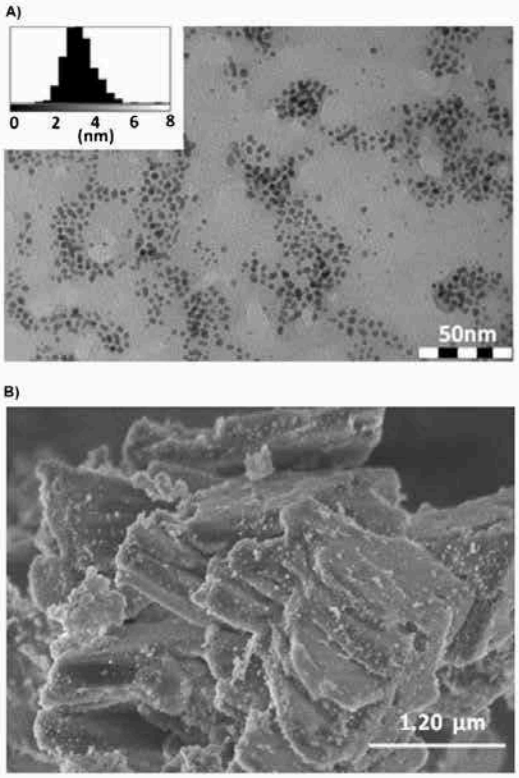

Figure 2. A) TEM image of crude **AuNPs(C)**, with the size distribution histogram (statistics over 408 NPs; min. = 1.39 nm; max = 7.48 nm; mean = 3.44 nm; standard deviation = 0.77 nm). B) SEM image of crude **AuNPs(C)** after precipitation with EtOH.

TEM analyses actually show that the crude **AuNPs(C)** contain both aggregated and well-dispersed spherical NPs, with a mean size of 3.4 (±0.8) nm (Figure 2A). Thus, there is a significant decrease in the average size of the nanoparticles compared to the starting thioether-coated AuNPs (5.8 (±1.2) nm). A similar observation had been made in the case of **NHCa**, for which an average size of 2.8 (±0.6) nm had been measured for the crude **AuNPs(A)**.[23] In contrast, in the case of **NHCb**, the crude **AuNPs(B)** had an average particle size of ~5.1 (±1.0) nm, which is more similar to the starting AuNPs.[23] This is probably due to the presence of long alkyl chains on the nitrogen atoms of **NHCb** that interact better with each other, and thereby improve the stability of the NHC-coated AuNPs, and prevent a surface etching process from occurring. Such results are consistent with the work recently reported by Glorius and Ravoo et al.[9b]

Crude **AuNPs(C)** were precipitated by addition of ethanol, and isolated after several cycles of centrifugation and washing. SEM showed the presence of a crystalline phase in the precipitate (Figure 2B) that was identified by powder XRD and ^{13}C solid-state NMR (Figure 3). Indeed, when comparing the diffractogram of the precipitated **AuNPs(C)** to those of the benzimidazolium salt **1c**, and of the **NHCc**–Au^{I} complexes **2c** and **3c** (for which a full description of the crystal structures and spectral data is provided in the Supporting Information), it is clear that the bis(NHC) Au^{I} complex **3c** is the crystalline byproduct. It is worth noting that the presence of AuNPs in the crude

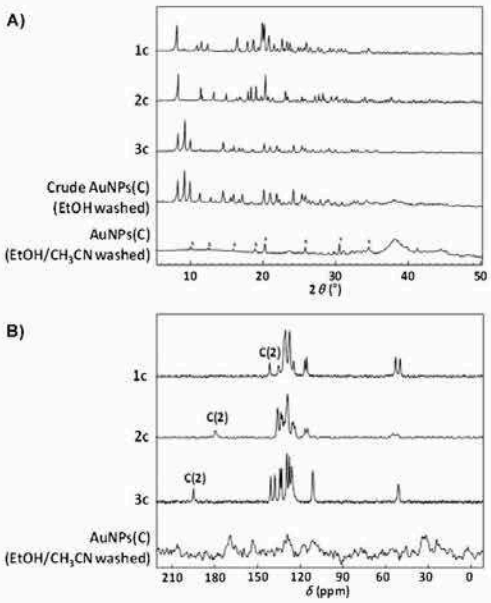

Figure 3. A) XRD powder patterns of compounds **1c**, **2c**, **3c**, crude **AuNPs(C)**, and **AuNPs(C)** after additional washing with CH_3CN (*reflections assigned to $Na_2B_4O_7{\cdot}5H_2O$, a byproduct formed during the reaction). B) ^{13}C CPMAS solid-state NMR spectra of **1c**, **2c**, **3c**, and **AuNPs(C)** after washing with EtOH and CH_3CN.

© 2016 Wiley-VCH Verlag GmbH & Co. KGaA, Weinheim

ChemPubSoc Europe

CHEMISTRY A European Journal Full Paper

AuNPs(C) sample is actually hardly noticeable by XRD due to the high quantity and high crystallinity of **3c**: only a weak Bragg reflection around $2\theta \sim 40^\circ$, characteristic of the (111) reflection of Au is visible (Figure 3A). The analysis of the ^{13}C CPMAS (cross-polarization magic angle spinning) solid-state NMR spectrum of the crude **AuNPs(C)** was also found to be consistent with the formation of the bis(NHC) Au^I complex **3c**, as shown by the characteristic chemical shift at $\delta = -190$ ppm of the carbon bound to Au^I (data not shown).[23,28] Thus, both XRD and ^{13}C solid-state NMR suggest that the etching of the AuNPs is related to the formation of the bis(NHC) Au^I complex **3c**. These results are fully consistent with our previous study on the grafting of **NHCa** and **NHCb** on AuNPs.[23]

Given that the bis(NHC) Au^I complex **3c** was soluble in acetonitrile, it was possible to wash the crude **AuNPs(C)** with this solvent to isolate the functionalized nanoparticles. These NPs were found to be insoluble in most solvents, and they were thus characterized by ^{13}C CPMAS solid-state NMR to identify organic species such as NHCs on their surface. Several difficulties were encountered when trying to record the ^{13}C NMR spectrum. Indeed, because several washes were needed to fully eliminate the diffraction peaks corresponding to the bis(NHC) Au^I complex, only a very small amount of residual NPs was collected. The solid-state NMR spectrum obtained on these NPs was very noisy, even after two days of acquisition (Figure 3B). Nevertheless, signals characteristic of organic species can be distinguished on this spectrum, suggesting the presence of **NHCc** at the AuNPs surface. It is worth noting that in our previous work, difficulties had also been encountered for recording the ^{13}C solid-state NMR spectra of the grafted NPs after complete washing, notably for AuNPs functionalized by **NHCa**.[23] So far, it is only in the case of **NHCb** ligands that a decent spectrum could be obtained, with broad signals and different chemical shifts for the carbene C(2) atom (at $\delta = \sim 170$ and 181 ppm).[23]

Modeling of functionalized AuNPs

As shown above, the characterization of the exact mode of grafting of NHCs at the surface of AuNPs can be particularly challenging, especially when the surface coverage of the nanoparticles is low and when these cannot be suspended in solution. Thus, in view of clarifying in a more general way the interaction between benzimidazol-2-ylidenes and AuNP surfaces, computational modeling was performed using DFT calculations. Given that NHCs have been shown to be able to bind to AuNPs of different size (ranging from ~1 to 6.8 nm),[18,19,23] two different approaches were used to model the grafting. On one hand, the functionalization of the larger AuNPs was modeled by considering a planar Au(111) surface, since it is predominant in relatively large AuNPs, as consequence of being the most stable surface.[29] In this case, periodic DFT calculations were performed using the Vienna Ab initio Simulation Package (VASP) code.[29] On the other hand, the functionalization of the smaller AuNPs was modeled by considering the Au_{38} gold cluster, which is a well-known Au cluster with a size of ~1 nm.[30] In this case, calculations were performed using a cluster-type approach and the Gaussian 09 code.[31] For both kinds of DFT investigations, the grafting of the benzimidazol-2-ylidene bearing a methyl substituent on the nitrogen atoms (**NHCa**) was studied to reduce the computational cost, and because our experimental studies had shown similar reactivity for **NHCa**, **NHCb**, and **NHCc**.

Grafting of NHCa on a planar Au(111) surface

The binding of a single **NHCa** ligand on a planar Au(111) surface was first studied. Only monodentate modes of coordination of the NHC at the Au surface were considered (through a single Au–C(2) bond), because a previous computational study had shown that it was energetically less favorable for the carbene to adopt bridging positions between surface Au atoms.[22] Here, different binding orientations with respect to the surface were studied for **NHCa** (Figure 4): perpendicular (Model A), tilted by -45° (Model B), and parallel (Model C).

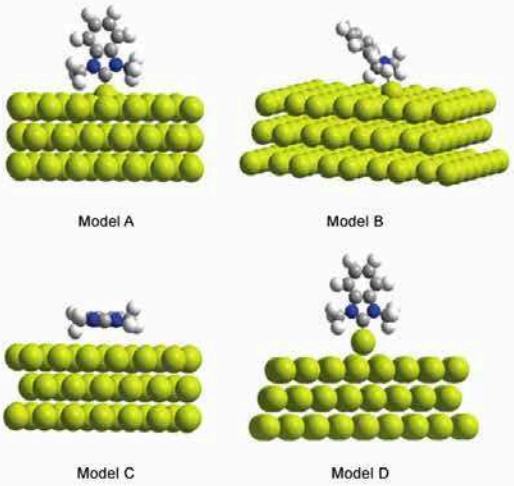

Figure 4. DFT-optimized geometries for the different grafting models of **NHCa** on the Au(111) surface (VASP code).

Looking at the orientation preference of the carbene at the Au(111) surface appeared as an important point to consider, because a recent computational investigation on the grafting of pyridine derivatives on Au had shown that depending on the nature of the substituents on the pyridine, either parallel or perpendicular configurations could be more favourable.[32] In the case of **NHCa**, the energies of these different configurations after geometry optimization are provided in Table 1, together with the average Au–C(2) distances.

Results presented in Table 1 clearly show that the perpendicular binding of **NHCa** with respect to the Au(111) surface (Model A) is more favourable than the other geometries, the adsorption energy being ~ -34.21 kcal mol^{-1}. Compared to Model B in which **NHCa** is not perpendicular to the surface, the energy difference is small (~ 3.76 kcal mol^{-1}), suggesting

© 2016 Wiley-VCH Verlag GmbH & Co. KGaA, Weinheim

ChemPubSoc Europe

CHEMISTRY A European Journal Full Paper

Table 1. Binding energies and Au–C(2) bond lengths for the optimized Models **A–D** (VASP code).

Model	Binding energy [kcal mol^{-1}]	Au–C(2) distance [Å]
A	−34.21	2.10
B	−30.45	2.11
C	−11.42	2.40
D	−63.55	2.03

that the angle is flexible and determined by the surface coverage. However, a closer look at the geometries of the optimized structures suggests that this may be because the perpendicular orientation represents the optimal balance between intermolecular interactions between the methyl substituents and the Au surface (dispersion–steric repulsion), and the best Au–C(2) orbital overlap. It is worth noting that in Models A and B, the Au atom is pulled up out of the surface by ~1 Å, and the Au–C(2) distance is ~2.1 Å, which is similar to what is observed in mono(NHC) and bis(NHC) Au^{I} complexes such as **2a** (d(Au–C(2)) ~ 1.98 Å)[33] and **3a** (d(Au–C(2)) ~ 2.01 Å).[23] This confirms that strong Au–C(2) bonds can form between the Au surface and the carbene. A similar phenomenon has been observed for other ligands such as thiols, for which the alkyl chain length can also influence the Au–S bond length.[34] In contrast, when the adsorption of a thioether ligand such as diethylthioether on Au(111) was considered (as a model of the di-*n*-dodecylthioether ligand initially present experimentally at the surface of the AuNPs), a much weaker adsorption energy (~ −14.36 kcal mol^{-1}) and a longer Au–S bond (~2.60 Å) were observed, which explains the ease with which these ligands could be removed from the surface during the synthesis (Figure S12 in the Supporting Information).

It should be noted that the pulling of a gold atom out of the surface in Models A and B can only be seen as a local minimum on the potential energy surface, without passing a possible activation energy barrier for the formation of a true adatom, and without introducing the filling up of the vacant site left in the bulk after displacement of this gold atom on top of the surface. However, the present optimized geometries might be considered as the initial step of a surface reconstruction induced by the grafting of a carbene. Such pulling of an Au atom out of the surface might also facilitate the release of mono(NHC) Au^{I} complexes, and thereby explain the formation of bis(NHC) Au^{I} complexes such as **3a–c** (vide infra).

The grafting of **NHCa** onto an adatom positioned at a face-centered cubic (*fcc*) position of the Au(111) surface was then studied, as a first approach towards determining how surface defects may affect the adsorption mode or energy of NHCs on Au. Such low coordinated atoms are indeed expected to be the most reactive sites on the nanoparticle surface.[35] In this case, only the adsorption of **NHCa** perpendicular to the surface was looked into (see Model D in Figure 4). The binding of the carbene was found to be even more favourable energetically than in Model A (−63.55 vs. −34.21 kcal mol^{-1}). In Model D, no steric hindrance between the methyl groups and the Au surface is observed and after geometry optimization, the Au–C(2) bond distance is ~2.03 Å, which is shorter than what had been observed for Model A, and very similar to what is experimentally measured for Au–NHC complexes. It is also worth noting that a similar adsorption energy (~ −67 kcal mol^{-1}) had been previously calculated for the binding of an imidazole-2-ylidene bearing aryl bromide functional groups onto an adatom.[25] On a more general perspective, the significant difference in adsorption energies of **NHCa** in Models A and D shows that the reactivity of the NHC will strongly depend on the gold surface structure. In view of analyzing in more detail the difference in affinity of **NHCa** for a variety of Au surface sites, we thus turned towards the modeling of its grafting onto smaller Au nanoparticles, which do not present any flat Au(111) surface.

Grafting of NHCa onto a Au_{38} cluster

Many models of nanoparticles and/or small clusters of metals, metal oxides, and metal chalcogenides have been theoretically investigated,[36] including by some of us.[37] Here, we decided to look into the adsorption of **NHCa** on the Au_{38} gold cluster, making the transition between the models of the defect-free flat facet and the irregular surface of the AuNPs. The structure of the Au_{38} cluster was first created, starting from the crystallographic data of $Au_{38}(SCH_2CH_2Ph)_{24}$,[38] and performing a geometry optimization on the bare Au_{38} core. The equilibrium geometry is shown in Figure 5a: it consists of two central atoms (highlighted in Figure 5b) surrounded by an ellipsoidal 21 gold frame (highlighted in Figure 5c and 5d), thereby forming an

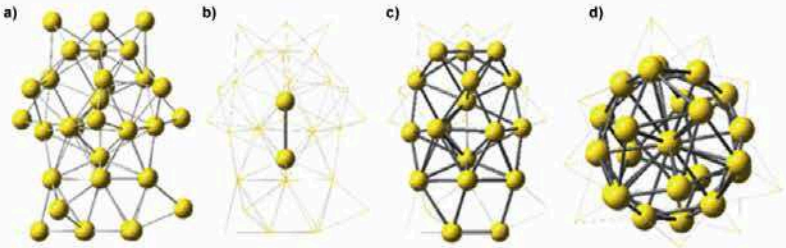

Figure 5. Equilibrium structures of the Au_{38} cluster at the DFT level (CAM-B3LYP LANL2MB). a) The Au_{38} cluster. b) The two central atoms. c) The 23 gold core (two central atoms + 21 Au frame). d) The Au_{23} gold core visualized from the bottom.

© 2016 Wiley-VCH Verlag GmbH & Co. KGaA, Weinheim

ChemPubSoc Europe

CHEMISTRY A European Journal Full Paper

Au_{23} core. Finally, the remaining 15 gold atoms are located on some of the triangular faces of the Au_{23} core. The metallic core of the cluster (or the bare cluster) belongs to a C_3 point group within a 0.01 Å tolerance.

Natural bonding orbital (NBO) analysis shows that the gold atoms of the bare cluster are separated in two differently charged populations (see Figure S13 in the Supporting Information). In the first group, the partial charges were negative, varying from −0.11 to −0.25 |e|, with the Au_{23} gold core belonging to this group. The rest of the atoms (on the surface of the cluster) belonged to the second group, with positive partial charges ranging from 0.20 to 0.29 |e|. Further analysis of the natural charge of every atom showed that they followed the C_3 symmetry, meaning that we could actually classify the 21 atoms of the Au_{21} shell frame and the 15 other atoms of the external surface in 12 different groups, each formed by three atoms possessing the same natural charge (see Figure S14 in the Supporting Information).

One atom out of each of these 12 different partial charge groups was taken to interact with a single **NHCa** ligand. The equilibrium geometries are shown in Figure 6. Immediately, it appeared that completely different core geometries were obtained depending on the binding site of **NHCa**. Further analysis of the different equilibrium geometries showed that the C_3 symmetry of the Au_{38} cluster was broken, and that in most cases, the binding of **NHCa** "pulled" the gold atoms closer to each other within the cluster. This could be highlighted by comparing the distribution of distances between gold atoms in the bare Au_{38} and in the cluster ligated to **NHCa** (see Figures S15 and S16 in the Supporting Information).

As shown in Table 2, in all cases, the NHC ligand was found to be strongly bound on the Au_{38} cluster surface, with binding energies ranging from −19.51 to −34.41 kcal mol^{-1} (Table 2). Such binding energies are in the same range as those computed herein on a flat Au(111) surface (between −11.42 and −34.21 kcal mol^{-1}, see Table 1), as well as with other previous DFT computations.[22,23] Interestingly, the binding strengths varied with the binding site, being larger when **NHCa** was attached to the least coordinated gold atoms. This is in line with what had been observed for the VASP calculations, when comparing models with/without an adatom (Models A and D) and it implies that some surface sites are more favourable to the binding of carbenes. The binding was found to be characterized by a charge transfer from the **NHCa** ligand to the Au_{23} core, with the natural charge of Au_{23} varying from −2.82 to −3.44 |e| (Table 2). Other methods to compute partial charges, such as the M–K[39] or the CHelpG scheme,[40] which are consistent with the electrostatic potential, also lead to a negatively charged Au_{23} core, but with a lower value. For example, for complex **6**, the M–K scheme with a gold van der Waals radius of 1.66 Å leads to a partial charge of −1.45 |e| on the inner Au_{23} core and +1.05 |e| for the 15 Au surface atoms, leading to an overall charge on Au_{38} of −0.4 |e|. For the same complex, the NBO scheme leads to a larger polarization between the Au_{23} core (−3.00 |e|) and the surrounding 15 Au atoms (+2.62 |e|) but to a similar overall charge of −0.38 |e| on the Au_{38} core. This clearly highlights the electron-donor nature of NHC ligands. More specifically, as shown in Table 2, the natural charge on the Au_{23} core varied with the position of the grafted ligand, and the electron-donor character of **NHCa** was enhanced when the coordination number of the gold atom (in its bare configuration) increased.

Table 2. Complex label (as shown in Figure 6), coordination number (CN),[a] charge of the gold atom in the bare cluster (NBO Au bare), natural charge of the Au_{23} core (NBO Au_{23}), binding energy (BE[b]), relative free energy ΔG and C–Au bond length of the **NHCa**–Au_{38} system.

n°	CN	NBO Au bare [|e|]	NBO Au_{23} [|e|]	BE [kcal mol^{-1}]	relat. ΔG [kcal mol^{-1}]	C–Au [Å]
1	7	−0.17	−3.44	−27.86	6.55	2.08
2	4	0.23	−3.15	−33.48	0.92	2.09
3	3	0.20	−3.15	−30.33	4.08	2.09
4	8	−0.11	−2.82	−29.59	4.82	2.08
5	8	−0.12	−3.10	−25.71	8.69	2.08
6	7	−0.22	−3.00	−34.41	0.00	2.08
7	8	−0.11	−2.86	−20.32	14.09	2.08
8	3	0.29	−3.15	−34.38	0.02	2.09
9	4	0.20	−3.03	−33.83	0.60	2.08
10	8	−0.14	−3.04	−19.51	14.90	2.08
11	8	−0.15	−2.85	−29.75	4.66	2.10
12	3	0.23	−3.08	−34.27	0.14	2.08

[a] CN is the coordination number of the gold atom in its bare configuration that interacts with the ligand. [b] BE represents the binding energy of the Au_{38}–NHC system. It is calculated as: $BE = \Delta G_{complex} - \Delta G_{bare\,complex} - n\Delta G_{ligand}$ in which the n is the number of ligands (in this case $n = 1$).

No significant difference was observed between the Au–C(2) bond lengths of the 12 equilibrium structures, which varied between ~2.08 and ~2.10 Å (Table 2). Such values are slightly higher than the experimental value observed for the bis(NHC) Au^I complex **3a**, but are in good agreement with previous DFT calculations of a single carbene adsorbed onto an Au(111) surface,[22,23] such as those presented above (Table 1). In the most stable cases, the shortest Au–C(2) bond length was 2.08 Å for the Au_{38} cluster calculations (configuration **6** in Figure 6), and 2.03 Å for the VASP calculations (Model D). The optimized geometries of the **NHCa**–Au_{38} system were also analyzed by measuring angles between the C_2 axis of **NHCa** and the Au_{38} cluster surface (see Figures S17–S19 in the Supporting Information). Among the 12 calculated configurations, different angles were observed between the gold cluster surface and **NHCa**, especially when looking at the C_2 axis of the ligand. In general, the NHC ligand was found to bind in an "on-top" position on a tetrahedron formed by four gold atoms. Qualitatively, the configuration in which the ligand was the most perpendicular to the surface was configuration **3** in Figure 6. However, no special relation could be found between the stability of the cluster and the angle of the ligand with respect to the cluster surface, nor with any other geometrical parameter.

Having analyzed the mode of binding of one NHC on Au_{38}, we then investigated the grafting of more ligands at the nanoparticle surface. First, we looked at the effect of the addition a second **NHCa** on a surface Au site. The **NHCa**–Au_{38} compound corresponding to configuration **6** (Figure 6) was used as starting point for this test, because this structure is the

 © 2016 Wiley-VCH Verlag GmbH & Co. KGaA, Weinheim

ChemPubSoc Europe

CHEMISTRY A European Journal Full Paper

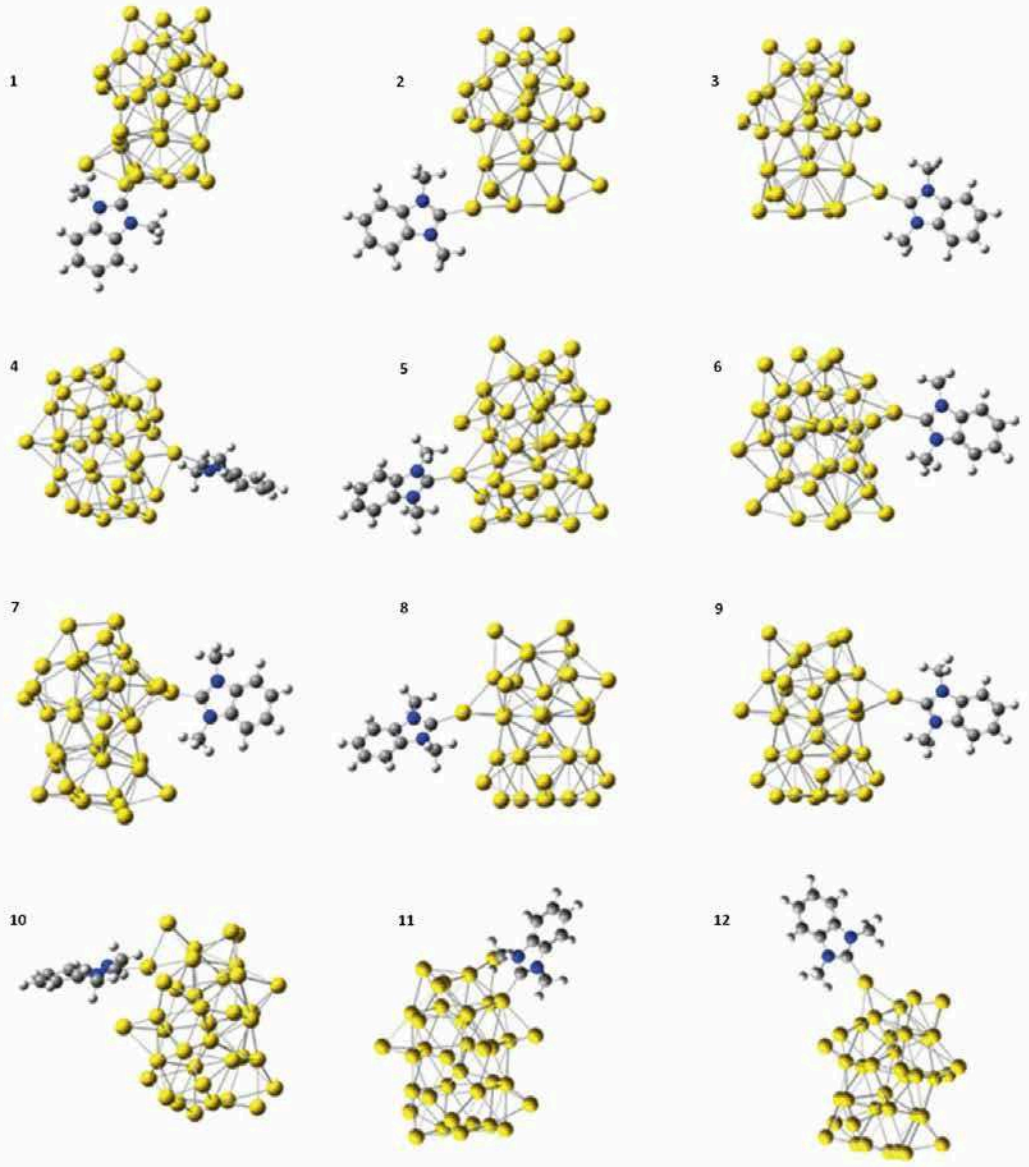

Figure 6. Equilibrium structures of the **NHCa**–Au_{38} system, computed at the CAM-B3LYP LANL2MB/6-31G(d) level in the gas phase.

most stable energetically in the gas-phase (Table 2, entry 6), and a second **NHCa** was added on a neighboring surface site. The final compound obtained after geometry optimization is shown in Figures 7a and b. Interestingly, the addition of a second ligand **NHCa** at this position did not induce a big distortion of the metallic core (see Figures S23 and S24 in the Supporting Information). The equilibrium structure of the Au_{38} cluster fully covered by nine **NHCa** ligands was then computed in the gas phase (Figure 7c and d). Because of the electron-donor character of the carbene ligands, the metallic core in $Au_{38}(NHCa)_9$ has a negative charge of $-2.57\,|e|$, see Figure S29 in the Supporting Information. The larger negative charge on the metallic core leads to an increase of the Coulomb repulsion between the gold atoms and larger distances between Au atoms, ranging from 2.67 to 12.27 Å, compared to 2.79 to 11.96 Å for the bare cluster (see Figures S23 and S24 in the

 © 2016 Wiley-VCH Verlag GmbH & Co. KGaA, Weinheim

ChemPubSoc Europe

CHEMISTRY A European Journal Full Paper

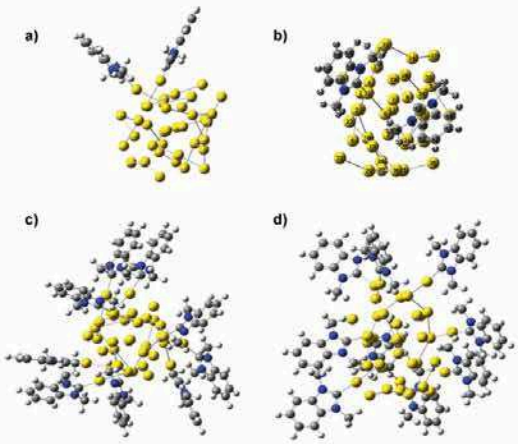

Figure 7. Equilibrium structures of the $(\mathbf{NHCa})_2$–Au_{38} system with two ligands **NHCa** close to each other computed at the CAM-B3LYP LANL2MB/6-31G(d) level in the gas phase: a) Top view, b) side view. Equilibrium structures of the $(\mathbf{NHCa})_9$–Au_{38} system computed at the same level: c) Top view, d) side view.

Supporting Information). Overall, these calculations underscore the strong flexibility of the Au_{38} core upon coordination of NHC ligands as simple as **NHCa** at its surface.

Possible mechanism to explain the formation of bis(NHC) Au^{I} complexes

By combining experimental and theoretical data, we propose as a first approximation the following mechanism to explain the formation of bis(NHC) Au^{I} complexes and NHC-grafted AuNPs (Figure 8):

1) At the initial state, the weakly adsorbed thioethers are gradually substituted by strongly bonded NHCs. The binding energies can be high (exceeding -34 kcal mol^{-1}, according to DFT calculations) and do not seem to depend on the size of the AuNPs, because they are similar for both systems in which NHCs are bound to a Au(111) surface (assimilated to the surface of a large AuNP) or to a Au_{38} cluster-type surface (assimilated to a small AuNP).

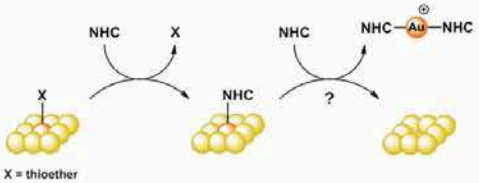

Figure 8. Proposed steps for the formation of bis(NHC) Au^{I} complexes by the reaction of NHCs with AuNPs. The AuNP surface is schematically represented here, and the Au atom removed from the AuNP surface is drawn in orange.

2) Although computational studies show that the binding energy between NHCs and AuNPs surface is high enough to ensure their stability, the absence of secondary interactions between **NHCa–c** (such as van der Waals interactions) can explain the poor stability of obtained AuNPs. The strength of the NHC–Au bonds leads to a repositioning of the Au atom with respect to the surface and consequently to surface reconstruction, with the formation of surface defects such as Au adatoms on the AuNP. Subsequently, the NHC–Au moiety may diffuse at the AuNP surface, and/or reconstruct the surface,[22] because the C–Au bonds compete with the Au–Au bonds.
3 Finally, the (mono)NHC–Au fragments released from the surface can react with the remaining NHC ligands in solution, by analogy with what has been observed previously with other types of ligands such as phosphines[15a] leading to the formation of bis(NHC) Au^{I} complexes and thereby to the erosion of the AuNPs. Surface reconstruction leading to etching is a commonly observed phenomenon with thiol coating agents.[42]

If characterizing molecular species such as bis(NHC) Au^{I} complexes is easy by using routine techniques such as ^{13}C NMR spectroscopy, more difficulties were encountered when characterizing the nanomaterials. In this context, calculating ^{13}C NMR spectra of NHC-coated AuNPs would be particularly useful to understand how ^{13}C NMR signals of NHC ligands are altered upon ligation to the Au surface.

Calculation of ^{13}C NMR spectra of NHCa bound to Au_{38} clusters

NMR spectroscopy is a uniquely suited technique to characterize molecular species present at the surface of MNPs, and to determine the presence of different surface sites.[42] Most of the time, spectral differences are observed between the "attached" molecular species and their "free" form, such as a line broadening or disappearance of some resonances, and/or altered chemical shifts, because the local environment of the surface-bound molecules is different and more diverse than in solution.[37] Given the difficulties we had encountered in characterizing the **NHCa**-functionalized AuNPs by NMR,[23] we decided to use DFT calculations to determine how ^{13}C NMR signals of **NHCa** might have been altered upon ligation to the AuNP surface, such information being useful for future studies of the grafting of other carbenes onto AuNP surfaces (Table 3).

The ^{13}C NMR chemical shifts of the molecular complex **3a** were first calculated in a polarizable continuum model (PCM) mimicking the effect of [D$_6$]DMSO as the solvent, with and without the BF_4^- counter anion. Results obtained for the cation showed a good agreement between the calculated and the experimental chemical shifts of complex **3a**, although all calculated signals were found at slightly higher chemical shifts (Table 3, see also Figure S26 and Table S10 in the Supporting Information). In particular, the calculated chemical shift of the carbene atom of complex **3a** is $\delta = 191.54$ ppm, which is close to the experimental value ($\delta = 190.19$ ppm). Taking into

© 2016 Wiley-VCH Verlag GmbH & Co. KGaA, Weinheim

ChemPubSoc Europe

CHEMISTRY A European Journal Full Paper

Table 3. Experimental and calculated ^{13}C NMR chemical shifts δ (ppm) and chemical shift differences $\Delta\delta$ for the carbene and N–Me group resonances.

	Carbene/δ [ppm][a]	N–Me/δ [ppm][a]
Experimental		
3a[b]	190.19	34.84
AuNP(a)[c]	180 (4)[d]	
Calculated		
3a ($-BF_4^-$)[e,g]	191.54 (1)[f]	36.89 (2)[f]
3a[e,h]	192.29–191.40 (2)[f]	30.14–29.27 (4)[f]
NHC_a–Au_{38} **6**[e,i]	189.62 (1)[f]	36.35–32.81 (2)[f]
NHC_a–Au_{38} **2**[e,j]	187.33 (1)[f]	33.61–32.68 (2)[f]
$(NHC_a)_2$–Au_{38}[e]	190.10–188.16 (2)[f]	36.07–32.71 (4)[f]
$(NHC_a)_9$–Au_{38}[e]	194.05–190.08 (9)[f]	36.01–30.72 (18)[f]

[a] The δ ranges represent the lowest and the highest chemical shifts in ppm. [b] Measured in [D$_6$]DMSO, see ref. [23]. [c] Measured in the solid state, see ref. [23]. [d] Number in parentheses correspond to the full width at half maximum. [e] Calculated at the CAM-B3LYP level in [D$_6$]DMSO. Tetramethylsilane (TMS) was used as the ^{13}C NMR reference. [f] Numbers in parentheses represent the number of signals calculated for a given configuration. [g] Calculated for complex **3a** without a BF_4^- anion. [h] Calculated for complex **3a** with a BF_4^- anion. [i] Calculated for configuration **6** in Figure 6. [j] Calculated for configuration **2** in Figure 6.

account the BF_4^- anion in the computation of the NMR spectrum leads to an overall better agreement with the experimental data, except in the case of the methyl resonances as can be seen in Figure S26 and in Table S10 in the Supporting Information.

To calculate the ^{13}C NMR chemical shifts of **NHCa** ligated to an AuNP surface, we first used the **NHCa**–Au_{38} compound corresponding to configuration **6** in Figure 6, this structure being the most stable energetically in the gas-phase (Table 2, entry 6). To be able to compare the calculated shifts for the **NHCa**–Au_{38} model with those of the molecular complexes **3a**, and to be able to discuss the trends, the equilibrium geometry of the **NHCa**–Au_{38} cluster was first optimized in a polarizable continuum model mimicking the effect of [D$_6$]DMSO as the solvent (see Figures S20–S22 in the Supporting Information). Compared to the gas-phase structure shown in Figure 6, only small differences were observed after geometry optimization in the solvent model: while Au–C(2) bond lengths were close to 2.08 Å in both cases, a slight decrease in the charge of the Au_{23} core was observed ($-3.00|e|$ in the gas-phase compared to $-2.89|e|$ charge in the presence of the [D$_6$]DMSO). As expected, calculated ^{13}C NMR signals for this **NHCa**–Au_{38} cluster were split because the NHC carbon atoms become nonequivalent at the AuNP surface (Table 3, and Figure S27 and Table S7 in the Supporting Information), the most important splitting being obtained for the two methyl groups ($\Delta\delta = 3.54$ ppm). It is also noticeable that all calculated ^{13}C NMR signals of the **NHCa**–Au_{38} cluster were found at lower chemical shifts compared to those calculated for complex **3a** (Table 3, and Table S10 in the Supporting Information). Indeed, the calculated chemical shift of the carbene atom ligated to the Au_{38} cluster was $\delta = 189.62$ ppm, which is still in the range of those observed for NHC-Au complexes. It is worth noting that the location of **NHCa** on the Au_{38} cluster has a small effect. Indeed, although most calculated ^{13}C NMR signals of the **NHCa**–Au_{38} cluster in configuration **2** in Figure 6 are similar to those calculated in configuration **6** (Table 3 and Table S7 in the Supporting Information), those of the methyl groups differ.

Adding an extra **NHCa** close to the first one (as in Figures 7a and b) had a significant impact on the computed NMR spectrum (Table 3, $(NHCa)_2$–Au_{38}). Indeed, all signals were split, due to the fact that each **NHCa** ligand experienced different chemical environments (see Figure S28 and Table S8 in the Supporting Information). This is even more noticeable in the case of the fully protected $(NHCa)_9$–Au_{38} cluster (Figures 7c and d), as shown by the range of calculated ^{13}C NMR chemical shifts for each type of C atom (shown in Figure 9 and Table 3, and Table S9 in the Supporting Information). Nevertheless, it is worth underscoring that for both the $(NHCa)_2$–Au_{38} and $(NHCa)_9$–Au_{38} models, the average values of calculated chemical shifts for each type of carbon remain in the same range, although a slight increase is observed in the chemical shift of the C atom of the carbene (see Table S10 in the Supporting Information).

These NMR calculations are the first of the kind to be carried out on models of NHC-functionalized AuNPs, and thus provide an interesting guideline to the discussion of experimental

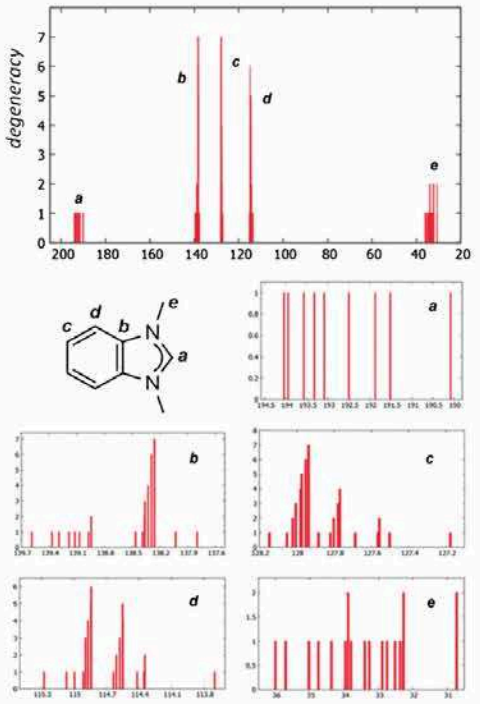

Figure 9. Calculated ^{13}C NMR spectrum of the $(NHCa)_9$–Au_{38} system in [D$_6$]DMSO. TMS (tetramethylsilane) was used as ^{13}C NMR reference. All calculations have been performed at the DFT CAM-B3LYP level of theory. The relativistic pseudopotential and basis set LANL2MB were used in the case of gold and for the other atoms 6–311 + G(2d,p) was employed.

© 2016 Wiley-VCH Verlag GmbH & Co. KGaA, Weinheim

ChemPubSoc Europe

CHEMISTRY A European Journal Full Paper

spectra. However, comparisons to available ^{13}C NMR data are still difficult to perform. The broadening of the NMR signals of the grafted NHCs can be clearly explained by looking at the study of the (**NHCa**)$_9$–Au$_{38}$ model, but it is more difficult to discuss the changes in chemical shifts (especially of the C atom of the carbene).[23] This is because calculations herein were performed on a simple **NHCa** ligand grafted on "small" Au$_{38}$ clusters, while experimental systems involve in general 1) more complex ligands (with different ligand–ligand interactions) and/or other sizes of particles (between ~1 and 6.8 nm), as well as 2) different analytical conditions (solid vs. solution NMR). Unfortunately, the complete modeling of such complex systems is still computationally prohibitive at this stage.

Conclusions

Many studies reported so far had shown that strong C–Au bonds are formed in the course of the formation of NHC-coated AuNPs.[9b, 20, 22] However, a strong C–Au binding energy is not a sufficient factor to ensure the stability of NHC-coated AuNPs. Here, for example, we performed a ligand exchange reaction between NHC ligands (benzimidazol-2-ylidenes) and thioether-coated AuNPs and observed the formation of bis(NHC) Au^I complexes, as well as the formation of smaller aggregated AuNPs. The decrease in size of the AuNPs and the formation of molecular of bis(NHC) Au^I complexes could be explained by the poor ability of benzimidazol-2-ylidenes used here to stabilize AuNPs.

Further details on the reactivity of NHCs at the surface of AuNPs were reached by combining experiments to computational modeling. The development of two types of computational models of the Au surface was found to be particularly useful, in order to be able to confirm the calculated trends and to generalize the conclusions to different sizes of nanoparticles. Calculations of NMR shifts were performed for the first time on these systems, showing that they can be used as an interesting guideline to discuss experimental spectra. Nevertheless, several challenges remain at this stage, which include 1) recording higher-sensitivity ^{13}C NMR spectra of functionalized AuNPs (using, for example, techniques like dynamic nuclear polarization),[42a] 2) developing more realistic computational models (involving notably more complex NHCs), and performing spectroscopic calculations on these complex models (such as NMR) to compare them with the experimental data.

Experimental Section

Materials

Reactions were performed using oven-dried glassware. Chemicals were obtained from Alfa–Aesar ($HAuCl_4 \cdot 3H_2O$, benzimidazole, di-*n*-dodecylsulfide, benzyl bromide), Sigma–Aldrich ($AgBF_4$), Panreac ($NaBH_4$), and Lancaster (tetra-*n*-octylammonium bromide), and used as received. The *N*,*N*-dibenzylbenzimidazolium bromide precursor, the AuNPs functionalized by di-*n*-dodecylsulfide, and complex **2c** were synthesized as described in the Supporting Information. All reactions were monitored by thin-layer chromatography using Merck© TLC Silica gel 60 F254 plates. ^1H and $^{13}C\{^1H\}$ solution NMR spectra were recorded in [D$_6$]DMSO on a Bruker 300 MHz spectrometer. Chemical shifts are reported in ppm, referenced to a DMSO solvent residual peak at $\delta = 2.50$ ppm for ^1H, and $\delta = 39.52$ ppm for ^{13}C. Abbreviations for ^1H NMR spectra used are as follows: s, singlet; d, doublet; m, multiplet. ESI mass spectra were recorded on a Q-Tof Waters 2001 MS spectrometer.

Synthesis

***N*,*N*-Dibenzylbenzimidazolium tetrafluoroborate salt (1c)**: *N*,*N*-Dibenzylbenzimidazolium bromide (0.280 g, 0.738 mmol) was dissolved in acetonitrile (25 mL). A solution of $AgBF_4$ (0.158 g, 0.812 mmol) in acetonitrile (5 mL) was then added dropwise leading to the precipitation of AgBr. The suspension was stirred for 16 h in the absence of light and the precipitate was removed by filtration. The filtrate was evaporated to dryness, and the white residue was dissolved in dichloromethane. The solution was heated to reflux for several minutes, and then filtered to remove insoluble impurities. The filtrate was concentrated to reach a volume of ~2 mL, and *n*-pentane was added, leading to the immediate formation of a precipitate. After filtration and several washings with *n*-pentane, the benzimidazolium salt was isolated as a white solid (89%, 0.250 g). ^1H NMR (300 MHz, [D$_6$]DMSO, 25 °C): $\delta = 5.79$ ppm (s, 4H, CH_2), 7.58–7.32 (m, 10H, H_{Ar}), 7.63 (dd, $^3J_{H-H} = 6.2$, $^4J_{H-H} = 3.1$ Hz, 2H, H_{Ar}), 7.97 (dd, $^3J_{H-H} = 6.2$, $^4J_{H-H} = 3.1$ Hz, 2H, H_{Ar}), 10.02 (s, 1H, C(2)-H); $^{13}C\{^1H\}$ NMR (75.4 MHz, [D$_6$]DMSO, 25 °C): $\delta =$ 50.0 ppm (CH_2), 114.0 (C_{Ar}), 126.8 (C_{Ar}), 128.3 (C_{Ar}), 128.8 (C_{Ar}), 129.0 (C_{Ar}), 131.1 (C_{Ar}), 133.9 (C_{Ar}), 142.7 (C(2)); HRMS (ESI-TOF$^+$): calcd for $C_{21}H_{19}N_2^+$ $[M]^+$: *m*/*z*: 299.1548; found: 299.1549.

Crude AuNPs(C): To a toluene solution (12 mL) of di-*n*-dodecylsulfide-protected AuNPs, the *N*,*N*-dibenzylbenzimidazolium tetrafluoroborate salt **1c** (0.198 g, 0.512 mmol) was added, followed by NaO*t*Bu (0.086 g, 0.895 mmol). The mixture was stirred for 16 h in absence of light. Absolute EtOH (50 mL) was added and the mixture was refrigerated at 4 °C for 2 h. After that, a dark precipitate was separated by centrifugation (10,000 rpm for 5 min). After removing the supernatant, absolute EtOH (15 mL) was added and centrifugation was performed. This washing procedure was repeated twice. Finally, the insoluble crude AuNPs were collected with *n*-pentane (10 mL) and the solvent was slowly evaporated under atmospheric pressure at room temperature. After drying under vacuum, crude **AuNPs(C)** were obtained as a violet solid.

Separation of bis(*N*,*N*-dibenzylbenzimidazol-2-ylidene)Au^I tetrafluoroborate complex 3c from crude AuNPs(C): Acetonitrile (20 mL) was added to the insoluble crude **AuNPs(C)** and the mixture was sonicated for 2 min. After centrifugation (10,000 rpm, 5 min), the supernatant was separated from the solid residue of **AuNPs(C)**. This procedure was repeated three times. The organic phases were then filtered through Celite and evaporated together to dryness. *n*-Pentane (10 mL) was added to the solid residue and the mixture was filtered and dried under vacuum. The complex was obtained as a white solid in 38% yield (45 mg). ^1H NMR (300 MHz, [D$_6$]DMSO, 25 °C): $\delta = 5.75$ ppm (s, 8H, CH_2), 5.82 (s, 8H, CH_2), 7.37–7.19 (m, 20H, H_{Ar}), 7.40 (dd, $^3J_{H-H} = 6.1$, $^4J_{H-H} = 3.1$ Hz, 4H, H_{Ar}), 7.46 (dd, $^3J_{H-H} = 6.1$, $^4J_{H-H} = 3.0$ Hz, 4H, H_{Ar}), 7.75 (dd, $^3J_{H-H} = 6.2$, $^4J_{H-H} = 3.0$ Hz, 4H, H_{Ar}), 7.82 ppm (dd, $^3J_{H-H} = 6.0$, $^4J_{H-H} = 3.0$ Hz, 4H, H_{Ar}). The ^1H NMR spectrum is actually complex (see the Supporting Information), due to the existence of an equilibrium in solution. HRMS (ESI-TOF$^+$): calcd for $C_{42}H_{36}N_4Au^+$ $[M]^+$: *m*/*z*: 793.2605; found: 793.2609.

© 2016 Wiley-VCH Verlag GmbH & Co. KGaA, Weinheim

ChemPubSoc Europe

CHEMISTRY A European Journal Full Paper

TEM and SEM images

Samples for TEM measurements were prepared by deposition of a drop of crude **AuNPs(C)** suspension on a copper grid. TEM measurements were carried out at 100 kV by using a JEOL 1200 EXII microscope. SEM measurements were conducted on a Hitachi S4800 instrument. Powdered samples were simply deposited on double-sided tape, and then Pt-metallized by sputtering under vacuum.

Powder XRD analyses

Powder XRD analyses were carried out on a Philips X'pert Pro MPD diffractometer by using $Cu_{K\alpha 1}$ radiation ($\lambda = 1.5406$ Å) in Bragg–Brentano scanning mode with a 2θ angle range from 4–40° (or 4–53°), and a time per step of 50 or 300 s, depending on the sample.

Single crystal analyses

CCDC 1034216 (**1c**), 1034217 (**2c**), and 1034213 (**3c**) contain the supplementary crystallographic data for this paper. These data are provided free of charge by The Cambridge Crystallographic Data Centre.

UV/Vis and fluorescence spectroscopy

Experimental details are given in the Supporting Information.

Solid-state NMR

All solid-state NMR experiments were performed on a Varian VNMRS 600 MHz (14.1 T) NMR spectrometer, using a 1.6 mm Varian T3 HXY MAS probe. The operating frequency for ^{13}C was 150.83 MHz. Temperature regulation was used during the experiments to avoid any heating of the sample over 25 °C during the spinning. ^{1}H–^{13}C CPMAS NMR spectra were recorded spinning at 25 or 30 kHz, using a contact time of 2.5 ms, and 100 kHz spinal-64 ^{1}H decoupling during acquisition. The recycle delays and number of transients acquired were adapted for each sample, as shown in Table S5 (see the Supporting Information). ^{13}C chemical shifts were referenced externally to adamantane (used as a secondary reference), the high frequency peak being set to $\delta = 38.5$ ppm.

Computational details

Periodic DFT calculations: Calculations were performed in the frame of periodic DFT by means of the VASP.[29] The electron–ion interactions were described by the projector augmented wave (PAW)[43] method, representing the valence electrons, as provided in the code libraries. The convergence of the plane-wave expansion was obtained with a cut-off of 500 eV. The generalized gradient approximation (GGA) was used with the functional of Perdew–Burke–Ernzerhof (PBE).[44] The sampling in the Brillouin zone was performed on the gamma point.

Since our system involves organic molecules in interaction, we introduced dispersion forces, by using the Grimme D2 method[45] as implemented in VASP 5.2.11. DFT-D2 Grimme (G, D2) describes the van der Waals interactions between an atom and its neighbors in a given radius, via a simple pair-wise force field. This force field is optimized for several popular DFT functionals. In this case, this operator takes one atom as a reference one, and calculates the interactions of this atom with those around until a given distance or radius, and the same is done for all the atoms of the system. The calculated dispersion energy is then added to the pure DFT energy: $E = E_{DFT} + E_{D2}$.

The Au(111) surface was modeled as a slab containing 3 layers of gold. The slab was cut out of the bulk face centered cubic cell of Au. This slab size was chosen by careful evaluation of the quality/costs ratio, after satisfactory convergence tests of the system. In the periodic DFT calculations, the surface is infinite in two dimensions, with a vacuum space in the z axis direction. In our calculations, the vacuum layer was about 20 Å length along z, which was found to be large enough to enable the adsorption of **NHCa**, while preventing its interaction with the consecutive repetitions of the unit cell. The bulk-optimized cell parameter a after optimization of the slab at the PBE level was found to be equal to 4.164 Å, which is in good agreement with the experimental data (4.078 Å) for a face-centered cubic cell of gold.[46] For the slab, the unit-cell parameter was equal to $a = 2.94$ Å.

During geometry optimizations of grafted surfaces, the bottom layer in the Au slab was kept frozen on the bulk positions, whereas the two others were allowed to relax. The structure of the ligands and complexes adsorbed at the surface of the slab in the different models were allowed to fully relax during the geometry optimizations. The adsorption energy ΔE_{ads} of **NHCa** on the Au(111) surface was calculated as follows: $\Delta E_{ads} = E_{Au\text{-}NHCa} - E_{Au} - E_{NHCa}$, in which $E_{Au\text{-}NHC}$ is the energy of the complete system (after geometry optimization), E_{Au} is the energy of the gold slab (after geometry optimization, alone), and E_{NHCa} is the energy of the **NHCa** carbene (after geometry optimization, alone).

DFT calculations on the Au_{38} cluster: All computations on the Au_{38} cluster were carried out at the density functional level of theory as implemented in Gaussian 09 program.[31] The long-range corrected functional CAM-B3LYP[47] was used together with the LANL2MB relativistic corrected pseudopotentials and basis sets[48,49] for the gold atoms and the 6-31G(d) Gaussian basis set for the carbene ligand. Frequency calculations on the equilibrium geometries showed no imaginary frequencies for all the reported structures. Natural population analysis and natural bond orbital methods[50,51] were used to compute the partial charges on the atoms of the clusters. Evaluation of the solvent ([D_6]DMSO) effect on the structure of the single carbene **NHCa** ligated Au_{38} cluster was performed using the polarizable continuum model (PCM).[52,53] NMR spectra were computed using the CAM-B3LYP functional together with the LANL2MB relativistic corrected pseudopotentials and basis sets for the gold atoms and the 6-311+G(2d,p) Gaussian basis set for the carbene ligand.

Acknowledgements

This work was supported by the University of Montpellier and the CNRS. We are grateful to the Labex "CheMISysT" program (ANR-10-LABX-05-01) for financial support of Dr. M. R.-C. The HINT COST action MP1202 is acknowledged for support. The periodic DFT calculations were performed using HPC resources from GENCI (CCRT/CINES/IDRIS) (Grant 2013-(x2013082022)) and the CCRE of Université Pierre et Marie Curie. Dr. B. Diawara from ENS Paris is kindly acknowledged for providing us with ModelView used in the visualization of the structures. G.L. thanks IDS FUNMAT for a PhD fellowship. G.L. and F.R. gratefully acknowledge access to the computational resources of CECI (Consortium des Equipements de Calcul Intensif). F.R. thanks

 © 2016 Wiley-VCH Verlag GmbH & Co. KGaA, Weinheim

ChemPubSoc Europe

CHEMISTRY A European Journal Full Paper

Fonds National de la Recherche Scientifique (Belgium) for its support.

Keywords: carbenes · DFT · gold · nanoparticles · surface

[1] a) A. Balanta, C. Godard, C. Claver, *Chem. Soc. Rev.* **2011**, *40*, 4973; b) A. Schätz, O. Reiser, W. J. Stark, *Chem. Eur. J.* **2010**, *16*, 8950; c) N. Yan, C. Xiao, Y. Kou, *Coord. Chem. Rev.* **2010**, *254*, 1179; d) M. Stratakis, H. Garcia, *Chem. Rev.* **2012**, *112*, 4469; e) M. Pagliaro, V. Pandarus, R. Ciriminna, F. Béland, P. Demma Carà, *ChemCatChem* **2012**, *4*, 432; f) A. Boullanger, S. Clément, V. Mendez, S. Daniele, C. Thieuleux, A. Mehdi, *RSC Adv.* **2013**, *3*, 725.

[2] a) E. Boisselier, D. Astruc, *Chem. Soc. Rev.* **2009**, *38*, 1759; b) B. Duncan, C. Kim, V. M. Rotello, *J. Controlled Release* **2010**, *148*, 122; c) L. Vigderman, E. R. Zubarev, *Adv. Drug Delivery Rev.* **2013**, *65*, 663; d) A. A. Sousa, J. T. Morgan, P. H. Brown, A. Adams, P. Mudiyanselage, G. Zhang, C. J. Ackerson, M. J. Kruhlak, R. D. Leapman, *Small* **2012**, *8*, 2277; e) K. Huang, H. Ma, J. Liu, S. Huo, A. Kumar, T. Wei, X. Zhang, S. Jin, Y. Gan, P. C. Wang, S. He, X. Zhang, X.-J. Liang, *ACS Nano* **2012**, *6*, 4486; f) X. Wu, X. He, K. Wang, C. Xie, B. Zhou, Z. Qing, *Nanoscale* **2010**, *2*, 2244.

[3] a) R. Sardar, A. M. Funston, P. Mulvaney, R. W. Murray, *Langmuir* **2009**, *25*, 13840; b) P. Alexandridis, *Chem. Eng. Technol.* **2011**, *34*, 15; c) P. Zhao, N. Li, D. Astruc, *Coord. Chem. Rev.* **2013**, *257*, 638.

[4] a) W. A. Herrmann, C. Köcher, *Angew. Chem. Int. Ed. Engl.* **1997**, *36*, 2162; b) D. Bourissou, O. Guerret, F. P. Gabbaie, G. Bertrand, *Chem. Rev.* **2000**, *100*, 39; c) W. A. Herrmann, *Angew. Chem. Int. Ed.* **2002**, *41*, 1290; *Angew. Chem.* **2002**, *114*, 1342; d) F. Glorius, *Top. Organomet. Chem.* **2007**, *21*, 1; e) E. A. B. Kantchev, C. J. O'Brien, M. G. Organ, *Angew. Chem. Int. Ed.* **2007**, *46*, 2768; *Angew. Chem.* **2007**, *119*, 2824; f) S. Würtz, F. Glorius, *Acc. Chem. Res.* **2008**, *41*, 1523; g) F. E. Hahn, M. C. Jahnke, *Angew. Chem. Int. Ed.* **2008**, *47*, 3122; *Angew. Chem.* **2008**, *120*, 3166; h) B. Alcaide, P. Almendros, A. Luna, *Chem. Rev.* **2009**, *109*, 3817; i) S. Díez-González, N. Marion, S. P. Nolan, *Chem. Rev.* **2009**, *109*, 3612; j) G. C. Fortman, S. P. Nolan, *Chem. Soc. Rev.* **2011**, *40*, 5151.

[5] a) M. Yoshimura, R. Kamisue, S. Sakaguchi, *J. Organomet. Chem.* **2013**, *740*, 26; b) L. J. L. Häller, M. J. Page, S. Erhardt, A. Macgregor, M. F. Mahon, M. A. Naser, A. Velez, M. K. Whittlesey, *J. Am. Chem. Soc.* **2010**, *132*, 18408; c) A. R. Naziruddin, C.-S. Zhuang, W.-J. Lin, W.-S. Hwang, *Dalton Trans.* **2014**, *43*, 5335.

[6] a) J. Yang, P. Li, Y. Zhang, L. Wang, *Dalton Trans.* **2014**, *43*, 7166; b) T. A. P. Paulose, S.-C. Wu, J. W. Quail, S. R. Foley, *Inorg. Chem. Commun.* **2012**, *15*, 37; c) B. Karimi, P. F. Akhavan, *Inorg. Chem.* **2011**, *50*, 6063.

[7] a) S. Gaillard, P. Nun, A. M. Z. Slawin, S. P. Nolan, *Organometallics* **2010**, *29*, 5402; b) R. Visbal, A. Laguna, M. C. Gimeno, *Chem. Commun.* **2013**, *49*, 5642.

[8] a) D. Enders, O. Niemeier, A. Henseler, *Chem. Rev.* **2007**, *107*, 5606; b) N. Marion, S. Díez-González, S. P. Nolan, *Angew. Chem. Int. Ed.* **2007**, *46*, 2988; *Angew. Chem.* **2007**, *119*, 3046; c) N. E. Kamber, W. Jeong, R. M. Waymouth, R. C. Pratt, B. G. G. Lohmeijer, J. L. Hedrick, *Chem. Rev.* **2007**, *107*, 5813; d) V. Nair, S. Vellalath, B. P. Babu, *Chem. Soc. Rev.* **2008**, *37*, 2691; e) A. J. Arduengo III, L. I. Iconaru, *Dalton Trans.* **2009**, 6903; f) V. Nair, R. S. Menon, A. T. Biju, C. R. Sinu, R. R. Paul, A. Jose, S. Vellalath, *Chem. Soc. Rev.* **2011**, *40*, 5336; g) A. T. Biju, N. Kuhl, F. Glorius, *Acc. Chem. Res.* **2011**, *44*, 1182; h) M. Fèvre, J. Pinaud, Y. Gnanou, J. Vignolle, D. Taton, *Chem. Soc. Rev.* **2013**, *42*, 2142; i) J.-F. Lefebvre, M. Lo, J.-P. Gisselbrecht, O. Coulembier, S. Clément, S. Richeter, *Chem. Eur. J.* **2013**, *19*, 15652.

[9] a) K. V. S. Ranganath, J. Kloesges, A. H. Schäfer, F. Glorius, *Angew. Chem. Int. Ed.* **2010**, *49*, 7786; *Angew. Chem.* **2010**, *122*, 7952; b) C. Richter, K. Schaepe, F. Glorius, B. J. Ravoo, *Chem. Commun.* **2014**, *50*, 3204; c) A. Ferry, K. Schaepe, P. Tegeder, C. Richter, K. M. Chepiga, B. J. Ravoo, F. Glorius, *ACS Catal.* **2015**, *5*, 5414; d) A. Rühling, K. Schaepe, L. Rakers, B. Vonhören, P. Tegeder, B. J. Ravoo, F. Glorius, *Angew. Chem. Int. Ed.* **2016**, *55*, 5856; *Angew. Chem.* **2016**, *128*, 5950..

[10] X. Ling, N. Schaeffer, S. Roland, M.-P. Pileni, *Langmuir* **2013**, *29*, 12647.

[11] a) P. Lara, O. Rivada-Wheelaghan, S. Conejero, R. Poteau, K. Philippot, B. Chaudret, *Angew. Chem. Int. Ed.* **2011**, *50*, 12080; *Angew. Chem.* **2011**, *50*, 12286; b) D. Gonzalez-Galvez, P. Lara, O. Rivada-Wheelaghan, S. Conejero, B. Chaudret, K. Philippot, P. W. N. M. van Leeuwen, *Catal. Sci. Technol.* **2013**, *3*, 99.

[12] a) P. Lara, A. Suarez, V. Collire, K. Philippot, B. Chaudret, *ChemCatChem* **2014**, *6*, 87; b) E. A. Baquero, S. Tricard, J. C. Flores, E. de Jesus, B. Chaudret, *Angew. Chem. Int. Ed.* **2014**, *53*, 13220; *Angew. Chem.* **2014**, *126*, 13436.

[13] a) M. Brust, M. Walker, D. Bethell, D. Schiffrin, R. Whyman, *J. Chem. Soc. Chem. Commun.* **1994**, 801; b) A. C. Templeton, W. P. Wuelfing, R. W. Murray, *Acc. Chem. Res.* **2000**, *33*, 27; c) R. Shenhar, V. M. Rotello, *Acc. Chem. Res.* **2003**, *36*, 549.

[14] a) A. G. Kanaras, F. S. Kamounah, K. Schaumburg, C. J. Kiely, M. Brust, *Chem. Commun.* **2002**, 2294; b) T. Peterle, P. Ringler, M. Mayor, *Adv. Funct. Mater.* **2009**, *19*, 3497; c) T. Peterle, A. Leifert, J. Timper, A. Sologubenko, U. Simon, M. Mayor, *Chem. Commun.* **2008**, 3438.

[15] a) R. Sharma, G. P. Holland, V. C. Solomon, H. Zimmermann, S. Schiffenhaus, S. A. Amin, D. A. Buttry, J. L. Yarger, *J. Phys. Chem. C* **2009**, *113*, 16387; b) H. Zhang, G. Schmid, U. Hartmann, *Nano Lett.* **2003**, *3*, 305; c) L. F. Chi, M. Hartig, T. Drechsler, T. Schwaack, C. Seidel, H. Fuchs, G. Schmid, *Appl. Phys. A* **1998**, *66*, 5187.

[16] a) Y. G. Kim, S.-K. Oh, R. M. Crooks, *Chem. Mater.* **2004**, *16*, 167; b) Y. Chen, Y.-M. Zhang, Y. Liu, *Chem. Commun.* **2010**, *46*, 5622.

[17] J. Turkevich, P. C. Stevenson, J. Hillier, *Discuss. Faraday Soc.* **1951**, *11*, 55.

[18] J. Vignolle, T. D. Tilley, *Chem. Commun.* **2009**, 7230.

[19] X. Ling, S. Roland, M. P. Pileni, *Chem. Mater.* **2015**, *27*, 414.

[20] J. Crespo, Y. Guari, A. Ibarra, J. Larionova, T. Lasanta, D. Laurencin, J. M. Lopez-de-Luzuriaga, M. Monge, M. E. Olmos, S. Richeter, *Dalton Trans.* **2014**, *43*, 15713.

[21] E. C. Hurst, K. Wilson, I. J. S. Fairlamb, V. Chechik, *New J. Chem.* **2009**, *33*, 1837.

[22] C. M. Crudden, J. H. Horton, I. I. Ebralidze, O. V. Zenkina, A. B. McLean, B. Drevniok, Z. She, H.-B. Kraatz, N. J. Mosey, T. Seki, E. C. Keske, J. D. Leake, A. Rousina-Webb, G. Wu, *Nat. Chem.* **2014**, *6*, 409.

[23] M. Rodríguez-Castillo, D. Laurencin, F. Tielens, A. Van der Lee, S. Clément, Y. Guari, S. Richeter, *Dalton Trans.* **2014**, *43*, 5978.

[24] a) S. G. Song, C. Satheeshkumar, J. Park, J. Ahn, T. Prekumar, Y. Lee, C. Song, *Macromolecules* **2014**, *47*, 6566; b) M. J. MacLeod, J. Johnson, *J. Am. Chem. Soc.* **2015**, *137*, 7974.

[25] a) T. Doneux, F. Tielens, P. Geerlings, C. Buess-Herman, *J. Phys. Chem. A* **2006**, *110*, 11346; b) A. V. Zhukhovitskiy, M. G. Mavros, T. V. Voorhis, J. A. Johnson, *J. Am. Chem. Soc.* **2013**, *135*, 7418.

[26] I. Favier, S. Massou, E. Teuma, K. Philippot, B. Chaudret, M. Gómez, *Chem. Commun.* **2008**, 3296.

[27] X.-M. Li, M. R. de Jong, K. Inoue, S. Shinkai, J. Huskens, D. N. Reinhoudt, *J. Mater. Chem.* **2001**, *11*, 1919.

[28] S. Guo, H. Sivaram, D. Yuan, H. V. Huynh, *Organometallics* **2013**, *32*, 3685.

[29] A. S. Barnard, X. M. Lin, L. A. Curtiss, *J. Phys. Chem. B* **2005**, *109*, 24465.

[30] H. Qian, W. T. Eckenhoff, Y. Zhu, T. Pintauer, R. Jin, *J. Am. Chem. Soc.* **2010**, *132*, 8280.

[31] Gaussian 09, Revision D.01, M. J. Frisch, G. W. Trucks, H. B. Schlegel, G. E. Scuseria, M. A. Robb, J. R. Cheeseman, G. Scalmani, V. Barone, B. Mennucci, G. A. Petersson, H. Nakatsuji, M. Caricato, X. Li, H. P. Hratchian, A. F. Izmaylov, J. Bloino, G. Zheng, J. L. Sonnenberg, M. Hada, M. Ehara, K. Toyota, R. Fukuda, J. Hasegawa, M. Ishida, T. Nakajima, Y. Honda, O. Kitao, H. Nakai, T. Vreven, J. A. Montgomery, Jr., J. E. Peralta, F. Ogliaro, M. Bearpark, J. J. Heyd, E. Brothers, K. N. Kudin, V. N. Staroverov, R. Kobayashi, J. Normand, K. Raghavachari, A. Rendell, J. C. Burant, S. S. Iyengar, J. Tomasi, M. Cossi, N. Rega, J. M. Millam, M. Klene, J. E. Knox, J. B. Cross, V. Bakken, C. Adamo, J. Jaramillo, R. Gomperts, R. E. Stratmann, O. Yazyev, A. J. Austin, R. Cammi, C. Pomelli, J. W. Ochterski, R. L. Martin, K. Morokuma, V. G. Zakrzewski, G. A. Voth, P. Salvador, J. J. Dannenberg, S. Dapprich, A. D. Daniels, Ö. Farkas, J. B. Foresman, J. V. Ortiz, J. Cioslowski, and D. J. Fox, Gaussian, Inc., Wallingford CT, **2009**.

[32] D. Mollenhauer, N. Gaston, E. Voloshina, B. Paulus, *J. Phys. Chem. C* **2013**, *117*, 4470.

[33] H. M. J. Wang, C. Y. L. Chen, I. J. B. Lin, *Organometallics* **1999**, *18*, 1216.

[34] E. Bedford, V. Humblot, C. Méthivier, F. Gu, C.-M. Pradier, F. Tielens, S. Boujday, *Chem. Eur. J.* **2015**, *21*, 14555.

[35] a) T. V. W. Janssens, B. S. Clausen, B. Hvolbaek, H. Falsig, C. H. Christensen, T. Bligaard, J. K. Norskov, *Top. Catal.* **2007**, *44*, 15; b) A. Corma, M. Boronat, S. González, F. Illas, *Chem. Commun.* **2007**, 3371; c) L. M.

 © 2016 Wiley-VCH Verlag GmbH & Co. KGaA, Weinheim

ChemPubSoc Europe

CHEMISTRY
A European Journal
Full Paper

Molina, B. Hammer, *Appl. Catal. A* **2005**, *291*, 21; d) J. L. C. Fajín, M. N. D. S. Cordeiro, J. R. B. Gomes, *Catalyst* **2011**, *1*, 40; e) N. B. Luque, E. Santos, J. Andres, F. Tielens, *Langmuir* **2011**, *27*, 14514.

[36] a) A. Fernando, K. L. D. M. Weerawardene, N. V. Karimova, C. M. Aikens, *Chem. Rev.* **2015**, *115*, 6112; b) B. Zhu, I. C. Oğuz, H. Guesmi, *J. Chem. Phys.* **2015**, *143*, 144309.

[37] a) F. Tielens, J. Andrés, *J. Phys. Chem. C* **2007**, *111*, 10342; b) B. Fresch, F. Remacle, *J. Phys. Chem. C* **2014**, *118*, 9790; c) G. Lugo, V. Schwanen, B. Fresch, F. Remacle, *J. Phys. Chem. C* **2015**, *119*, 10969.

[38] a) G. Kresse, J. Hafner, *Phys. Rev. B* **1993**, *48*, 13115; b) G. Kresse, J. Hafner, *J. Phys. Condens. Matter* **1994**, *6*, 8245.

[39] a) U. C. Singh, P. A. Kollman, *J. Comput. Chem.* **1984**, *5*, 129; b) B. H. Besler, K. M. Merz, P. A. Kollman, *J. Comput. Chem.* **1990**, *11*, 431.

[40] C. M. Breneman, K. B. Wiberg, *J. Comput. Chem.* **1990**, *11*, 361.

[42] a) C. Vericat, M. E. Vela, G. Benitez, P. Carro, R. C. Salvarezza, *Chem. Soc. Rev.* **2010**, *39*, 1805; b) C. Schoenenberger, J. A. M. Sondag-Huethorst, J. Jorritsma, L. G. J. Fokkink, *Langmuir* **1994**, *10*, 611.

[43] a) C. Bonhomme, C. Gervais, D. Laurencin, *Prog. Nucl. Magn. Reson. Spectrosc.* **2014**, *77*, 1; b) L. E. Marbella, J. E. Millstone, *Chem. Mater.* **2015**, *27*, 2721; c) L. M. Martínez-Prieto, A. Ferry, P. Lara, C. Richter, K. Philippot, F. Glorius, B. Chaudret, *Chem. Eur. J.* **2015**, *21*, 17495; d) J. Cure, Y. Coppel, T. Dammak, P. F. Fazzini, A. Mlayah, B. Chaudret, P. Fau, *Langmuir* **2015**, *31*, 1362.

[44] a) P. E. Blöchl, *Phys. Rev. B* **1994**, *50*, 17953; b) G. Kresse, D. Joubert, *Phys. Rev. B* **1999**, *59*, 1758.

[45] a) J. P. Perdew, K. Burke, M. Ernzerhof, *Phys. Rev. Lett.* **1996**, *77*, 3865; b) J. P. Perdew, K. Burke, M. Ernzerhof, *Phys. Rev. Lett.* **1997**, *78*, 1396.

[46] S. Grimme, *J. Comput. Chem.* **2006**, *27*, 1787.

[47] A. Maeland, T. B. Flanagan, *Can. J. Phys.* **1964**, *42*, 2364.

[48] T. Yanai, D. P. Tew, N. C. Handy, *Chem. Phys. Lett.* **2004**, *393*, 51.

[49] P. J. Hay, W. R. Wadt, *J. Chem. Phys.* **1985**, *82*, 299.

[50] P. J. Hay, W. R. Wadt, *J. Chem. Phys.* **1985**, *82*, 270.

[51] A. E. Reed, L. A. Curtiss, F. Weinhold, *Chem. Rev.* **1988**, *88*, 899.

[52] J. P. Foster, F. Weinhold, *J. Am. Chem. Soc.* **1980**, *102*, 7211.

[55] J. Tomasi, B. Mennucci, R. Cammi, *Chem. Rev.* **2005**, *105*, 2999.

[56] E. Cancès, B. Mennucci, J. Tomasi, *J. Chem. Phys.* **1997**, *107*, 3032.

Received: March 16, 2016
Published online on June 27, 2016

© 2016 Wiley-VCH Verlag GmbH & Co. KGaA, Weinheim

6.2 References

1. Marion, N., et al., *AuI-catalyzed cycloisomerization of 1,5-enynes bearing a propargylic acetate: formation of unexpected bicyclo[3.1.0]hexene.* Chemical Communications, 2006(19): p. 2048-2050.
2. Ferry, A., et al., *Negatively Charged N-Heterocyclic Carbene-Stabilized Pd and Au Nanoparticles and Efficient Catalysis in Water.* ACS Catalysis, 2015. **5**(9): p. 5414-5420.
3. Song, S.G., et al., *N-Heterocyclic Carbene-Based Conducting Polymer–Gold Nanoparticle Hybrids and Their Catalytic Application.* Macromolecules, 2014. **47**(19): p. 6566-6571.
4. Visbal, R., et al., *N-Heterocyclic Carbene Ligands as Modulators of Luminescence in Three-Coordinate Gold(I) Complexes with Spectacular Quantum Yields.* Journal of the American Chemical Society, 2013. **135**(12): p. 4712-4715.
5. Li, K., et al., *Light-emitting platinum(ii) complexes supported by tetradentate dianionic bis(N-heterocyclic carbene) ligands: towards robust blue electrophosphors.* Chemical Science, 2013. **4**(6): p. 2630-2644.
6. MacLeod, M.J. and J.A. Johnson, *PEGylated N-Heterocyclic Carbene Anchors Designed To Stabilize Gold Nanoparticles in Biologically Relevant Media.* Journal of the American Chemical Society, 2015. **137**(25): p. 7974-7977.
7. Mercs, L. and M. Albrecht, *Beyond catalysis: N-heterocyclic carbene complexes as components for medicinal, luminescent, and functional materials applications.* Chemical Society Reviews, 2010. **39**(6): p. 1903-1912.
8. Vignolle, J. and T.D. Tilley, *N-Heterocyclic carbene-stabilized gold nanoparticles and their assembly into 3D superlattices.* Chemical Communications, 2009(46): p. 7230-7232.
9. Crespo, J., et al., *Ultrasmall NHC-coated gold nanoparticles obtained through solvent free thermolysis of organometallic Au(i) complexes.* Dalton Transactions, 2014. **43**(42): p. 15713-15718.
10. Rodriguez-Castillo, M., et al., *Reactivity of gold nanoparticles towards N-heterocyclic carbenes.* Dalton Transactions, 2014. **43**(16): p. 5978-5982.
11. Ling, X., et al., *Nanocrystals: Why Do Silver and Gold N-Heterocyclic Carbene Precursors Behave Differently?* Langmuir, 2013. **29**(41): p. 12647-12656.
12. Serpell, C.J., et al., *Haloaurate and halopalladate imidazolium salts: structures, properties, and use as precursors for catalytic metal nanoparticles.* Dalton Transactions, 2013. **42**(5): p. 1385-1393.
13. Rodríguez-Castillo, M., et al., *Experimental and Theoretical Study of the Reactivity of Gold Nanoparticles Towards Benzimidazole-2-ylidene Ligands.* Chemistry – A European Journal, 2016: p. n/a-n/a.
14. Crudden, C.M., et al., *Ultra stable self-assembled monolayers of N-heterocyclic carbenes on gold.* Nat Chem, 2014. **6**(5): p. 409-414.
15. Hurst, E.C., et al., *N-Heterocyclic carbene coated metal nanoparticles.* New Journal of Chemistry, 2009. **33**(9): p. 1837-1840.
16. Cancès, E., B. Mennucci, and J. Tomasi, *A new integral equation formalism for the polarizable continuum model: Theoretical background and applications to isotropic and anisotropic dielectrics.* The Journal of Chemical Physics, 1997. **107**(8): p. 3032-3041.
17. Mennucci, B., *Polarizable continuum model.* Wiley Interdisciplinary Reviews: Computational Molecular Science, 2012. **2**(3): p. 386-404.

Chapter VII. Dynamics of phosphine and 1, 3 – dimethyl – 1H – benzimidazolium ligand on gold nanocluster surface

7.1 Introduction

Gold nanoclusters (GNC) have received a lot of attention in recent years due to the wide range of applications they offer. [1-11] Compared to their nanoparticles counterpart, GNCs have a well – defined stoichiometry of the metallic core and the ligand shell which makes the understanding of the relation between their structure and properties easier. Most of the metallic cores that appear in stoichiometric GNCs are not stable without capping by the ligand shell and ligand protection is required in order to preserve their structure and hence their properties. On the other hand, it is well known that the ligand layer modifies the structure of the bare cluster [12, 13] which leads to a modification of their chemical, surface and optical properties. [8, 14-16] Tuning the ligand capping can therefore be used as an advantage to control the properties of GNC's.

Several ligands have been used over the years to passivate GNCs and nanoparticles, for instance; amines,[17] thioethers,[18] thiolates [19-23] and phosphines [14, 24-29] leading to a large range of clusters with different properties and nuclearities. The use of N – Heterocyclic carbenes as capping ligands recently received a lot of attention, since they – as phosphine ligands – are σ donor [30] but show a stronger metal – ligand bond, even stronger than thiolates. [31, 32] Moreover, it is possible to modify the organic group bearing the N atoms and also the heterocyclic backbone leading to the possibility of tuning the size, reactivity and steric and electronic properties of GNCs and gold nanocrystals. [33-35] However, the structural determination and ligand organization analysis of such materials turns out to be very complicated because of their small size and also, in the carbene case, because of the formation of [NHC – Au – NHC]$^+$ and NHC – Au – Cl complexes [31, 33, 34] which makes the study of the grafting of NHCs on gold nanocluster surfaces very challenging (here NHC refers to 1, 3 – dimethyl – 1H – benzimidazolium ligand). Therefore computational chemistry can be used to provide insight and understand how the structure and optical properties are affected by the ligand layer.

In this chapter, we analyze three different protected gold clusters. Their structural, electronic and optical properties are studied using DFT at the CAM – B3LYP level. The Au_{13}, the tetrahedral Au_{20} and the Au_{38} cores have been used as models since these clusters can be synthesized [25, 36-39] and the crystallographic data for the first and the last one are available. [26, 40-42] Even though no crystallographic structure for the tetrahedral Au_{20} is available, its structure has been well – characterized by high angle annular dark field (HAADF) scanning transmission electron microscopy (STEM) as reported by Palmer *et al.* [43]

We start the chapter by comparing the structural and optical properties of four different icosahedral ligand protected Au_{13} clusters. Among them, two were already studied in chapter III and reference [11]: the

icosahedral Au_{13} protected by the C_2 – bridged diphosphine ligand ($Ph_2P{-}(CH_2)_2{-}PPh_2$ known as dppe) that yields the cluster $[Au_{13}dppe_5Cl_2]^{3+}$ (already synthesized [26]), and the one protected by the $P(Ph_2)CH_3$ ligand which leads to the $[Au_{13}(P(Ph_2)CH_3)_8Cl_4]^+$ cluster. Two others Au_{13} clusters are proposed in this work and their properties investigated. They result from substituting the phosphines by the benzimidazole – 2 – ylidene ($C_7N_2H_4$ – $(CH_3)_2$), ligand as shown in figure 1e) in the phosphine protected Au_{13} clusters.

We also chose to investigate the properties of the tetrahedral Au_{20} cluster. Previous studies showed that Au_{20} clusters exhibit promising structural features and properties and high stability. [36, 43-45] The tetrahedral Au_{20} presents an atomic packing very similar to gold in bulk but since it belongs to the ultrasmall cluster class it shows different properties.[45, 46] Because all its atoms are actually on the surface, the T_d Au_{20} cluster shows high surface area and low coordinated atoms at the corners, which could be used for catalytic applications. It has been shown computationally that Au_{20} shows highly sensitive properties on composition, that is to say, only one atom dopant, for instance $Au_{19}Ag$, it is enough to modify its electronic structure and hence its properties which opens the possibility of tuning them [2, 47]. For instance, E.S. Kryachko and F. Remacle confirmed computationally that the void Au_{20} clusters are good candidates to host a metal atom in the hollow cavity. [48] Also, DFT studies suggest that Au_{20} could be used as catalyst, for instance, for CO oxidation [2, 3] or pollutants treatment.[47] This cluster has been synthesized [36] and well characterized experimentally; [43, 49] – showing its tetrahedral characteristic shape – and also theoretically. [2, 44, 45, 48, 50-53].

On the other hand, the understanding of how ligands organize on the nanocluster surface is also a key ingredient for the tuning of their properties. Therefore the synthesized and well-characterized Au_{38} is also investigated in this work. This cluster shows a larger surface area and it is not as symmetric as the other two. It is an ideal candidate to perform a phosphine size reactivity study on its surface and to have an insight on the prediction of at which site a ligand is going to preferentially interact. We chose to use a model for the phosphine ligand (PPh_3; triphenylphosphine), which is commonly used in gold cluster synthesis [54-56] for our studies of site reactivity. We replaced the phenyl groups by hydrogens in the triphenylphosphine in order to save computational cost as done in previous computational studies [12, 27, 28, 57-62]. Our results on the site reactivity of PH_3 are compared to those we get with the carbene NHC ligand which are discussed in chapter VI and in reference [34].

7.2 Structure and natural charge distribution

The equilibrium geometries of the bare Au_{13}^{5+}, $[Au_{13}NHC_{10}Cl_2]^{3+}$ and the $[Au_{13}NHC_8Cl_4]^+$ clusters are shown in figure 1, the $Au_{20}(PH_3)_8$ and the NHC protected analogue in figure 2. The equilibrium geometry of the $Au_{38}(PH_3)_9$ cluster is plotted in figure 3 and the one of the $Au_{38}(NHC)_9$ cluster is given in figure 7d in the publication in chapter VI (reference [34] in this chapter).

By comparing the four Au_{13} structures (the $[Au_{13}dppe_5Cl_2]^{3+}$ and $[Au_{13}(P(Ph_2)CH_3)_8Cl_4]^+$ from ref [11] and the two NHC protected analogues shown in figure 1), we find that substitution of phosphine ligands by

NHC leads to a slight expansion of the Au_{13} core. Distances from the Au central atom to those forming the icosahedron range from 2.78 to 2.87 Å for the $[Au_{13}dppe_5Cl_2]^{3+}$, from 2.81 to 2.89 Å for $[Au_{13}(P(Ph_2)CH_3)_8Cl_4]^+$, from 2.88 to 2.93 Å for $[Au_{13}NHC_{10}Cl_2]^{3+}$ and from 2.90 to 2.95 Å for the $[Au_{13}NHC_8Cl_4]^+$ cluster. We find that the NHC pulls the gold atom out of the cluster as found in our previous computational work on the Au_{38} – NHC complex. [34]

We found that the metal core in $[Au_{13}NHC_{10}Cl_2]^{3+}$ belongs to S_{10} whereas the $[Au_{13}NHC_8Cl_4]^+$ preserves I_h symmetry within 0.3 Å of tolerance in the atomic positions. No significant deformation (other than the dilatation) is caused by the NHC ligands compared to their phosphine (dppe and $P(Ph_2)CH_3$) protected analogues. It is possible to see that, chloride atoms (in green in figure 1) are placed as far away as possible from the metal core. This arises by the steric rigidity of the NHC ligand layer which is similar to that of the dppe and $P(Ph_2)CH_3$ ligands in protected 13 – gold clusters studied in reference [11].

For both the geometries of the ligand coated Au_{20} clusters shown in figure 2, the metal core keeps its tetrahedral shape after PH_3 substitution by NHC, Au – Au distances range from 2.66 to 8.59 Å and from 2.65 to 9 Å for the $Au_{20}(PH_3)_8$ and $Au_{20}NHC_8$, respectively. This confirms the high stability of the tetrahedral Au_{20} bare cluster. [2, 36, 45] However, by comparing the six equivalent edges between the NHC and the PH_3 capped Au_{20} in figure 2c, we find that the difference in length ranges from 0.01 to 0.68 Å. In the most distorted cases, two of the edges contract from 8.48 Å to 7.99 Å and from 8.37 to 7.69 Å and one expands from 8.15 to 8.48 Å when PH_3 is substituted by NHC.

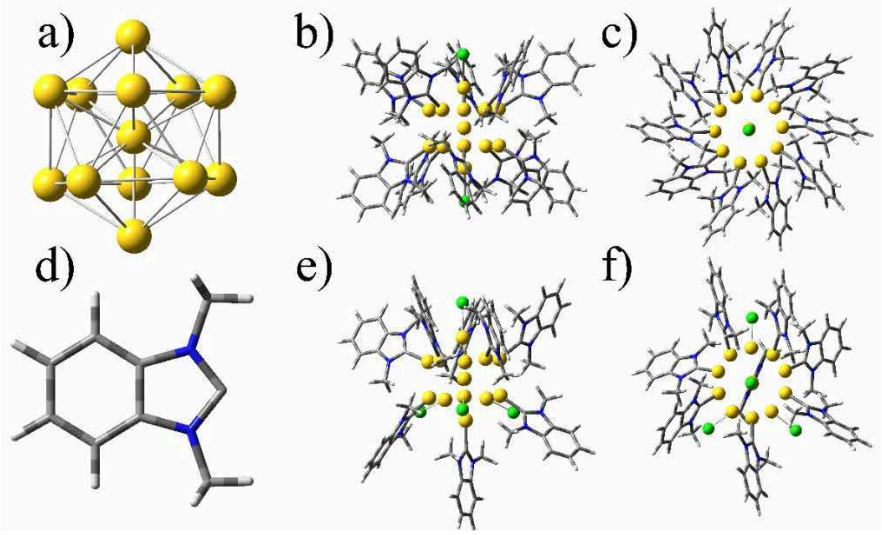

***Figure* 1**. *Equilibrium geometry of the bare Au_{13}^{5+} cluster (panel a)), of $[Au_{13}NHC_{10}Cl_2]^{3+}$ (panel b))and an upper view in panel c). Panel d) shows the carbene ligand used in this study. Panel e) the $[Au_{13}NHC_8Cl_4]^+$ cluster and its upper view in panel f). Equilibrium geometries were calculated in the gas phase using DFT at the CAM-B3LYP level. The LANL2MB pseudopotential and basis set were used for Au atoms and the 6*

– 31G(d) basis set for the atoms of the ligand layer. Yellow atoms stand for Au, green spheres Cl, blue junctions represent N, gray C and H is shown in white.

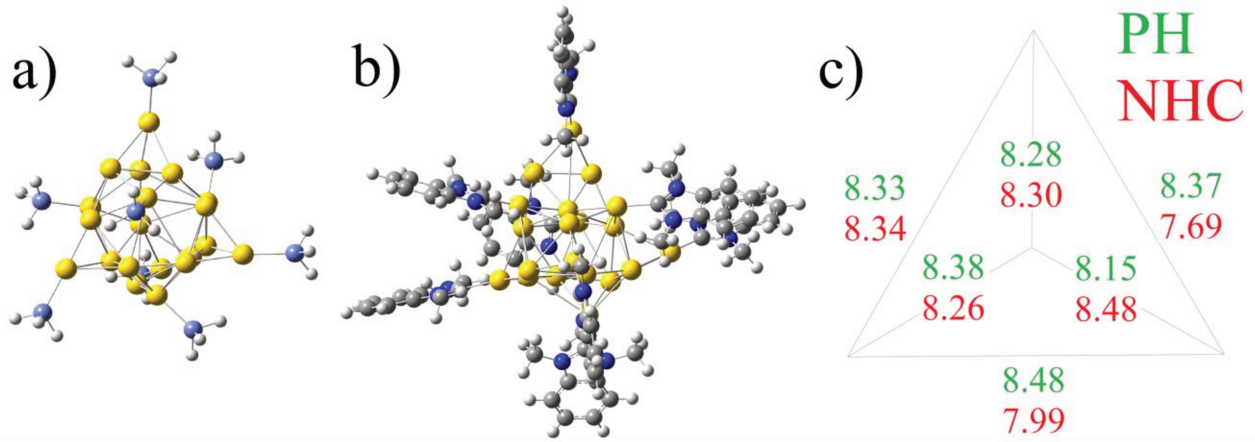

Figure 2. *Equilibrium geometry of (a) the $Au_{20}(PH_3)_8$, b) the $Au_{20}NHC_8$ clusters and c) schematic comparison of the Au_{20} edges lengths in Å. Calculations have been performed in the gas phase using DFT at the CAM-B3LYP level. The LANL2MB pseudopotential and basis set were used for Au atoms and the 6 – 31G(d) basis set for the atoms of the ligand layer. Yellow atoms stand for Au, blue represents N, gray C and H atoms are shown in white.*

The analysis of the Au_{38} core structure shows the same pattern as found for the Au_{13} and the Au_{20} cores. Au – Au distances in the $Au_{38}NHC_9$ range from 2.67 to 12.27 Å [34] which indicates a dilatation of the metal core – compared to PH_3 (2.72 – 11.98 Å) and compared to the bare Au_{38} (2.79 to 11.96 Å).

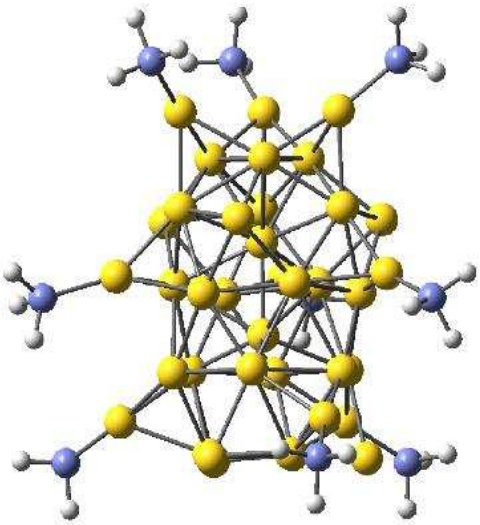

***Figure 3**. Equilibrium geometry of the phosphine – coated Au_{38} cluster studied. Au atoms are in yellow, S is represented by blue junctions, C in grey, P in purple, N in blue spheres and H in white. Calculations have been performed in the gas phase at the DFT CAM – B3LYP LANL2MB / 6 – 31G (d) level. The $Au_{38}NHC_9$ can be seen in reference [34].*

Table 1 shows a comparison of the different parameters evaluated in the gold core structure. It can be seen that in all clusters, the Au – C bond length (for Au – NHC) is shorter than the Au – P in the phosphine capped clusters. This suggests that the carbene – Au bond is stronger.

***Table* 1.** *Cluster stoichiometry, the length of the Au – L bond of phosphine and carbene passivated clusters and total partial charge on the ligand shell (phosphine or NHC; labeled NBO ligand shell) and on the metal core (NBO Au_n, n = 13, 20 or 38). Calculations have been performed in the gas phase at the DFT CAM – B3LYP LANL2MB / 6 – 31G (d) level of theory. The number in brackets is the natural charge per ligand.*

Cluster Stoichiometry	Au – L (Å)	NBO ligand shell (|e|)	NBO Au_n (|e|)
$[Au_{13}(dppe_5)_{10}Cl_2]^{3+}$	2.37	4.39	-0.34
$[Au_{13}NHC_{10}Cl_2]^{3+}$	2.08	3.98 (0.39)	0.10
$[Au_{13}(P(PH_2)CH_3)_8Cl_4]^{+}$	2.35 – 2.38	3.40 (0.43)	-0.10
$[Au_{13}NHC_8Cl_4]^{+}$	2.07 – 2.08	2.98 (0.37)	0.28
$Au_{20}(PH_3)_8$	2.37 – 2.46	1.71 (0.21)	-1.71
$Au_{20}NHC_8$	2.06 – 2.12	2.30 (0.29)	-2.30
$Au_{38}(PH_3)_9$	2.41 – 2.43	1.74 (0.19)	-1.74
$Au_{38}NHC_9$	2.10 – 2.11	2.57 (0.29)	-2.57

In table 1 we report the total partial charge on the ligand layer (labeled as *NBO ligand shell*) and on the metal core. The positive partial charge on the ligand shell, in all the gold clusters studied, shows that both ligands have an electron – donor character, which was expected. However, table 1 shows that for the $[Au_{13}NHC_{10}Cl_2]^{3+}$ and the $[Au_{13}NHC_8Cl_4]^{+}$ a positive metal core is found. This could be explained by the fact that, in this case, NHC shows a weaker electron – donor character compared to the dppe and the $P(Ph_2)CH_3$ ligand.

The opposite effect takes place for the two neutral clusters cases. Compared to PH_3, NHC shows a stronger electron – donor character in the Au_{38} and Au_{20} clusters (see table 1). In both clusters, partial charges of 0.29 |e|/NHC and approximately 0.20 |e|/PH_3 are found for the Au_{38} and Au_{20} clusters, respectively. However, we have to recall that the presence of the phenyl group and, more important, the charge state (+3 and +1 in the Au_{13}) have a significant impact on the charge redistribution between the ligand shell and the metal core, its structure and also on its optical profile. [11] For these reasons and the presence of the chloride, the properties of the positively charged Au_{13} are different from the neutral Au_{20} and Au_{38} ones.

7.3 Optical properties

We report in this section the effect of substitution of phosphines by NHC's on the lowest electronic transition of the three model clusters, with Au_{13}, Au_{20} and Au_{38} cores.

The electronic structure of the two NHC capped Au_{13} clusters maintain significant similarities to the superatomic molecular orbitals (SAMO) as in the icosahedral Au_{13}^{5+} (see figure 4 and 6). [28] Thus, the two clusters; $[Au_{13}NHC_{10}Cl_2]^{3+}$ and the $[Au_{13}NHC_8Cl_4]^{+}$ can be described as superatomic units with a 8 – electron S^2P^6 closed electronic shell. However, the modification of the Au_{13} structure due to the substitution of dppe by NHC leads to a splitting of the five virtual *d* – SAMO's (shown in figure 4) and hence the UV – Vis spectrum is also modified. We recall that after phosphine exchange by NHC, the Au_{13} core undergoes a dilatation and it is known that the superatomic *d* orbitals splitting is very sensitive on the Au – Au distance. [63]

The DOS of the two NHC capped clusters shows that the three quasi – degenerate highest occupied molecular orbitals (HOMO, HOMO − 1, and HOMO – 2, see figure 4 and 6) and the virtual orbitals are mainly composed of *s* and *p* atomic orbitals highly localized on the gold core (larger than 70 % in both clusters) while the *d* band lies lower in energy.

The computed UV – Vis spectrum of the $[Au_{13}NHC_{10}Cl_2]^{3+}$ cluster is shown in figure 5 (together with that of the $[Au_{13}dppe_5Cl_2]^{3+}$). Reference [11] shows that for the $[Au_{13}dppe_5Cl_2]^{3+}$ cluster the bands at wavelengths >350 nm originate from transitions from threefold – quasi degenerate HOMO (HOMO, HOMO – 1 and HOMO – 2) to the five LUMO to LUMO + 5 SAMOs. The first band in the UV – Vis spectrum of the $[Au_{13}dppe_5Cl_2]^{3+}$ cluster found around 460 nm (see figure 5) involves transitions from the HOMO and HOMO – 1 to the 2 – fold quasi degenerate LUMO while the second band centered at 370 nm involves the HOMO – 2 to (again) the LUMO. Three bands can be detected in the $[Au_{13}NHC_{10}Cl_2]^{3+}$ spectrum in the visible region. The three of them, as in the dppe protected cluster, originate from excitations involving transition from the quasidegenerate *p* – SAMO (HOMO to HOMO – 2) to the *d* – SAMO set (LUMO, LUMO + 1 and LUMO + 2, see figure 4). The lowest optical band, found from 448.49 to 459.23 nm, with a small oscillator strength is due to excitations involving transitions from the HOMO to the LUMO. The second one is centered at 411 nm and corresponds mainly to a 2 – fold quasi degenerate HOMO – 1 to LUMO + 1 set of orbitals. The third band is found around 358 nm and originates from excitation involving mainly HOMO to LUMO + 2 transitions.

In both cases, the $[Au_{13}dppe_5Cl_2]^{3+}$ and of the $[Au_{13}NHC_{10}Cl_2]^{3+}$ clusters, the bands originate from excitations of molecular orbitals of the same nature: from the 3 – fold quasi degenerate HOMO to HOMO – 2 to the LUMO to LUMO + 5 set.

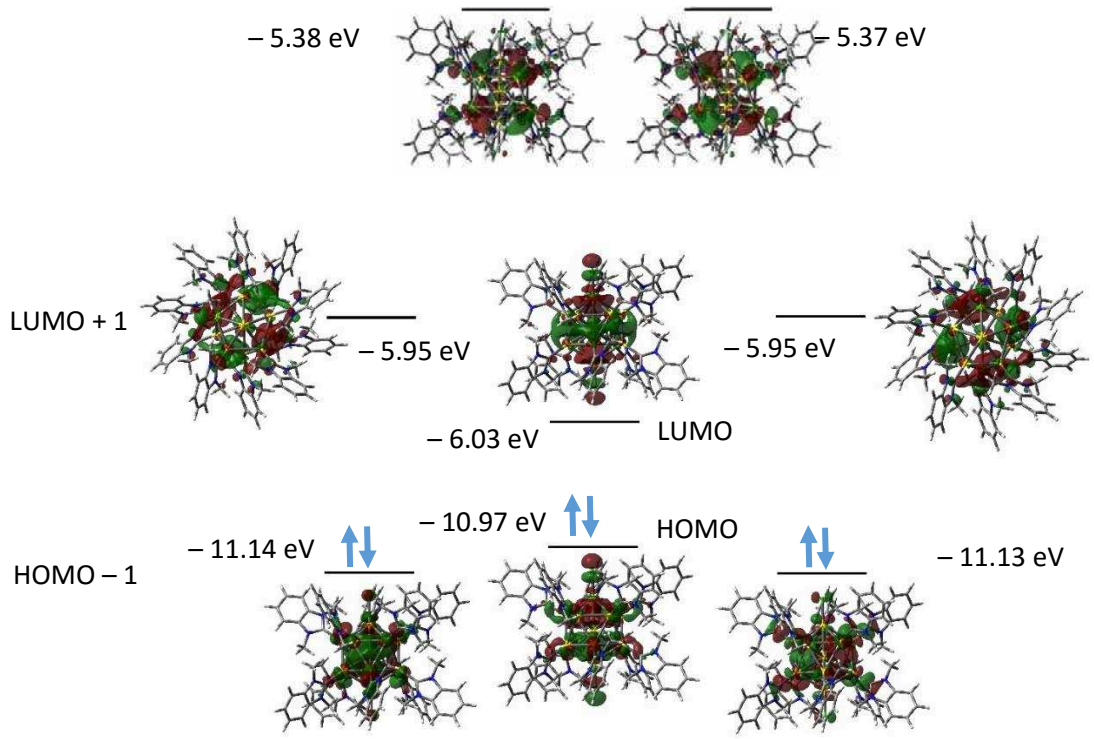

Figure 4. *MO diagram of the $[Au_{13}NHC_{10}Cl_2]^{3+}$ cluster. Isocontours of the frontier molecular orbitals are shown as well as the orbital energy in eV. The degeneracy threshold is 0.13 eV and the isovalue is 0.02 $Å^{-3}$. The CAM – B3LYP functional was used together with the LANL2MB pseudopotential and basis set for Au and the 6 – 31G(d) basis set for the ligand layer.*

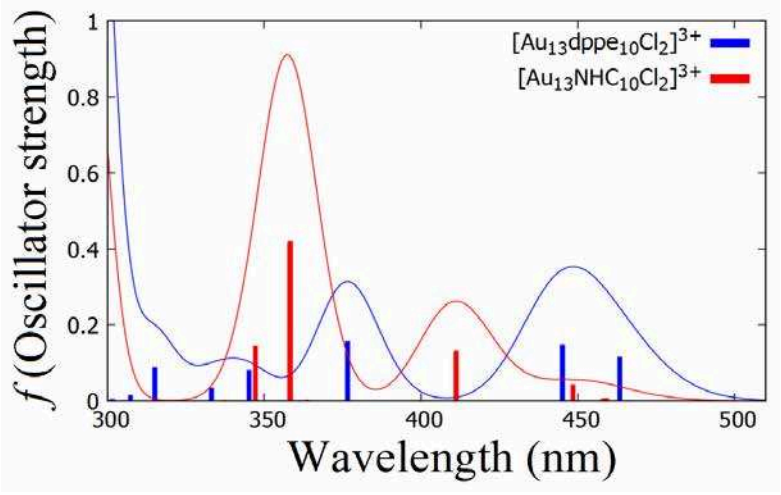

Figure 5. *Computed UV − Vis absorption spectra of the $[Au_{13}dppe_5Cl_2]^{3+}$ (taken from ref. [11]) and $[Au_{13}NHC_{10}Cl_2]^{3+}$ clusters. The spectra are computed at the TD – DFT level at the equilibrium geometry of the ground state. The CAM – B3LYP functional was used together with the LANL2MB pseudopotential and basis set for Au and the 6 – 31G(d) basis set for the ligand layer.*

On the other hand, it is possible to see in figure 6 ($[Au_{13}NHC_8Cl_4]^+$) that after modification of the NHC/Cl ratio the 3 – fold quasi degenerate HOMO (HOMO, HOMO – 1 and HOMO – 2) and the 5 molecular orbital set LUMO, LUMO + 1, LUMO + 2 and LUMO + 3 maintain a resemblance with the superatomic orbital of the bare Au_{13}^{+5}. [28]

Figure 7 shows the UV – Vis spectrum of the $[Au_{13}NHC_8Cl_4]^+$ cluster together with the $P(Ph_2)CH_3$ analogue. The two optical profiles look much closer to each other. 3 bands can be detected in figure 7 in both spectra in the Vis region. Again, these bands (in both clusters) originate from excitations involving transitions from the 3 – fold quasi degenerate HOMO to the *d* – SAMO set (composed of LUMO, LUMO + 1 and the LUMO + 2, see figure 6). The lowest energy band in the UV – Vis of the $[Au_{13}NHC_8Cl_4]^+$ cluster ranges from 465.40 to 491.30 nm and can be attributed mostly to HOMO – LUMO transitions. Contribution to HOMO and LUMO superatomic orbitals comes mostly from the Au_{13} core (larger than 70 %). The second band (with very small oscillator strength) ranges from 390.57 to 421.54 nm and is composed from excitations involving mainly HOMO – 1 to LUMO + 1 excitations. Finally, the third one ranges from 353.18 to 375.38 nm and it arises principally from excitations involving HOMO and HOMO – 1 to LUMO + 2 transitions.

By comparing both UV – Vis spectra of the NHC protected clusters, it is possible to see that even though the two Au_{13} have very similar equilibrium geometries, their UV – Vis spectra are quite different (compare figure 5 and 7, red curves). Hence, our study confirms that the UV – Vis spectra is dependent on the NHC/Cl ratio as observed by Konishi *et al.* in ref [25] for phosphine ligand protected Au_{13} clusters suggesting that the ligand – to – metal charge transfer is an important parameter in the electronic transitions in these clusters.

As mentioned in reference [11] in chapter III, the core in the $[Au_{13}dppe_5Cl_2]^{3+}$ preserves I_h symmetry while in $[Au_{13}(P(Ph_2)CH_3)_8Cl_4]^{3+}$ cluster belongs to S_{10} within 0.3 Å of tolerance in the atomic positions whereas for the NHC coated analogues; the $[Au_{13}NHC_{10}Cl_2]^{3+}$ belongs to C_5 and $[Au_{13}NHC_8Cl_4]^+$ to C_1 (within the same tolerance threshold). It is clear that the NHC ligand induces a more significant distortion on the metal core than phosphines. As a consequence, we obtain completely different degeneracy schemes of the molecular orbitals of the NHC protected Au_{13} compared to those of the phosphine analogues. This is reflected on the computed H – L gaps values and optical absorption profiles. The opening of the HOMO – LUMO (H – L) gap going from $[Au_{13}NHC_8Cl_4]^+$ to $[Au_{13}NHC_{10}Cl_2]^{3+}$ is the opposite to what it is found for the phosphine ligated analogues where this broadening of the H – L gap is correlated with an increase on the positive partial charge in the Au_{13} core. We report a H – L gap of 4.95 eV and 4.73 eV for $[Au_{13}NHC_{10}Cl_2]^{3+}$ (with a partial charge of 0.10 |e| on the Au_{13}) and $[Au_{13}NHC_8Cl_4]^+$ (with a partial charge of 0.28 |e| on the Au_{13}), respectively.

By comparing both NHC coated cationic Au_{13} clusters in figure 8, we realize that they do not follow the trend "*the more negative the metal core, the more the UV – Vis spectrum is red shifted*" found for the

set of clusters $[Au_{25}(SR)_{18}]^q$ (with q = – 1, +1 and R being CH_3 or the phenyl group) reported in chapter III. [11] This can be attributed to the higher distortion to the Au_{13} by the NHC leading to a completely different MO landscape. We recall that for the NHC, the opening of the gap is correlated to a decrease of positive charge on the metal core. Therefore, the NHC capped cationic Au_{13} clusters are not expected to follow the trend discussed in chapter III, reference [11]. The lowest energy transition in the $[Au_{13}NHC_{10}Cl_2]^{3+}$ spectrum is shifted by 0.18 eV to higher energies compared to $[Au_{13}NHC_8Cl_4]^+$. Thus, the H – L gap opening correlates well with the blue shift in the UV – Vis spectra when going from $[Au_{13}NHC_8Cl_4]^+$ to $[Au_{13}NHC_{10}Cl_2]^{3+}$.

In both NHC coated cationic Au_{13} clusters, the third band is centered at ~360 nm. This band, as mentioned above originates from excitations involving transitions from the 3 – fold quasi degenerate *p* – SAMO to the LUMO + 2 orbital. It is possible to see in figure 4 and 6 that the separation between those orbitals is very small in both cases (~5.59 eV and ~5.65 eV for $[Au_{13}NHC_{10}Cl_2]^{3+}$ and $[Au_{13}NHC_8Cl_4]^+$, respectively).

Next, we show in figure 9 the UV – Vis spectra for the two capped Au_{20}. The analysis of Au_{20} metal core structures for both type of ligands showed that due to the high stability of the Au_{20} core, both clusters have very similar equilibrium geometries. It is well known that the optical properties are highly dependent on the nuclearity and the geometry of the metal core and the partial charge on it. [11, 63, 64]

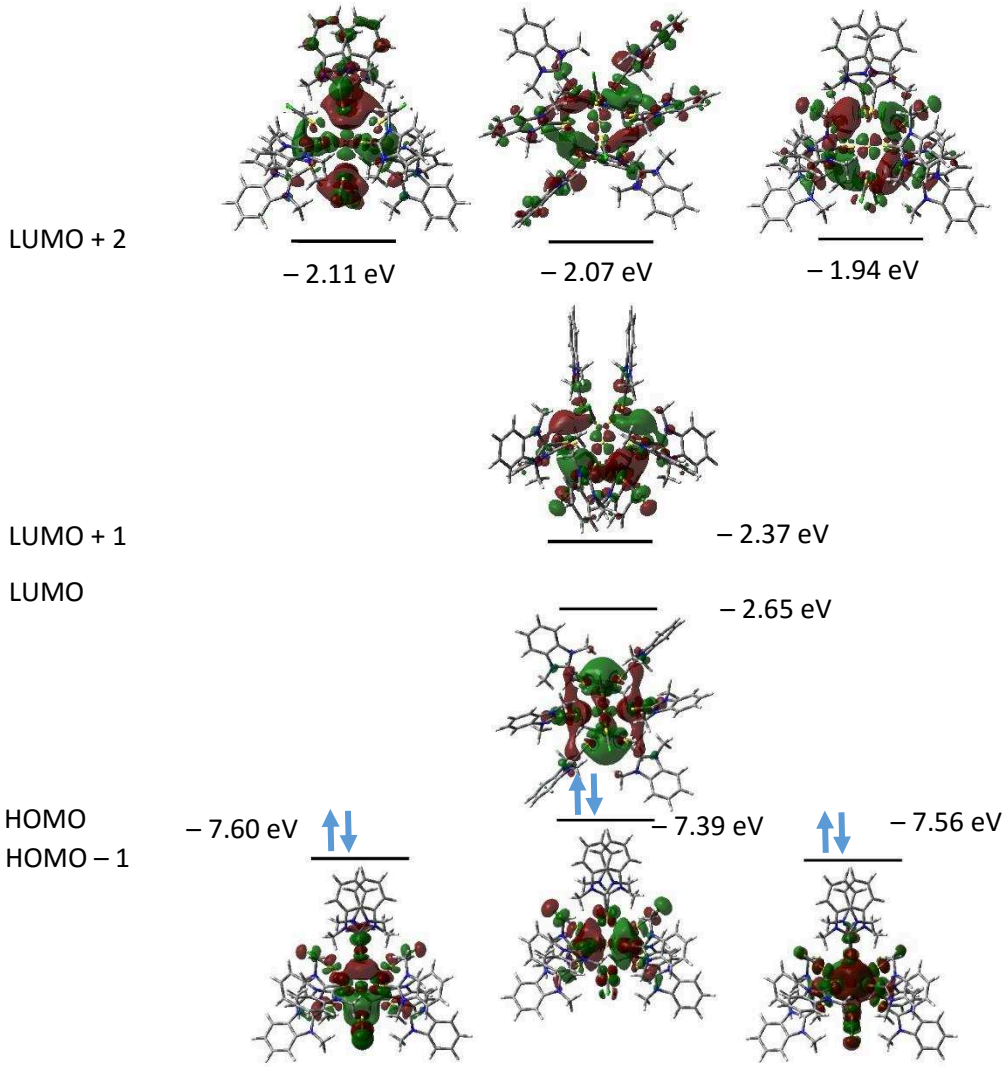

Figure 6. *MO diagram of the $[Au_{13}NHC_8Cl_4]^+$ cluster. Isocontours of the frontier molecular orbitals are shown as well as the orbital energy in eV. The degeneracy threshold is 0.13 eV and the isovalue 0.02 $Å^{-3}$. The CAM – B3LYP functional was used together with the LANL2MB pseudopotential and basis set for Au and the 6 – 31G(d) basis set for the ligand layer.*

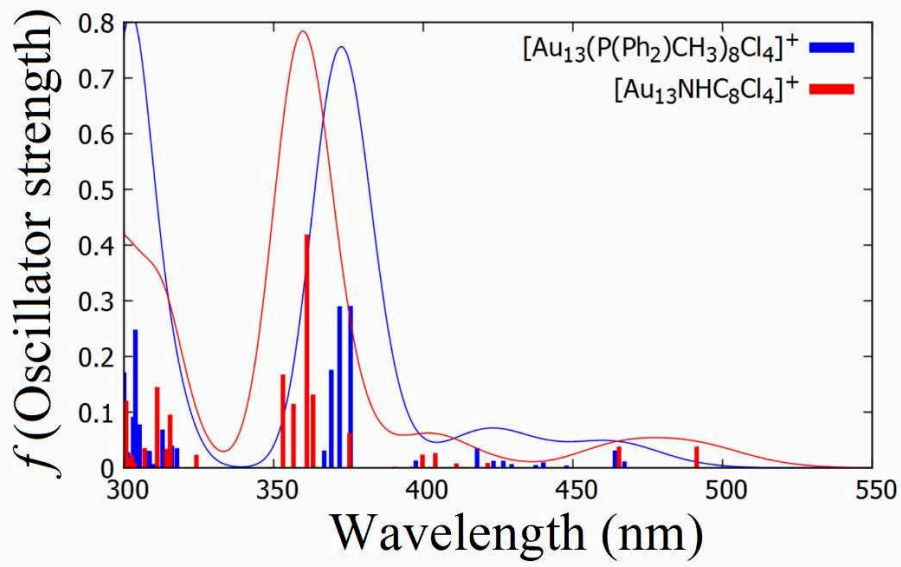

Figure 7. *Computed UV − Vis absorption spectra of the $[Au_{13}(P(Ph_2)CH_3)_8Cl_4]^{3+}$ (taken from ref. [11]) and $[Au_{13}NHC_{10}Cl_2]^{3+}$ clusters. The electronic excited states are computed at the TD-DFT level. The CAM – B3LYP functional was used together with the LANL2MB pseudopotential and basis set for Au and the 6 – 31G(d) basis set for the ligand layer.*

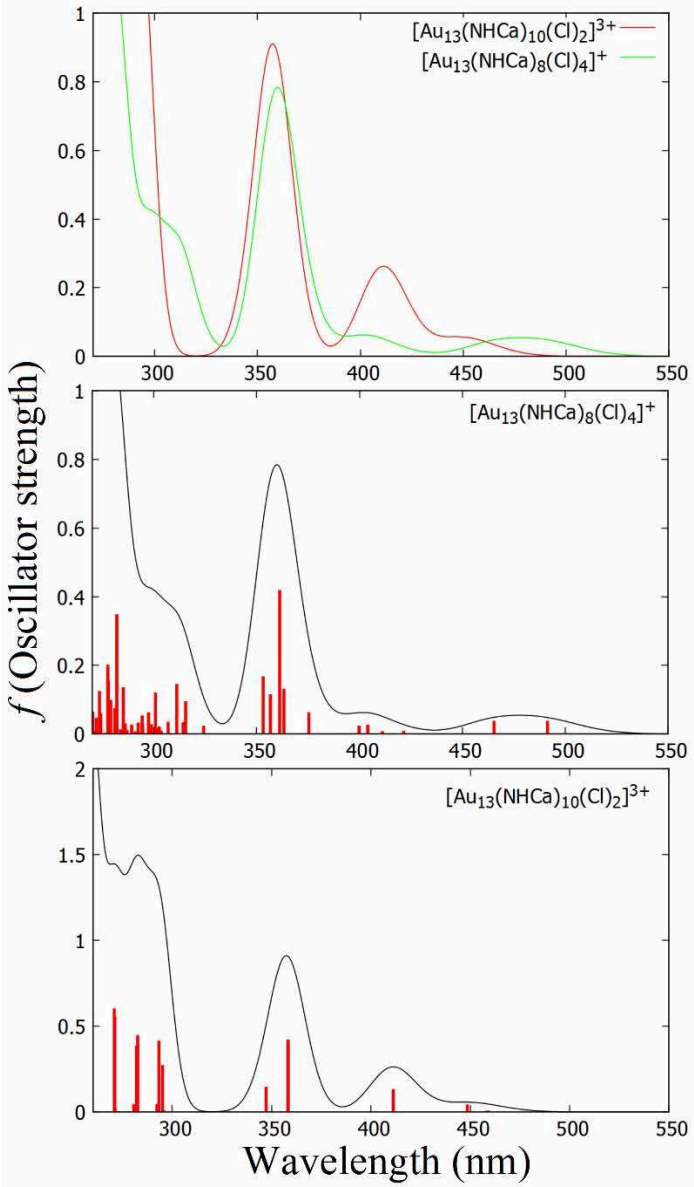

Figure 8. *Computed UV − Vis absorption spectra of the $[Au_{13}NHC_8Cl_4]^{3+}$ (and $[Au_{13}NHC_{10}Cl_2]^{3+}$ clusters. The electronic excited states are computed at the TD-DFT level. The CAM – B3LYP functional was used together with the LANL2MB pseudopotential and basis set for Au and the 6 – 31G(d) basis set for the ligand layer.*

In the two Au_{20} clusters, the lowest transition is mainly due to an HOMO − LUMO excitation with sp → sp character. The lowest excitation energies are found at 1.96 and 1.62 eV for the $Au_{20}(PH_3)_8$ and the $Au_{20}NHC_8$ cluster, respectively. The latter has the more negatively charged metal core (– 2.30 |e|, see table 1). Interestingly, we show in Figure 9 that the UV – Vis spectrum is qualitatively and globally shifted to the

red as the metallic core is becoming more negatively charged. Therefore, this system follows the trend "*the more negative the metal core, the more the UV – Vis spectrum is red shifted*". [11]

The last example discussed here is the Au_{38} cluster. Structures compared in the previous sections lead to the conclusion that NHC produces a dilatation of the metallic core by pulling the Au atoms. Exchange of PH_3 with NHC results in a different equilibrium geometry for the Au_{38} core. Table 1 reports the global natural charge on the metal core; – 2.57 |e| and -1.74 |e| was found for the $Au_{38}NHC_9$ [34] and $Au_{38}(PH_3)_9$ clusters, respectively and their UV – Vis spectra are shown in figure 10 for comparison. The electronic transitions present very small oscillator strengths. In both cases, the lowest transition is mainly composed by HOMO – LUMO excitations with sp → sp character. Again, it is possible to see that, even though both Au_{38} cores do not have the same structure, the UV – Vis spectra of the $Au_{38}NHC_9$ is overall red shifted as the charge on the metal core becomes more negative compared to the one of the $Au_{38}(PH_3)_9$.

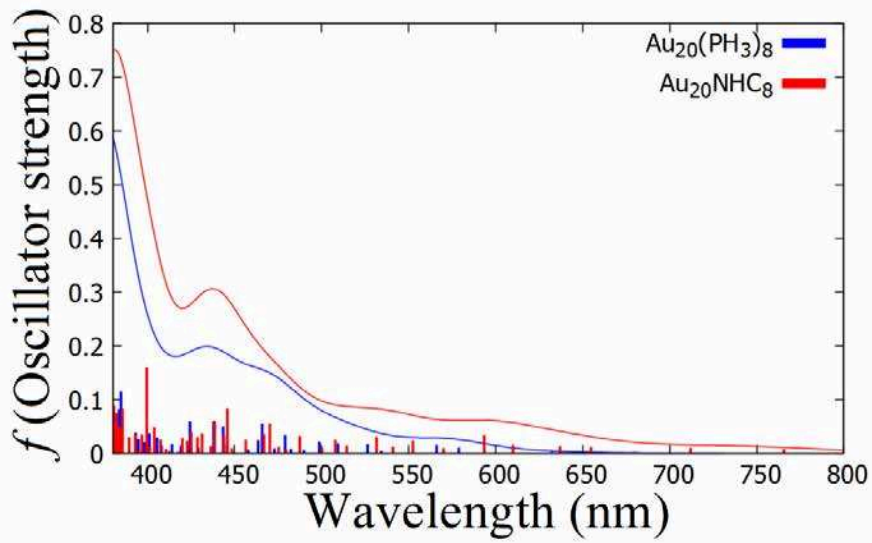

***Figure 9**. Computed UV − Vis absorption spectra of the $Au_{20}NHC_8$ and $Au_{20}(PH_3)_8$ clusters. The excited electronic states are computed at the TD – DFT level. The CAM – B3LYP functional was used together with the LANL2MB pseudopotential and basis set for Au and the 6 – 31G(d) basis set for the ligand layer.*

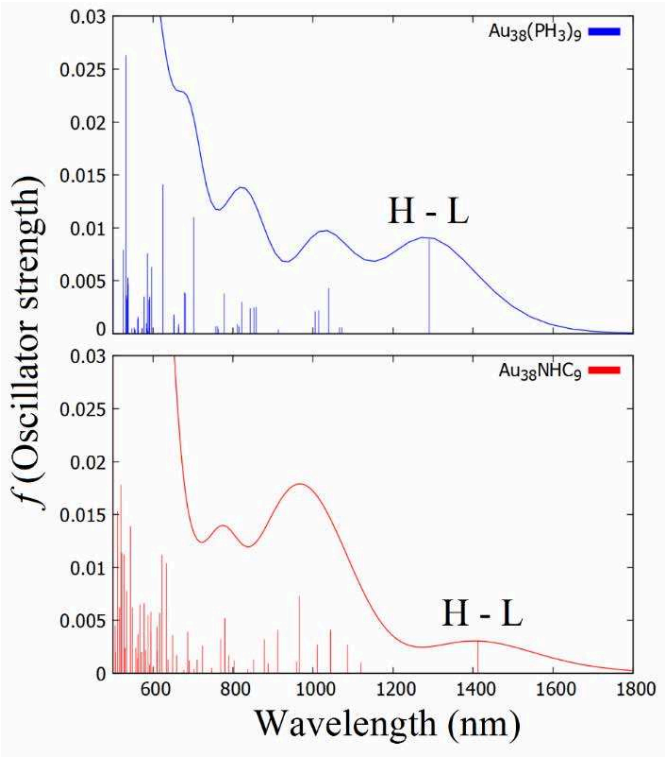

***Figure 10**. Comparison of the computed optical spectra between the phosphine and the NHC protected Au_{38} clusters. The excited electronic states are computed at the TD – DFT level. The CAM – B3LYP functional was used together with the LANL2MB pseudopotential and basis set for Au and the 6 – 31G(d) basis set for the ligand layer.*

7.4 Site reactivity of the PH_3 on the Au_{38} cluster surface. Comparison with NHC

Previous computational studies have shown that the organization of the ligands on the metal surface of the nanocluster is an important parameter that governs the electron localization in the metal core.[11, 12, 65] In view of the trends discussed in the previous sections, the organization of the ligand shell can be used at advantage to tune the optical properties of such systems. [11] Therefore, it is highly important to understand the mode of grafting of ligands on the gold nanocluster. In reference [34] we performed a study of the absorption of a single NHC on different type of atoms on the Au_{38} surface. We took the $Au_{38}(SCH_2CH_2Ph)_{24}$ as a starting geometry for our calculations. [40] By optimizing the bare Au_{38} core we find that the 38 gold atoms are arranged as follows: 2 central atoms surrounded by 21 gold atoms forming a ellipsoidal backbone and finally, the 15 gold atoms remaining are located on some of the triangular faces of the Au_{21} ellipsoid (for further details consult [34] in chapter VI). The distribution of the computed partial charges in the Au_{38} equilibrium geometry follows the C_3 symmetry so that one can group the partial charges on gold atoms on the surface according to the C_3 symmetry operation. 12 different groups of charged gold atoms have been

found. One atom out of each of these 12 different partial charged groups was taken to interact with a single NHC ligand.

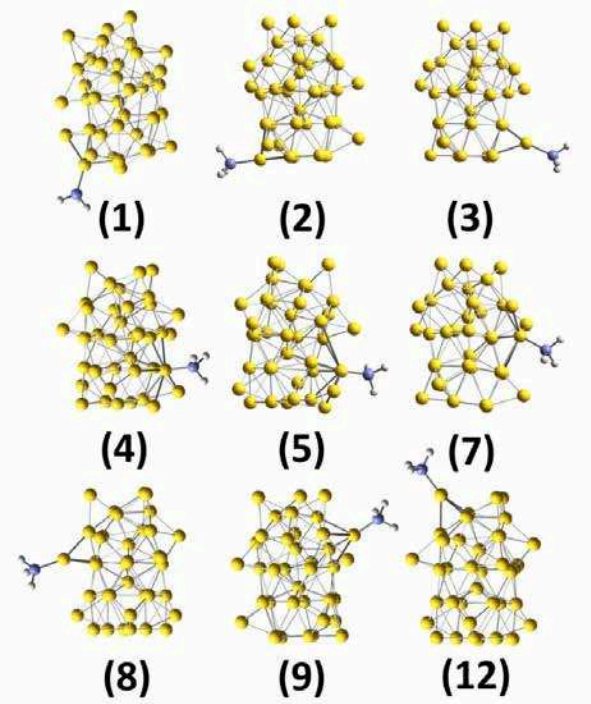

Figure 11. *Equilibrium geometries of the different Au_{38} – PH_3 complex configurations studied. Au atoms are in yellow, P in purple and H in white. Calculations have been performed in the gas phase at the DFT CAM – B3LYP LANL2MB / 6 – 31G (d) level. Unfortunately, no equilibrium structure was found for configurations 6, 10 and 11.*

Here, we performed the same analysis as in reference [34] but using the PH_3 as a model for PPh_3 to save computational cost. The equilibrium geometries at the DFT level in the gas phase are shown in figure 11 while the parameters describing the binding are given by table 2.

It can be seen in table 6 that the PH_3 ligand weakly interacts with the metallic surface and figure 11 shows that it tends to take an “on top” position when physisorbed. [12] The computed binding energies ranges from 0.00 to – 0.47 eV. Table 6 shows that, in all the configurations, after absorption of the PH_3, charge redistribution between the Au_{38} and the ligand leads to a negatively charged gold core. [12, 13] Notice that the partial charge on the metal core is not the same for all cases, it varies depending on the ligand absorption site, however no special relation has been found between the charge on the metallic core in the complex and any other parameter as coordination number (C.N) or the binding energy (B.E.), for instance. The partial charge on the Au_{38} ranges from – 0.20 |e| to – 0.35 |e|.

Table 2. *Complex label, relative free energy (ΔG), binding energy (B.E.), HOMO – LUMO (H – L) gap, the natural charge of the Au atom bound to the phosphine ligand in the bare cluster (NBO Au – PH_3), the natural charge of the metallic core in the complex (NBO Au_{38}), P – Au bond length (P – Au length) and coordination number (C.N). Results for configurations 6, 10 and 11 are not shown since unfortunately we did not find any equilibrium geometry in these cases. Calculations have been performed in the gas phase at the DFT CAM – B3LYP LANL2MB / 6 – 31G (d) level of theory.*

Complex Label	Relative ΔG (eV)	Binding Energy (eV)	H – L Gap (eV)	NBO Au – PH_3 |e|	NBO Au_{38}	P – Au Length (Å)	C.N.
8	0.00	-0.47	2.85	0.29	-0.29	2.39	3
2	0.00	-0.46	2.67	0.22	-0.32	2.38	4
12	0.04	-0.42	2.80	0.23	-0.24	2.40	3
3	0.14	-0.33	2.85	0.20	-0.26	2.40	3
9	0.15	-0.32	2.44	-0.28	-0.28	2.39	4
1	0.24	-0.23	3.04	-0.17	-0.29	2.38	7
5	0.41	-0.06	2.78	-0.12	-0.20	2.41	8
7	0.45	-0.02	2.85	-0.11	-0.29	2.40	9
4	0.47	0.00	2.68	-0.11	-0.35	2.44	8
6	-	-	-	-0.22	-	-	8
10	-	-	-	-0.14	-	-	8
11	-	-	-	-0.15	-	-	8

*B.E. represents the binding energy of the Au_{38} – NHC system. It is calculated as: where the *n* is the number of ligands (in this case *n* = 1).

* C.N. is the coordination number of the gold atom in its bare configuration that interacts with the ligand.

Table 2 also shows that the Au – P bond length ranges from 2.44 Å to 2.48 Å, which is in a good agreement with previous calculations.[12] It can be seen that the binding strength increases as the partial charge of the gold atoms in the bare cluster becomes more positive and the coordination number decreases, which makes sense regarding the electron donor character of the PH_3 ligand. HOMO – LUMO (H – L) gap ranges from 2.44 to 3.04 eV. Again, no special relation has been found between the H – L gap and any other parameter.

The structural analysis of the different PH_3 – Au_{38} complexes show that the binding of a single phosphine does not induce a strong distortion. This can be seen in Figure 12 where we show the histogram of Au – Au distances between the 38 gold atoms (that is to say, all possible distances between all pairs of

atoms in the metal core). Note that, by comparing Figure 12 “Bare” (on top) with the other figures, the binding of a single phosphine does not induce a strong distortion of the metal core since the histograms are very similar. We can observe 3 different distance groups. The first group in figure 12 represents the distances between the atoms directly connected. The second one is a collection of all the distances between neighbor atoms which are not directly bound and finally, the third one stands for those atoms that are relatively far. In all cases, except for the case 3, 9 and 12, the count of “distances” in the first group ranges between 35 and 40. Results for the 6, 10 and 11 configuration are not shown since unfortunately we did not find any equilibrium geometry in these cases.

Additionally, figure 13 shows the histogram of radial distances for the bare (on top) and the 9 (out of 12) different configurations studied. We have plotted two spheres with “r” and “r + 1 Å” of radius (where r goes from 0 Å to 7 Å), taking as the origin the point between the two central atoms and counting the gold atoms in between the spheres (see the two central atoms in figure 13). As can be seen in figure 13, most of the histogram of radial distances follow the same profile; around 1.4 Å we have the two central atoms and a maximum in the Au atom population is found around 3.5 Å. For 1, 4 and 5 cases the phosphine succeeded to slightly deform the core.

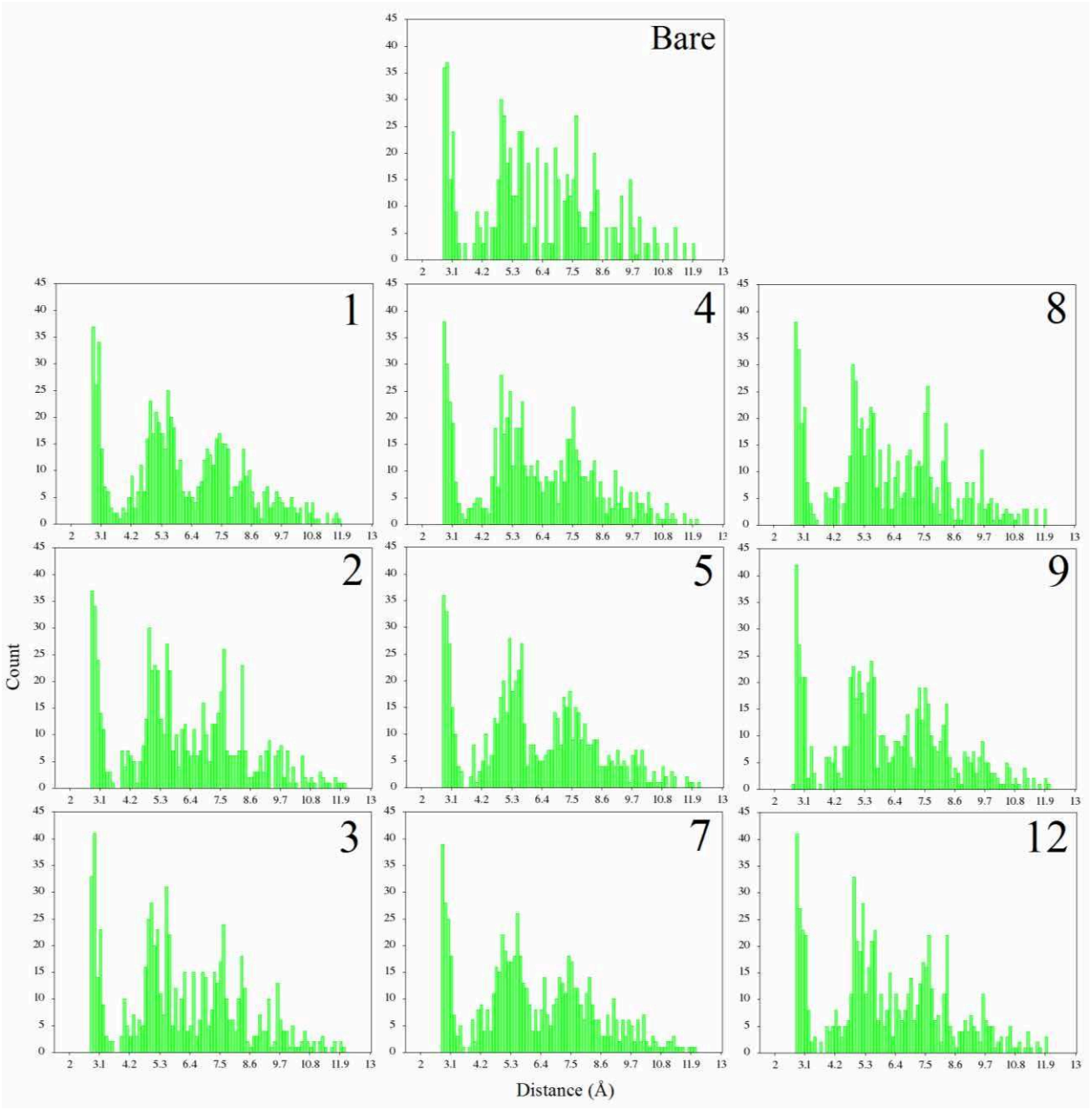

***Figure 12**. Histogram of the Au – Au distances of the bare and the different PH_3 – Au_{38} complexes structures. The equilibrium structures have been computed at the DFT LANL2MB / 6 – 31G(d) level.*

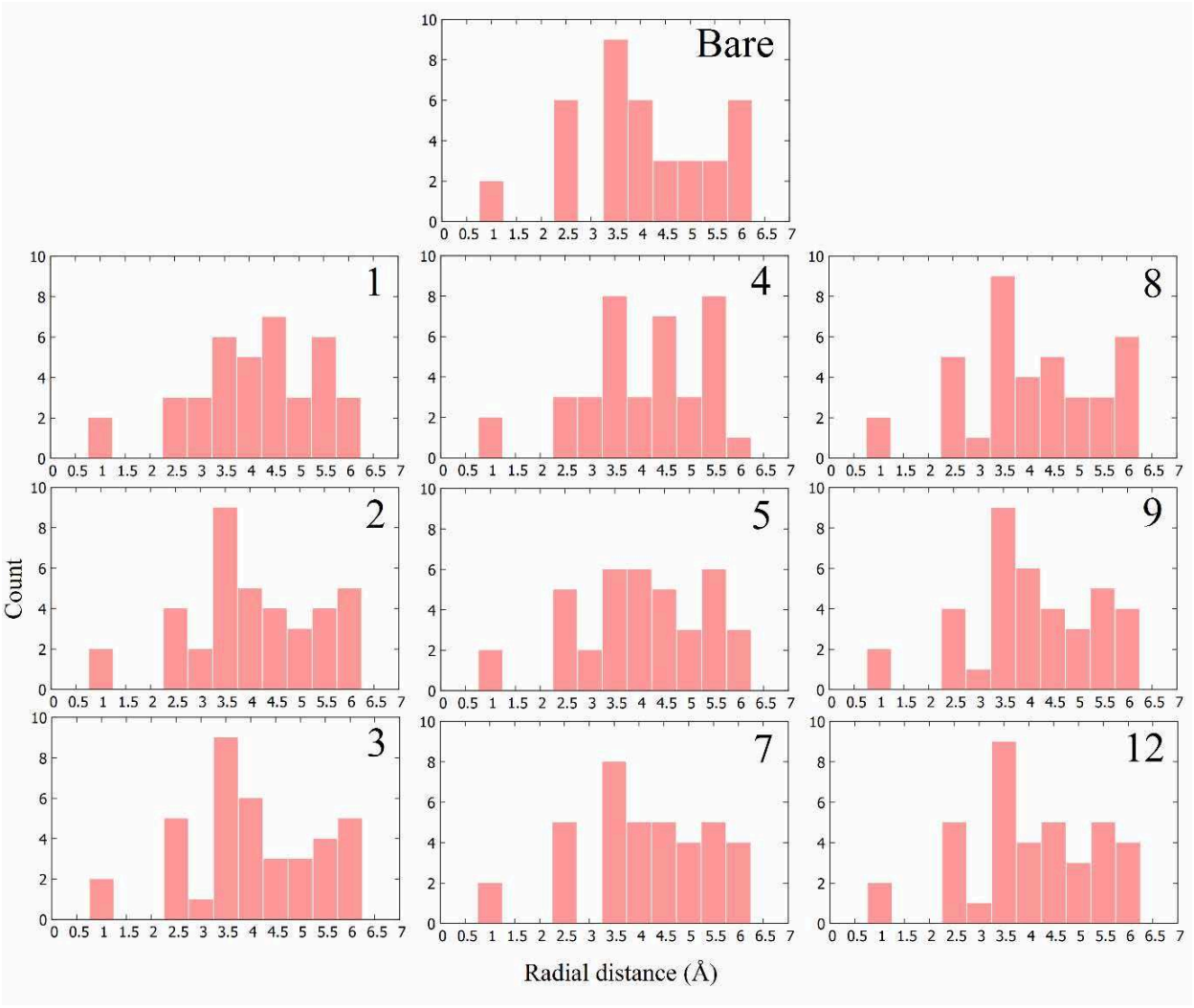

***Figure 13**. Histogram of the radial distances of gold atoms in the bare Au_{38} and the different PH_3 – Au_{38} complexes structures. The equilibrium structures have been computed at the DFT LANL2MB / 6 – 31G(d) level.*

Our study of the adsorption of PH_3 on the Au_{38} surface shows that the positively charged gold atoms in the bare configuration are the best candidates for the phosphine to interact. Those configurations are 8, 2 and 12 (see table 2). The partial charges are symmetric with respect to the C_3 axis. The configuration 8 corresponds to one of the three atoms at the top of the cluster (see the 3 atoms in the green circles in figure 14), configuration 2 represents one of the three atoms at the middle of the Au_{38} (see the 3 atoms in the black circles in figure 14) and configuration 12 corresponds to one of the three atoms at the bottom of the cluster (see the 3 atoms in the purple circles in figure 14).

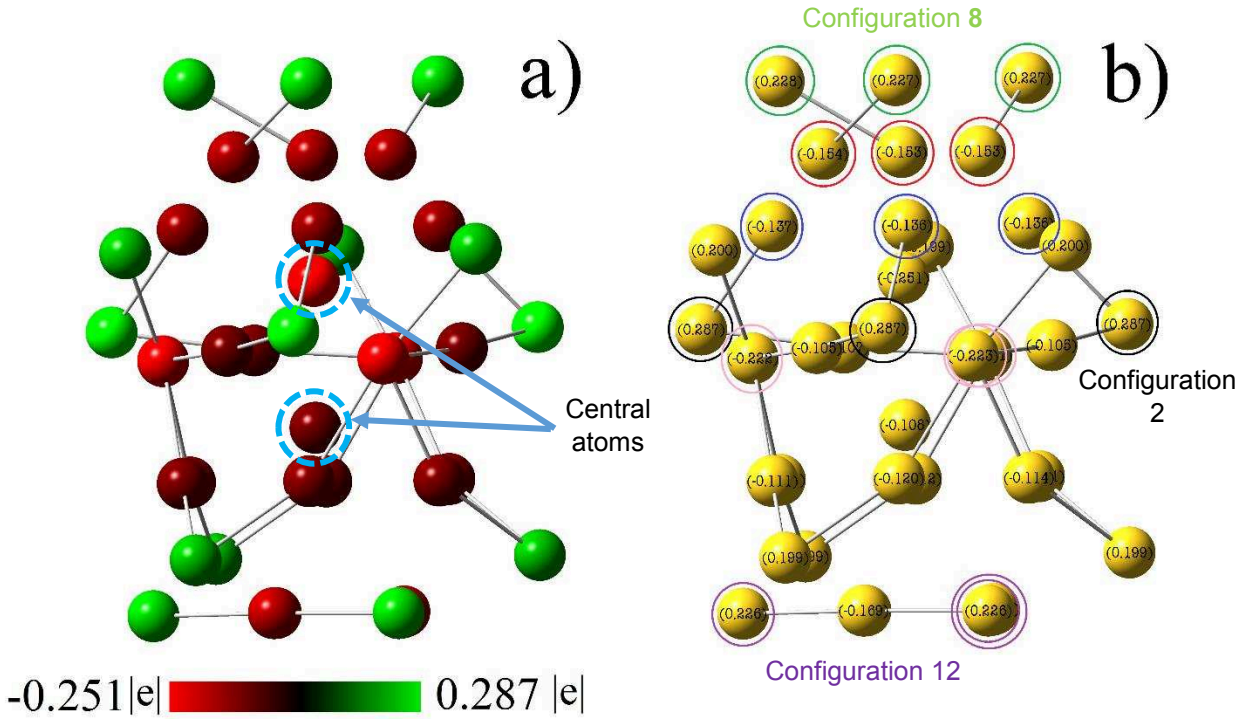

***Figure 14**. Natural charges of the gold atoms in the bare Au_{38} in its equilibrium geometry computed at the DFT level. The relativistic pseudopotential and basis set LANL2MB was used for gold and the 6 – 31G(d) for the ligands. Circles of the same colour highlight the gold atoms of the same charge. The double circle represents an atom on the back of another.*

As shown in figure 3, in the fully ligated Au_{38} cluster, the binding of a phosphine ligand is only taking place on Au atoms that in the bare Au_{38} cluster have the highest positive natural charge. Site that correspond to the highest values of binding energy (see table 2) also correspond to the Au atoms that have the smallest coordination number in the bare cluster, which shows a good correlation between the fully phosphine ligation and the single interaction study.

In addition, in table 3 we report the deformation energy (E_d) of the different configurations of the PH_3 – Au_{38} and the NHC – Au_{38} set of complexes. The E_d at 0 K is defined as $E_d = E^*_{bare} - E_{bare}$ where E^*_{bare} is the electronic energy of the bare cluster in the complex geometry and E_{bare} is the electronic energy of the bare cluster. It can be seen that in the phosphine case E_d ranges from 0.05 to 0.42 eV while for the NHC it ranges from 0.05 to 0.93 eV. In all configurations compared, NHC shows a larger E_d which confirms quantitatively that NHC induces a stronger distortion on the Au_{38} core.

***Table 3**. Deformation energy (E_d) of the system Au_{38} – L. L being PH_3 or NHC ligand. Equilibrium structures of configuration 6, 10 and 11 have not been found in the phosphine case.*

Configuration label	PH_3 (eV)	NHC (eV)
1	0.28	0.38
2	0.07	0.12
3	0.05	0.10
4	0.23	0.47
5	0.31	0.58
6	0.00	0.05
7	0.42	0.93
8	0.06	0.09
9	0.13	0.15
10	0.00	0.76
11	0.00	0.17
12	0.06	0.12

7.5 Conclusions

Our calculations confirm that PH_3 weakly binds a gold nanocluster surface adopting an "on top" position. NHC, on the other hand, forms strong covalent bonds with gold. No significant structural reorganization of the metal core was observed for PH_3 capped clusters while the distortion upon binding NHC is significant. For both the phosphine and NHC ligands, the binding is characterized by a charge transfer from the ligand shell to the metal core. When interacting on the Au_{20} and Au_{38} nanocluster surfaces, NHC shows a stronger electron – donor character.

By comparing both NHC coated cationic Au_{13} clusters, we notice that now, the opening of the gap is correlated to a decrease of positive charge on the metal core which is the opposite effect as found for the phosphine cationic Au_{13} analogues. This is attributed to the higher distortion of the metal core produced by the NHC ligand shell leading to a complete different degeneracy scheme of the molecular orbitals compared to that of the phosphine analogues. he H – L gap opening correlates well with the blue shift in the UV – Vis spectra when going from $[Au_{13}NHC_8Cl_4]^+$ to $[Au_{13}NHC_{10}Cl_2]^{3+}$.

On the other hand, the stability of the Au_{20} nanocluster is confirmed since no significant modification of the tetrahedral geometry of metal core has been observed when PH_3 is exchanged by NHC. This is highlighted by very similar optical profiles both capped Au_{20} clusters.

Upon comparing the PH_3 and NHC capped Au_{20} and Au_{38} clusters, the trend "*the more negative the metal core, the more the UV – Vis spectrum is red shifted*" found for the set of clusters $[Au_{25}(SR)_{18}]^q$ (with q = – 1, +1 and R being CH_3 or the phenyl group) [11] is also followed.

Our study of the PH_3 – Au_{38} complex and the fully ligated $Au_{38}NHC_9$ provides understanding of how PH_3 adsorbs on a gold nanocluster surface; PH_3 will only interact with the most positively charged and less coordinated Au atoms. The set of PH_3 – Au_{38} complexes and the fully ligated $Au_{38}(PH_3)_9$ studies show a good agreement, since the nine PH_3 in the fully ligated nanocluster are attached to the gold atoms with the highest natural charge and the smallest coordination number.

Further studies on the effect of the organic group bearing the N atoms, the heterocyclic backbone in the NHC or on the P atoms should be performed in order to understand the role of interligand interaction on the stability, reactivity and optical properties of nanoclusters. The comprehension of the effect of the ligand shell on the structure and properties of bare metal nanoclusters is essential to functionalize these nanomaterials.

7.6 References

1. Yamazoe, S., K. Koyasu, and T. Tsukuda, *Nonscalable Oxidation Catalysis of Gold Clusters.* Accounts of Chemical Research, 2014. **47**(3): p. 816-824.
2. Molina, L.M. and B. Hammer, *The activity of the tetrahedral Au20 cluster: charging and impurity effects.* Journal of Catalysis, 2005. **233**(2): p. 399-404.
3. Gao, Y., N. Shao, Y. Pei, Z. Chen, and X.C. Zeng, *Catalytic Activities of Subnanometer Gold Clusters (Au16–Au18, Au20, and Au27–Au35) for CO Oxidation.* ACS Nano, 2011. **5**(10): p. 7818-7829.
4. Liu, Y., H. Tsunoyama, T. Akita, S. Xie, and T. Tsukuda, *Aerobic Oxidation of Cyclohexane Catalyzed by Size-Controlled Au Clusters on Hydroxyapatite: Size Effect in the Sub-2 nm Regime.* ACS Catalysis, 2011. **1**(1): p. 2-6.
5. Liu, C., B. Yang, E. Tyo, S. Seifert, J. DeBartolo, B. von Issendorff, P. Zapol, S. Vajda, and L.A. Curtiss, *Carbon Dioxide Conversion to Methanol over Size-Selected Cu4 Clusters at Low Pressures.* Journal of the American Chemical Society, 2015. **137**(27): p. 8676-8679.
6. Dervishi, E., S. Bourdo, J.A. Driver, F. Watanabe, A.R. Biris, A. Ghosh, B. Berry, V. Saini, and A.S. Biris, *Catalytic Conversion of Graphene into Carbon Nanotubes via Gold Nanoclusters at Low Temperatures.* ACS Nano, 2012. **6**(1): p. 501-511.
7. Wallace, W.T. and R.L. Whetten, *Coadsorption of CO and O2 on Selected Gold Clusters: Evidence for Efficient Room-Temperature CO2 Generation.* Journal of the American Chemical Society, 2002. **124**(25): p. 7499-7505.
8. Corma, A., P. Concepción, M. Boronat, M.J. Sabater, J. Navas, M.J. Yacaman, E. Larios, A. Posadas, M.A. López-Quintela, D. Buceta, E. Mendoza, G. Guilera, and A. Mayoral, *Exceptional oxidation activity with size-controlled supported gold clusters of low atomicity.* Nat Chem, 2013. **5**(9): p. 775-781.
9. Kauffman, D.R., D. Alfonso, C. Matranga, H. Qian, and R. Jin, *Experimental and Computational Investigation of Au25 Clusters and CO2: A Unique Interaction and Enhanced Electrocatalytic Activity.* Journal of the American Chemical Society, 2012. **134**(24): p. 10237-10243.
10. Sun, C., Y. Yuan, Z. Xu, T. Ji, Y. Tian, S. Wu, J. Lei, J. Li, N. Gao, and G. Nie, *Fine-Tuned H-Ferritin Nanocage with Multiple Gold Clusters as Near-Infrared Kidney Specific Targeting Nanoprobe.* Bioconjugate Chemistry, 2015. **26**(2): p. 193-196.
11. Lugo, G., V. Schwanen, B. Fresch, and F. Remacle, *Charge Redistribution Effects on the UV–Vis Spectra of Small Ligated Gold Clusters: a Computational Study.* The Journal of Physical Chemistry C, 2015.
12. Dufour, F., B. Fresch, O. Durupthy, C. Chaneac, and F. Remacle, *Ligand and Solvation Effects on the Structural and Electronic Properties of Small Gold Clusters.* The Journal of Physical Chemistry C, 2014. **118**(8): p. 4362-4376.
13. Periyasamy, G. and F. Remacle, *Ligand and Solvation Effects on the Electronic Properties of Au55 Clusters: A Density Functional Theory Study.* Nano Letters, 2009. **9**(8): p. 3007-3011.
14. Konishi, K., *Phosphine-Coordinated Pure-Gold Clusters: Diverse Geometrical Structures and Unique Optical Properties/Responses*, in *Gold Clusters, Colloids and Nanoparticles I*, P.D.M. Mingos, Editor. 2014, Springer International Publishing: Cham. p. 49-86.
15. de Silva, N., J.-M. Ha, A. Solovyov, M.M. Nigra, I. Ogino, S.W. Yeh, K.A. Durkin, and A. Katz, *A bioinspired approach for controlling accessibility in calix[4]arene-bound metal cluster catalysts.* Nat Chem, 2010. **2**(12): p. 1062-1068.
16. Wang, Y., X.-K. Wan, L. Ren, H. Su, G. Li, S. Malola, S. Lin, Z. Tang, H. Häkkinen, B.K. Teo, Q.-M. Wang, and N. Zheng, *Atomically Precise Alkynyl-Protected Metal Nanoclusters as a Model Catalyst:*

Observation of Promoting Effect of Surface Ligands on Catalysis by Metal Nanoparticles. Journal of the American Chemical Society, 2016. **138**(10): p. 3278-3281.

17. Gomez, S., K. Philippot, V. Colliere, B. Chaudret, F. Senocq, and P. Lecante, *Gold nanoparticles from self-assembled gold() amine precursors.* Chemical Communications, 2000(19): p. 1945-1946.
18. Kanaras, A.G., F.S. Kamounah, K. Schaumburg, C.J. Kiely, and M. Brust, *Thioalkylated tetraethylene glycol: a new ligand for water soluble monolayer protected gold clusters.* Chemical Communications, 2002(20): p. 2294-2295.
19. Zeng, C., T. Li, A. Das, N.L. Rosi, and R. Jin, *Chiral Structure of Thiolate-Protected 28-Gold-Atom Nanocluster Determined by X-ray Crystallography.* Journal of the American Chemical Society, 2013. **135**(27): p. 10011-10013.
20. Lopez-Acevedo, O. and H. Häkkinen, *Derivatives of the thiolate-protected gold cluster Au25(SR)18 -1.* The European Physical Journal D, 2011. **63**(2): p. 311-314.
21. Negishi, Y., K. Nobusada, and T. Tsukuda, *Glutathione-Protected Gold Clusters Revisited: Bridging the Gap between Gold(I)−Thiolate Complexes and Thiolate-Protected Gold Nanocrystals.* Journal of the American Chemical Society, 2005. **127**(14): p. 5261-5270.
22. Beqa, L., D. Deschamps, S. Perrio, A.-C. Gaumont, S. Knoppe, and T. Bürgi, *Ligand Exchange Reaction on Au38(SR)24, Separation of Au38(SR)23(SR')1 Regioisomers, and Migration of Thiolates.* The Journal of Physical Chemistry C, 2013. **117**(41): p. 21619-21625.
23. Peterle, T., A. Leifert, J. Timper, A. Sologubenko, U. Simon, and M. Mayor, *Multidentate thioether ligands coating gold nanoparticles.* Chemical Communications, 2008(29): p. 3438-3440.
24. Galan, B.R., E.S. Wiedner, M.L. Helm, J.C. Linehan, and A.M. Appel, *Effects of Phosphine–Carbene Substitutions on the Electrochemical and Thermodynamic Properties of Nickel Complexes.* Organometallics, 2014. **33**(9): p. 2287-2294.
25. Shichibu, Y., K. Suzuki, and K. Konishi, *Facile synthesis and optical properties of magic-number Au13 clusters.* Nanoscale, 2012. **4**(14): p. 4125-4129.
26. Shichibu, Y. and K. Konishi, *HCl-Induced Nuclearity Convergence in Diphosphine-Protected Ultrasmall Gold Clusters: A Novel Synthetic Route to "Magic-Number" Au13 Clusters.* Small, 2010. **6**(11): p. 1216-1220.
27. Guidez, E.B., A. Hadley, and C.M. Aikens, *Initial Growth Mechanisms of Gold-Phosphine Clusters.* The Journal of Physical Chemistry C, 2011. **115**(14): p. 6305-6316.
28. Fresch, B., E. Hanozin, F. Dufour, and F. Remacle, *Interplay of structural and electronic stabilizing factors in neutral and cationic phosphine protected Au13 clusters.* The European Physical Journal D, 2012. **66**(12): p. 1-9.
29. Shichibu, Y., Y. Negishi, T. Tsukuda, and T. Teranishi, *Large-Scale Synthesis of Thiolated Au25 Clusters via Ligand Exchange Reactions of Phosphine-Stabilized Au11 Clusters.* Journal of the American Chemical Society, 2005. **127**(39): p. 13464-13465.
30. Nolan, S.P., *N-Heterocyclic Carbenes in Synthesis.* WILEY-VCH Verlag GmbH and Co. KGaA, 2006.
31. Hurst, E.C., K. Wilson, I.J.S. Fairlamb, and V. Chechik, *N-Heterocyclic carbene coated metal nanoparticles.* New Journal of Chemistry, 2009. **33**(9): p. 1837-1840.
32. Ling, X., N. Schaeffer, S. Roland, and M.-P. Pileni, *Superior Oxygen Stability of N-Heterocyclic Carbene-Coated Au Nanocrystals: Comparison with Dodecanethiol.* Langmuir, 2015. **31**(47): p. 12873-12882.
33. Rodriguez-Castillo, M., D. Laurencin, F. Tielens, A. van der Lee, S. Clement, Y. Guari, and S. Richeter, *Reactivity of gold nanoparticles towards N-heterocyclic carbenes.* Dalton Transactions, 2014. **43**(16): p. 5978-5982.
34. Rodríguez-Castillo, M., G. Lugo-Preciado, D. Laurencin, F. Tielens, A. van der Lee, S. Clément, Y. Guari, J.M. López-de-Luzuriaga, M. Monge, F. Remacle, and S. Richeter, *Experimental and*

Theoretical Study of the Reactivity of Gold Nanoparticles Towards Benzimidazole-2-ylidene Ligands. Chemistry – A European Journal, 2016: p. n/a-n/a.

35. Zhukhovitskiy, A.V., M.G. Mavros, T. Van Voorhis, and J.A. Johnson, *Addressable Carbene Anchors for Gold Surfaces.* Journal of the American Chemical Society, 2013. **135**(20): p. 7418-7421.
36. Zhang, H.-F., M. Stender, R. Zhang, C. Wang, J. Li, and L.-S. Wang, *Toward the Solution Synthesis of the Tetrahedral Au20 Cluster.* The Journal of Physical Chemistry B, 2004. **108**(33): p. 12259-12263.
37. Qian, H., Y. Zhu, and R. Jin, *Size-Focusing Synthesis, Optical and Electrochemical Properties of Monodisperse Au38(SC2H4Ph)24 Nanoclusters.* ACS Nano, 2009. **3**(11): p. 3795-3803.
38. Qian, H., M. Zhu, U.N. Andersen, and R. Jin, *Facile, Large-Scale Synthesis of Dodecanethiol-Stabilized Au38 Clusters.* The Journal of Physical Chemistry A, 2009. **113**(16): p. 4281-4284.
39. Menard, L.D., H. Xu, S.-P. Gao, R.D. Twesten, A.S. Harper, Y. Song, G. Wang, A.D. Douglas, J.C. Yang, A.I. Frenkel, R.W. Murray, and R.G. Nuzzo, *Metal Core Bonding Motifs of Monodisperse Icosahedral Au13 and Larger Au Monolayer-Protected Clusters As Revealed by X-ray Absorption Spectroscopy and Transmission Electron Microscopy.* The Journal of Physical Chemistry B, 2006. **110**(30): p. 14564-14573.
40. Qian, H., W.T. Eckenhoff, Y. Zhu, T. Pintauer, and R. Jin, *Total Structure Determination of Thiolate-Protected Au38 Nanoparticles.* Journal of the American Chemical Society, 2010. **132**(24): p. 8280-8281.
41. MacDonald, M.A., P. Zhang, N. Chen, H. Qian, and R. Jin, *Solution-Phase Structure and Bonding of Au38(SR)24 Nanoclusters from X-ray Absorption Spectroscopy.* The Journal of Physical Chemistry C, 2011. **115**(1): p. 65-69.
42. Copley, R.C.B. and D.M.P. Mingos, *Synthesis and characterization of the centred icosahedral cluster series [Au9MIB4Cl4(PMePh2)8][C2B9H12], where MIB= Au, Ag or Cu.* Journal of the Chemical Society, Dalton Transactions, 1996(4): p. 491-500.
43. Wang, Z.W. and R.E. Palmer, *Direct atomic imaging and dynamical fluctuations of the tetrahedral Au20 cluster.* Nanoscale, 2012. **4**(16): p. 4947-4949.
44. Krishnamurty, S., G.S. Shafai, D.G. Kanhere, B. Soulé de Bas, and M.J. Ford, *Ab Initio Molecular Dynamical Investigation of the Finite Temperature Behavior of the Tetrahedral Au19 and Au20 Clusters.* The Journal of Physical Chemistry A, 2007. **111**(42): p. 10769-10775.
45. Li, J., X. Li, H.-J. Zhai, and L.-S. Wang, *Au20: A Tetrahedral Cluster.* Science, 2003. **299**(5608): p. 864-867.
46. Kryachko, E.S. and F. Remacle, *The magic gold cluster Au20.* International Journal of Quantum Chemistry, 2007. **107**(14): p. 2922-2934.
47. Cortés-Arriagada, D., M.P. Oyarzún, L. Sanhueza, and A. Toro-Labbé, *Binding of Trivalent Arsenic onto the Tetrahedral Au20 and Au19Pt Clusters: Implications in Adsorption and Sensing.* The Journal of Physical Chemistry A, 2015. **119**(26): p. 6909-6918.
48. Kryachko, E.S. and F. Remacle, *20-Nanogold Au20(T d) and Low-Energy Hollow Cages: Void Reactivity*, in *Advances in the Theory of Quantum Systems in Chemistry and Physics*, E.P. Hoggan, et al., Editors. 2012, Springer Netherlands: Dordrecht. p. 571-598.
49. Gruene, P., D.M. Rayner, B. Redlich, A.F.G. van der Meer, J.T. Lyon, G. Meijer, and A. Fielicke, *Structures of Neutral Au7, Au19, and Au20 Clusters in the Gas Phase.* Science, 2008. **321**(5889): p. 674-676.
50. Wu, K., J. Li, and C. Lin, *Remarkable second-order optical nonlinearity of nano-sized Au20 cluster: a TDDFT study.* Chemical Physics Letters, 2004. **388**(4–6): p. 353-357.
51. Wang, J., G. Wang, and J. Zhao, *Structures and electronic properties of Cu20, Ag20, and Au20 clusters with density functional method.* Chemical Physics Letters, 2003. **380**(5–6): p. 716-720.

52. King, R.B., Z. Chen, and P.v.R. Schleyer, *Structure and Bonding in the Omnicapped Truncated Tetrahedral Au20 Cluster: Analogies between Gold and Carbon Cluster Chemistry.* Inorganic Chemistry, 2004. **43**(15): p. 4564-4566.
53. De, H.S., S. Krishnamurty, and S. Pal, *Density Functional Investigation of Relativistic Effects on the Structure and Reactivity of Tetrahedral Gold Clusters.* The Journal of Physical Chemistry C, 2009. **113**(17): p. 7101-7106.
54. Johnson, G.E., A. Olivares, D. Hill, and J. Laskin, *Cationic gold clusters ligated with differently substituted phosphines: effect of substitution on ligand reactivity and binding.* Physical Chemistry Chemical Physics, 2015. **17**(22): p. 14636-14646.
55. Johnson, G.E., T. Priest, and J. Laskin, *Synthesis and Characterization of Gold Clusters Ligated with 1,3-Bis(dicyclohexylphosphino)propane.* ChemPlusChem, 2013. **78**(9): p. 1033-1039.
56. Pettibone, J.M. and J.W. Hudgens, *Gold Cluster Formation with Phosphine Ligands: Etching as a Size-Selective Synthetic Pathway for Small Clusters?* ACS Nano, 2011. **5**(4): p. 2989-3002.
57. Hakkinen, H., *Atomic and electronic structure of gold clusters: understanding flakes, cages and superatoms from simple concepts.* Chemical Society Reviews, 2008. **37**(9): p. 1847-1859.
58. Goel, S., K.A. Velizhanin, A. Piryatinski, S.A. Ivanov, and S. Tretiak, *Ligand Effects on Optical Properties of Small Gold Clusters: A TDDFT Study.* The Journal of Physical Chemistry C, 2012. **116**(5): p. 3242-3249.
59. Guliamov, O., A.I. Frenkel, L.D. Menard, R.G. Nuzzo, and L. Kronik, *Tangential Ligand-Induced Strain in Icosahedral Au13.* Journal of the American Chemical Society, 2007. **129**(36): p. 10978-10979.
60. Shafai, G., S. Hong, M. Bertino, and T.S. Rahman, *Effect of Ligands on the Geometric and Electronic Structure of Au13 Clusters.* The Journal of Physical Chemistry C, 2009. **113**(28): p. 12072-12078.
61. Schwerdtfeger, P., H.L. Hermann, and H. Schmidbaur, *Stability of the Gold(I)–Phosphine Bond. A Comparison with Other Group 11 Elements.* Inorganic Chemistry, 2003. **42**(4): p. 1334-1342.
62. Guidez, E.B. and C.M. Aikens, *Time-Dependent Density Functional Theory Study of the Luminescence Properties of Gold Phosphine Thiolate Complexes.* The Journal of Physical Chemistry A, 2015. **119**(14): p. 3337-3347.
63. Aikens, C.M., *Effects of Core Distances, Solvent, Ligand, and Level of Theory on the TDDFT Optical Absorption Spectrum of the Thiolate-Protected Au25 Nanoparticle.* The Journal of Physical Chemistry A, 2009. **113**(40): p. 10811-10817.
64. Zhu, M., C.M. Aikens, F.J. Hollander, G.C. Schatz, and R. Jin, *Correlating the Crystal Structure of A Thiol-Protected Au25 Cluster and Optical Properties.* Journal of the American Chemical Society, 2008. **130**(18): p. 5883-5885.
65. Fresch, B. and F. Remacle, *Tuning the Properties of Pd Nanoclusters by Ligand Coatings: Electronic Structure Computations on Phosphine, Thiol, and Mixed Phosphine–Thiol Ligand Shells.* The Journal of Physical Chemistry C, 2014. **118**(18): p. 9790-9800.

Conclusions and Perspectives

Density functional theory is a powerful tool to investigate ligand – metal interactions. It offers good quality results at relatively low computational cost. Moreover, it also offers, in our specific case, comprehension of the effect of the ligand shell on the metal core morphology, electronic structure, ligand drafting modes and optical properties.

In our study, computation of UV – Vis spectra at the TD – DFT / CAMB3LYP level, of the Au_{13}, Au_{25}, and Au_{28} metallic cores protected by thiolate, chloride, and phosphine ligand demonstrated that it is possible to tune the energy of the absorption band of gold clusters by the ligand shell engineering considering charge redistribution effects between ligand shell and metallic core. Our results suggest also that capping the GNCs with ligands with different electron donor and acceptor character offers the possibility of tuning their optical properties by controlling the spatial organization of the ligands on the metal surface. However, experimentally, the synthesis and structural determination of GNCs where we can control the organization of ligands on the metal surface in such small systems is very challenging and more work has to be done in order to understand the role of interligand interactions, their stability and mode of grafting of the ligand – Au bond. [1]

Experimentally, we show by ESI – MS that by combining 4ATP (4 – aminothiophenol) and TP (thiophenol) ligands in the *adapted* Demessence synthesis [2] method, we preserve the Au_{25} nuclearity. Our ESI – MS results evidence a set of $Au_{25}(ATP)_x(TP)_{18-x}$ clusters with different ATP/TP ratios. However, the addition of DDT leads to aggregation of the clusters producing nanoparticles. FT – IR spectroscopy confirms the absorption of two different ligands on the gold surface and SAXS shows that we have a very good correlation between the distance between two clusters and the length of the ligand protecting them. ESI – MS, FT – IR and UV – Vis spectroscopy and SAXS characterization techniques provide detailed information on the structural determination and on the optical properties evaluation of GNCs. On the other hand, these techniques do not provide information about the organization of the ligands in the shell and this is a very important parameter on the tuning of GNCs properties. [3-7]

Furthermore, we have analyzed, in collaboration with the Institut Charles Gerhardt in the Université de Montpellier, France the reactivity of *n* – heterocyclic carbene (NHC) absorbed on gold nanosurfaces. Ligand exchange reaction of thioethers protected gold nanoparticles was performed to obtain their NHC protected GNC analogues. Experimental results of the Montpellier group show that several NHC bearing different group on the N atoms, for instance: methyl, hexyl and benzyl groups' show similar reactivity while protecting a gold nanosurface. The protection of gold nanoparticles by different NHCs is accompanied by the erosion of the gold core, leading to a smaller particle diameter and by the formation of the bis(NHC) gold complexes ($[NHC – Au – NHC]^+$).

In order to understand the mode of grafting and surface reconstruction, we carried out DFT computations on the NHC protected Au_{38} model cluster.[8] A computational study on the NHCa – Au_{38} (NHC bearing CH_3 on the N atoms: 1, 3 – dimethyl – 1H – benzimidazolium, called here NHCa) complex was performed. Our results confirm a strong covalent Au – C bond (even stronger than thiolates which explains why it is possible to exchange them by NHC) and – as in phosphine protected GNC – NHCa adopts an "ion top position". Interestingly, our computations show that even the binding of a single NHCa induces a significant distortion of the metal framework followed by a charge transfer from the ligand shell to the metal core. This confirms the electron – donor character of NHCa. Further studies on the effect of the organic group bearing the N atoms, the phenyl backbone on the NHC should be performed to understand the role of interligand interaction on the stability, reactivity and optical properties of NHC capped GNCs.

The joint experimental-theoretical study allows to propose a possible mechanism explaining the formation of [NHC – Au – NHC]+ complexes. First, the thioethers absorbed on the gold nanoparticle precursor are substituted by the NHCs. Next, surface reconstruction occurs due to the strong Au – C bond. The NHC – Au moiety may diffuse on the gold nanoparticle surface. Finally, the release of NHC – Au fragment makes possible the reaction with a single NHC to form the bis(NHC) Au^{I} complex ($[NHC – Au – NHC]^{+}$) leading to a decrease of the nanoparticle size. However, the NHC reactivity on gold surfaces is very complex and more studies should be carried out to understand the mechanisms of GNCs formation using NHC ligands as capping agents since the NHC coated GNCs exhibit a very poor stability. It appears that not only a strong Au – ligand bond is necessary to ensure the nanocluster stability but also interligand interactions.

With the purpose to reinforce our understanding on the NHC drafting modes and in addition to explore their optical properties, a comparison of the fully ligated PH_3 and 1, 3 – dimethyl – 1H – benzimidazolium (NHCa) GNC with different metal core (Au_{13}, the tetrahedral Au_{20} and the Au_{38} cores) was also undertaken. Our computations show that in all of the 3 different fully protected metal cores the Au – P bond is weaker than the Au – NHC one. Additionally, our study confirms that the absorption optical profiles are dependent on the NHC/chloride ratio as observed by Konishi *et al.*[9] for phosphine ligand protected Au_{13} clusters suggesting that the ligand – to – metal charge transfer is an important parameter in understanding the electronic transitions in these clusters.

Furthermore, our computations on the PH_3 – Au_{38} complex show that PH_3 will only interact on those positively charged and less coordinated Au atoms. We can conclude then that there is a site selectivity for the reactivity for the PH_3 interacting on the Au_{38} surface which allows predicting where the PH_3 is likely to be adsorbed. The PH_3 – Au_{38} complex and the fully ligated $Au_{38}(PH_3)_9$ studies show a good agreement, since the nine PH_3 in the fully ligated nanocluster are attached on those gold atoms showing the more positive natural charge and the shortest coordination number.

Finally, the understanding of the effect of ligand shell protection on the core and electronic structure and on the optical properties as well as the study of the mode of ligand grafting on the metal surface opens the door for GNC functionalization to design materials for specific applications. Our computations confirm that the electron donor or acceptor character, the spatial organization of the ligands and the charge state of the cluster play an important role in the regulation of the electron density in the metallic core. On the longer term, our results motivate the use of computational chemistry to assist the design of nanocluster synthesis methodologies where we can control the composition of the ligand layer to tune the properties of small gold nanoclusters.

References

1. Lugo, G., et al., *Charge Redistribution Effects on the UV–Vis Spectra of Small Ligated Gold Clusters: a Computational Study.* The Journal of Physical Chemistry C, 2015.
2. Lavenn, C., et al., *Functionalized gold magic clusters: Au25(SPhNH2)17.* Nanoscale, 2012. **4**(23): p. 7334-7337.
3. Periyasamy, G. and F. Remacle, *Ligand and Solvation Effects on the Electronic Properties of Au55 Clusters: A Density Functional Theory Study.* Nano Letters, 2009. **9**(8): p. 3007-3011.
4. Dufour, F., et al., *Ligand and Solvation Effects on the Structural and Electronic Properties of Small Gold Clusters.* The Journal of Physical Chemistry C, 2014. **118**(8): p. 4362-4376.
5. Goel, S., et al., *Ligand Effects on Optical Properties of Small Gold Clusters: A TDDFT Study.* The Journal of Physical Chemistry C, 2012. **116**(5): p. 3242-3249.
6. Tlahuice-Flores, A., R.L. Whetten, and M. Jose-Yacaman, *Ligand Effects on the Structure and the Electronic Optical Properties of Anionic Au25(SR)18 Clusters.* The Journal of Physical Chemistry C, 2013. **117**(40): p. 20867-20875.
7. Shibu, E.S., et al., *Ligand Exchange of Au25SG18 Leading to Functionalized Gold Clusters: Spectroscopy, Kinetics, and Luminescence.* The Journal of Physical Chemistry C, 2008. **112**(32): p. 12168-12176.
8. Qian, H., et al., *Total Structure Determination of Thiolate-Protected Au38 Nanoparticles.* Journal of the American Chemical Society, 2010. **132**(24): p. 8280-8281.
9. Shichibu, Y., K. Suzuki, and K. Konishi, *Facile synthesis and optical properties of magic-number Au13 clusters.* Nanoscale, 2012. **4**(14): p. 4125-4129.

Appendices

1. Supporting information: Charge Redistribution Effects on the UV-Vis Spectra of Small Ligated Gold Clusters: a Computational Study. (Chapter III)

Charge Redistribution Effects on the UV-Vis Spectra of Small Ligated Gold Clusters : a Computational Study

G. Lugo, V. Schwanen, B. Fresch and F. Remacle

Department of Chemistry, University of Liège, B4000 Liège, Belgium

Supporting Information

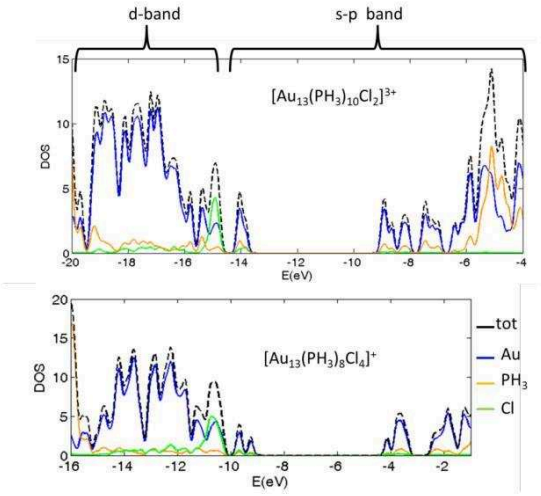

Figure S1: Density of states (DOS) of the $[Au_{13}(PH_3)_{10}Cl_2]^{3+}$ and $[Au_{13}(PH_3)_8Cl_4]^{+}$ clusters. The figure shows the contribution from the gold atoms and the ligands (PH_3 and Cl).

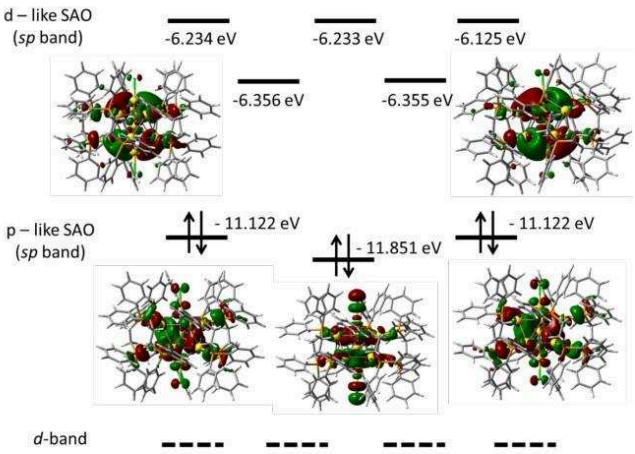

Figure S2: Molecular orbital energy diagram of the $[Au_{13}(dppe)_5Cl_2]^{3+}$ cluster. Isocontours of the frontier molecular orbitals are shown as well as the orbital energy in eV. The degeneracy threshold is 0.13 eV and the isovalue 0.02.

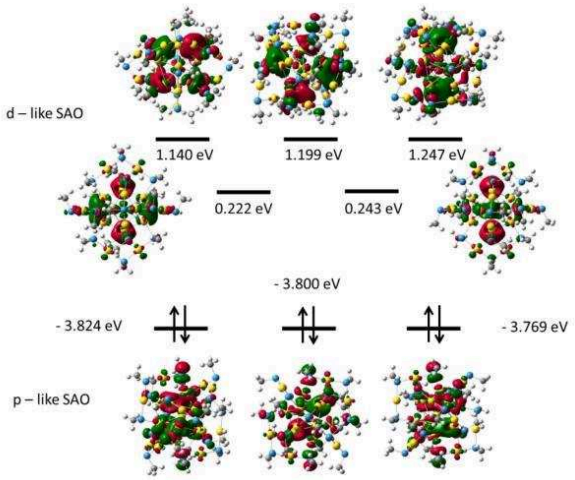

Figure S3: Molecular orbital energy diagram of the $[Au_{25}(SCH_3)_{18}]^-$ cluster. The super atomic structure is shown by the isocontours of the frontier molecular orbitals as well as the orbital energy in eV. The degeneracy threshold is 0.13 eV and isovalue 0.02.

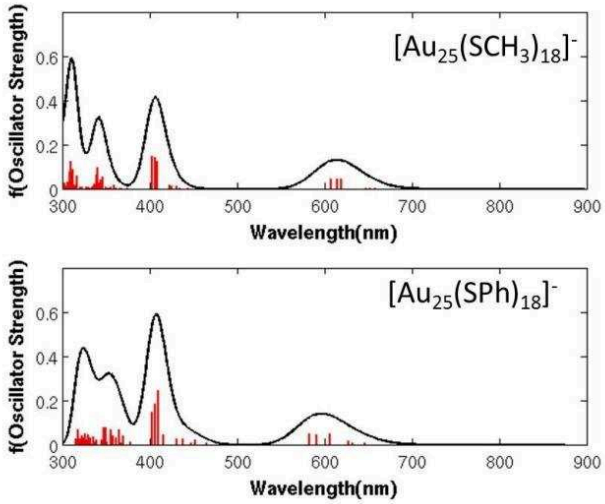

Figure S4. Computed optical absorption spectra of the ligated Au_{25} clusters. Top $[Au_{25}(SCH_3)_{18}]^-$, bottom $[Au_{25}(SPh)_{18}]^-$. The spectra show the blue shift experienced by the transition around 600 nm when the methyl is substituted by the phenyl radical.

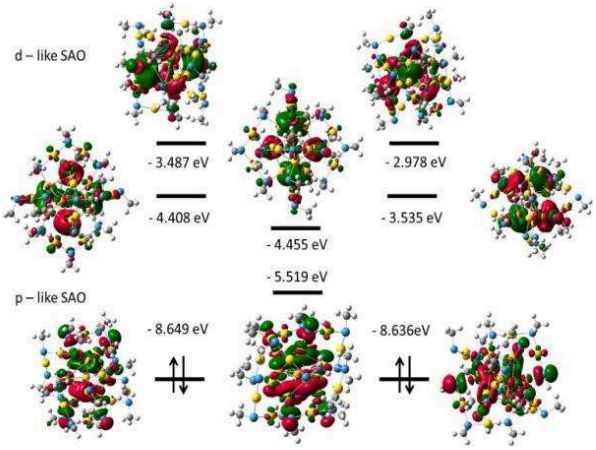

Figure S5: Molecular orbital energy diagram of the $[Au_{25}(SCH_3)_{18}]^+$ cluster. The super atomic structure is shown by the isocontours of the frontier molecular orbitals as well as the orbital energy in eV. The degeneracy threshold is 0.13 eV and isovalue 0.02.

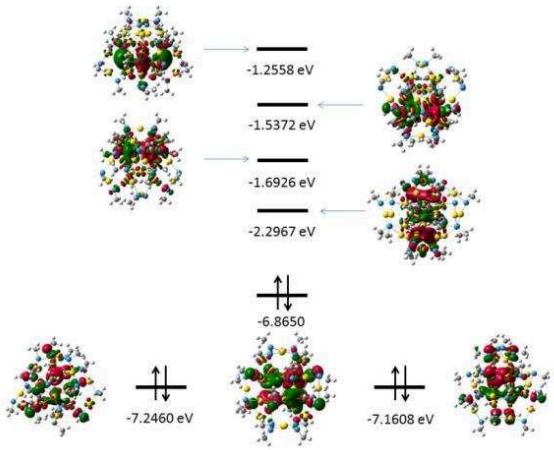

Figure S6. Molecular orbital diagram of $Au_{28}(SCH_3)_{20}$ cluster. No superatomic structure in the frontiers molecular orbitals has been found. The degeneracy threshold is 0.13 eV and isovalue 0.02.

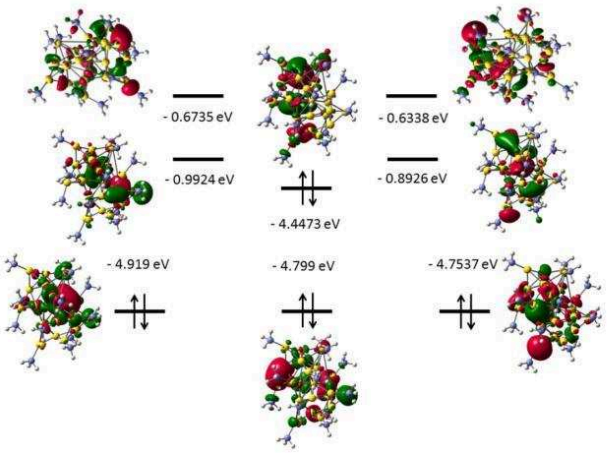

Figure S7. Molecular orbital diagram of $Au_{28}(PH_3)_{13}$ cluster. No superatomic structure in the frontiers molecular orbitals is found. The degeneracy threshold is 0.13 eV and isovalue 0.02.

2. Supporting information: Experimental and Theoretical Study of the Reactivity of Gold Nanoparticles towards Benzimidazole-2 – ylidene Ligands. (Chapter VI)

CHEMISTRY
A European Journal

Supporting Information

Experimental and Theoretical Study of the Reactivity of Gold Nanoparticles Towards Benzimidazole-2-ylidene Ligands

María Rodríguez-Castillo,[a] Gustavo Lugo-Preciado,[b] Danielle Laurencin,[a] Frederik Tielens,*[c] Arie van der Lee,[d] Sébastien Clément,[a] Yannick Guari,[a] José M. López-de-Luzuriaga,[e] Miguel Monge,[e] Françoise Remacle,*[b] and Sébastien Richeter*[a]

chem_201601253_sm_miscellaneous_information.pdf

III. Computational studies

1. Grafting of the diethylthioether on a planar Au(111) surface

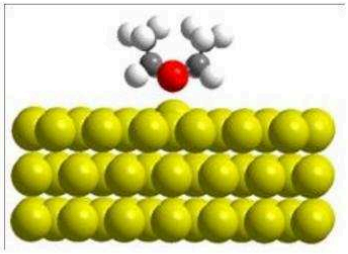

Figure S12. Optimized geometry of the diethyl-thioether grafted on a Au surface (adsorption energy ~ -14.36 kcal.mol^{-1}).

2. Grafting of NHCa on a Au_{38} cluster

Charge distribution in the Au_{38} cluster

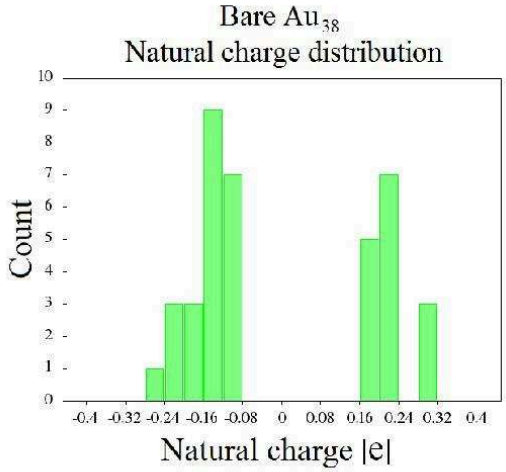

Figure S13. Natural charge distribution of the bare Au_{38} cluster. The equilibrium structure and the natural charges were calculated at the DFT CAM B3LYP LANL2MB / 6 – 31G(d) level.

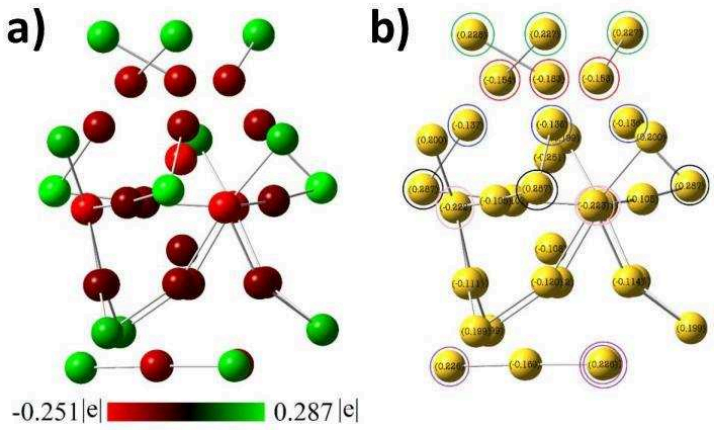

Figure S14. Natural charges of the gold atoms in the bare Au_{38} cluster at its equilibrium geometry at the CAM B3LYP DFT level. a) Au_{38} cluster charges represented by colors. b) Values of the natural charges in |e|. Circles of the same color highlight the gold atoms of equal charge. The 38 gold atoms, except for the 2 central ones (that is to say 36 gold atoms) can be classified depending on their natural charge, each group containing 3 atoms with the same charge and 12 groups in total. The double circle represents an atom on the back of another.

Distribution of distances among the 38 gold atoms

Figure S15 shows the distribution of distances among the 38 gold atoms. The one corresponding to the bare Au_{38} cluster is named "Bare". The others correspond to Au_{38} clusters ligated to one **NHCa** ligand. As it can be seen, binding a single **NHCa** ligand induces a strong distortion of the metallic core. We can observe 3 different populations (or peaks). The first peak represents the distances among those atoms directly connected, for instance, in the case of the bare configuration, Figure S15 shows that this population of distances goes from 2.794 Å to 3.176 Å. The second one is a collection of all the distances of neighboring atoms which are not bound and finally, the third one stands for those atoms relatively far. In all cases, except for cases 8 and 9, the population of "distances" in the first peak increases (larger count in Figure S15), and the population of the other two peaks decreases, suggesting that the presence of **NHCa** is pulls the gold atoms closer.

In order to help us understand how **NHCa** distorts the metallic core we have plotted two spheres with "r" and "r + 1 Å" of radius (where r goes from 0 Å to 7 Å), taking as the origin the point between the two central Au atoms and counting the gold atoms in between the spheres. Figure S16 shows the distribution of gold atoms in the cluster. Again, as in Figure S15, we can observe that the presence of **NHCa** strongly modifies the structure of the core. After single ligand interaction, the C_3 symmetry is broken in the metallic core and comparing the "bare" configuration in Figure S16 with the other 12 configurations, we can see that the number of atoms in the radial distance range around 6 Å decreases while some atoms move to smaller distances (with respect to the center of the spheres) indicating that the presence of the carbene tends to pull the gold atoms.

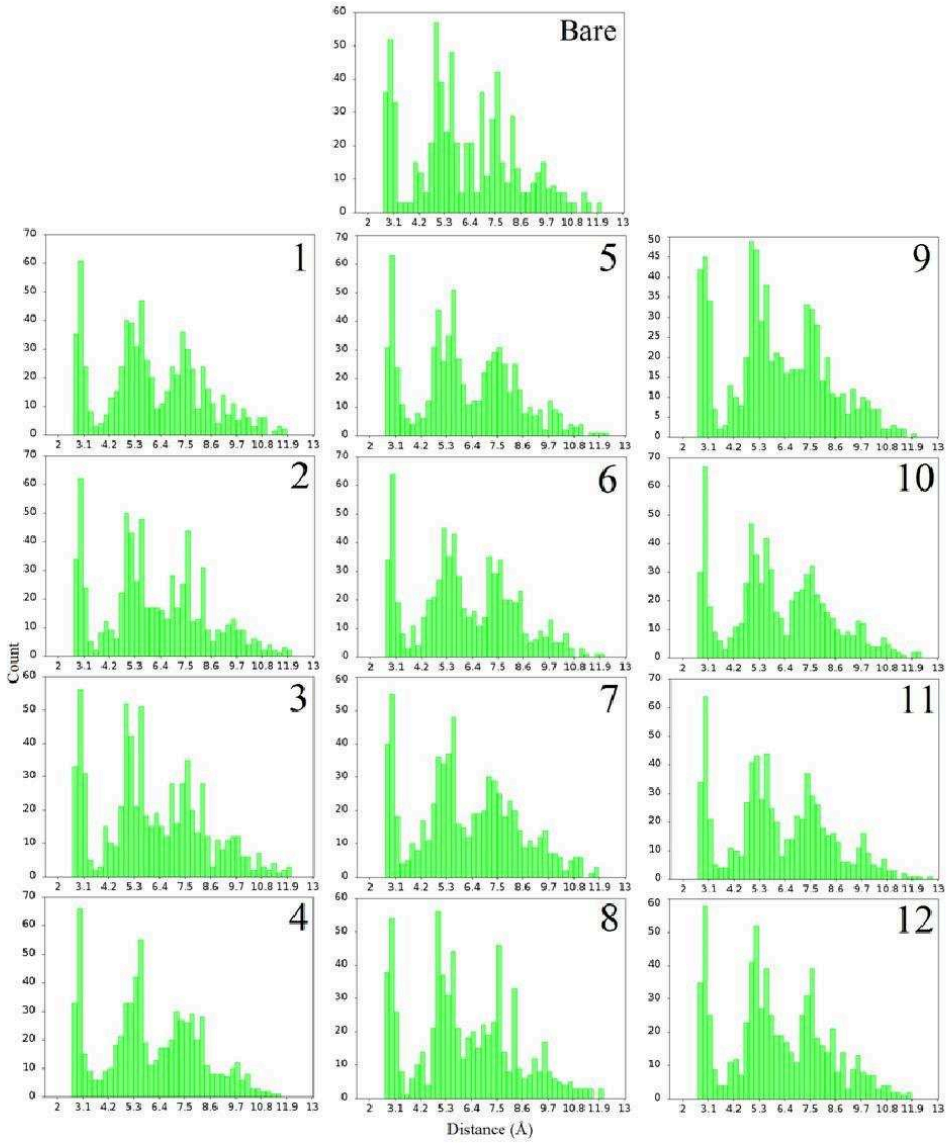

Figure S15. Distribution of distances among gold atoms in the bare Au_{38} and in **NHCa**-ligated clusters in the gas phase. The equilibrium structure and the natural charges have been calculated at the CAM B3LYP DFT LANL2MB / 6 – 31G(d) level. The numbering of the panels refers to the numbering of the equilibrium geometries shown in Figure 6 of the main text. Further explanations are given on page S15.

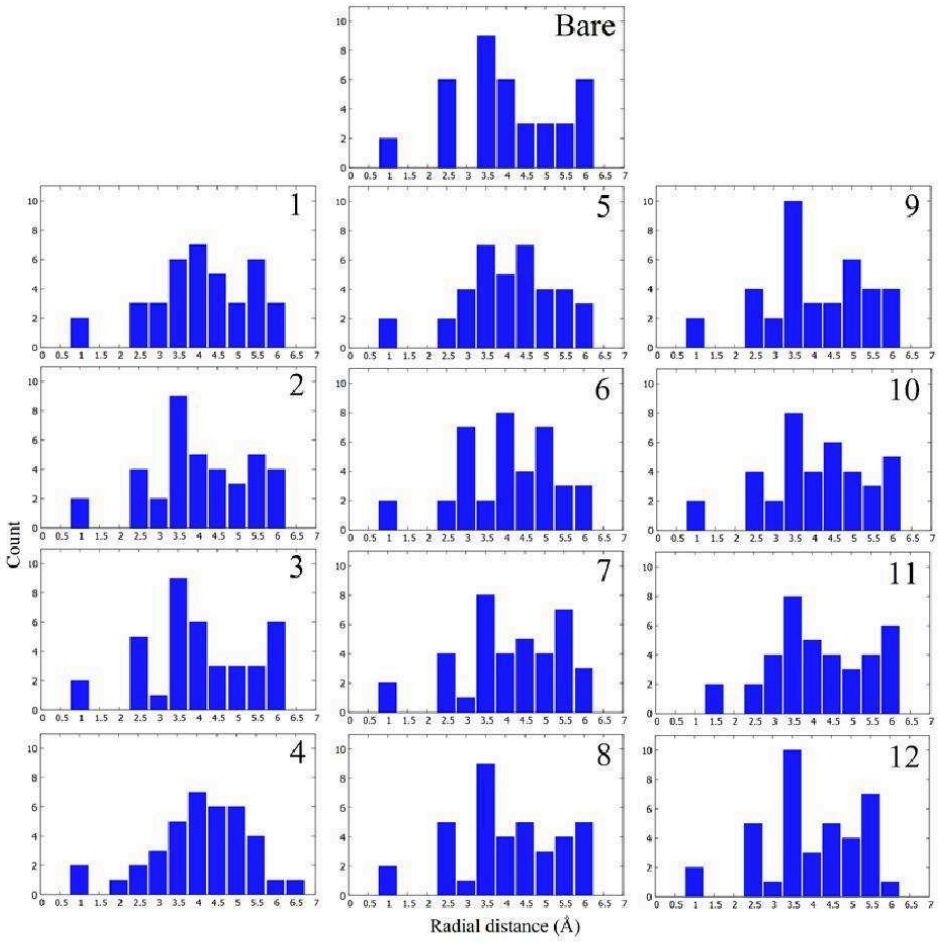

Figure S16. Radial distribution of the gold atoms in the bare Au_{38} and in **NHCa**-ligated clusters in the gas phase. The equilibrium structure and the natural charges have been calculated at the CAM B3LYP DFT LANL2MB / 6 – 31G(d) level. The numbering of the panels refers to the numbering of the equilibrium geometries shown in Figure 6 of the main text. Further explanations are given on page S15.

Geometry of NHCa-Au$_{38}$ clusters

Different angles were measured in order to analyze the geometry of the bonding. Figure S17 shows the two types of angles that were taken into account. No flat surface could be found on the Au_{38} cluster. Therefore we decided to take the angle between the C_2 axis and the atom which best, qualitatively, represented the closest surface, that is, the gold atom at the top taking as a reference the position of the gold atom bound to the carbon in the ligand. Figure S18 shows in blue the gold atoms that form the angle shown in Figure S17 a), while Figure S19 shows in a similar way the gold atoms which define the angle in Figure S17 b). Qualitatively, the most perpendicular ligand arrangement, that is to say, where the C_2 ligand axis is perpendicular to the surface of the cluster, is in configuration 3. The NHC ligand, in most of the cases, binds in an "on top" position on a tetrahedron formed by 4 gold atoms. No special relation was found between the stability of the cluster and the angle of the ligand and the cluster surface nor with any other parameter.

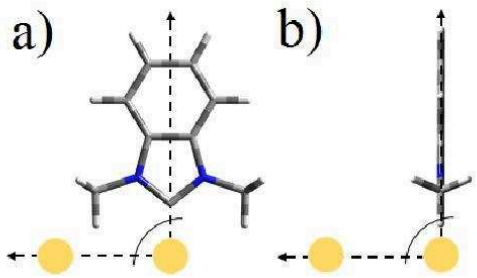

Figure S17. The two types of angles measured in the complex: a) is the angle formed by the C_2 ligand axis and the line between the gold atom bound to the NHC and the gold atom forming the smallest angle in the *same plane* of the ligand, and b) is the angle formed by the C_2 ligand axis and the line between the gold atom bound to the NHC and the gold atom forming the smallest angle in the *plane perpendicular* to the ligand. Yellow represents gold, gray stands for carbon, white for hydrogen and blue for nitrogen.

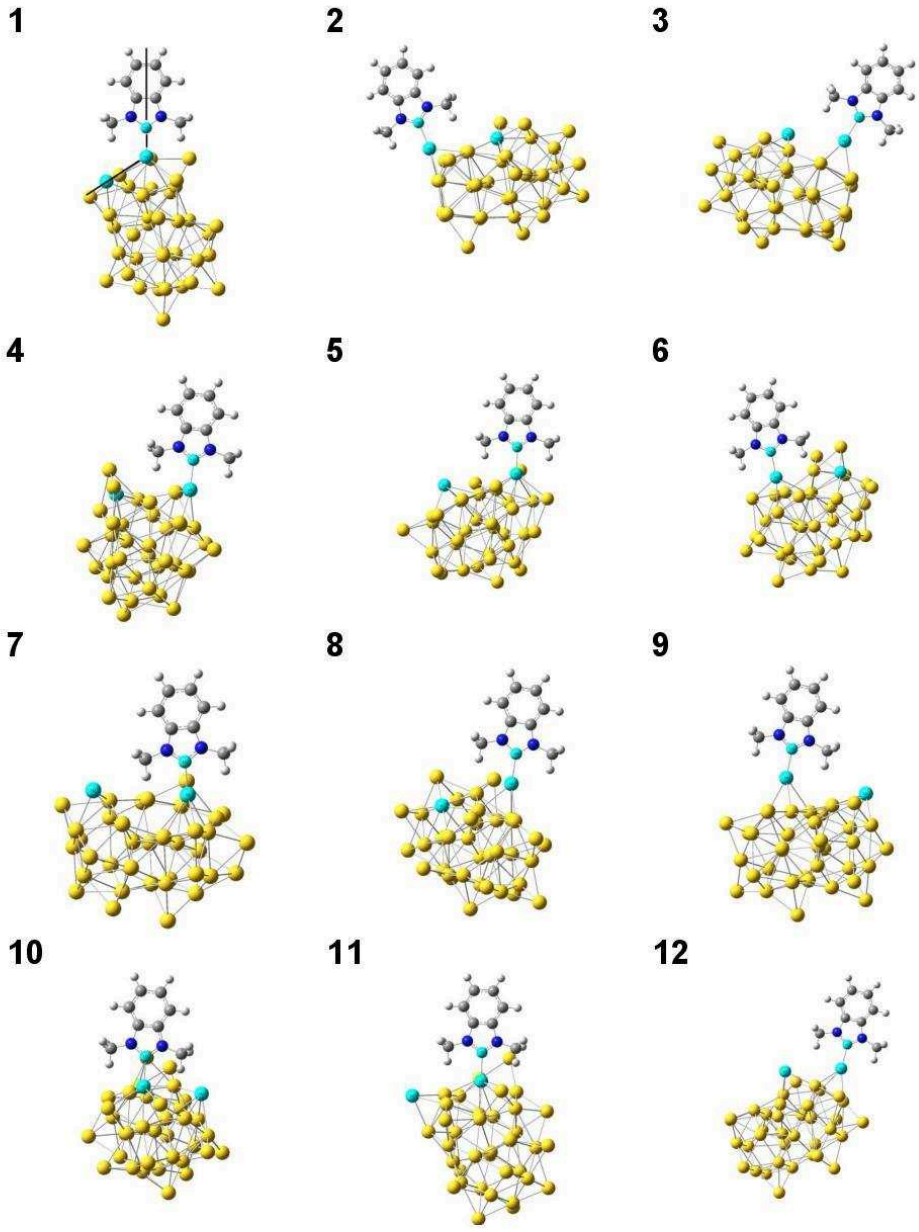

Figure S18. This scheme shows one of the angles measured in the complex (see Figure S17 a)). The angle is formed by the C_2 ligand axis and the line between the gold atom bound to the NHC and the gold atom forming the smallest angle in the same plane as the ligand (atoms in turquoise). Only configuration **1** shows the two lines forming the angle.

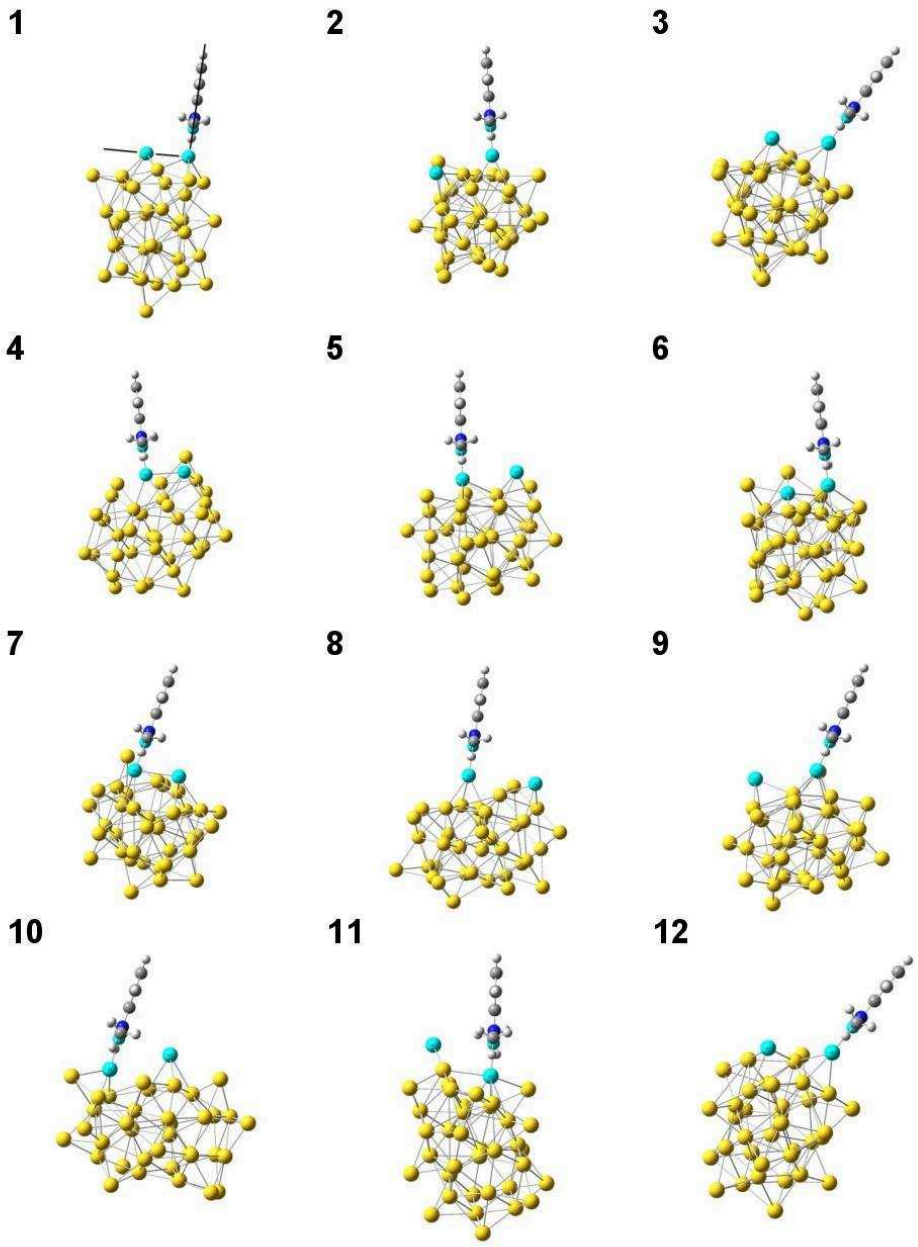

Figure S19. This scheme shows one of the angles measured in the complex (see Figure S17 b)). The angle is formed by the C_2 ligand axis and the line between the gold atom bound to the NHC and the gold atom forming the smallest angle in the plane perpendicular to the ligand (atoms in turquoise). Only configuration **1** shows the two lines forming the angle.

Geometry of the NHCa-Au$_{38}$ cluster in DMSO-d_6 (configuration 6)

The most stable configuration of the **NHCa**-Au$_{38}$ cluster (labeled 6 in the Figure 6 of the manuscript) was used as starting configuration for optimization. The equilibrium structure of the complex was optimized once again but now in the presence of DMSO-d_6 as a solvent. The geometry optimization has been performed at the DFT CAM-B3LYP level. The relativistic pseudopotential and basis set LANL2MB was used in the case of the gold cluster, while 6 – 31G(d) was employed for the NHC ligand. The polarizable continuum model (PCM) was used to evaluate the effect of the DMSO. Figure S20 shows the optimized structure of **NHCa**-Au$_{38}$.

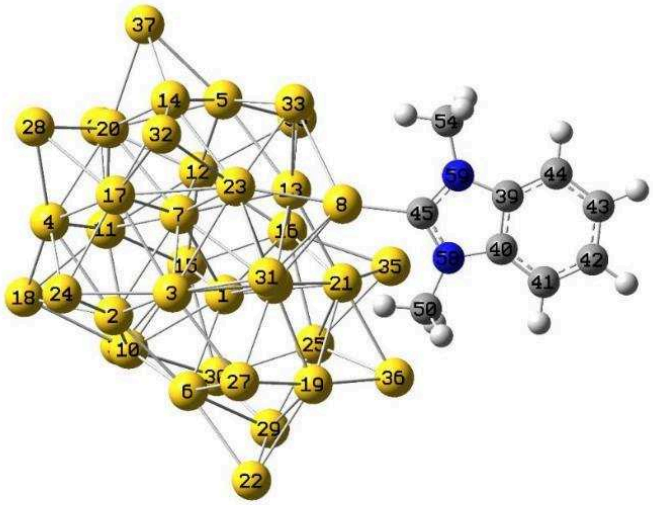

Figure S20. Equilibrium structure of the **NHCa**-Au$_{38}$ cluster in DMSO-d_6 (configuration 6).

Distribution of distances among the 38 gold atoms and radial distribution of gold atoms in NHCa-Au$_{38}$ cluster in the gas phase and d_6-DMSO.

The distributions of distances among all the 38 gold atoms for the **NHCa**-Au$_{38}$ cluster in the gas phase and in DMSO-d_6 are shown in Figures S21a and S21b respectively. As it can be seen, there is no significant difference between these two distributions. The distribution of gold atoms as a function of the radial distance taken from a reference point (which is the middle point laying on the straight line linking the two central Au atoms 1 and 7 of the Au$_{38}$ cluster in Figure S20) for the **NHCa**-Au$_{38}$ cluster in the gas phase and in DMSO-d_6 are shown in Figures S22a and S22b, respectively. Some differences can be seen, but no significant impact can be detected. For example, the C(45)-Au(8) distances are very similar, since it is 2.08295 Å in the gas phase and 2.08247 Å in DMSO. The largest distance between Au atoms (which corresponds in both cases to the distance between Au(22) and Au(37), see Figure S20) is 11.95 Å in the gas phase and 12.12 Å in DMSO-d_6.

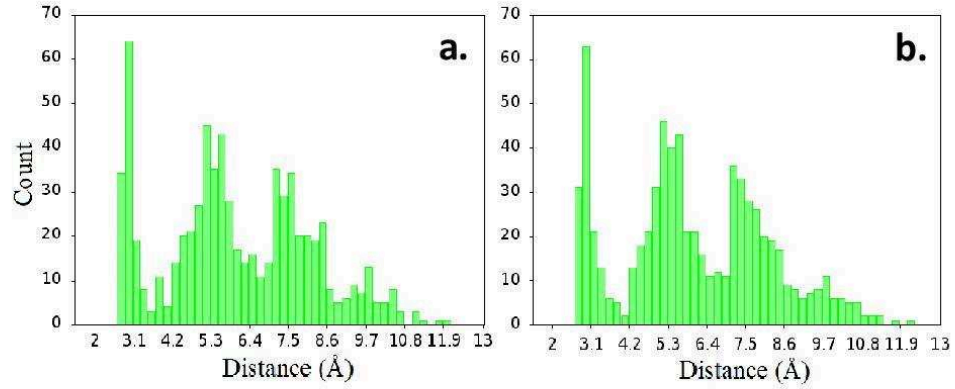

Figure S21. Distribution of distances among gold atoms of the **NHCa**-Au_{38} cluster in the gas phase (a) and in DMSO-d_6 (b). The equilibrium structure and the natural charges have been calculated at the DFT LANL2MB / 6 – 31G(d) level.

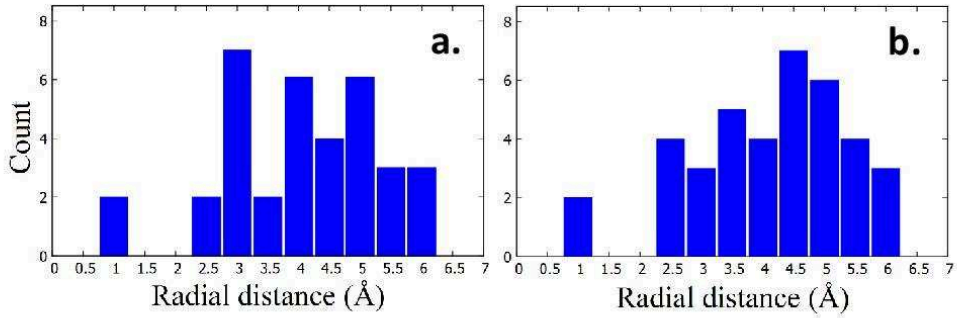

Figure S22. Radial distribution of the gold atoms of the **NHCa**-Au_{38} in the gas phase (a) and in DMSO-d_6 (b). The equilibrium structure and the natural charges have been calculated at the DFT LANL2MB / 6 – 31G(d) level.

Distribution of distances among the 38 gold atoms and radial distribution of gold atoms atoms in the bare Au_{38}, NHCa-Au_{38}, $(NHCa)_2$-Au_{38} and $(NHCa)_9$-Au_{38} clusters in the gas phase.

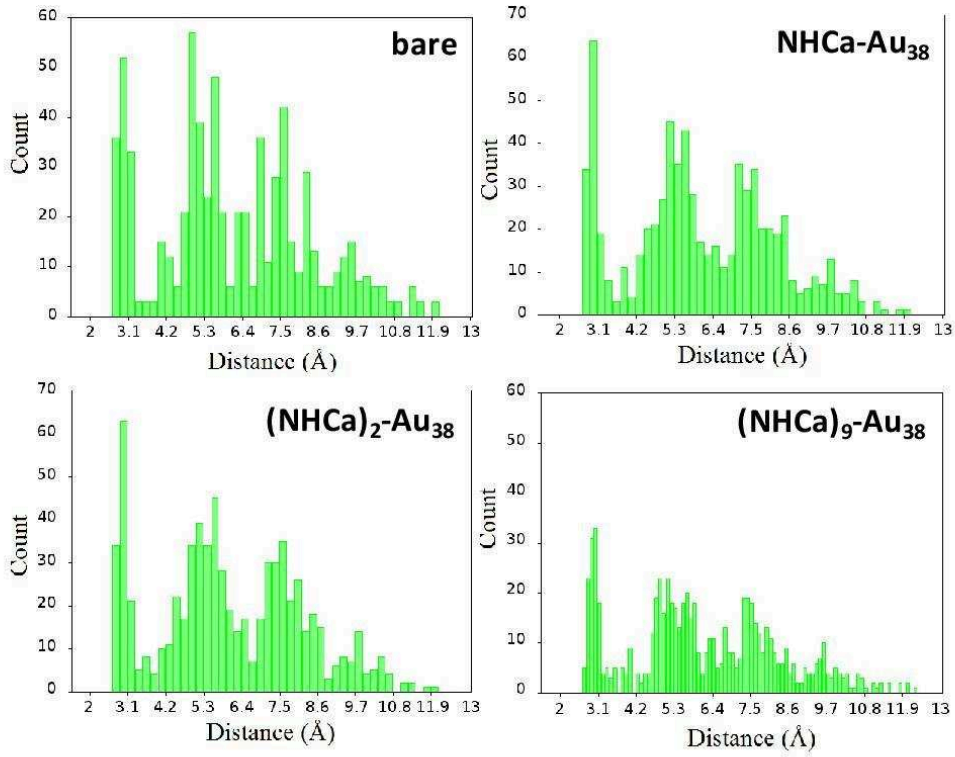

Figure S23. Distribution of distances among gold atoms in the bare Au_{38}, **NHCa**-Au_{38}, (**NHCa**)$_2$-Au_{38} and (**NHCa**)$_9$-Au_{38} clusters in the gas phase. The equilibrium structures have been calculated at the DFT CAMB – B3LYP level using the pseudopotential and basis set LANL2MB in the case of gold while the 6 – 31G(d) basis set was used in the case of the NHC ligand.

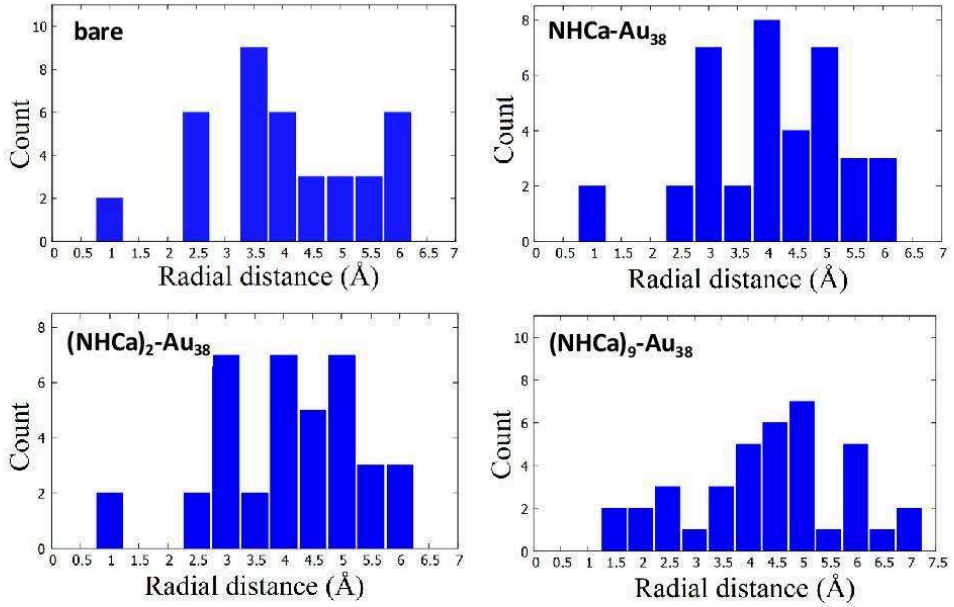

Figure S24. Radial distribution of the gold atoms of the bare Au_{38}, **NHCa**-Au_{38}, (**NHCa**)$_2$-Au_{38} and (**NHCa**)$_9$-Au_{38} clusters in the gas phase. The equilibrium structures have been calculated at the DFT CAMB – B3LYP level using the pseudopotential and basis set LANL2MB in the case of gold while the 6 – 31G(d) basis set was used in the case of the NHC ligand.

3. Calculation of NMR spectra.

Calculation of ^{13}C NMR chemical shifts for the complex 3a.

Geometry of complex **3a** was optimized with and without the counter ion BF_4^- and the ^{13}C NMR spectra were calculated and compared to experimental data (Figure S26).

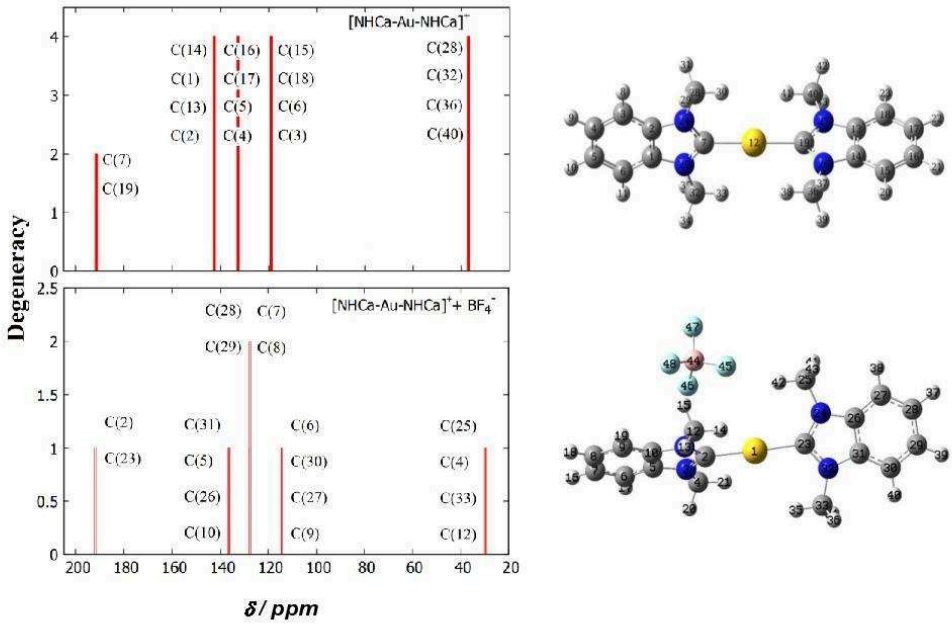

Figure S26. Computed ^{13}C NMR spectra of complex **3a** with (bottom) and without (top) BF_4^- anion in DMSO-d_6. TMS (tetramethylsilane) was used as ^{13}C NMR reference. All calculations were performed at the DFT CAM – B3LYP level of theory. The relativistic pseudopotentials and basis set LANL2DZ were used in the case of gold while 6 – 311+G(2d,p) was employed for the other atoms.

Calculation of ^{13}C NMR chemical shifts for the NHCa-Au_{38} cluster.

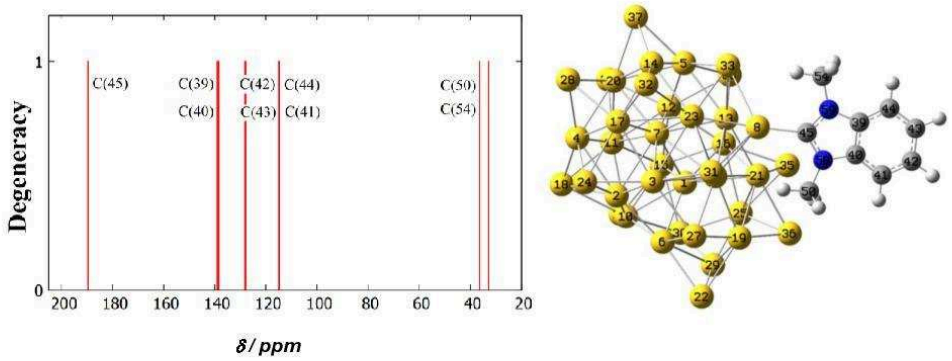

Figure S27. Computed ^{13}C NMR spectrum of **NHCa**-Au_{38} cluster in configuration 6 (see Figure 6) in DMSO-d_6. TMS (tetramethylsilane) was used as ^{13}C NMR reference. Calculations were performed at the DFT CAM – B3LYP level of theory; the relativistic pseudopotential and basis set LANL2MB were used in the case of gold while 6 – 311+G(2d,p) was employed for the other atoms.

Table S7. Values of the computed ^{13}C NMR chemical shifts in DMSO-d_6 of the **NHCa**-Au_{38} cluster and their degeneracy. TMS (tetramethylsilane) was used as ^{13}C NMR reference.

Label	Configuration 6 Computed δ ppm (degeneracy)	Configuration 2 Computed δ ppm (degeneracy)
C(45)	189.62 (1)	187.33 (1)
C(39)	138.99 (1)	138.13 (1)
C(40)	138.42 (1)	138.32 (1)
C(42)	128.15 (1)	128.30 (1)
C(43)	127.94 (1)	128.27 (2)
C(44)	114.85 (1)	115.02 (1)
C(41)	114.70 (1)	115.19 (1)
C(50)	36.35 (1)	32.68 (1)
C(54)	32.81 (1)	33.61 (1)

Calculation of ^{13}C NMR chemical shifts for the $(NHCa)_2$-Au_{38} cluster.

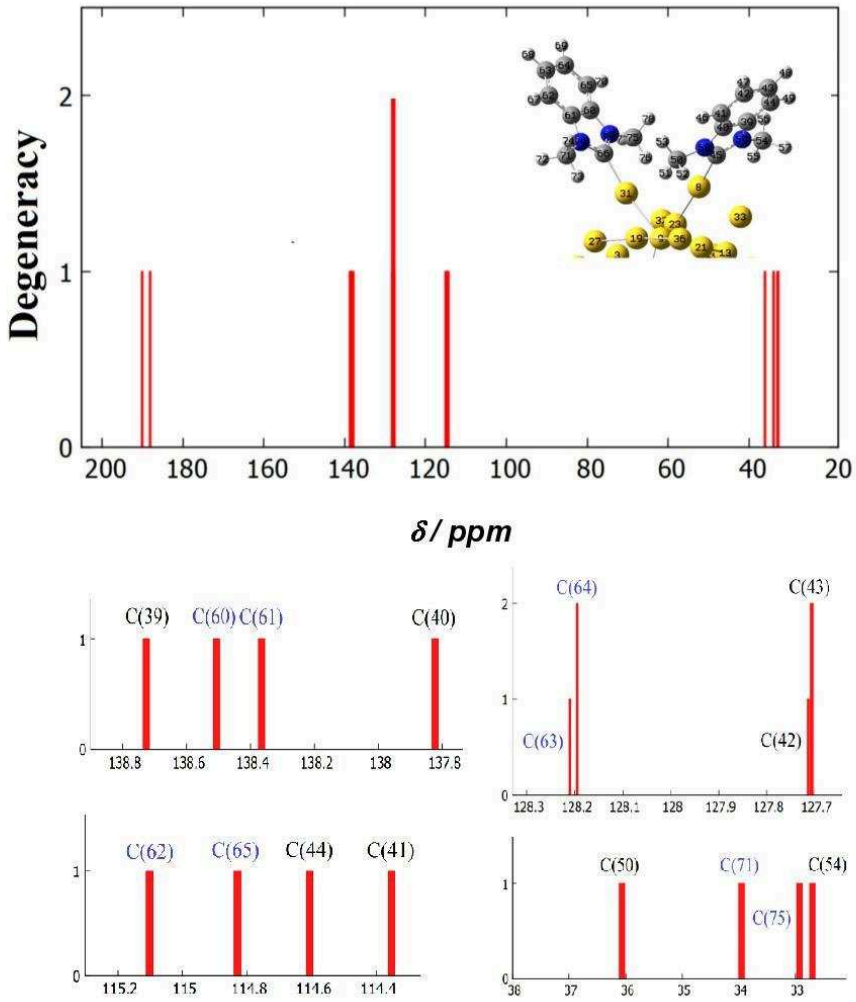

Figure S28. Computed ^{13}C NMR spectrum of the the $(\mathbf{NHCa})_2$–Au_{38} system in DMSO-d_6. TMS (tetramethylsilane) was used as ^{13}C NMR reference. All calculations have been performed at the DFT CAM–B3LYP level of theory. The relativistic pseudopotential and basis set LANL2MB were used in the case of gold while for the other atoms 6–311+G(2d,p) was employed.

Table S8. Values of the computed ^{13}C NMR chemical shifts of the (**NHCa**)$_2$-Au$_{38}$ cluster and their degeneracy in DMSO-d_6. TMS (tetramethylsilane) was used as ^{13}C NMR reference. All calculations have been performed at the DFT CAM–B3LYP level of theory. The relativistic pseudopotential and basis set LANL2MB were used in the case of gold while for the other atoms 6–311+G(2d,p) was employed.

	Label	Computed δ ppm (degeneracy)
	C(75)	32.9322 (1)
NHCa	C(71)	33.9555 (1)
on Au n°31	C(62)	115.102 (1)
	C(65)	114.83 (1)
	C(63)	128.21 (1)
	C(64)	128.195 (2)
	C(61)	138.366 (1)
	C(60)	138.506 (1)
	C(66)	190.104 (1)
	C(54)	32.705 (1)
NHCa	C(50)	36.069 (1)
on Au n°8	C(41)	114.352 (1)
	C(44)	114.607 (1)
	C(42)	127.706 (2)
	C(43)	127.713 (1)
	C(40)	137.824 (1)
	C(39)	138.726 (1)
	C(45)	188.164 (1)

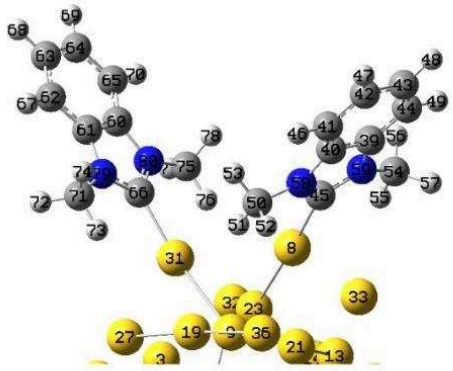

Calculation of ^{13}C NMR chemical shifts for the (NHCa)$_9$-Au$_{38}$ cluster.

Table S9. Computed ^{13}C NMR chemical shifts of the (**NHCa**)$_9$-Au$_{38}$ cluster in DMSO-d_6. TMS (tetramethylsilane) was used as ^{13}C NMR reference. All calculations have been performed at the DFT CAM–B3LYP level of theory. The relativistic pseudopotential and basis set LANL2MB were used in the case of gold while for the other atoms 6–311+G(2d,p) was employed.

Au$_{38}$(NHCa)$_9$

Signal Label	Interval of δ (ppm)			Δδ (ppm)
a	190.08	to	194.05	**3.97**
b	137.80	to	139.59	**1.79**
c	127.18	to	128.15	**0.97**
d	113.70	to	115.28	**1.58**
e	30.72	to	36.01	**5.29**

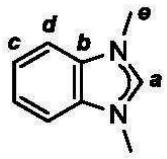

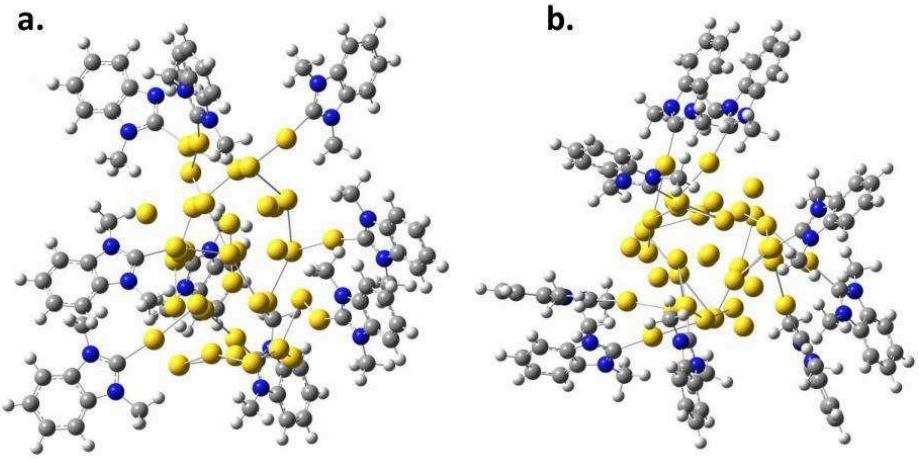

*Front view (a) and side view (b) of the (**NHCa**)$_9$-Au$_{38}$ cluster.*

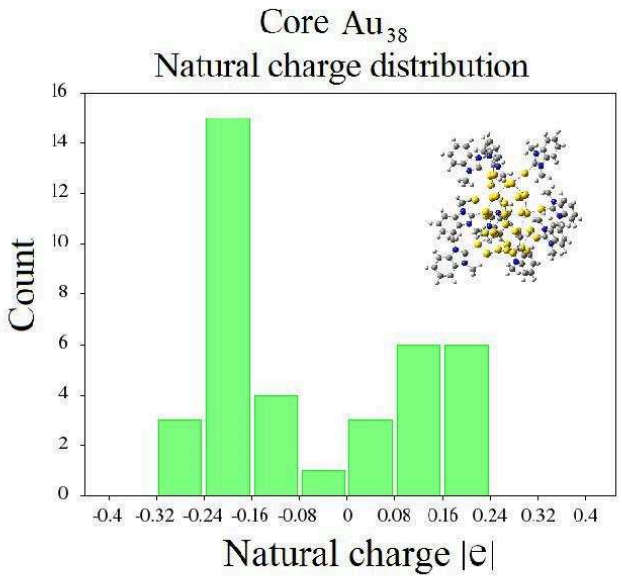

Figure S29. Natural charge distribution of the core Au_{38} of the (**NHCa**)$_9$-Au_{38} cluster. The equilibrium structure and the natural charges were calculated at the DFT CAM B3LYP LANL2MB / 6 – 31G(d) level.

Table S10. Overview of the experimental and computed ^{13}C NMR chemical shifts of the compounds presented in the manuscript in DMSO-d_6. TMS (tetramethylsilane) was used as ^{13}C NMR reference.

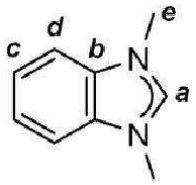

	^{13}C δ (ppm)[a,b]				
	carbene *a*	**aromatic *b***	**aromatic *c***	**aromatic *d***	**N-Me *e***
[(**NHCa**)$_2$Au]BF$_4$ exp. **3a**	190.19	133.59	124.64	112.14	34.84
[(**NHCa**)$_2$Au]$^+$ calc.	191.54 (2)	142.51 (4)	132.60 (4)	119.00 (4)	36.89 (4)
[(**NHCa**)$_2$Au]BF$_4$ calc. **3a**	192.29 (1) 191.40 (1)	136.92 (1) 136.53 (1) 136.39 (1) 136.13 (1)	127.93 (1) 127.90 (2) 127.32 (1) 127.29 (1)	114.68 (1) 114.58 (1) 114.42 (1) 114.05 (1)	30.14 (1) 29.63 (1) 29.42 (1) 29.27 (1)
(**NHCa**)-Au$_{38}$ config. 6	189.62 (1) ***Δδ = 0.00***	138.99 (1) 138.42 (1) ***Δδ = 0.57***	128.15 (1) 127.94 (1) ***Δδ = 0.21***	114.85 (1) 114.70 (1) ***Δδ = 0.15***	36.35 (1) 32.81 (1) ***Δδ = 3.54***
(**NHCa**)-Au$_{38}$ config. 2	187.33 (1) ***Δδ = 0.00***	138.32 (1) 138.13(1) ***Δδ = 0.19***	128.30 (1) 128.27 (1) ***Δδ = 0.03***	115.19 (1) 115.02 (1) ***Δδ = 0.17***	33.68 (1) 32.61 (1) ***Δδ = 1.07***
(**NHCa**)$_2$-Au$_{38}$	190.10 188.16 ***Δδ = 1.94***	138.51 (1) 138. 37 (1) 138.73 (1) 137.82 (1) ***Δδ = 0.69***	on Au(31) 128.21 (1) 128.20 (1) on Au(8) 127.71 (1) 127.71 (1) ***Δδ = 0.50***	115.10 (1) 114.83 (1) 114.61 (1) 114.35 (1) ***Δδ = 0.75***	33.93 (1) 32.96 (1) 36.07 (1) 32.71 (1) ***Δδ = 3.36***
(**NHCa**)$_9$-Au$_{38}$	from 194.05 to 190.08 ***Δδ = 3.97***	from 139.59 to 137.80 ***Δδ = 1.79***	from 128.15 to 127.18 ***Δδ = 0.97***	from 115.28 to 113.70 ***Δδ = 1.58***	from 36.01 to 30.72 ***Δδ = 5.29***

[a] Numbers in parentheses represent the degeneracy for a given configuration.

[b] Computational studies were performed at the CAM-B3LYP.

IV. References

[1] *CrysAlis PRO*. Agilent (2012); Agilent Technologies, Yarnton, England.
[2] Van der Lee, A. *J. Appl. Crystallogr.* **2013**, *46*, 1306.
[3] Palatinus, L.; Chapuis, G. *J. Appl. Crystallogr.* **2007**, *40*, 786.
[4] Betteridge, P. W.; Carruthers, J. R.; Cooper, R. I.; Prout, K.; Watkin, D. J. *J. Appl. Crystallogr.* **2003**, *36*, 1487.
[6] Hu, J. J.; Li, F.; Hor, T. S. A. *Organometallics*, **2009**, *28*, 1212.
[7] Jian, F.; Wang, H.; Xiao, H.; Liu, G. *Jiegou Huaxue* **2003**, *22*, 669.
[8] Guo, S.; Sivaram, H.; Yuan, D.; Huynh, H. V. *Organometallics*, **2013**, *32*, 3685.
[9] Rodríguez-Castillo, M.; Laurencin, D.; Tielens, F.; Van der Lee, A.; Clément, S.; Guari, Y.; Richeter, S. *Dalton Trans.* **2014**, *43*, 5978.
[10] (a) Wang, H. M. J.; Chen, C. Y. L.; Lin, J. B. *Organometallics* **1999**, *18*, 1216. (b) Wang, H. M. J.; Vasam, C. S.; Tsai, T. Y. R.; Chen, S.-H.; Chang, A. H. H.; Lin, I. J. B. *Organometallics,* **2005**, *24*, 486.
[11] Huynh, H. V.; Guo S.; Wu, W. *Organometallics*, **2013**, *32*, 4591.
[12] Amendola, V.; Bergamaschi, G.; Boiocchi, M.; Frabbrizzi, L.; Fusco, N. *Dalton Trans.* **2011**, *40*, 8367.